

The Impact of Topographic and Geological Features on Deformations of the Upper Crust

Dissertation

zur Erlangung des akademischen Grades doctor rerum naturalum

(Dr. rer. nat.)



vorgelegt dem Rat der Chemisch-Geowissenschaftlichen Fakultät der
Friedrich-Schiller-Universität Jena

von Diplom-Geophysiker André Gebauer
geboren am 09. November 1978 in Sömmerda

Gutachter

1. PD Dr. habil. Corinna Kroner, GFZ Potsdam
2. Prof. Dr. Gerhard Jentsch, FSU Jena
3. Prof. Dr. Georg Kaufmann, FU Berlin

Tag der öffentlichen Verteidigung: 08.07.2009

Zusammenfassung

Deformationen werden mit verschiedensten Instrumenten beobachtet, wie z.B. Strainmeter, Neigungsmesser, Seismometer und permanente GPS Stationen. Die beobachteten Deformationen setzen sich aus:

- periodischen Signalen (Gezeiten, ...)
- aperiodischen Signalen (Tektonik, ...)
- lokalen Einflüssen (Hohlraum Effekt, topografische Effekte, ...)

zusammen.

Untersuchungen haben gezeigt, dass viele durch die lokale Umgebung bedingte Effekte um einige Größenordnungen größer sein können als das eigentlich zu untersuchende Signal. Die zusätzlichen Signale werden durch die Geometrie des Messstollens (Cavity-Effekt), die Topographie, strukturgeologische und lithologische Gegebenheiten erzeugt unter Einwirkung von hydrologischen, und meteorologischen Änderungen sowie Gezeiten bzw. Ozeanauflastgezeiten (Harrison, 1976; Harrison & Herbst 1977). Um z.B. das rein tektonische Signal untersuchen zu können, ist es unabdingbar, alle anderen Anteile in den Datensätzen zu entfernen. Die im Rahmen dieser Arbeit vorgenommenen Untersuchungen dienen der Verbesserung des Verständnisses der zugehörigen Transfermechanismen und Wechselwirkungen.

In der vorliegenden Arbeit wird die Finite-Elemente-Methode mit elastischer Rheologie benutzt, um die genannten Effekte systematisch zu analysieren. Als Belastung werden beispielhaft Luftdruckänderungen betrachtet, da diese ein dominantes Störsignal darstellen. Es werden verschiedene Szenarien untersucht: Einheitliche Belastung sowie Luftdruckfronten, die in verschiedenen Richtungen über das Modell wandern, und reale meteorologische Ereignisse. Durch die verwendete elastische Rheologie können die Deformationsamplituden entsprechend der Größe realer Luftdruckänderungen skaliert werden.

Um die verschiedenen Effekte und Quellen der zusätzlichen Deformationen besser zu verstehen, wird eine dreigeteilte Untersuchung durchgeführt:

- (1) eine allgemeine systematische Untersuchung, in der Kastenmodelle verwendet werden, um generelle lokale Deformationsphänomene zu verstehen,
- (2) eine Untersuchung der lokal induzierten Deformationen für vier ausgesuchte Breitbandstationen und

- (3) Untersuchungen zu Effekten auf regionaler Skala am Beispiel von Mitteleuropa, wo sich die unter (2) betrachteten Observatorien befinden.

Für die Untersuchungen von (1) und (2) ergeben sich signifikante zusätzliche Signale sowohl für den Einfluss des Hohlraums wie auch für den der Topografie und Geologie. Es zeigt sich, dass jeder Einflussfaktor für jede Deformationskomponente berücksichtigt werden muss. Die größten Deformationsamplituden treten dominant in Komponenten auf, die senkrecht zu den untersuchten Effekten orientiert sind. Topografisch induzierte Signale liegen in der Größenordnung von 2 nstrain für Strainmeter und 2 nrad für Neigungsmesser bei einer Luftdruckänderung von 1 hPa . Signale, welche durch Hohlräume induziert sind, betragen ca. 50% der topografisch bedingten Einflüsse. Die aus der Geologie herrührenden Einflüsse wiederum sind etwa 3.5-mal größer.

Für zukünftige Observatorien können folgende Empfehlungen für Umgebungsbedingungen gegeben werden: die Topographie sollte möglichst einfach und eben sein; über dem Messtollen sollte die Überdeckung mindestens 150 m betragen, wobei der Stollen vorzugsweise gerade verlaufen sollte. Die Messinstrumente sollten so weit wie möglich und symmetrisch zu den Stollenwänden installiert werden.

Regionale Deformationen werden hauptsächlich durch die Luftdruckverteilung geprägt. Signale, die auf die Topografie und Geologie zurückgehen, liegen unter 2% und sind somit momentan vernachlässigbar. Die herkömmliche Methode zur Bestimmung regionaler Deformationen basiert auf Greenschen Funktionen. Die Ergebnisse der FE-Modellierung, der Greenschen Funktionen und beobachteten Deformationen zeigen eine sehr gute Übereinstimmung. Komplexere Ansätze als Greensche Funktionen, um Störeinflüsse zu eliminieren, bringen derzeit keine Verbesserung.

Insgesamt zeigt die vorliegende Arbeit, dass um Störeinflüsse entsprechend den Anforderungen heutiger geodynamischer Untersuchungen in den Beobachtungsdaten eliminieren zu können, die Belastungen in ihrer räumlichen und zeitlichen Variation besser bekannt sein müssen, als es heutzutage der Fall ist.

Abstract

Deformations are observable by various kinds of instruments, e.g. strainmeter, tiltmeter, seismometer, GPS-permanent station. The observed deformations contain signals of different amplitudes and greatly diverse origin:

- periodic signals (tides, ...)
- aperiodic signals (tectonics, ...)
- local effects (cavity effect, topographic effect, ...)

Investigations show that many effects caused by local surroundings of the instrument can be some orders of magnitude larger than the signals of interest. Reductions of the residual variations are indispensable for the extraction of e.g. the pure tectonical signal. One of the challenges in view of the reductions is to understand transfer mechanisms between loading and local conditions such as topography, cavity, and geological features, which lead to additional or modified deformations.

In this study systematic numerical modeling using the Finite-Element method with elastic rheology is carried out to estimate these effects. Barometric pressure changes are used as an example for the load in order to analyze the additional deformations. Different scenarios are simulated: a uniform load, a pressure front which moves over the model in different directions and actual meteorological events. As an elastic rheology is considered, the effects can be scaled to actually occurring barometric pressure variations.

In order to understand the different effects and sources related to the additionally produced deformations, the study is divided into three parts:

- (1) a principle systematic study, in which box models are used to understand the general deformation phenomena,
- (2) a study of deformations at four selected broadband observatories, and
- (3) investigations related to effects on regional scales for the example of Central Europe, where the observatory sites considered under (2) are located.

Significant strain and tilt signals are found for each of the effects (cavity, topography, lithology, and geology) studied under (1) and (2). From the investigation follows, that each impact factor needs to be considered individually for the instrument components. The largest deformation amplitudes occur dominantly in components with perpendicular orientation to the investigated effect. Amplitudes related to effects induced by the topography are in the order of magnitude of about 2 nstrain for strainmeters and about

2 nrad for tiltmeters for a barometric pressure load of 1 hPa. Effects caused by the cavity, in which the instruments are installed are estimated in the range of 50% of the topographic effect. Geology-related effects can be up to 3.5 times larger than effects due to the topography.

Conclusions regarding future observatory sites are: a simple and flat topography should be preferred; a minimum coverage of approximately 150 m should exist above the gallery, which should be simple and straight-line; and the instruments ought to be installed symmetrical as far as possible from the gallery walls.

For regional scales emerges that deformations are dominantly controlled by the barometric pressure distribution. The effects related to topographic and geological features are below 2% and thus presently negligible. A good agreement is found between deformations derived from a Green's function approach and FE-modeled deformations. Comparisons of modeled with observed deformations show also a good agreement. This confirms the suitability of Green's functions as a tool to compute large-scale loading effects.

The overall consequence of the investigations is that in order to provide reductions of disturbing effects, which satisfy present day demands in geodynamic studies, the load fields in their spatial and temporal variations need to be known in much more detail as presently the case.

Table of Contents

Zusammenfassung.....	I
Abstract.....	III
Table of Contents.....	V
List of Figures	VII
List of Tables.....	XIV
1 Introduction	1
2 Motivation, aims & scopes, and method.....	4
3 Deformations	5
3.1 Instruments.....	5
3.2 Signal content of observations	10
3.3 Impact factors under investigation.....	16
4 Numerical modeling.....	17
5 Principle investigations.....	20
5.1 Model assembly	20
5.2 Loading scenario.....	24
5.3 Results of principle studies.....	26
5.3.1 Cavity effect.....	26
5.3.2 Topographic effect.....	33
5.3.2.1 Effect of slope angles and heights on the models	33
5.3.2.2 Effects related to the instrument location	45
5.3.2.3 Effect of gallery length	46
5.3.2.4 Effect of valley width.....	51
5.3.3 Lithological effects.....	53
5.3.3.1 Effect of rock properties for homogeneous parameterized models	53
5.3.3.2 Effect of different lithological units	55
5.3.4 Effects related to faults.....	64
5.3.4.1 Effects for the plain model type	64
5.3.4.2 Effects for the 30° slope model type.....	67
5.4 Comparison of modeled and observed deformation amplitudes	71
5.5 Discussion	72
6 Effects at Central European observatories.....	73
6.1 Modeled observatories	73
6.1.1 Geodetic Observatory Wettzell.....	75
6.1.2 Sopron Observatory	76
6.1.3 Geodynamic Observatory Moxa	77
6.1.4 Black Forest Observatory.....	78

Table of Contents

6.1.5	Load scenario	79
6.2	Results.....	80
6.2.1	Geodetic Observatory Wettzell	81
6.2.1.1	Strain	81
6.2.1.2	Tilt.....	82
6.2.1.3	Displacements	83
6.2.2	Sopron Observatory	85
6.2.2.1	Strain	85
6.2.2.2	Tilt.....	86
6.2.2.3	Displacements	86
6.2.3	Geodynamic Observatory Moxa	88
6.2.3.1	Strain	89
6.2.3.2	Tilt.....	89
6.2.3.3	Displacements	91
6.2.4	Black Forest Observatory	92
6.2.4.1	Strain	92
6.2.4.2	Tilt.....	93
6.2.4.3	Displacements	95
6.3	Discussion	96
6.3.1	Strain	96
6.3.2	Tilt.....	97
6.3.3	Displacements	99
6.4	Brief comparison to observations	99
7	Investigation of deformations related to Central Europe	103
7.1	Model of Central Europe.....	103
7.2	Barometric pressure load	107
7.3	Results.....	108
7.3.1	Uniform barometric pressure load for model 1 – 5	108
7.3.2	Barometric pressure cap	113
7.3.3	The ‘Kyrill’ event	118
7.4	Discussion	124
8	Discussion, Conclusions and Outlook	125
	References	129
	Appendix	135
	Acknowledgements	159
	Selbständigkeitserklärung	161
	Curriculum Vitae.....	163

List of Figures

Fig. 3.1: Principles of deformation observations	5
Fig. 3.2: Examples for instruments sensitive to deformations. a – detection unit of the strainmeter at SOP (pers. comm. Mentés, 2008); b – quartz-tube strainmeter (right) and place for laser interferometric strainmeter (left) at MOX (pers. comm. Kühnel, 2004); c – ASKANIA borehole tiltmeter during installation at the KTB; d – STS-2 seismometer (rear right), STS-1 seismometer (three components below glass jar) installed at MOX (pers. comm. Jahr, 2008); e – GPS antenna of Sutherland (pers. comm. Kroner, 2008); f – view of WET with the radio antenna for VLBI (BKG, 2006).	6
Fig. 3.3: Measuring principle of strainmeters.	7
Fig. 3.4: Basic principles of tilt measurements: a – vertical pendulum (after Jacoby, 1966); b – horizontal pendulum (Melchior, 1983); c – water tube tiltmeter (Peters, 1978).	8
Fig. 3.5: Measurement principle of vertical tiltmeters (after Kümpel, 1982).	8
Fig. 3.6: Measurement principles of seismometers (after Bormann, 2002).	10
Fig. 3.7: Observable effects in deformation measurements (modified after Crossley et al., 1999) not scaled.	11
Fig. 3.8: Signal content of tilt measurements, classification after Kümpel (1982).	11
Fig. 3.9: Contents of deformation time series, according to origin and effects.	12
Fig. 3.10: Data example for effects on strain observations at Sopron observatory (pers. comm. Mentés, 2008).	13
Fig. 3.11: Data example for tilt records (after Gebauer, 2006; Gebauer et al., 2007).	14
Fig. 3.12: 24 hour data example of horizontal components of STS-1 seismometer at the BFO, during a sudden barometric pressure change: The tides are eliminated (pers. comm. Zürn, 2007).	15
Fig. 3.13: Impact factors: a, b – deformation of a cavity due to barometric pressure loads, c – topography, d – geology (different lithological units bordering, fault).	16
Fig. 4.1: Workflow for development of models with complex topography respectively gallery geometry.	19
Fig. 5.1: Model types considered in the principle studies.	21
Fig. 5.2: Gallery and instrumentation for studies of the pure cavity effect.	21
Fig. 5.3: Galleries and instrumentation included in the slope and valley model type and model modifications for the determination of topography-related effects.	22
Fig. 5.4: Models to investigate the effects induced by geological features.	23
Fig. 5.5: Barometric pressure loads used in the present study.	25
Fig. 5.6: Moving directions of the high pressure area relative to the model and the included gallery.	26
Fig. 5.7: Results for the cavity effect in the gallery for different rock coverage (comp. Fig. 5.2) for 1 hPa uniform barometric pressure load (different scaling).	26
Fig. 5.8: Tilt amplitudes obtained for different depths for a tiltmeter base length of 5 m and 10 m for a load acting only on the surface.	28
Fig. 5.9: Sketch of deformed gallery for barometric pressure load on the surface showing the deformation of tiltmeters at different depths.	28

List of Figures

Fig. 5.10: Signals with regard to a moving high pressure area for strain- and tiltmeters components perpendicular to the pressure front.....	30
Fig. 5.11: Deformation results regarding the cavity effect of a 300 m deep gallery and moving high pressure area for 1 hPa load acting only on the surface (comp. Fig. 5.6).	31
Fig. 5.12: Deformations due to the cavity effect for the 50 m long gallery in depths below the surface of 25 m, 50 m, 100 m, 200 m, and 300 m. For barometric pressure load a moving high pressure area (comp. Fig. 5.6) is used considering the following two load cases: barometric pressure acts only on the surface, and on the surface and inside the gallery.	32
Fig. 5.13: Displacements related to a 30° slope model and 1 hPa barometric pressure load.	34
Fig. 5.14: Deformations obtained for the slope and valley models with gallery type A included Fig. 5.3a (different scaling). See Fig. 5.3c, f for model type and modification. The three columns correspond to the different combinations of deformations obtained in front and inside the gallery and the pressure loading being limited to the surface and acting additionally also inside the gallery.	36
Fig. 5.15: Deformations obtained for the slope and valley models with gallery type B included Fig. 5.3b (different scaling). See Fig. 5.3c, f for model type and modification.	37
Fig. 5.16: Deformations obtained for the slope model for varying slope angle and height (see Fig. 5.3a, c, d) with gallery type A included (different scaling).	39
Fig. 5.17: Deformations obtained for the slope and valley models for a 90° slope angle with gallery type A included (different scaling).	40
Fig. 5.18: Deformation results for a 30° slope model type and gallery type A (Fig. 5.3a) caused by a moving high pressure area.	43
Fig. 5.19: Deformation results for a 90° slope model type and gallery type A (Fig. 5.3a) caused by a moving high pressure area.	43
Fig. 5.20: Deformation results for a 30° valley model type and gallery type A (Fig. 5.3a) caused by a moving high pressure area.	44
Fig. 5.21: Deformation results for a 30° slope model type and gallery type B (Fig. 5.3a) caused by a moving high pressure area.	44
Fig. 5.22: Deformations obtained for the slope and valley models with gallery type A and location of the strainmeter inside the gallery.	45
Fig. 5.23: Deformation effects depending on the gallery length (different scaling) for a 30° and 90° slope model (and gallery type A, Fig. 5.3a, e) for a 1 hPa barometric pressure load.	47
Fig. 5.24: Deformation effects depending on the gallery length (different scaling) for 30° slope and valley model types (and gallery type A, Fig. 5.3a, e) for a 1 hPa barometric pressure load (different scaling, the not shown tilt component perpendicular to the gallery has no signal).	48
Fig. 5.25: Deformation results for 30° slope model type and gallery of type A with variable lengths (50 m to 800 m) for a parallel to the gallery moving high pressure area.	50
Fig. 5.26: Deformations obtained for the valley type model (slope angle 30°) with gallery type A for variable valley width (different scaling).	51
Fig. 5.27: Deformation results for various valley widths and 30° reference slope model and parallel to gallery moving high pressure area (different scaling).	52
Fig. 5.28: Results for different material parameters for a slope model (slope angle 30°) and gallery type A included (different scaling).	54
Fig. 5.29: Results for different material parameters for a valley model (slope angle 30°) and gallery type A included.	54
Fig. 5.30: Results for different material parameters for a slope model (slope angle 30°) and gallery type B included.	55

List of Figures

Fig. 5.31: Model conditions for 30° slope model to investigate the effects of lithological units.....	56
Fig. 5.32: Deformation results for different rock types (G-granite, L-limestone, M-marlstone, S-sandstone) various distances of the lithological border to the instrument location using the plain model type (different scaling).....	57
Fig. 5.33: Sketch illustrating deformations related to different adjacent to each other rock types for uniform barometric pressure loading a plain model.	58
Fig. 5.34: Moving directions of the high pressure area related to the investigation of the impact of two different lithological units on deformations.	58
Fig. 5.35: Deformation results for different rock types adjacent to each other(sandstone - granite) in various distances to the instrument location for high pressure areas moving across the plain model type.	59
Fig. 5.36: Comparison of strain amplitudes obtained for models containing on the one hand geological and on the other hand topographic features.....	60
Fig. 5.37: Deformation results for a 30° slope model type and lithological units. The border of the lithological unit is oriented parallel to the gallery (comp. Fig. 5.31a).....	61
Fig. 5.38: Deformation results for a 30° slope model type with gallery type A included and parallel to the gallery oriented lithological border (comp. Fig. 5.31a) for a parallel to the gallery moving high pressure area (different scaling).	62
Fig. 5.39: Deformation results for a 30° slope model type and different lithological units. The border of the lithological unit is oriented perpendicularly to the gallery (comp. Fig. 5.31b).....	63
Fig. 5.40: Deformation results for a 30° slope model type and different lithological units (sandstone - granite). The border of the lithological unit is oriented perpendicularly to the gallery (comp. Fig. 5.31c). The tilt component perpendicularly oriented to the gallery is not shown as no signal occurs.....	64
Fig. 5.41: Deformation results for moving high pressure areas for the plain model type and faults.....	66
Fig. 5.42: Deformations related to the plain model type and a fault for a moving high pressure area.	66
Fig. 5.43: Deformation results for a 30° slope model type and gallery type A. Parallel to the gallery in a distance of 50 m a fault with a length of 300 m and a depth of 100 m is included. For load orthogonally moving high pressure areas are considered.	68
Fig. 5.44: As Fig. 5.43, but the fault is located at the entrance of the gallery and is perpendicularly oriented.....	69
Fig. 5.45: As Fig. 5.43, but the fault is located 50 m behind the gallery head and is perpendicularly oriented to the gallery.	70
Fig. 5.46: Observed deformations in the EW-strain component and barometric pressure at Moxa observatory compared to modeled deformations (a). The deformation is modeled using a valley model type with a slope angle of 20° and a height of 100 m (b).....	71
Fig. 6.1: Map of Central Europe and locations of the observatories Moxa (MOX), Wettzell (WET), Black Forest (BFO), and Sopron (SOP).	74
Fig. 6.2: Sketch of the model for the Geodetic Observatory Wettzell (a) and the plain reference model (b) with assumed instrumentation.....	75
Fig. 6.3: Sketch of the model of Sopron Observatory (a) and the slope type reference model (b) with assumed instrumentation.	76
Fig. 6.4: Sketch of the model for Geodynamic Observatory Moxa (a) and the valley type reference model (b) with assumed instrumentation.....	77
Fig. 6.5: (a) Sketch of the model for the Black Forest Observatory (BFO). The black line marks the boundary between granite (lower part) and sandstone (top). The gallery	

List of Figures

comprises (from entrance to the end) the Heinrich Gang, the Felix Kluff with the pendulum chamber, the seismometer chamber and the strainmeter array. (b) Instrumentation for the comparison at the BFO: Pendulum chamber: ASKANIA tiltmeter and four points P9 to P12 in niches used in Steffen (2006) for tilt calculations. Seismometer chamber: 8 points at three concrete piers at the northern (P1 to P4) and southern wall (P5 to P8) used in Steffen (2006) for tilt calculations. Strainmeter array: three strainmeter in NW-SE, NE-SW and NS direction as well as a water tube tiltmeter. T1 and T2 denote the two ends of the water tube tiltmeter.....	78
Fig. 6.6: (a) Three different moving directions of a high pressure area over a model. Letters in brackets denote the moving direction of the high pressure area in Fig. 6.7 , Fig. 6.9 and Fig. 6.12 . (b) Sketch of a full load cycle with the loaded model area at specific time steps.	79
Fig. 6.7: Tilt and strain deformations for instruments at the gyroscope and ASKANIA borehole tiltmeter location at the Geodetic Observatory Wettzell (black and red lines) and the plain reference model (green) for high pressure areas from three different directions; (a) WE moving, (b) NS moving, (c) NE-SW moving high pressure area. Note the different scaling for tilt components. All results refer to 1 hPa of pressure change.	83
Fig. 6.8: (a) Topography of the model of the Geodetic Observatory Wettzell. (b) horizontal (arrows) and vertical (contour map) displacements for the whole model being loaded by a high pressure area (1 hPa). (c) same as (b), but only for WE displacements. (d) same as (b), but only for NS displacements.	84
Fig. 6.9: Variations for the (WE) strainmeter (black), the tiltmeter (red) and the seismometer (blue) at Sopron Observatory and the plain reference model (green) for high pressure areas from three different directions; (a) WE moving, (b) NS moving, (c) NE-SW moving high pressure area. Note the different scaling for tilt components. All results are referenced to 1 hPa of pressure change.	87
Fig. 6.10: West-east cross section through Sopron Observatory model explaining the deformations for WE moving high pressure area at different time steps. The cross section of the undeformed surface is four times vertically exaggerated. The deformed surface is sketched to illustrate the deformation mechanism. Arrows next to the gallery denote the acting force induced by the actual load at the strainmeter location.	87
Fig. 6.11: (a) Topography of Sopron Observatory model. (b) horizontal (arrows) and vertical (contour map) displacements when the whole model is loaded by a high pressure area (1 hPa). (c) same as (b), but only for WE displacements. (d) same as (b), but only for NS displacements.	88
Fig. 6.12: Variations for the strainmeter (black), three tiltmeters at different depth in a borehole (red) and the seismometer (black) at the Geodynamic Observatory Moxa and the plain reference model (green) for high pressure areas from three different directions; (a) WE moving, (b) NS moving, (c) NE-SW moving high pressure area. The strainmeter and seismometer are installed inside the gallery, the tiltmeters in the valley bottom in front of the gallery. Note the different scaling for tilt components. All results are referenced to 1 hPa of pressure change.....	90
Fig. 6.13: (a) Topography of the model of the Geodynamic Observatory Moxa. (b) horizontal (arrows) and vertical (contour map) displacements when the whole model is loaded by a high pressure area (1 hPa). (c) same as (b), but only for WE displacements. (d) same as (b), but only for NS displacements.	91
Fig. 6.14: Deformations at the Black Forest Observatory for (a) the three strainmeters in NE-SW (blue), NW-SE (green), and NS direction (red), (b) the water tube tiltmeter, (c) the ASKANIA tiltmeter (d) the seismometer points in the seismometer chamber and (e) the tiltmeters in the niches in the pendulum chamber. Note the different scaling for tilt components. All results are referenced to 1 hPa of pressure change.	94
Fig. 6.15: (a) Topography of the Black Forest Observatory model. (b) horizontal (arrows) and vertical (contour map) displacements when the whole model is loaded by a high pressure area (1 hPa). (c) same as (b), but only for WE displacements. (d) same as (b), but only for NS displacements.	95

Fig. 6.16: Comparison of observed and calculated signals at Sopron Observatory from January 1 st 2007 to February 1 st 2007 (31 d). On the afternoon of January 18 th the windstorm 'Kyrill' reached the German and Dutch coasts moving eastward over Central Europe. (a) strainmeter observation (red) and reduced signal (brown) for model tides (green); (b) detided strainmeter observation (brown), barometric pressure observation (blue) and strainmeter signal until January 29 th calculated from barometric pressure signal with a regression coefficient obtained from modeling results for full load (time step 50%); (c) tide and barometric pressure reduced strainmeter data, from modeling (red), from data analysis (brown), and temperature (orange). Negative values denote extension.....	101
Fig. 6.17: Comparison of observed signals at Black Forest Observatory from January 1 st 2007 to February 1 st 2007 (31 d). On the afternoon of January 18 th the winter storm 'Kyrill' reached the German and Dutch coasts moving eastward over Central Europe. (a) Tilt observations in NS (red) and EW component (green) are tide- and drift-reduced and barometric pressure observation (blue). (b) EW-tilt observations tide, drift, and barometric pressure reduced with regression coefficient derived from modeling (light green) and from data analysis (dark green). (c) NS-tilt observations tide, drift, and barometric pressure reduced with regression coefficient derived from modeling (light red) and from data analysis (dark red).....	102
Fig. 7.1: Digital Terrain Model (DTM) used in modeling of Central Europe derived from Etopo2 (80x vertical exaggeration).....	104
Fig. 7.2: Model set-up for investigations related to Central Europe and assumed instrumentation at observatories considered. The colors mark units with identical the material parameters (comp. Tab. 7.1 , Fig. 7.2).....	105
Fig. 7.3: (a.) Barometric pressure cap above the Geodynamic Observatory Moxa and 350 km south of it with diameter of 100 km 200 km and 300 km. (b.) Barometric pressure field for Central Europe on January 1 st 2007 at 20:00 MEZ. Additionally shown is the simplified path of the 'Kyrill' centre.	107
Fig. 7.4: Displacements for model 1 (comp. Tab. 7.1) and a uniform barometric pressure load of 1 hPa.	108
Fig. 7.5: Displacements for model 2 (comp. Tab. 7.1) and a uniform barometric pressure load of 1 hPa.	109
Fig. 7.6: Displacements for model 3 (comp. Tab. 7.1) and a uniform barometric pressure load of 1 hPa.	110
Fig. 7.7: Displacements for model 4 (comp. Tab. 7.1) and a uniform barometric pressure load of 1 hPa.	111
Fig. 7.8: Displacements for model 5 (comp. Tab. 7.1) and a uniform barometric pressure load of 1 hPa.	112
Fig. 7.9: Displacements obtained at the surface for a 1 hPa barometric pressure cap of 100 km, 200 km and 300 km diameter above the geodynamic observatory Moxa using the model 5 (comp. Fig. 7.2 , Tab. 7.1 , and Tab. 7.2).	114
Fig. 7.10: Vertical deformations for an east-west cross section through the Geodynamic Observatory Moxa for a 1 hPa barometric pressure cap with a diameter of 100 km, 200 km and 300 km using the model 5 (comp. Fig. 7.2 , Tab. 7.1 , and Tab. 7.2).....	115
Fig. 7.11: Vertical deformations for an east-west cross section through the Geodynamic Observatory Moxa for a 1 hPa barometric pressure cap with a diameter of 300 km the model 3, 4, 5, 6, 7, 8, 9, 10, and Green's functions (comp. Fig. 7.2 , Tab. 7.1 , and Tab. 7.2).....	115
Fig. 7.12: Strain and tilt amplitudes calculated at the five observatory sites for model 3 and 5. As load the 1 hPa barometric pressure cap is considered. Additionally, the borders of the 'sediments' and different rocks of the upper crust (1-10) are shown (comp. Fig. 7.2 , Tab. 7.1 , and Tab. 7.2). The vertical displacement is obtained from model 5.....	117

List of Figures

Fig. 7.13: Modeled displacements at the observatories BFO, MOX, SOP, TRS, and WET for the storm 'Kyrill' in January 2007. The results are obtained from Green's functions (pers. comm. Klügel, 2009), and the model types 3, 4, and 5. The first column shows the displacements for Green's function and the observed pressure at each observatory from January 16 th 00:00 CET to January 22 nd 00:00 CET. The results for FE modeled vertical displacements are given in the second column and horizontal displacements in the third column of the four models for same time window.....	119
Fig. 7.14: Comparison of the displacements calculated with Green's function and model 10 for the 'Kyrill' event.....	120
Fig. 7.15: Comparison of the deformations for an actual barometric pressure field (d): 'Kyrill' event at January 16 th 20:00 CET (a) and uniform barometric pressure change of 1 hPa (b). (c) the difference of the vertical displacements (a)-(b).....	121
Fig. 7.16: Modeled and observed vertical displacements from the superconducting gravimeter CD034 at MOX.....	123
Fig. 7.17: Observed tilt variations at the observatory site WET compared with modeled tilt changes (amplitudes multiplied by factor 10) using the model 10 and Green's function, and barometric pressure in the time window.....	124
App. Fig. 1: Deformation results for slope model types (slope angle varied between 15° and 90° in 5° step, and 300 m slope height) and gallery type A for the parallel to the gallery moving high pressure area (different scaling).....	136
App. Fig. 2: As App. Fig. 1 but for high pressure area moving perpendicularly to gallery.....	137
App. Fig. 3 : As App. Fig. 1 but for high pressure area moving diagonally to gallery.....	138
App. Fig. 4: Deformation results for valley model types (slope angle varied between 15° and 90° in 5° step, and 300 m slope height) and gallery type A included for the parallel to the gallery moving high pressure area (different scaling).....	139
App. Fig. 5: As App. Fig. 4 but for high pressure area moving perpendicularly to gallery.....	140
App. Fig. 6: As App. Fig. 4 but for high pressure area moving diagonally to gallery.....	141
App. Fig. 7: Deformation results for a 30° slope model type of a slope height of 300 m and gallery type B included related to the moving height pressure areas.....	142
App. Fig. 8: Deformations obtained for the 30° slope model type and gallery type A and high pressure area moving parallel to the gallery.....	142
App. Fig. 9: As App. Fig. 8 but for high pressure area moving perpendicularly to gallery.....	143
App. Fig. 10: As App. Fig. 8 but for high pressure area moving diagonally to gallery.....	143
App. Fig. 11: Deformation results for a 90° slope model type (slope height varied between 25 m and 300 m) and gallery type A for the parallel to the gallery moving high pressure area (different scaling).....	144
App. Fig. 12: As App. Fig. 11 but for high pressure area moving perpendicularly to gallery....	145
App. Fig. 13: As App. Fig. 11 but for high pressure area moving diagonally to gallery.....	146
App. Fig. 14: Deformation results for a 90° valley model type (slope height varies between 25 m and 300 m) and gallery type A for the parallel to the gallery moving high pressure area (different scaling).....	147
App. Fig. 15: As App. Fig. 14 but for high pressure area moving perpendicularly to gallery....	148
App. Fig. 16: As App. Fig. 14 but for high pressure area moving diagonally to gallery (different scaling).....	149
App. Fig. 17: Deformation results for 30° slope model type and variable gallery lengths of type A (50 m to 800 m) for a perpendicular to the gallery moving high pressure area.....	150
App. Fig. 18: As App. Fig. 17 but for high pressure area moving diagonally to gallery.....	151

List of Figures

App. Fig. 19: Deformation results for perpendicular to gallery moving high pressure area related to the effect of the valley width and reference slope model for a slope angle of 30° (different scaling).....	152
App. Fig. 20: Deformation results for diagonal to gallery moving high pressure area related to the effect of the valley width and reference slope model for a slope angle of 30° (different scaling).....	152
App. Fig. 21: Deformation results for a 30° slope model type and gallery type A and parallel to the gallery oriented lithological border (comp. Fig. 5.31a) for a perpendicular to the gallery moving high pressure area (different scaling).....	153
App. Fig. 22: Deformation results for a 30° slope model type and gallery type A and parallel to the gallery oriented lithological border (comp. Fig. 5.31a) for a diagonal to the gallery moving high pressure area (different scaling).....	154
App. Fig. 23: Deformation results for a 30° slope model type and gallery type A and perpendicular to the gallery oriented lithological border (comp. Fig. 5.31b) for a parallel to the gallery moving high pressure area.....	155
App. Fig. 24: Deformation results for a 30° slope model type and gallery type A. Parallel to the gallery in a distance of 50 m a fault with a length of 300 m and a depth of 100 m is included. For load the diagonally moving high pressure areas are considered.....	156
App. Fig. 25: Deformation results for a 30° slope model type and gallery type A and fault located at the gallery entrance, perpendicularly oriented. For load diagonally moving high pressure areas are considered.	156
App. Fig. 26: Deformation results for a 30° slope model type and gallery type A included and fault located 50 m behind the gallery head perpendicular oriented. For load diagonally moving high pressure areas are considered.	157
App. Fig. 27: Locations of barometric pressure observations used for calculation of the pressure field and defined rectangular cells loading the model and locations of observatories of interest.....	158

List of Tables

Tab. 3.1: Instruments and their monitored quantity.....	6
Tab. 5.1: Local conditions at the broadband observatories Geodynamic Observatory Moxa (MOX), Black Forest Observatory (BFO), Geodetic Observatory Wettzell (WET), and Sopron Observatory (SOP).....	20
Tab. 5.2: Material parameters for principle study.....	22
Tab. 5.3: Assumed instrumentation and local conditions for models of principle study.....	24
Tab. 5.4: Deformations obtained for different lithologies with 300 m coverage above a 50 m long gallery.....	29
Tab. 5.5: Maximum amplitudes of the different effects calculated in the principle study for 1 hPa barometric pressure load.....	72
Tab. 6.1: Material parameters used in the modeling. The rock parameters are taken for Wettzell observatory (WET) from Klügel et al. (2000) and for BFO from Steffen (2006). For Sopron (SOP) the data is supplied by Mentés (pers. comm.) and for Moxa (MOX) by Kroner et al. (2005).....	74
Tab. 6.2: Tilt estimates of the EW and NS components for the 12 points in the seismometer and pendulum chamber at BFO (Fig. 6.5) under full load (time step 50%) from this study and from Steffen (2006). Units in nrad/hPa.....	99
Tab. 7.1: Model types and parameterization for Central Europe.....	106
Tab. 7.2: Material parameters of the upper crust derived from 'EuCrust-07' (Tesauro et al., 2008).....	106

1 Introduction

In the present investigation deformation signals generated by barometric pressure loading the earth's surface are studied. By observing deformations a wide field of applications is touched ranging from scientific studies (e.g. [Asch et al., 1987](#); [Jahr et al., 1991](#); [Jentzsch et al. 2000](#); [Wilhelm et al., 1997](#)), hazard assessment related e.g. to earthquakes or active volcanoes, and to engineering aspects. For scientific studies, different geodynamic phenomena (e.g. tides, tectonics) and effects related to anthropogenic activities are investigated by deformation observations with high dynamics. Therefore, several kinds of instruments ([Fig. 3.2](#)) and methods, respectively, are used:

- (borehole-) strainmeters,
- (borehole-) tiltmeters,
- seismometers,
- gravimeters,
- permanent GPS stations (Global Positioning System),
- VLBI (Very Long Baseline Interferometry),
- InSar (Interferometric Synthetic Aperture Radar), ...

This study focuses on observations with strain-, tilt-, and seismometers which are deployed temporarily or permanently at special observatory sites. At permanent observatories like the Geodynamic Observatory Moxa (MOX) ([Jahr et al., 2001](#)) or the Black Forest Observatory (BFO) ([Emter et al., 1999](#)) a number of meteorological and hydrological parameters are monitored in parallel for reduction purposes.

For region-specific studies the instruments are temporarily deployed in e.g. tectonic active areas as the Hunsrück ([Bonatz et al., 1983](#)), or the Anatolian fault zone ([Westerhaus, 1997](#); [Berckhemer et al., 1991](#)). Deformations induced by water level changes in a reservoir were e.g. investigated at Blå Sjø (Norway) ([Jentzsch & Koß 1997](#)). Anthropogenic deformations induced by water injection were studied at the Continental Deep Drilling Site in Germany (KTB) ([Jahr et al. 2005; 2006a; b; c; 2008](#)).

At the west coast of the United States of America a large-scale project was initiated to monitor large-scale crustal dynamics. With the Plate Boundary Observatory (PBO) the three-dimensional strain field is studied along the western plate margin ([Barbour et al., 2008](#); [Borsa et al., 2008](#); [Hodgkinson et al., 2008](#); [Silver et al. 1998](#)). The PBO

comprises more than 200 instrument sites with a 200 m scientific well drilled at each station. All wells are equipped with a high resolution borehole strainmeter (Gladwin, 1984; Gladwin & Hart, 1985) at the bottom, a borehole seismometer about 6 m above, a tiltmeter in about 45 m depth, a groundwater level sensor, and at the well head a GPS antenna. Depending on the instrument sites disturbing effects are to be expected, which need to be understood and reduced to study deformation in time series related to e.g. tectonics.

Generally an effect of meteorological and hydrological variations (barometric pressure, temperature, ground water level, soil moisture ...) on deformations is found. Investigations of these effects were carried out among others by Sorrels (1971), Sorrels et al. 1971, Weise (1991), Zürn & Widmer (1995), Beaudin et al. (1996), Weise et al. (1999), Mentés & Eperné-Pápai (2002), Kroner et al. (2005), Zürn & Wieland (2006), and Zürn et al. (2007). For an elimination of these impacts commonly a linear regression coefficient is used, which reduces the additional signals often only to some extent. Hence, other reduction methods were investigated, e.g. by Exß & Zürn (2002), and Zürn & Neumann (2002). Depending on the surroundings of the instrument site additional signals occur due to the cavity, in which the instruments are installed, or the topography (Emter & Zürn, 1985; Sato & Harrison, 1990; Brimich et al., 1998; Zadro & Breitenberg, 1999). These were theoretically investigated by Harrison (1976) and Harrison & Herbst (1977). Signals related to these local conditions superimpose the deformations caused by tides and tectonics in a complex pattern.

Numerical modeling using the Finite-Element method can help to understand these complex interactions. Using this method investigations for simplified 3D-models of the Geodynamic Observatory Moxa and the Black Forest Observatory were carried out to determine the impact of barometric pressure changes on horizontal deformation components (Fischer, 2002; Kroner et al., 2005; Steffen, 2006; Steffen et al., 2006). It emerged that small changes in geometrical features (e.g. including a cleft system; Kroner et al., 2005) can significantly change the deformation amplitude.

The present study also applies the Finite-Element method. In a first step for general understanding 'box models' are developed to separately investigate effects caused by the cavity (gallery), topography, and geology. In each detailed study one parameter is changed in order to investigate the respective impact (Gebauer et al. 2009). The features and parameters for the box models are based on the multi-sensor stations the Geodynamic Observatory Moxa (MOX), the Black Forest Observatory (BFO), the So-

pron Geodynamical Observatory (SOP), and the Geodetic Observatory Wettzell (WET), which are studied in detail in a further step.

Finally, the regional effect of topography and lithological heterogeneities on deformations is investigated exemplarily for Central Europe where the previously mentioned multi-sensor stations are located. Investigation related to regional effects on deformations were carried out e.g. by Wang (1997) and Métivier et al. (2005). Wang (1997) investigated the impact of Earth's rotation, ellipticity, and lateral mantle heterogeneities. The determined effects are too small to be verifying by observations with the present accuracy of measurements. From the study of Métivier et al. (2005) emerges in a weak impact (of about 1%) due to the ellipticity. Both emphasizes the necessity for further investigations e.g. with respect to topography and lateral inhomogeneities.

2 Motivation, aims & scopes, and method

Deformation time series are composed of various signals of diverse origin (chapter 3.2). Some of these signals such as the solid earth and oceanic tides are well investigated (Wilhelm et al., 1997). Effects caused by the environment, e.g. related to barometric pressure, temperature, ground water level variations are also known, but so far not well so investigated and understood. The additional signals are induced by the cavity in which the instruments are installed, by the topography, as well as by structural-geological and lithological features. The knowledge about the additionally induced deformations is important for the various observation techniques (chapter 3.1) for analysis and interpretation of the data with regard to geodynamics.

Changes in barometric pressure produce the largest disturbing amplitudes in deformations. Based on this and due to the simple way of application, this load is used for this study. But the results are transferable to other loads. Furthermore, the investigations contribute to the development of improved reductions of load induced noise in the deformation components. For future observatory sites criteria can be derived according to which a selection should be made in order to reduce noise sources.

In order to achieve these objectives Finite-Element models are set up for the study of the various impact factors. The advantage of this study is that due to the known input parameter each factor can be investigated separately.

3 Deformations

3.1 Instruments

Deformations are measurable by various kinds of instruments. Three general observation principles exist (Fig. 3.1) for monitoring of:

- distance changes between two points (strain),
- horizontal and vertical tilt,
- displacement of points at the Earth's surface.

For these observations a number of instruments with different resolutions were developed and installed, temporarily or permanently, at observation sites worldwide.

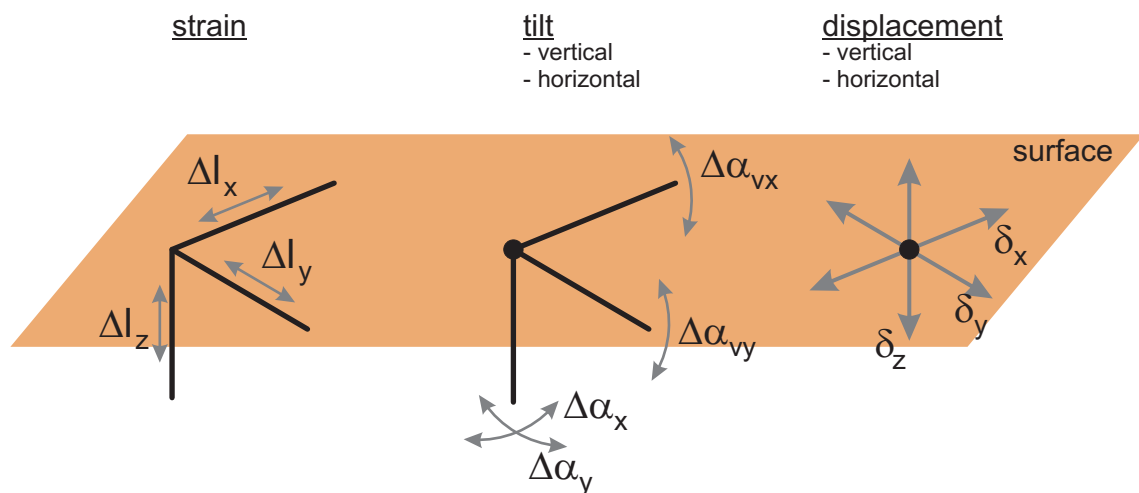


Fig. 3.1: Principles of deformation observations.

Instruments of interest in the present studies are summarized in Tab. 3.1. The observed signals go back to different sources, e.g. gravimeters are sensible to vertical displacements and to time-dependent mass changes.

In the following a brief description of the instruments is given: strainmeter (Fig. 3.2a, b), tiltmeter (Fig. 3.2c), and seismometer (Fig. 3.2d). The observation techniques for gravimetry, GPS (Fig. 3.2e) and VLBI (Fig. 3.2f) will not be discussed, but more information is found e.g. in Strang & Borre (1997), Takahashi et al. (2000), Seeber (2003), Hefty & Husa (2003), Kaplan & Hegerty (2005).

3 Deformations

Tab. 3.1: Instruments and their monitored quantity.

instrument	quantity measured
strainmeter	strain (change in distance)
tiltmeter	tilt
seismometer	acceleration, tilt
gravimeter	mass attraction, vertical displacement
GPS/VLBI	displacement

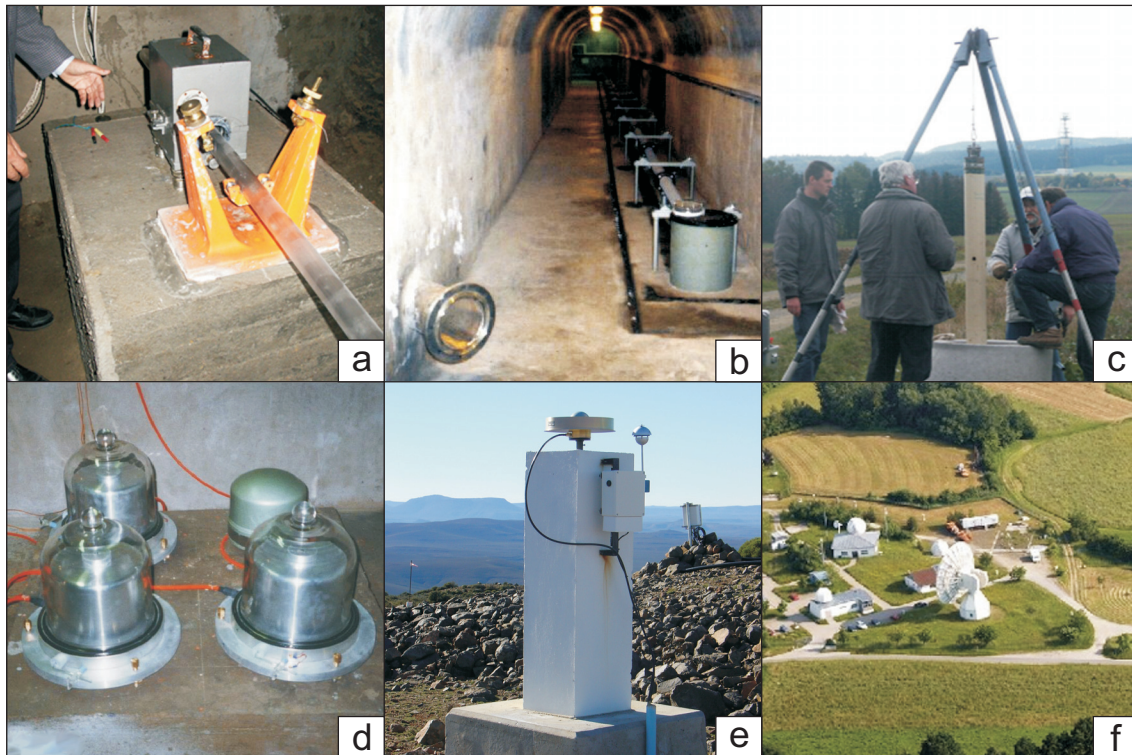


Fig. 3.2: Examples for instruments sensitive to deformations. a – detection unit of the strainmeter at SOP (pers. comm. Mentés, 2008); b – quartz-tube strainmeter (right) and place for laser interferometric strainmeter (left) at MOX (pers. comm. Kühnel, 2004); c – ASKANIA borehole tiltmeter during installation at the KTB; d – STS-2 seismometer (rear right), STS-1 seismometer (three components below glass jar) installed at MOX (pers. comm. Jahr, 2008); e – GPS antenna of Sutherland (pers. comm. Kroner, 2008); f – view of WET with the radio antenna for VLBI (BKG, 2006).

Strainmeter

Strainmeters are deployed to measure changes in the distance between two defined points (Fig. 3.3). For observing the changes different types of instruments are available:

- quartz-tube strainmeter,
- invar-wire strainmeter,
- (Michelson, Fabry-Perot) laser Interferometric strainmeter, and
- borehole strainmeter

3 Deformations

In the literature many publications with details on the various strainmeter instruments are found (e. g. Agnew, 1986, 1987; Berger & Lovberg, 1969, 1970; Wyatt et al., 1982; Zumberge & Wyatt, 1998; Sacks et al., 1971; Gladwin, 1984; Sakata & Sato, 1986; Gladwin & Hart, 1985; Hart et al., 1996; Jentzsch et al., 2006).

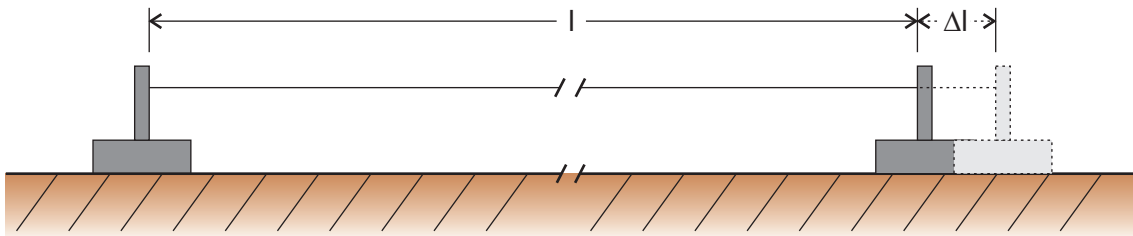


Fig. 3.3: Measuring principle of strainmeters.

For calculating the strain ε the extension change Δl is divided by the base length l of the instrument (3.1).

$$(3.1) \quad \varepsilon = \frac{\Delta l}{l}$$

The unit of ε has no dimension, but it is denoted with the name 'nstrain' for nanostrain. For comparison, 1 nstrain corresponds to a change in length by 1 μm with respect to a base length of 1 km. Strainmeters typically have a nominal resolution of 0.2 nstrain in the time domain. Deformations in this order of magnitude or bigger are thus significant in this study. In Europe the tides have maximum amplitudes in the range of some 10 nstrain.

Due to the very short base length borehole-strainmeters are more affected by the local surroundings (Agnew, 1986, 1987).

Tiltmeter

For tilt observations two principle methods have to be considered (comp. Fig. 3.1): on the one hand the observation of vertical tilts (Fig. 3.4a), and on the other hand the monitoring of horizontal tilts (Fig. 3.4b, c) (Agnew, 1986, 1987). The vertical tilt is observable by borehole tiltmeters (Graf, 1964), e.g. the ASKANIA borehole tiltmeter (Große-Brauckmann, 1979; Große-Brauckmann & Rosenbach, 1979; Gomez et al., 1995). Horizontal tilts are monitored with horizontal pendulums (e.g. the long-base tiltmeter of Grotta Gigante, Trieste, Italy (Breitenberg et al., 2006)) or water tube tiltmeters (e.g. at the Walferdange Underground Laboratory for Geodynamics, Luxembourg (d'Oreye & Zürn, 2005; Boudin et al., 2008)).

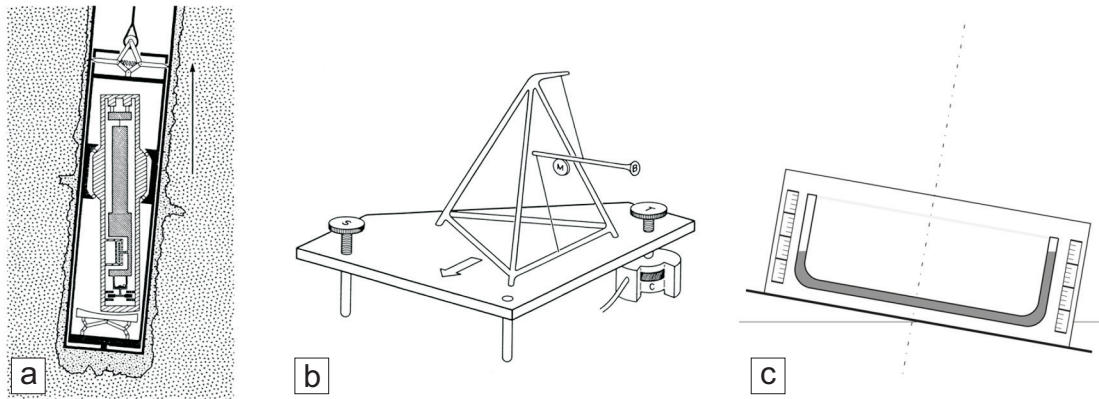


Fig. 3.4: Basic principles of tilt measurements: a – vertical pendulum (after Jacoby, 1966); b – horizontal pendulum (Melchior, 1983); c – water tube tiltmeter (Peters, 1978).

For tide-related changes in Europe maximum amplitudes of about 100 nrad (≈ 20 msec) occur for sites faraway from the coast. The resolution of tiltmeter can be illustrated by an example: If one side of a 1,000 km long bar is tilted by 1 mm, this corresponds to 1 nrad.

In the present study instruments for vertical tilt observations are considered such as the ASKANIA borehole tiltmeter (Askania, 1968; Bodenseewerk Geosystem, 1978). The nominal resolution is about 1 nrad.

Disturbing effects can be caused by gravitational mass attraction (Fig. 3.5). A mass in the vicinity deflects the instrument. A constant mass distribution only leads to constant amplitudes. Problematic are changing masses e.g. due to moving high/low pressure areas.

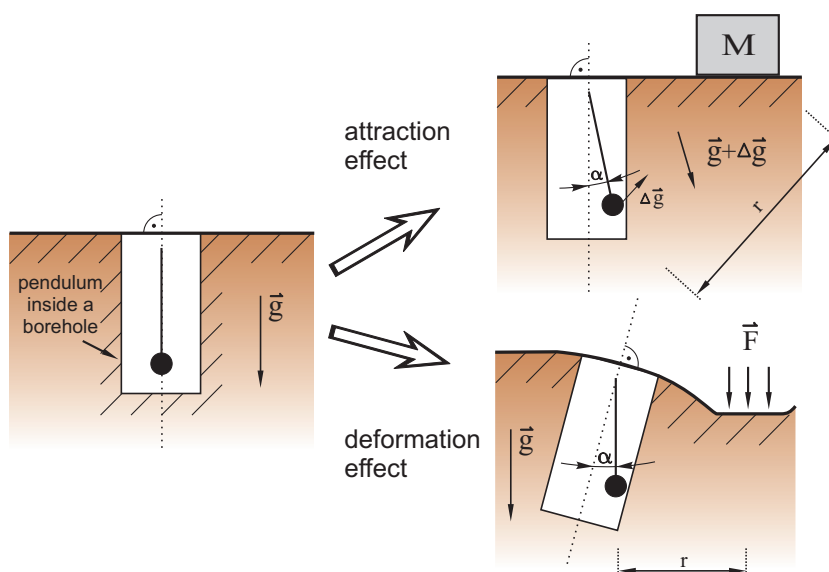


Fig. 3.5: Measurement principle of vertical tiltmeters (after Kämpel, 1982).

Apart from this, tilting is induced by deformations of the Earth's surface (Fig. 3.5) due to the earth's tides, barometric pressure changes, pore pressure change... . The attraction part is at maximum 50% of the deformation effect (Kümpel, 1982, Rabbel & Zschau, 1985). In this study only the deformation related effect is considered.

Seismometer

Seismometers monitor high frequency ground motion, mostly the acceleration, which are related to earthquakes or other sources. The mass-spring system is a useful mathematical model for a seismometer, but it is imperfect for a practical design. Modern measurement principles are given in Fig. 3.6. Most seismometers are of the pendulum type, using a mass rotating around an axis. Measurement principles for horizontal components are the Garden-gate suspension (Fig. 3.6a), the Inverted pendulum (Fig. 3.6b), or Leaf-spring astatic suspension (Fig. 3.6e). For the vertical component the LaCoste suspensions (Fig. 3.6c, d), Leaf-spring astatic suspensions (Fig. 3.6f) are possible.

Modern instruments such as the often used broadband seismometer STS-2 (Fig. 3.6g) monitor the ground motion in three components. The principle of these instruments is a homogeneous triaxial arrangement of three identical sensor constructions whose sensitive axes are inclined against the vertical like the edges of a cube standing on its corner. The vertical, north-south, and east-west directions are derived from these three sensors.

The noise induced by barometric pressure in the vicinity of seismometers has similar effects on the instrument like on tiltmeters. The largest force is gravity. It is normally cancelled by the suspension, but when the seismometer is tilted, the projection of the vector of gravity onto the axis of sensitivity changes, producing a force that is in most cases undistinguishable from a seismic signal (Bormann, 2002). Thus for modeling purposes the seismometer can be treated similar to tiltmeters.

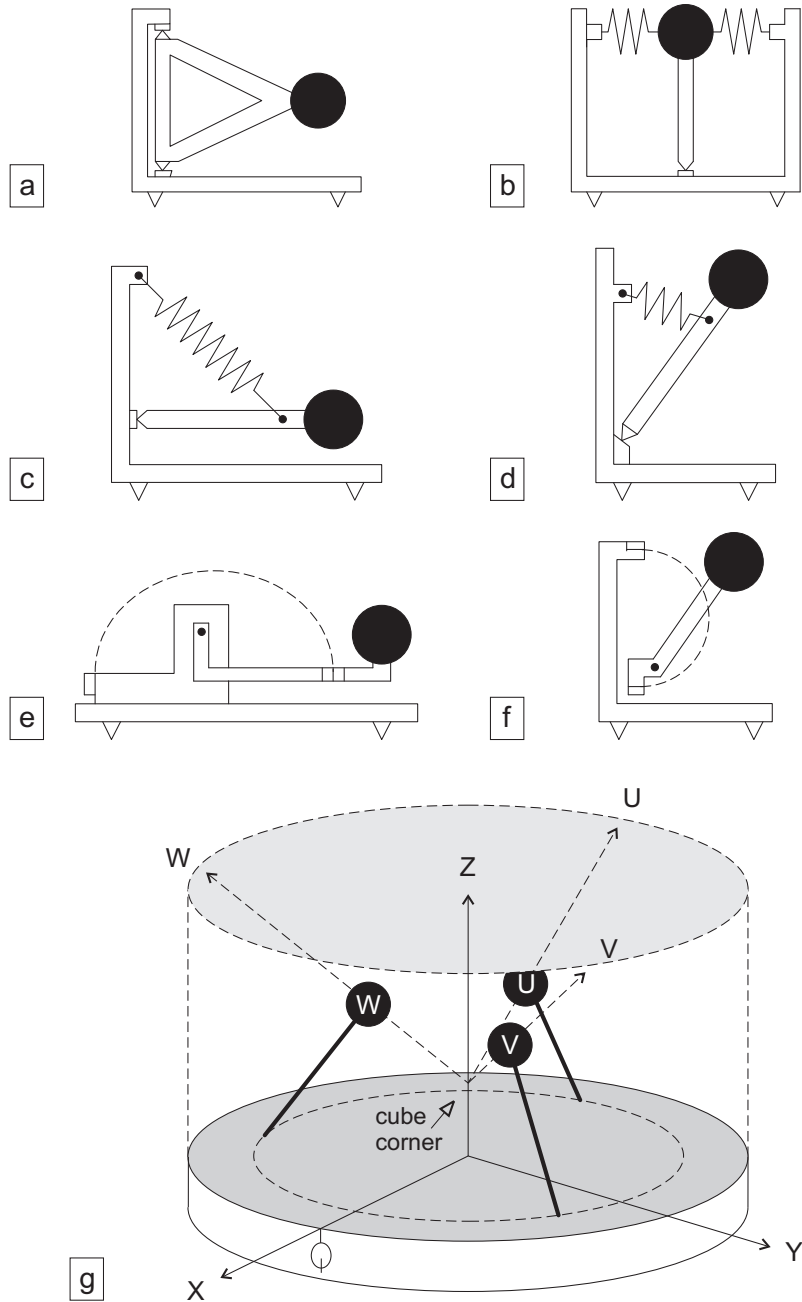


Fig. 3.6: Measurement principles of seismometers (after [Bormann, 2002](#)).

3.2 Signal content of observations

Phenomena which lead to deformations have different amplitudes and frequencies and are of different spatial extent. E.g. the earth tides are a well known and well investigated global signal in geodynamics.

In [Fig. 3.7](#) effects contained in deformation measurements are summarized. Shown are the signals of interest and the disturbing effects caused by atmosphere and hydro-

3 Deformations

logy. For tiltmeter observations [Kümpel \(1982\)](#) has summarized the signals depending on frequency band and physical cause ([Fig. 3.8](#)).

From [Fig. 3.8](#) it becomes clear that the various effects superimpose and a separation is difficult. One possible method to extract signals of interest is to reduce the record for individual effects based on models. The tides e.g. can be easily predicted as their physical origin is well known. For periodic signals a frequency-dependent high-, low-, or band pass filtering can possibly help, but the signal of interest might be modified by the filter. With respect to aperiodic contributions the reduction is difficult.

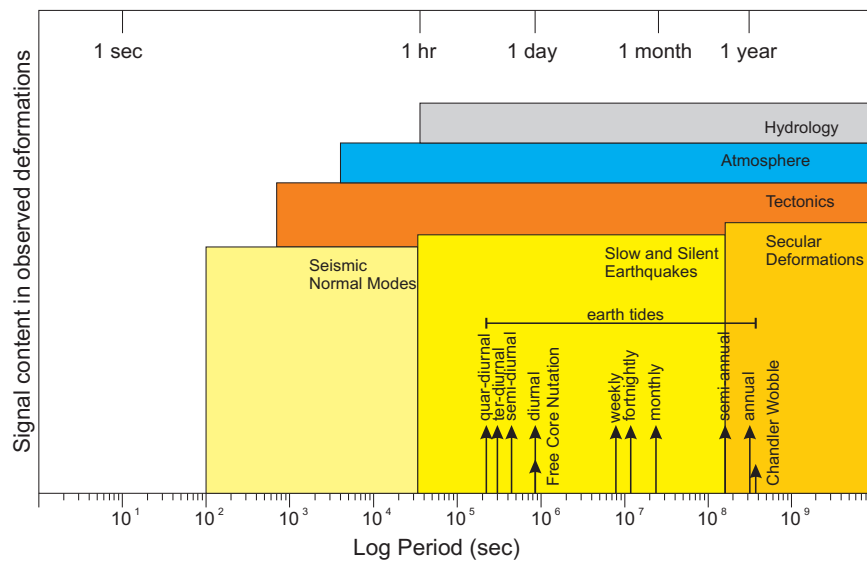


Fig. 3.7: Observable effects in deformation measurements (modified after [Crossley et al., 1999](#)) not scaled.

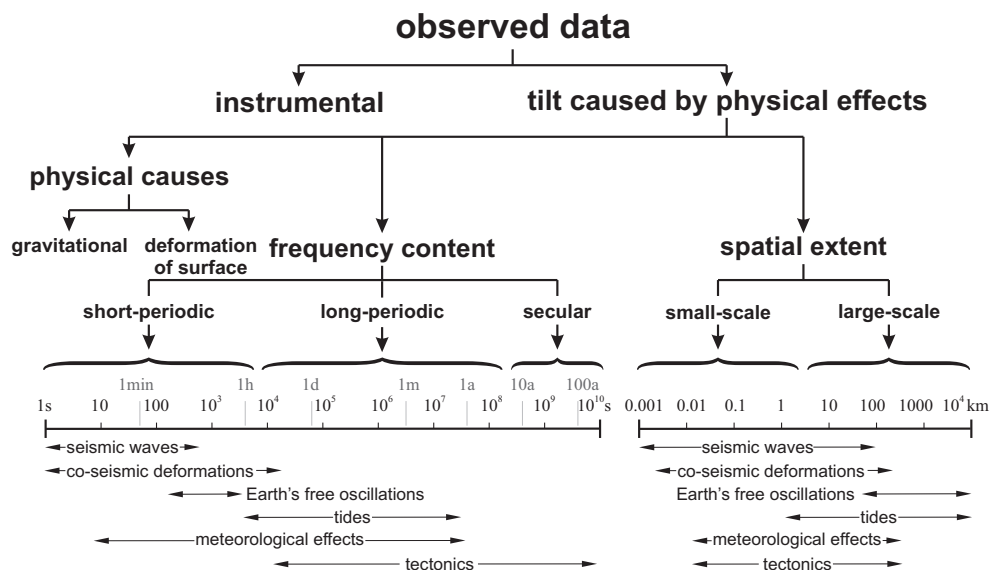


Fig. 3.8: Signal content of tilt measurements, classification after [Kümpel \(1982\)](#).

3 Deformations

By the Finite-Element method potential disturbing sources can be investigated. Fig. 3.9 gives a slightly different view on the signal content of observed deformations. It is separated into periodic and aperiodic as well as locally induced components. Related to the local situation, noise sources can be associated with the cavity (gallery) geometry, the topography and geological features (different lithological units, faults ...). Barometric pressure, temperature and pore pressure changes induce the additional effects. Additionally illustrated is tidal loading which is also modified by the local situation. Furthermore, the material parameters of the surrounding rocks are of importance in the scale of the effects: Young's modulus (E), Poisson ratio (ν) or Lamé's parameters (λ , μ) and density (ρ).

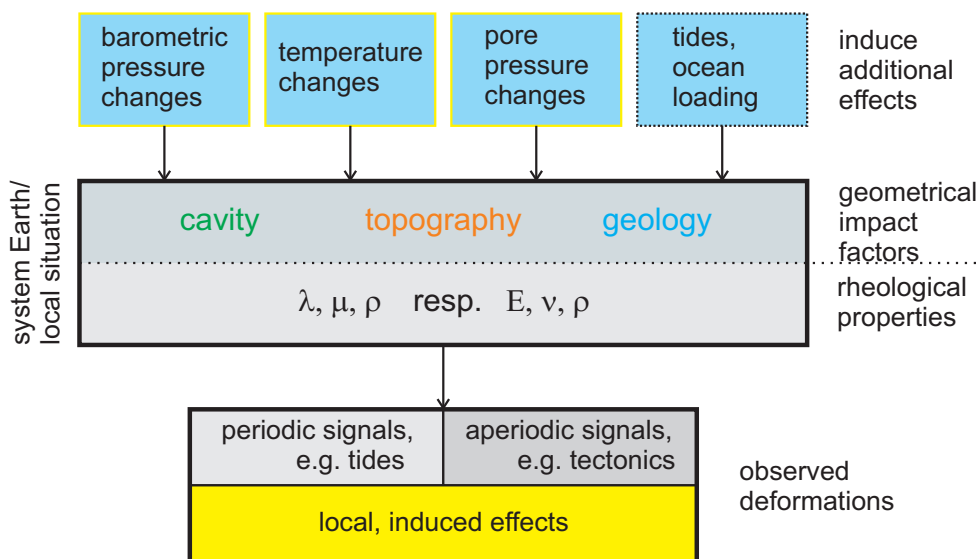


Fig. 3.9: Contents of deformation time series, according to origin and effects.

Several investigations have been carried out regarding environmental effects, e.g. an investigation related to hydrology for the long base tiltmeter at the Sainte-Croix-aux-Mines (Longuevergne, 2008) or general by Wolfe et al. (1981), Dal Moro & Zadro (1998).

In Fig. 3.10, Fig. 3.11, Fig. 3.12 examples for different disturbances in deformation records are given.

For the strainmeter at Sopron an example of 1 month is shown in Fig. 3.10. The observed data (red line, Fig. 3.10a) is reduced by subtraction of the already known tides (green line). The detided time series (brown line) still has signals among others from tectonics and effects by the local surroundings. By comparing the reduced data with the barometric pressure recorded in parallel a good correlation is found for large amplitudes in pressure changes (Fig. 3.10b). The large pressure change on January 23,

3 Deformations

2007 is due to the windstorm 'Kyrill', an extended low pressure area. For smaller changes, meaning also smaller spatial extent, the correlation is not so pronounced. This means the correlation of strain and barometric pressure depends on the frequency.

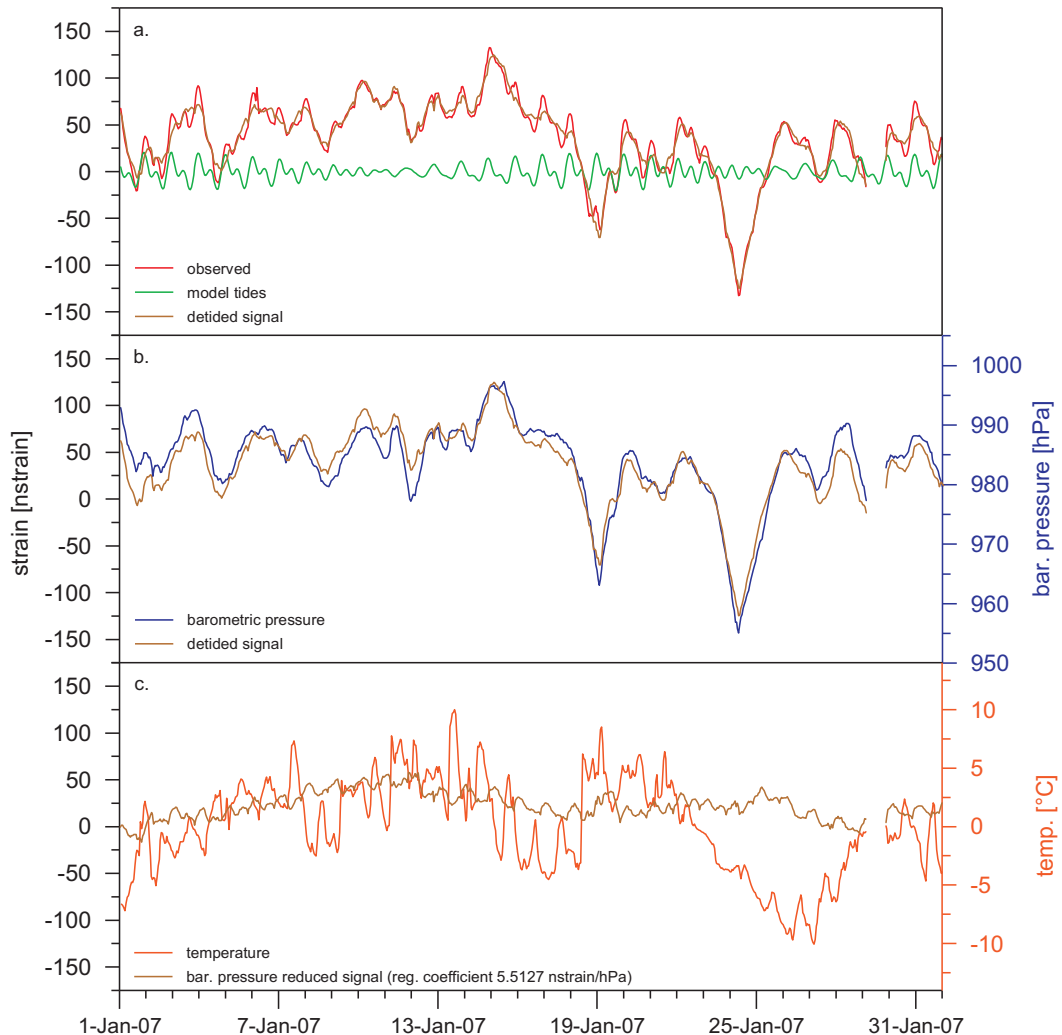


Fig. 3.10: Data example for effects on strain observations at Sopron observatory (pers. comm. Mentés, 2008).

By reducing the data using a linear regression coefficient ($5.5127 \text{ nstrain/hPa}$) the barometric pressure effect is eliminated, but the result still contains short- and long-periodic signals (Fig. 3.10c). There are two main reasons for this: on the one hand an insufficient reduction of barometric pressure effects; on the other hand the reduced time series contains other effects, e.g. caused by adiabatic processes associated with temperature changes (Fig. 3.10c). This example demonstrates the difficulty of data analysis, when effects have amplitudes some orders of magnitude bigger than the signals of interest.

3 Deformations

In Fig. 3.11, an example for effects in tiltmeter records is presented. The deformation was recorded in year 2005 with an ASKANIA borehole tiltmeter installed 1.8 km in the west of the KTB (continental deep drilling site, Germany) in a depth of 45.5 m during a large-scale injection experiment (Gebauer, 2006; Gebauer et al., 2007; Jahr et al., 2005; 2006a; b; c; 2008).

Apart from this instrument four additional tiltmeters were installed around the KTB. Compared to the other instrument sites this site ('Mittelberg') was the least disturbed, as it showed only a low and linear drift, and small effects caused by groundwater level changes (Zeumann et al., 2009).

The ASKANIA borehole tiltmeter monitors deformations in two orthogonal directions. About 5 months of north-south and east-west transformed components are shown in Fig. 3.11. After tidal and drift reduction, a correlation is found between tilt and barometric pressure changes (Fig. 3.11 bottom).

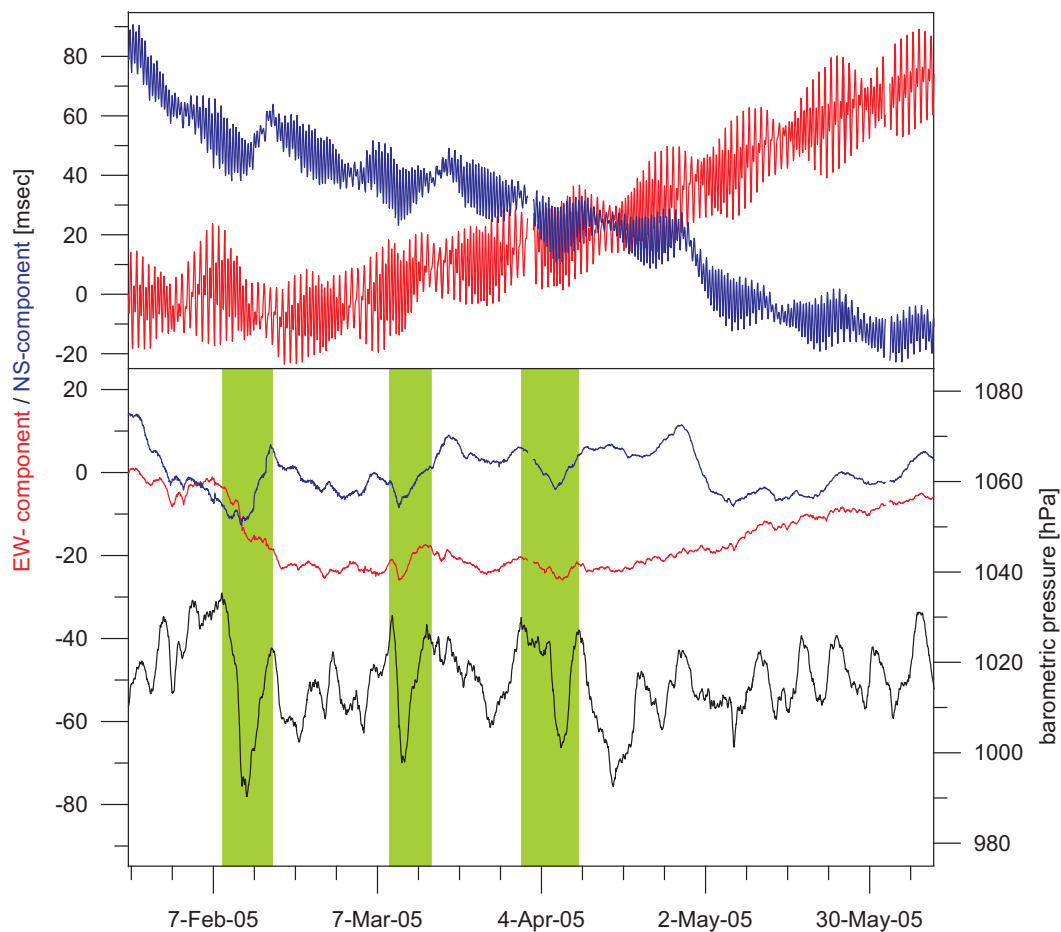


Fig. 3.11: Data example for tilt records (after Gebauer, 2006; Gebauer et al., 2007).

3 Deformations

Investigations regarding the dependency of tilt on barometric pressure (e.g. marked by the 3 green bars) result in an average regression coefficient of 0.244 msec/hPa (1.22 nrad/hPa) for the EW-component and of 0.255 msec/hPa (1.125 nrad/hPa) for the NS-component.

Typically bigger than the impact of barometric pressure variations is the effect of pore pressure changes. These were extensively investigated, among other, by [Kümpel \(1982, 1988, and 1989\)](#), [Kümpel et al. \(1996\)](#), [Weise \(1991 and 1992\)](#), [Weise et al. 1999](#), [Lehmann \(2001\)](#), and [Fabian \(2004\)](#). In the recent past, investigations of pore pressure changes were carried out for the long baseline tiltmeter at Sainte-Croix-aux-Mines [Boudin et al. \(2008\)](#), [Longuevergne et al. \(2007\)](#), [Longuevergne \(2008\)](#) and [Longuevergne et al. \(2008\)](#). The general goal of Longuevergne's investigation was to reduce the hydrological effect. Furthermore, the impact of temperature changes on tiltmeters was studied by [Beavan & Bilham \(1977\)](#).

The third example demonstrates the difficulty related to the impact of barometric pressure changes on seismological records. The 24 h STS-1 record of a seismically period installed at the BFO shows in both horizontal (NS and EW) components additional signals, which correlate with barometric pressure changes ([Fig. 3.12](#)).

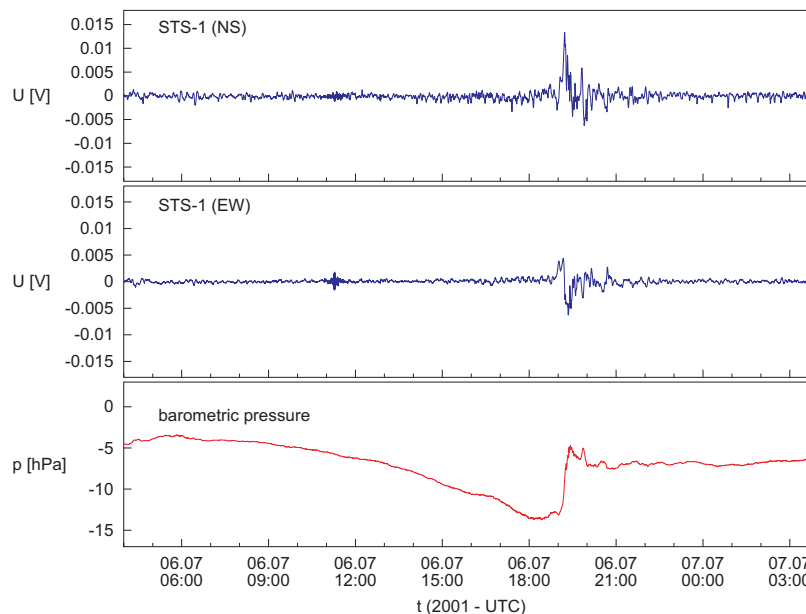


Fig. 3.12: 24 hour data example of horizontal components of STS-1 seismometer at the BFO, during a sudden barometric pressure change: The tides are eliminated (pers. comm. Zürn, 2007).

3.3 Impact factors under investigation

As previously mentioned, a number of factors exist which can affect deformation measurements. The present investigations are carried out in order to understand the amplitudes and transfer mechanisms. In previous studies often only one instrument on a selected instrument site was considered. Here a general study is made at effects caused by barometric pressure changes for different instruments in similar conditions using the Finite-Element method. Both, strain and tilt effects are considered. The results can be transferred to other sites.

In detail the impact of cavities (Fig. 3.13a, b), of topography (Fig. 3.13c), and of geology (Fig. 3.13d) is investigated by systematic changes of geometric features of the models related to the observatory sites. For the studies related to Central Europe and large-scale deformations the local effects are not considered, but effects caused by regional changes in topography and rocks parameters.

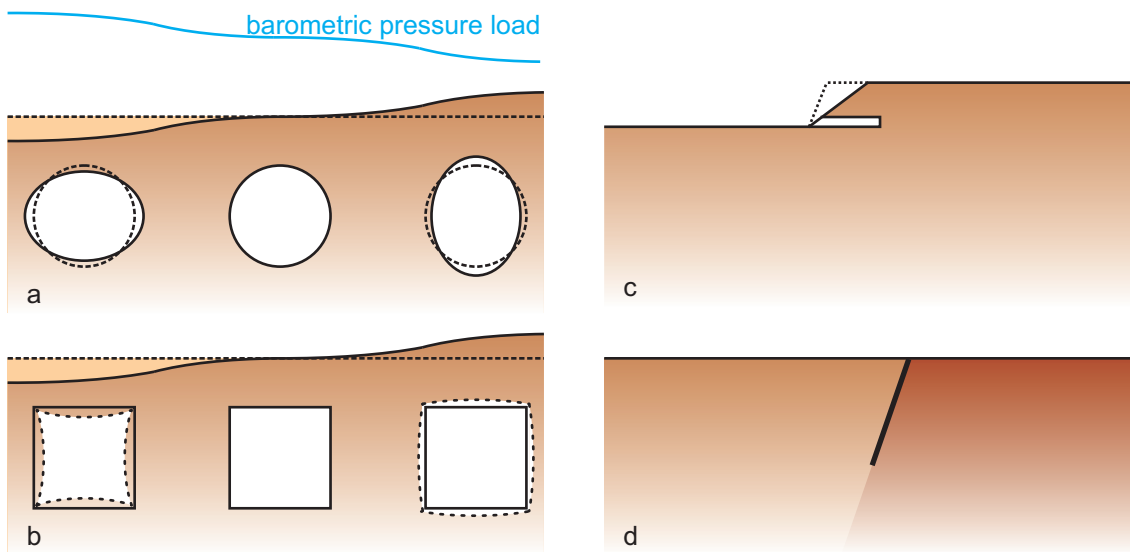


Fig. 3.13: Impact factors: a, b – deformation of a cavity due to barometric pressure loads, c – topography, d – geology (different lithological units bordering, fault).

4 Numerical modeling

The Finite-Element method (FEM) is a numerical analysis technique which is applied to complex engineering or physical problems. More information about the method is found e.g. in [Zienkiewicz \(1971\)](#), [Schwarz \(1991\)](#) and [Zienkiewicz et al. \(2005\)](#).

In the method the assumption is made that a complex domain can be divided into a number of smaller subsets in which the differential equations are roughly solved. By assembling the set of equations for each region, the behavior over the entire problem domain is determined.

The individual regions are referred to as elements and the subdivision into a finite number of elements is called discretization. Elements are connected at nodes. It is a prerequisite that the solution is continuous along common boundaries of joint elements.

For this study the FEM-software package *ABAQUS* is used. This software provides several element types for discretization of physical-mathematical problems. Two types of 3-dimensional elements are used for meshing the model: linear or quadratic tetrahedral and hexahedral elements ([Abaqus Inc., 2007](#)).

An elastic rheology is used for deformation analysis by barometric pressure load due to the assumption of a state process and a non existing relaxation. The strain components (ε_{kl}) depend linearly on the stress components (σ_{ij}) and are described by Hooke's law in most general form:

$$(4.1) \quad \sigma_{ij} = C_{ijkl} \varepsilon_{kl}$$

The elastic parameter tensor consists of a set of 81 coefficients represented by C_{ijkl} , which is reduced to two elastic parameters in case of isotropy: the Young's modulus E and the Poisson ratio ν or the Lamé's constants λ and μ , respectively. The advantage using elastic rheology is that the results can be scaled according to the load, which is the actually occurring barometric pressure variation.

The 'pressure load' ([Abaqus Inc., 2007](#)) is a surface load which acts always orthogonal on the surface. For advanced load scenarios the uniform load is applied, acting also on the whole model surface and can be modified using functions written in program languages *C* or *Fortran*.

The boundary conditions are: nodes at the model bottom must not move in vertical direction and the nodes at the vertical boundaries must not move in horizontal direction perpendicular to the model sides.

For developing the box models with simplified topography and gallery the CAE application of *ABAQUS* is used. First the model geometry is created, followed by the definition of the material parameters, the boundary conditions, and the load. In a final step the geometry is meshed and the numerical problem solved. For all model computations of the principle study, quadratic hexahedral elements are used, which are well deformable by shear forces. To validate the quality of the mesh a sensitivity analysis was carried out. With respect to the deformation amplitude, the used element type and size yield an uncertainty of less than 5%. Regarding the volume of the elements, a side length of about 1 m inside the galleries and outwards up to 250 m was found to be adequate. The element number of the models is thus in the range of 58,000 for the box models.

For developing the models with complex topography and gallery, respectively, and Central Europe an additional program *HyperMesh* of Altair Engineering, Inc. (Altair Engineering, Inc., 2008) is used. The workflow for these models (Fig. 4.1) differs from the above mentioned. A digital terrain model (DTM) and all other necessary geometric features, like the gallery, geological borders, or faults, are used to create a solid mesh. Using the DTM and a simple, self programmed mesh-generator a shell element mesh (S3/S4-elements, Abaqus Inc., 2007) is created and saved as an *ABAQUS* input-file. This input-file is imported into *HyperMesh*, where the complete geometry of the final model is created. With this the geometry is meshed with tetrahedral elements and exported as *ABAQUS* input-file. In *ABAQUS* CAE material parameters, boundary conditions, and the pressure load are defined.

Node sets are selected according to assumed instruments for which the deformation is calculated. Using the extracted displacement in three directions in space at the nodes of interest the deformations can be calculated. The strain is computed as described in formula (3.1). For the determination of tilts two vertically aligned nodes are used. For tiltmeters the vertical distance between these nodes is larger (about 2 m) than for seismometers (about 0.3 m). For the calculation of the tilt the upper point is assumed as fixed. Using the relative horizontal displacement between the nodes and the vertical distance the tilt is determined.

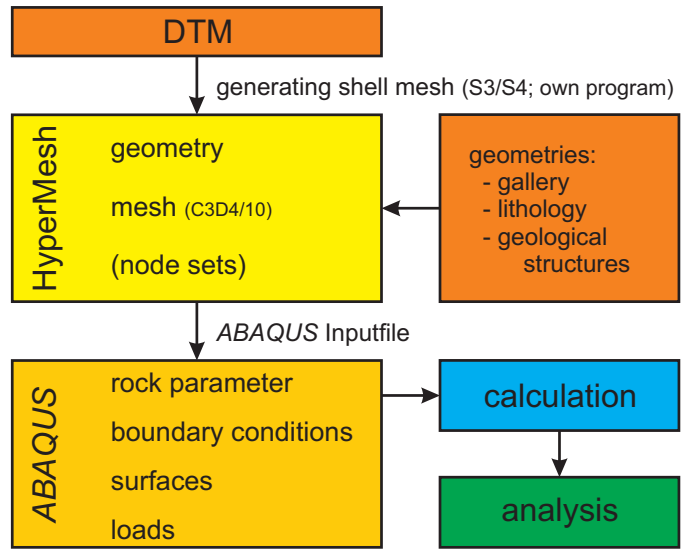


Fig. 4.1: Workflow for development of models with complex topography respectively gallery geometry.

5 Principle investigations

For the principle investigations box models are developed in order to study various impact factors (comp. chapter 3.3). These models are created based on the local conditions at the Geodynamic Observatory Moxa (MOX), the Black Forest Observatory (BFO), the Geodetic Observatory Wettzell (WET), and the Sopron Observatory (SOP) (Tab. 5.1). To investigate the different effects several features, respectively, parameters of the box models are systematically modified while others are kept constant.

Tab. 5.1: Local conditions at the broadband observatories Geodynamic Observatory Moxa (MOX), Black Forest Observatory (BFO), Geodetic Observatory Wettzell (WET), and Sopron Observatory (SOP).

	topography	rocks in vicinity	coverage [m]
MOX	wide valley	greywacke, schist	max. 35
BFO	narrow valley	gneiss, sandstone	max. 183
WET	plain	gneiss	-
SOP	scarp	gneiss	max. 30

5.1 Model assembly

For the estimation of essential effects on deformations, model types with three basic topographies are considered: a plain, a slope, and a valley type (Fig. 5.1a-c). All models have a dimension of 5,000 m × 5,000 m and a vertical extension of at least 1,600 m below the upper surface. This model size is chosen in order to ensure that points which are used for the determination of deformations are sufficiently far away from the model boundaries, and thus are not affected by boundary effects. For the determination of deformations for all models a similar instrumentation is considered.

The plain model type (Fig. 5.1a), which is used for the investigation of the pure cavity effect, also serves as reference for studies of topography-related effects. To investigate the pure cavity effect, a short (50 m) and a long (100 m) gallery (Tab. 5.3) are incorporated into the plain model located at various depths between 5 m and 300 m below the surface (Fig. 5.2). The height and width of the gallery are always 2 m.

For studies of deformation effects related to topography the slope and valley model type (Fig. 5.1b, c) are modified. The angle of the slope is changed between 15° and 90° in 5° increments (Fig. 5.3c, f). Additionally, the height of the slope is increased to 100 m, 200 m, and 300 m for the slope and valley model type (Fig. 5.3d). The maxi-

5 Principle investigations

imum slope height of 300 m is for an estimation of deformations under extreme conditions. In the valley model the width of the valley bottom is generally about 100 m and additionally changed in one investigation in 100 m steps up to a width of 400 m (Fig. 5.3g). Besides a gallery running perpendicularly to the strike of the topography (gallery type A, Fig. 5.3a), a second gallery is included to the right at the end of the first one parallel to the topography (gallery type B, Fig. 5.3b). Details on the galleries and the assumed instrumentation are summarized in Tab. 5.3. Apart from the instrument sites inside the gallery, effects for the same deformation components are determined at the surface 30 m in front of the gallery entrance to compare the results related to the investigated impact factors. For investigations regarding the effect of the gallery length related to the topography gallery type A is used with a varying length between 50 m and 800 m (Fig. 5.3e).

For the above mentioned investigations the models are parameterized according to PREM (Dziewonski & Anderson 1981). Here, only parameters of the upper crust. Additionally, material parameters for different lithologies taken from Angenheister (1982) and Berckhemer (1991) are considered (Tab. 5.2).

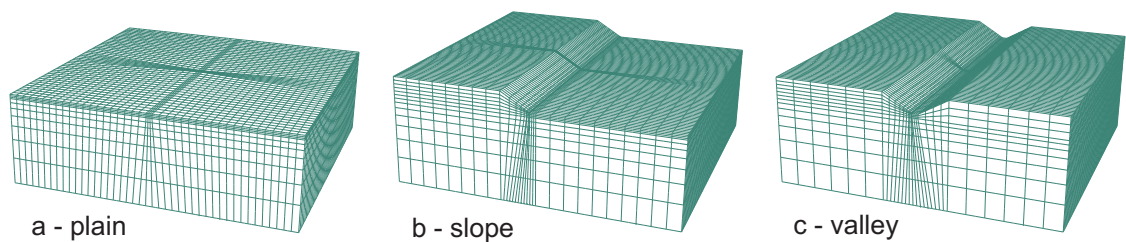


Fig. 5.1: Model types considered in the principle studies.

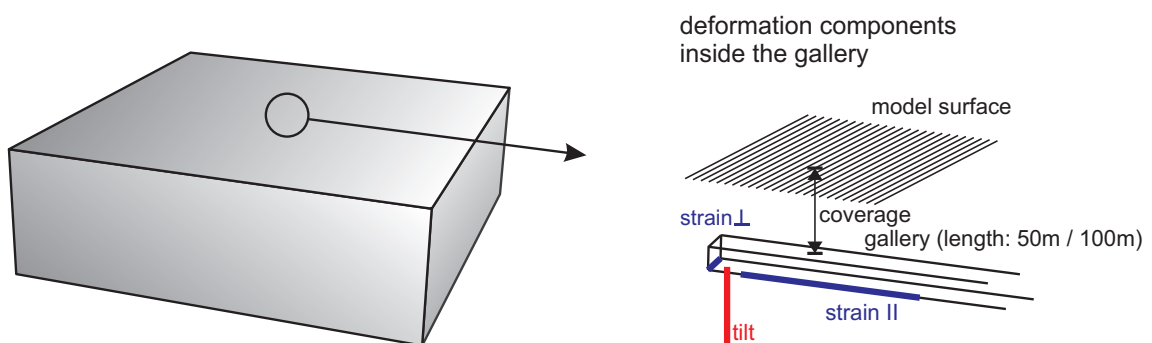


Fig. 5.2: Gallery and instrumentation for studies of the pure cavity effect.

5 Principle investigations

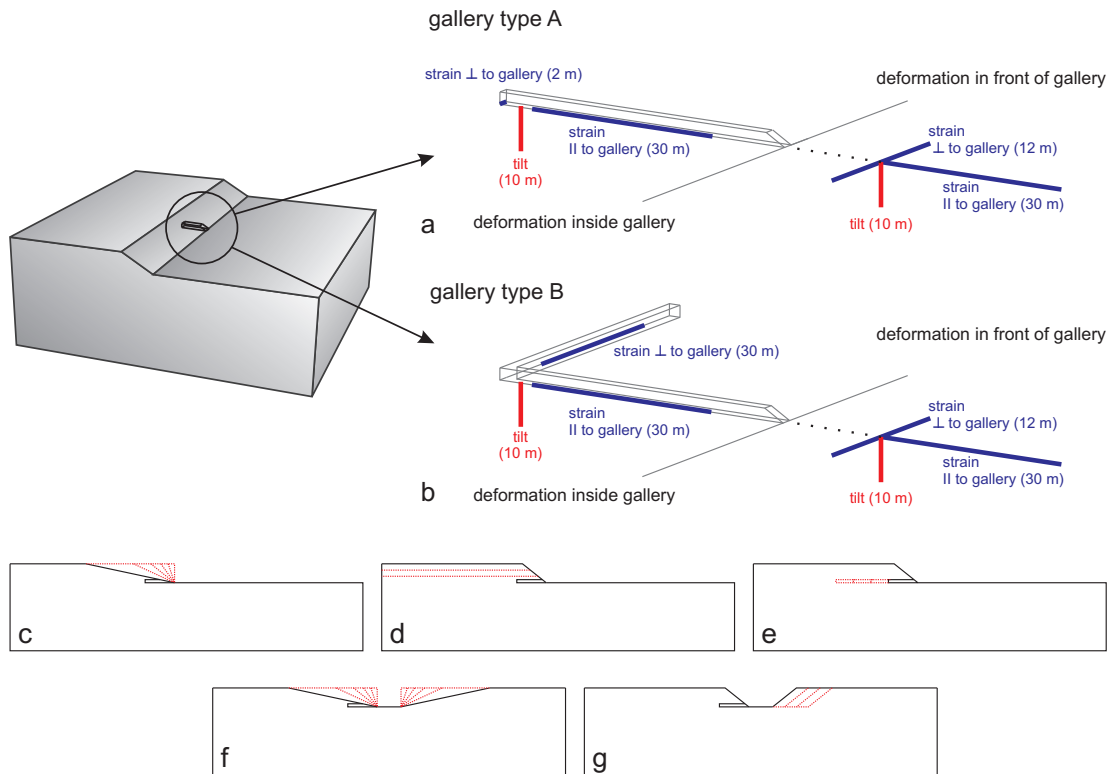


Fig. 5.3: Galleries and instrumentation included in the slope and valley model type and model modifications for the determination of topography-related effects.

Tab. 5.2: Material parameters for principle study.

	sandstone	marlstone	limestone	granite	PREM
density [kg/m ³]	1,900	2,500	2,500	2,700	2,600
Young's modulus [GPa]	16.0	40.2	65.0	80.0	68.8
Poisson ratio [1]	0.34	0.32	0.30	0.26	0.28

In addition to effects caused by the cavity and topography the impact of geological features e.g. due to different lithological units is investigated. In order to study this effect the distance between the instrument and the lithological border is varied (Fig. 5.4a), assuming the lithological units have full contact without any frictional effects. From the geological point of view this assumption is possibly not the best, but appropriate for the estimation of the maximum effects to be expected. The plain model and one modification of the slope model type are considered. The different lithological units are parameterized for rock combinations given in Tab. 5.2. These materials are chosen by their general occurrence in nature and existence in the vicinity of observatory sites.

The second aspect of geological features concerns the investigation of the effect caused by a fault in the surroundings of the instrument site (Fig. 5.4b). Different dimensions of the fault and distances to the instrument site are investigated. The fault is realized in the models as a rectangular intersection with frictionless contact conditions. In

5 Principle investigations

nature faults, cracks, respectively, fissures have very complex structures and behavior, expressed in stress accumulation or friction coefficients (Byerlee, 1978; Zoback & Healy, 1984; Moore et al., 1996; Scholz, 2000). For modeling of large-scale faults a very low friction coefficient of 0.05 is used (Bird and Kong, 1994; Chéry et al. 2001, 2004; Heidbach and Drewes, 2003). Observation sites usually are located far away from larger faults, unless the point of interest is the fault as in the case of the San Andreas Fault (SAFOD, 2009). Thus in the vicinity of an observatory site usually only small faults are found (fissures, cracks). Based on the assumption that barometric pressure load only causes small displacements and no stress will accumulate, the modeled deformations are the maximal displacements to be expected. The dimensions of the modeled fault are usually 100 m for the length at the surface and 30 m in depth, but also varied.

For all deformation components (strain and tilt), the notation of the directions is with respect to the orientation of the gallery type A. The conventions for the deformations are that positive strain values correspond to dilatation and negative ones to compression for all strain components. For positive values of the tilt component parallel to the gallery, the bottom end of the tiltmeter moves in opposite direction of the gallery entrance. Positive values of the tilt component perpendicular to the gallery the bottom of the tiltmeter moves with respect to the gallery type A to the right, when viewed from the entrance of this gallery. For the reference deformation in front of the gallery the same convention is used.

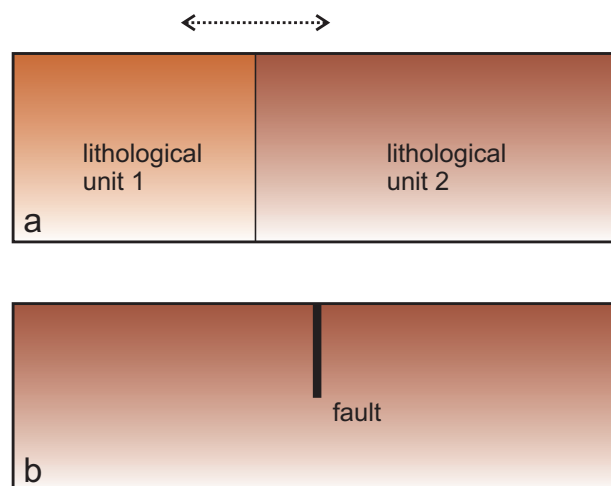


Fig. 5.4: Models to investigate the effects induced by geological features.

Tab. 5.3: Assumed instrumentation and local conditions for models of principle study.

model type	observation site	dimension of the gallery	instrumentation	base length of the instrument	location of the instrument relative to gallery entrance
plain	short/long gallery	2x2x50 m ³ 2x2x100 m ³	strain parallel to gallery	30 m	end 5 m in front of the head
			strain perpendicular to gallery	2 m	at bottom of the gallery head
			tilt	10 m	central 2.5 m before gallery end
	at surface	-	strain parallel to gallery	30 m	30 m distance to gallery entrance
			strain perpendicular to gallery	12 m	midpoint located at endpoint of strain parallel to gallery
			tilt	10 m	upper end located at endpoint of strain parallel to gallery
slope/ valley	gallery type A (Fig. 5.3a)	2x2x50 m ³ and length variation up to 800 m	strain parallel to gallery	30 m	5 m distance to the gallery head on left bottom
			strain perpendicular to gallery	2 m	at bottom of the gallery head
			tilt	10 m	central 2.5 m before gallery end
	gallery type B (Fig. 5.3b)	2x2x50 m ³ with extension at the head of the gallery to right of 2x2x50 m ³	strain parallel to gallery	30 m	5 m distance to the gallery head on left bottom
			strain perpendicular to gallery	30 m	at bottom of the gallery head
			tilt	10 m	5 m distance to the gallery head of the extension on left bottom
	30 m in front gallery at surface (Fig. 5.3a,b)	-	strain parallel to gallery	30 m	30 m distance to gallery entrance
			strain perpendicular to gallery	12 m	midpoint located at endpoint of strainmeter parallel to gallery
			tilt	10 m	upper end located at cross point of strains

5.2 Loading scenario

For all models barometric pressure is assumed as source of loading. Two different principle situations are considered (Fig. 5.5):

- barometric pressure acts uniformly on the total model (static load),
- a high pressure area (pressure front) moves across the model (dynamic load).

Additionally, it has to be taken into account, whether the gallery is protected from pressure changes by an air lock. An example for such a station is the Black Forest Observatory (Richter et al., 1995).

5 Principle investigations

A nominal amplitude of 1 hPa is considered in all studies. Compared to low pressure areas high pressure areas are associated with lower wind velocities and less precipitation which can produce additional signals. Due to this, a high pressure area is better suited for comparison with observed data. But, it is reasonable to use strong barometric pressure changes associated with low pressure areas and to take into account the disadvantages. Therefore, as actual example, the winter storm 'Kyrill' is selected for a comprehensive comparison.

Typical pressure changes in Central Europe amount to several hPa in some hours. Barometric pressure events occur with dimensions of 1,000-2,000 km and amplitudes of up to 20 hPa (Holton, 2004). An extreme event occurred in Central Europe in November 18th, 2004, during which pressure decreased by 18 hPa in 10 h and increased again to its former level in another 10 h.

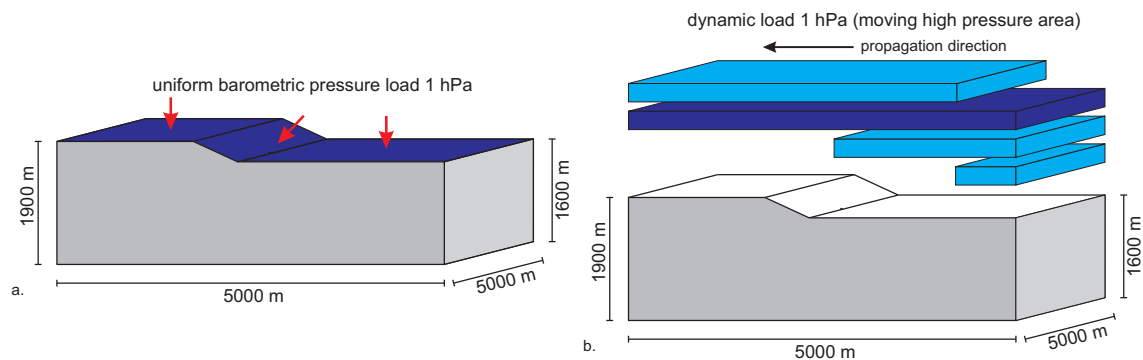


Fig. 5.5: Barometric pressure loads used in the present study.

The moving high pressure area corresponds to the model dimensions so that at one time step the model is completely covered by the load, and at another one completely unloaded. The change of the amplitude at the pressure front is realized as a step from 0 to 1 hPa. Since elastic rheology is considered, only the location of the barometric pressure front relative to the instrument site is important. Hence, the time scale is denoted in percentages of a full cycle of loading and un-loading with the special time points:

- 25%: the front of the high pressure area is found at the center of the model
- 50%: the whole model surface is loaded
- 75%: the front of the decreased barometric pressure is found at the center of the model.

For detailed studies three movement directions of the high pressure area are selected: parallel, perpendicular, and diagonal to the gallery (Fig. 5.6). Pressure areas moving in opposite direction generate deformations reversed in time.

5 Principle investigations

plain model type and included gallery

30° slope model type and included gallery type A

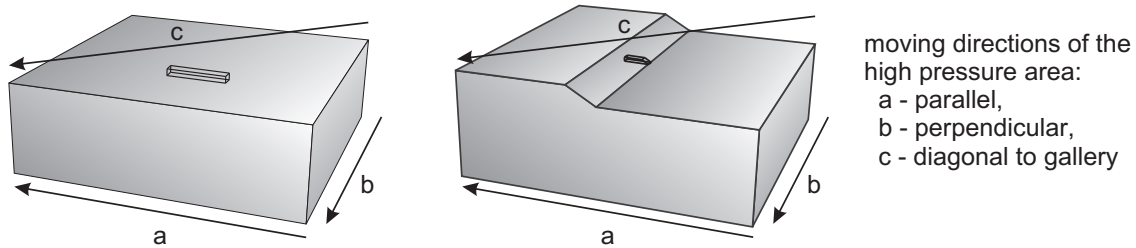


Fig. 5.6: Moving directions of the high pressure area relative to the model and the included gallery.

5.3 Results of principle studies

5.3.1 Cavity effect

Uniform barometric pressure load

The results for the estimation of the cavity effect are given in Fig. 5.7. For this detail study the plain model is used (comp. Fig. 5.2). Generally, for the longer gallery (100 m) about 20% smaller deformations occur than for the shorter one (50 m) for all components. A relation is found between the deformations and the geometry of the gallery, which is discussed in the following.

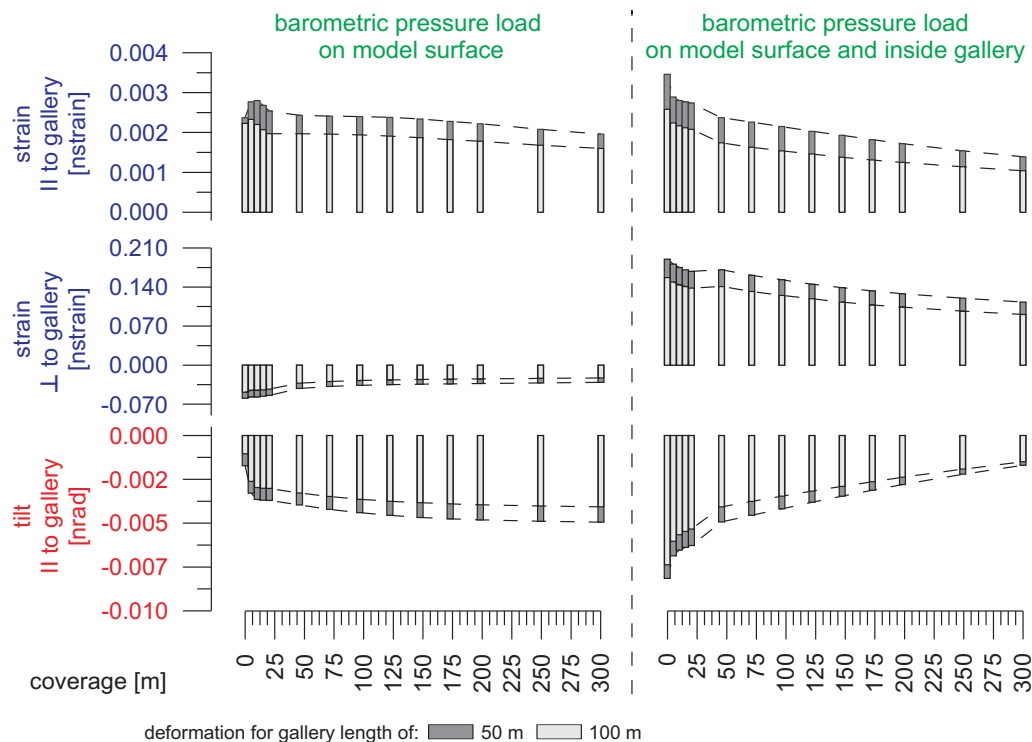


Fig. 5.7: Results for the cavity effect in the gallery for different rock coverage (comp. Fig. 5.2) for 1 hPa uniform barometric pressure load (different scaling).

Strainmeter

The strain component parallel to the gallery with a length of 50 m shows dilatation of up to 0.0035 nstrain with generally non-linearly decreasing amplitudes for increasing coverage. This effect is presently below the detection level of the assumed instruments. In contrast, the signals in the strain component perpendicular to the gallery of up to 0.2 nstrain are detectable for an about 6 times (6 hPa) higher barometric pressure load acting only at the surface and about 2 times (2 hPa) for an additional load acting also inside the gallery. As expected the biggest amplitudes occur for a coverage of only a few meters. If barometric pressure is acting only on the model surface compression is found in the order of magnitude of up to 0.065 nstrain. With barometric pressure acting additionally inside the gallery the effect reverses and dilatation occurs of up to 0.19 nstrain. This order of magnitude decreases non-linearly to 0.113 nstrain for a coverage of 300 m. The reversal from compression to dilatation shows that the two barometric pressure loads counteract with the internal acting pressure load causing the larger effect. For typically occurring barometric pressure variations in the order of a few hPa a minimum rock coverage above the gallery can be estimated: e.g. for a pressure amplitude of 10 hPa and a gallery depth of 1000 m the component oriented perpendicularly to the gallery is not affected. The signals in the tilt- and strainmeter component oriented parallel to the gallery, under the known conditions, are not affected by commonly occurring barometric pressure events. In principle, this result was already obtained by [Harrison \(1976\)](#) based on fairly simple numerical modeling (2-D), both for strain and tilt. Due to the improved numerical possibilities of today this new study reveals much more reliable results.

Tiltmeter

The change for the tilt components is more complex. The bottom of the tiltmeter moves always in direction of the center of the gallery with a maximum amplitude of -0.008 nrad. For increasing coverage the amplitude increases non-linearly towards a maximum value of -0.0041 nstrain for a barometric pressure load acting only on the model surface decreasing with 0.002 nstrain per 100 m of increased coverage with an additional load acting inside the gallery.

In order to understand the unexpected behavior of increasing amplitudes for increasing coverage and barometric pressure an additional study is carried out. In this study the load acts only on the model surface. To study the tilt component in parallel to the gallery the plain model with a 50 m long gallery and a coverage of 50 m ([Fig. 5.8](#)) is used.

5 Principle investigations

The tilt is estimated for a base length of 5 m and 10 m of the instrument at different depths. As expected the direction of the tilt signal in depths between 0 m and 5 m like 0 m and 10 m points towards the center point of the gallery. The direction changes for tiltmeters at a greater depth. The explanation for this is a symmetric circular movement of the points above and below the ends of the gallery relative to a vertical plane oriented in direction along the gallery (Fig. 5.9).

The infinitesimally rotated volume (green circles in Fig. 5.9) has different diameters depending on the geometry and the physical properties of the model. Therefore, to explain the occurring deformations some rotated regions are needed. The points in the example given in Fig. 5.8 near the ends (above and below) of the gallery move outwards and points about more than 12.5 m away from the gallery head inwards.

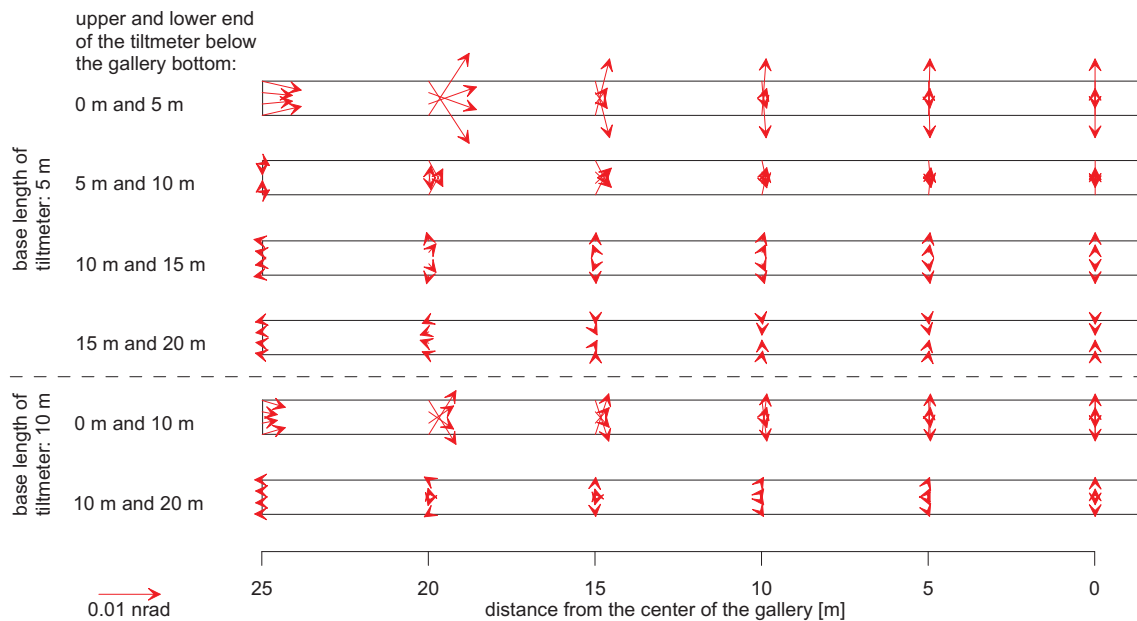


Fig. 5.8: Tilt amplitudes obtained for different depths for a tiltmeter base length of 5 m and 10 m for a load acting only on the surface.

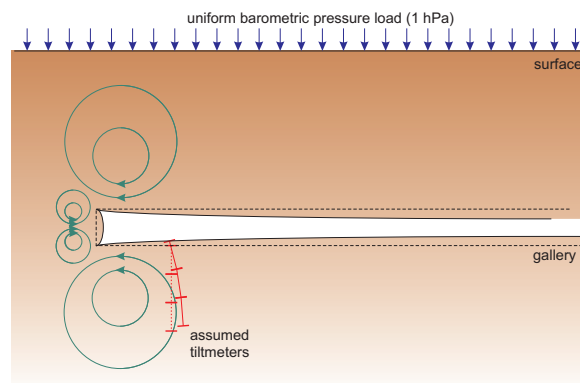


Fig. 5.9: Sketch of deformed gallery for barometric pressure load on the surface showing the deformation of tiltmeters at different depths.

Lithology

Estimating the impact of the lithology on the cavity effect the parameterization of [Tab. 5.2](#) for different rock types is used. In [Tab. 5.4](#) the effects are summarized, which are obtained for the 50 m long gallery with a coverage of 300 m. Rocks with a low Young's modulus lead, as expected, to the biggest deformation. The increase of the Young's modulus causes an approximately exponential decrease in the deformation effects. The strain component parallel to the gallery e.g. has an amplitude of 0.002 nstrain for PREM and of 0.009 nstrain for sandstone if the barometric pressure load acts only on the surface. Significant disturbing deformation amplitudes occur only for the strain component perpendicularly oriented to the gallery.

Tab. 5.4: Deformations obtained for different lithologies with 300 m coverage above a 50 m long gallery.

	strain component parallel to gallery [10^{-3} nstrain]	strain component perpendicular to gallery [10^{-3} nstrain]	tilt component parallel to gallery [10^{-3} nstrain]
barometric pressure load of 1 hPa at surface			
sandstone	9.41	-270.0	-14.20
marlstone	3.88	-96.5	-5.94
limestone	2.48	-51.8	-3.91
PREM	2.43	-41.7	-3.96
granite	2.13	-27.8	-3.62
barometric pressure load of 1 hPa on surface and in gallery			
sandstone	8.56	526.0	-15.60
marlstone	3.65	238.0	-6.99
limestone	2.38	164.0	-4.77
PREM	2.37	171.0	-4.93
granite	2.11	160.0	-4.56

Moving high pressure area

The deformations resulting for the pure cavity effect are given in [Fig. 5.11](#) for a high pressure area moving in three different directions ([Fig. 5.6](#)) using the plain model type and a 50 m long gallery (comp. [Fig. 5.2](#)). The deformations obtained are caused by the load acting only on the model surface. For comparison to the deformations obtained inside the 300 m deep gallery, the deformations determined at the surface are also given. As expected, for parallel and perpendicularly to the gallery moving high pressure areas the deformation components at the surface oriented parallel to the barometric pressure front show no signal. For a high pressure area moving diagonally across the model a combination of the two orthogonally moving areas with 50% reduced deformation amplitudes is found.

Strainmeter

In the following, the focus is on components parallel to the gallery with a high pressure area moving parallel to the gallery (Fig. 5.11). The dilatation in the strain component is caused by the increasing load at the surface up to time point 25%. Thus, the deformation amplitude increases due to the decreasing distance between the observation point and the pressure front. This deformation is sketched in detail in Fig. 5.10.

Depending on the distance of the strainmeter to the barometric pressure front all three possible responses found: undeformed, extension, and compression. When the barometric pressure front crosses the instrument location, the deformation changes from dilatation to compression with a maximum amplitude of ± 0.38 nstrain. By the time the surface is completely loaded (time point 50%), the amplitude of the strain decreases non-linearly to 0 nstrain (cf. Fig. 5.10). The deformation of the un-loading process is symmetrical to the loading one.

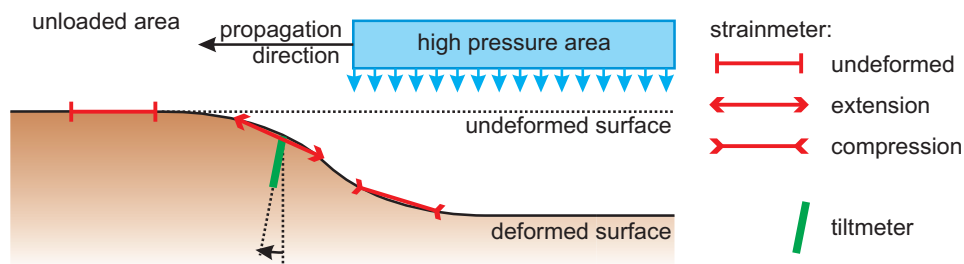


Fig. 5.10: Signals with regard to a moving high pressure area for strain- and tiltmeters components perpendicular to the pressure front.

Compared to the deformation determined at the surface for the parallel strain component in the 300 m deep gallery reversed amplitudes are obtained, when a high pressure area crosses the site, caused by the cavity effect. Investigations related to the increased coverage above the gallery show a successive change from the deformations observed at the surface to the deformations determined on the 300 m deep gallery.

Deformations related to different depths of the gallery are summarized in Fig. 5.12. For a coverage above the gallery of up to 25 m, the maximum-minimum structure is similar to the deformations determined at the surface. For greater depths between the maxima of the maximum-minimum structure, two new reversal points are generated with increased amplitudes. At a depth of 100 m, the four maxima have the same order of magnitude of 0.113 nstrain. For greater gallery depths the first maxima of the maximum-minimum structure become smaller until they disappear. Here the maxima have an amplitude of 0.16 nstrain at a gallery depth of 300 m below the surface.

The strain component perpendicular to the gallery shows deformations in a non-detectable order of magnitude (about -0.03 nstrain) even for typical barometric pressure amplitudes.

When barometric pressure acts additionally inside the gallery (Fig. 5.12), changes in the deformations are found for the strain component perpendicular to the gallery. For a high pressure area moving parallel to the gallery the amplitudes reverses. In contrast the response of the strain component perpendicular to the gallery is more complex. For lesser depths (about up to 100 m) the maximum amplitudes related to the barometric pressure load additionally acting inside the gallery are reduced by about 40%. For greater depths the maximum amplitudes are increased up to 25%.

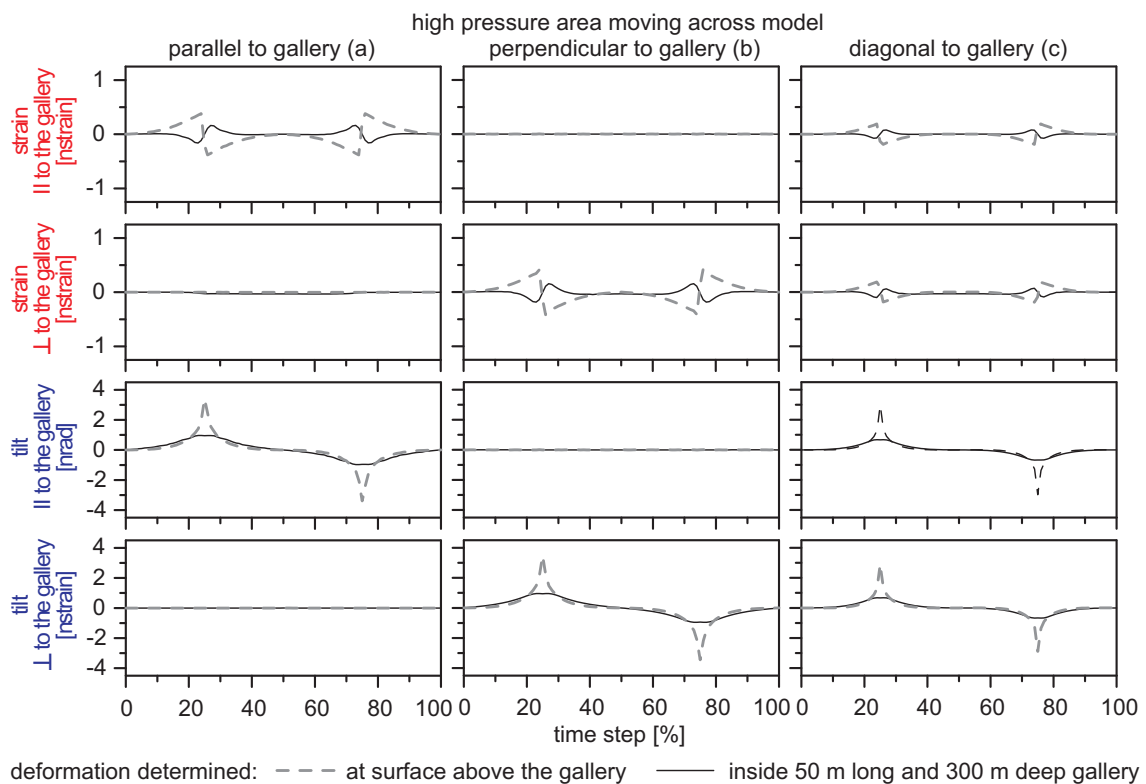


Fig. 5.11: Deformation results regarding the cavity effect of a 300 m deep gallery and moving high pressure area for 1 hPa load acting only on the surface (comp. Fig. 5.6).

Tiltmeter

The tilt component parallel to the gallery shows decreasing maximum amplitudes for increasing coverage of 25 m with a decrease from 2.4 nrad to 0.96 nrad for 300 m. The decrease is caused by the coverage, where the deformation is absorbed (Fig. 5.11). As expected, the biggest tilt amplitudes occur at the largest barometric pressure gradients, when the pressure front is found above the instrument location and the bottom of the tiltmeter moves towards the un-loaded part of the surface (see Fig. 5.10).

5 Principle investigations

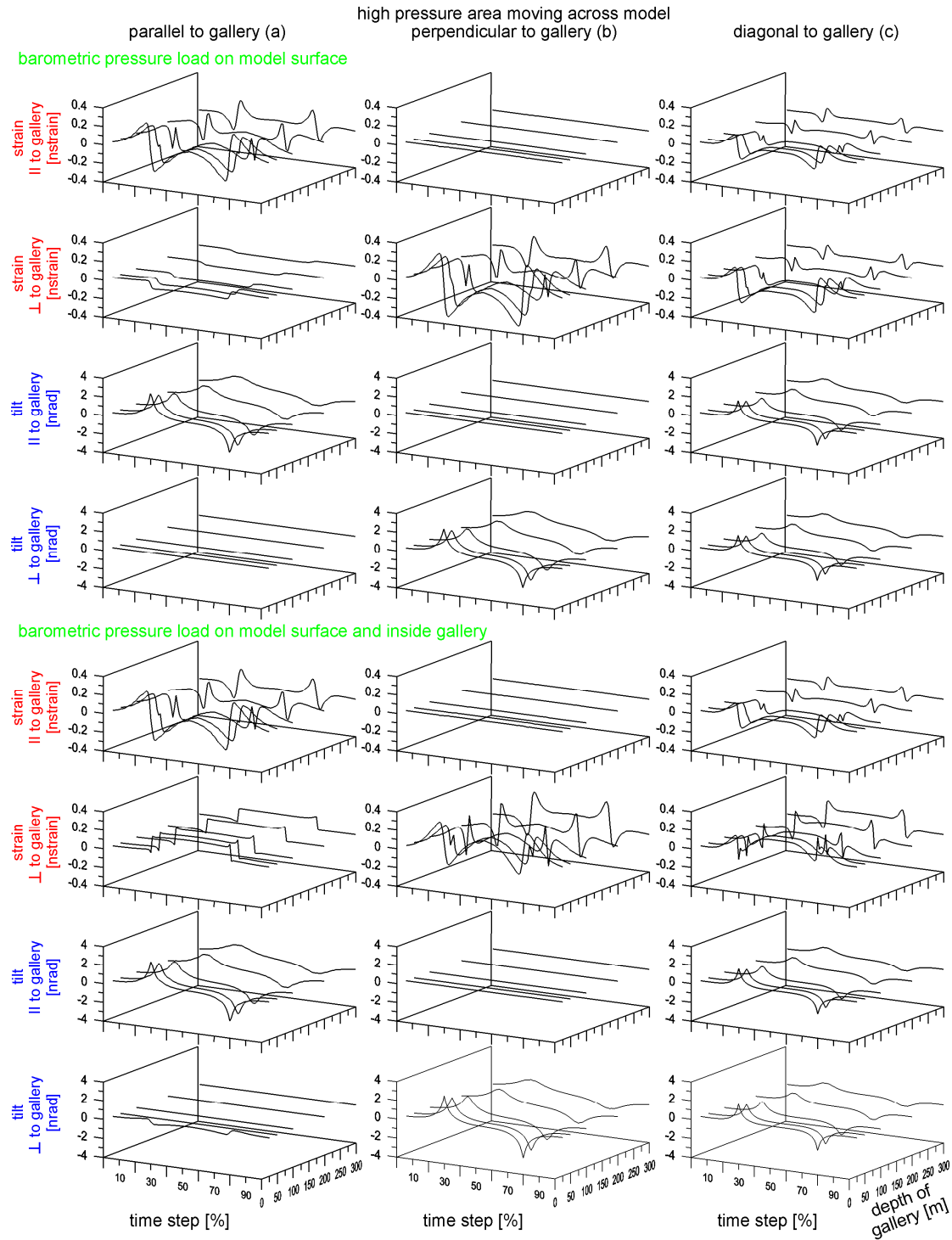


Fig. 5.12: Deformations due to the cavity effect for the 50 m long gallery in depths below the surface of 25 m, 50 m, 100 m, 200 m, and 300 m. For barometric pressure load a moving high pressure area (comp. Fig. 5.6) is used considering the following two load cases: barometric pressure acts only on the surface, and on the surface and inside the gallery.

5.3.2 Topographic effect

5.3.2.1 Effect of slope angles and heights on the models

One of the first step is to investigate the effect of a changing slope angle for a constant slope height for the model types slope and valley (comp. Fig. 5.3c, f), assuming a uniform barometric pressure load (with both, pressure acting on the surface only and additionally inside the gallery). In the following the different investigations are discussed in detail.

Slope angle changes for slope model type and gallery type A

Strainmeter

Dilatation is obtained for the strain component parallel to the gallery (Fig. 5.14):

- in front of the gallery: a non-linear increase from 0.4 nstrain of up to 0.7 nstrain
- inside the gallery:
 - o for slope angle changes from 15° to 25° the amplitude increases from 0.4 nstrain to 0.45 nstrain;
 - o for slope angle changes from 25° to 50° a decrease is obtained down to 0.26 nstrain and constant values for larger angles.

Changes in the deformations for the strain component perpendicular to the gallery are (Fig. 5.14):

- in front of the gallery: dilatation with a decrease from 0.002 nstrain to 0.0009 nstrain for increased slope angles;
- inside the gallery with a load only at the surface: compression with a nearly linear increase in the amplitudes from -0.05 nstrain to -0.068 nstrain for increased slope angles;
- inside the gallery with a load at the surface and inside the gallery: dilatation with an almost linear decrease from 0.2 nstrain to 0.15 nstrain for increased slope angles from 15° to 90°.

The very small almost non-measurable deformation amplitudes in front of the gallery are caused by the cavity effect. The points at the surface in front of the gallery move in direction to the entrance.

Tiltmeter

The component parallel to the gallery has the following amplitude changes (Fig. 5.14):

- in front of the gallery: a linear increase from 0.08 nrad to 0.34 nrad occurs for increased slope angles;
- inside the gallery for both uniform load cases, a non-linear increase from -0.74 nrad to -1.83 nrad is found for increased slope angles.

Due to the effect of the slope the deformation components oriented parallel to the gallery show approximately one order of magnitude larger amplitudes compared to the perpendicularly oriented component. The hydrostatic acting barometric pressure affects the slope which is compressed in direction of the higher plateau (Fig. 5.13). Therefore, due to the barometric pressure at the plateau which compresses the rock in vertical direction, stress accumulates at the upper edge of the slope flank. The horizontal displacement ($U_{horizontal}$) has amplitudes one order of magnitude smaller (Fig. 5.13) compared to the total magnitude (U_{mag}).

At the foot of the slope dilatation is found as shown for the strainmeter perpendicular to the gallery (comp. Fig. 5.14 and Fig. 5.13). This effect amplifies for an increasing slope angle. Additionally, an increase of compression inside the gallery is found for the strain component oriented parallel for increased slope angles.

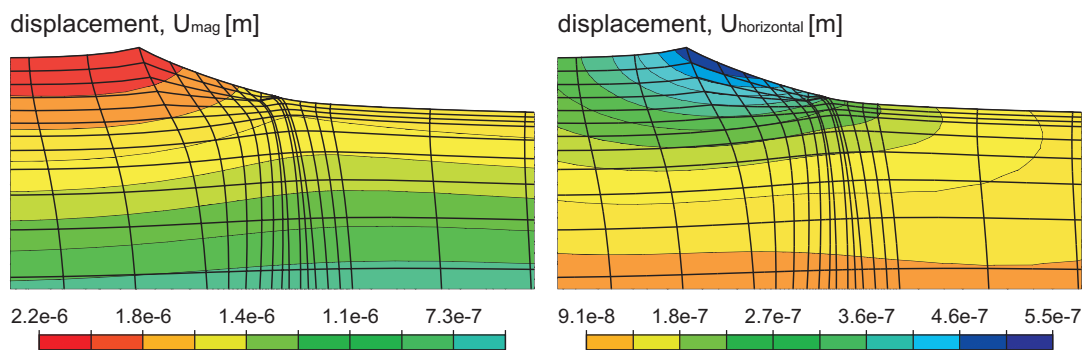


Fig. 5.13: Displacements related to a 30° slope model and 1 hPa barometric pressure load.

Slope angle changes for valley model types and gallery type A

Comparing the deformations of the valley model type with the deformations of the slope model type it emerges (Fig. 5.14):

Strainmeter

- for the strain component parallel to the gallery, the deformations are approximately twice as large as the ones related to the slope model;

5 Principle investigations

- for the strain component perpendicular to the gallery, differences in the amplitudes are less than 15%. The amplitudes determined inside the gallery for both uniform load cases are similar.

Tiltmeter

- the amplitude of the tilt component parallel to the gallery determined in front of it is strongly reduced due to the symmetrical load on both slopes and the plateaus and
- for the instrument location inside the gallery, the amplitude is about 30% larger for both load cases than for slope model type.

The increased amplitudes of the valley model are caused by the topography especially the additional hill flank. The mechanism for the slope model type is explained in [Fig. 5.13](#).

Slope angle changes for slope and valley model type and gallery type B

When gallery type B is incorporated instead of A ([Fig. 5.15](#)) the following differences are obtained:

Strainmeter

- the effects for the parallel strain component are similar to the results for the cavity effect
- for strain components perpendicular to the gallery no change in amplitudes related to the slope and valley model type occurs.

Tiltmeter

- the tilt component perpendicular to the gallery observed inside the gallery with a load only acting on the surface shows increasing amplitudes from -0.047 nrad to -0.072 nrad. Due to the additional load inside the gallery, this tilt effect is amplified by a factor 2.5.
- for tilt components perpendicular to the gallery no change in amplitudes related to the slope and valley model type occurs.

Significant deformations are found for the components parallel to the gallery, which are caused by the topography. The deformations obtained for components oriented perpendicularly to the gallery are more closely related to the cavity effects. The resulting amplitudes of these components are mostly below the detection level for barometric pressure changes less than 10 hPa.

5 Principle investigations

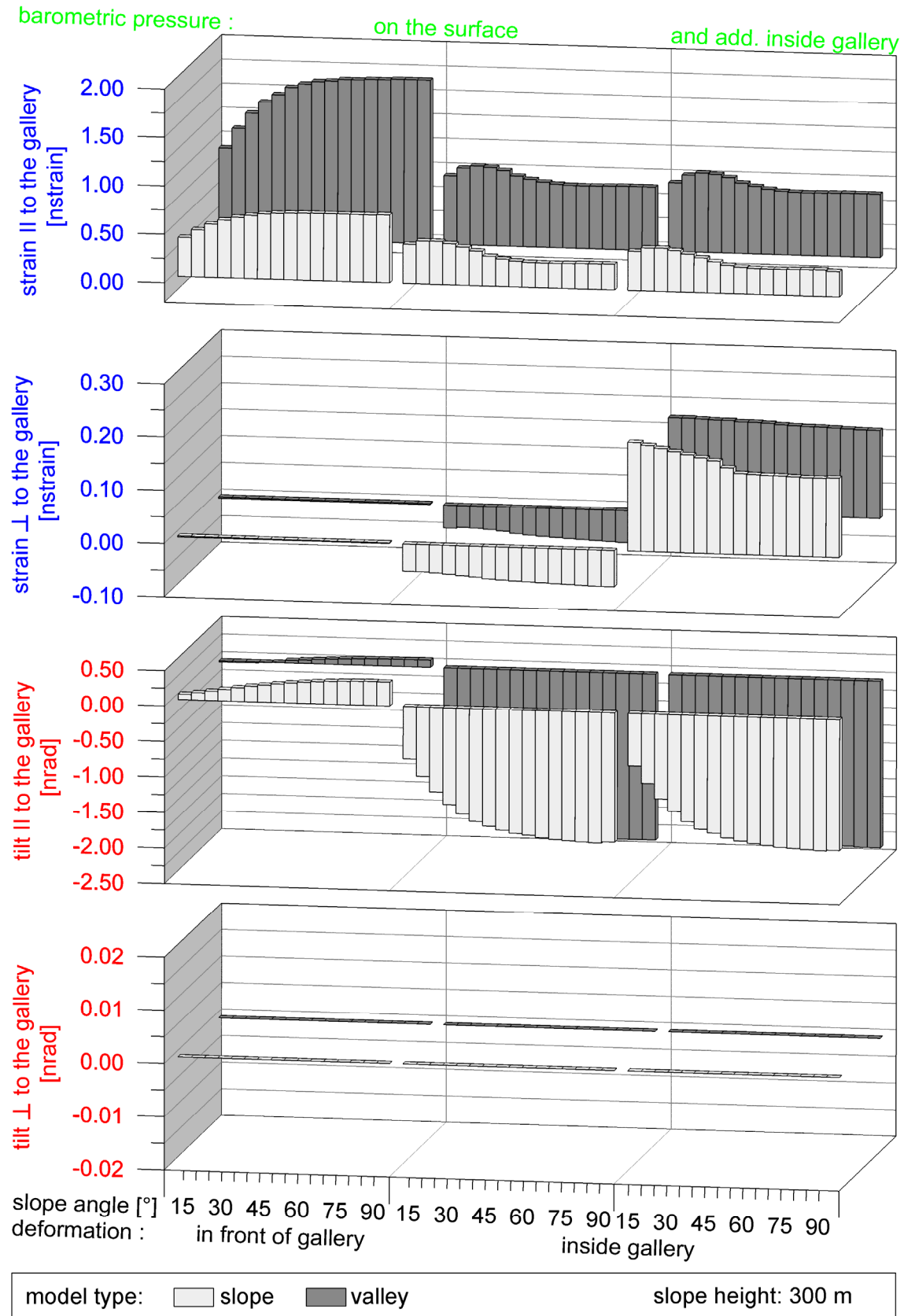


Fig. 5.14: Deformations obtained for the slope and valley models with gallery type A included Fig. 5.3a (different scaling). See Fig. 5.3c, f for model type and modification. The three columns correspond to the different combinations of deformations obtained in front and inside the gallery and the pressure loading being limited to the surface and acting additionally also inside the gallery.

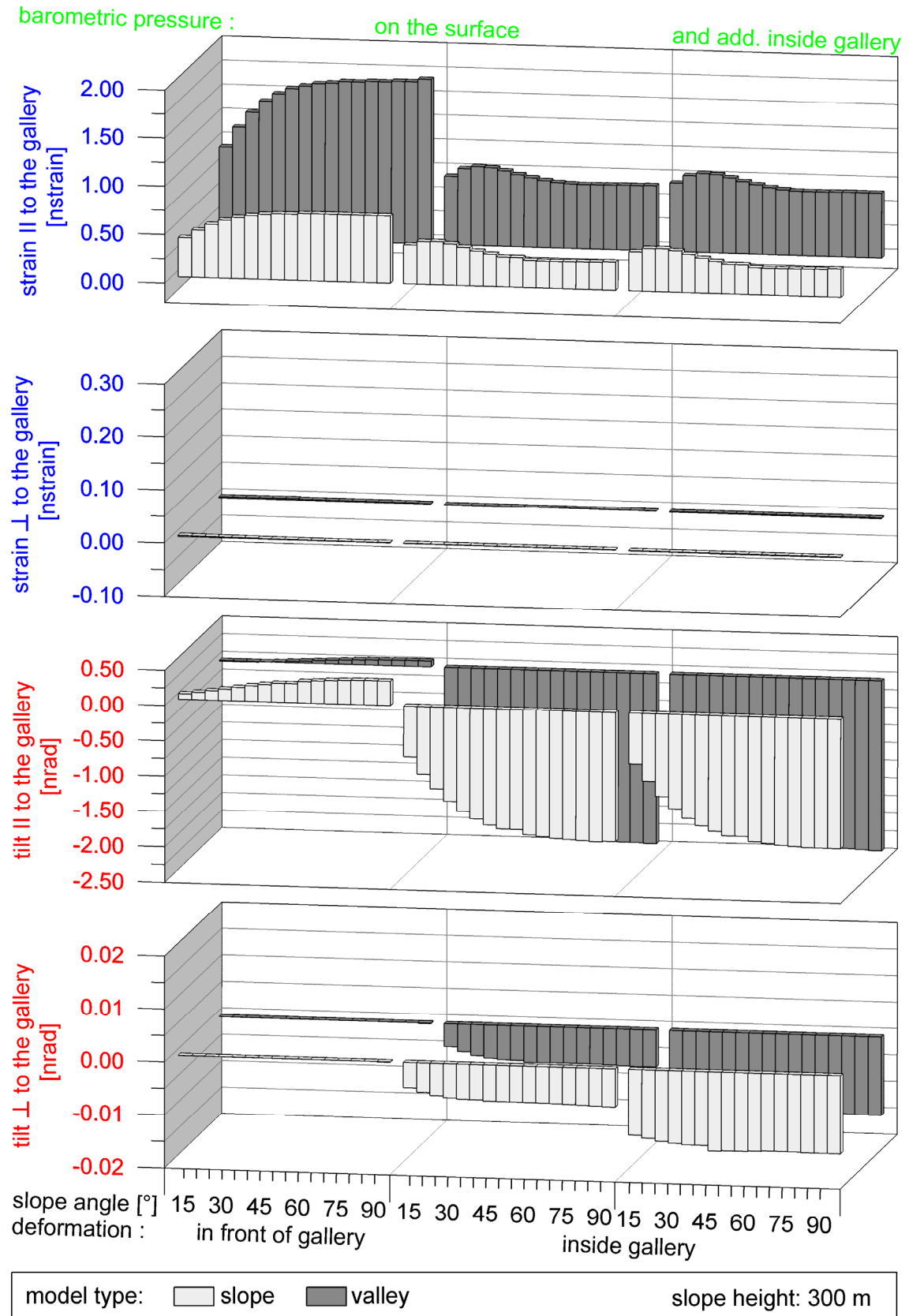


Fig. 5.15: Deformations obtained for the slope and valley models with gallery type B included Fig. 5.3b (different scaling). See Fig. 5.3c, f for model type and modification.

Slope height changes for slope model type and gallery type A

A further investigation is carried out by changing the slope height (Fig. 5.16). Heights of 100 m, 200 m and 300 m are considered for the slope model and gallery type A for the initially mentioned load cases. The dependence of the deformation amplitude on the slope height is non-linear: the amplitude change for an increase in the coverage from 100 m to 200 m is larger than for an increase from 200 m to 300 m. Here, the change in the deformation components parallel to the gallery is less than 50%, and for the strain component perpendicular to the gallery less than 5% of the maximum amplitude. One interesting result is the shift of the maximum amplitude of the strain component parallel to the gallery with decreasing height from 25° slope angle to 15° for deformations inside the gallery.

The deformations which occur with changes in the slope height for a slope angle of 90° are given in Fig. 5.17. The previously described non-linear dependence for a changed slope height is seen especially e.g. for the strain component perpendicular to the gallery determined in front of the gallery.

Strainmeter

The changes in the deformations for the strain component parallel to the gallery when varying the slope height between 25 m and 300 m for the 90° slope model type are as follows:

- in front of the gallery dilatation increases from 0.16 nstrain to 0.7 nstrain
- inside the gallery (load on surface and additionally inside the gallery): a change from compression (-0.16 nstrain) to dilatation (0.23 nstrain) occurs for a slope height of 100 m.

For the strain component perpendicular to the gallery:

- in front of the gallery the deformation is not observable
- inside the gallery with a load acting only on the surface compression decreases from -0.072 nstrain to -0.062 nstrain
- inside the gallery with a load acting on the surface and inside the gallery, dilatation decreases from 0.16 nstrain to 0.12 nstrain.

Tiltmeter

For the tilt component parallel to the gallery the following results emerge:

- in front of the gallery the deformation increases approximately linearly from -0.02 nrad to 0.34 nrad

5 Principle investigations

- inside the gallery with a load acting on the surface and inside the gallery a non-linear increase from -0.4 nrad to -1.8 nrad occurs.

Comparing the deformations obtained for the slope and valley model types differences are found for the components parallel to the gallery. For the strain component the amplitudes are about 3 times larger for deformations inside and in front of the gallery than for the case uniform of loading. For the same component, a shift of the reversal point (from compression to dilatation) emerges related to the valley type models. The reversal point for the slope model type is found for a coverage of 100 m and for the valley model type at 50 m. Due to the assumed symmetry of the valley the deformation for the tilt component determined in front of the gallery is about one third of the results of the slope model type. The deformation amplitudes inside the gallery related to a load on the surface and additionally inside the gallery for a 25 m slope height increase by a factor 2 and for a 300 m only by a factor 1.2.

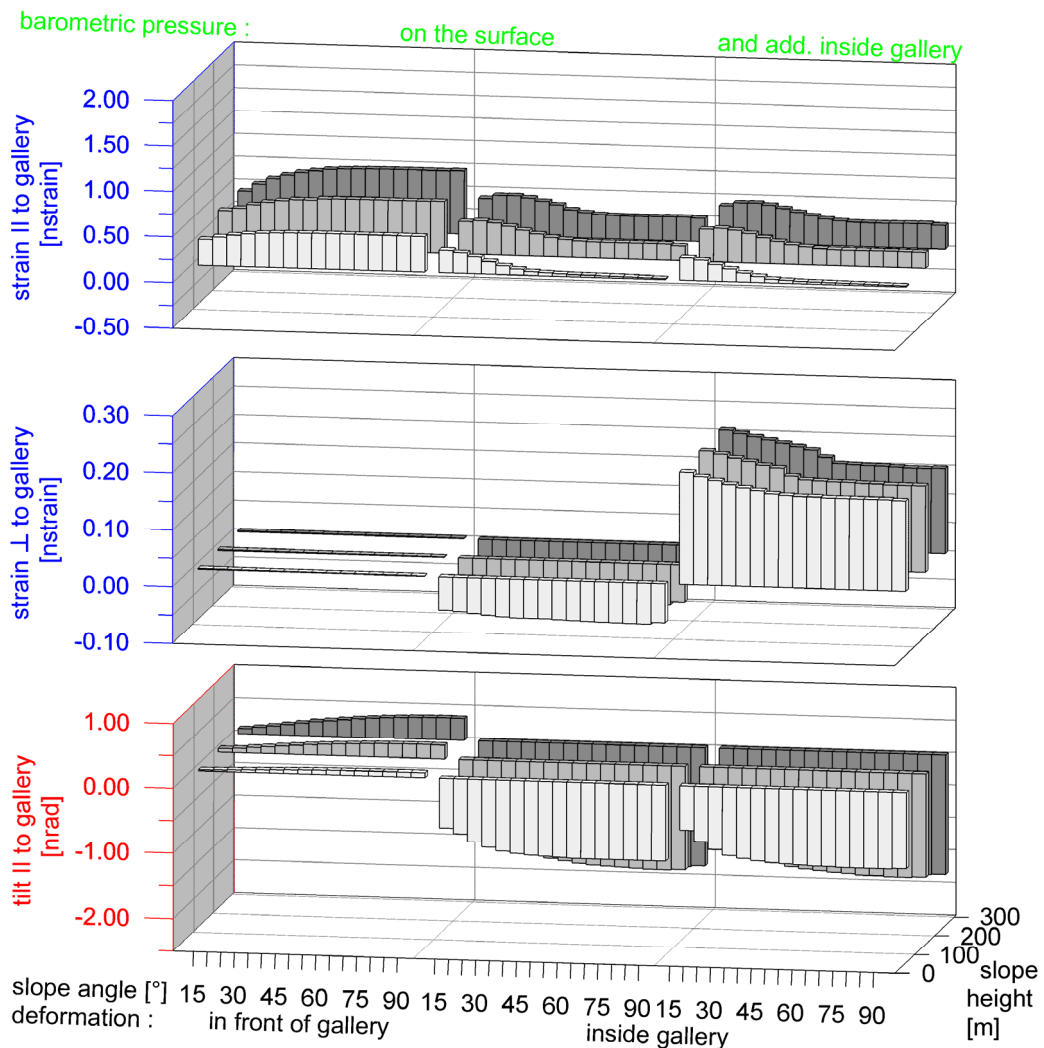


Fig. 5.16: Deformations obtained for the slope model for varying slope angle and height (see Fig. 5.3a, c, d) with gallery type A included (different scaling).

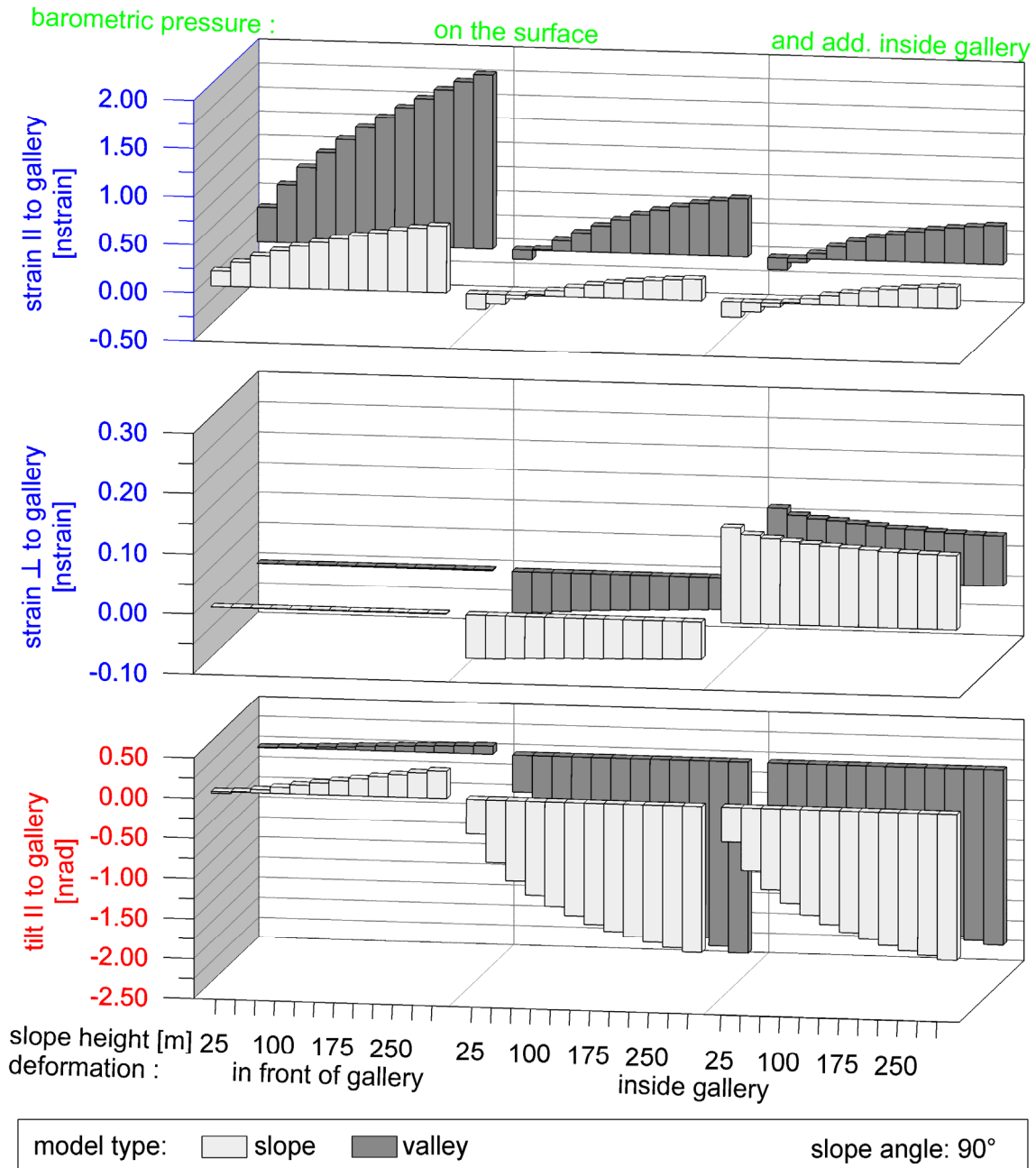


Fig. 5.17: Deformations obtained for the slope and valley models for a 90° slope angle with gallery type A included (different scaling).

Moving high pressure area

Effects in deformations related to the topography are exemplarily given for a 30° slope model and gallery type A in [Fig. 5.18](#). The amplitudes are in the same order of magnitude as obtained for the cavity effect.

An additional signal caused by the topography occurs in the deformation components parallel to the gallery. This signal can be extracted using the results of the pure

cavity effect, shown in [Fig. 5.11](#), and [Fig. 5.12](#) for the strain component parallel to the gallery in front of the gallery.

The difference of the deformations (strain and tilt) between the plain model and the 30° slope model for the high pressure zone moving parallel to the gallery reflects the effect of the topography. This difference is similar to the deformations related to the 30° slope model type for the high pressure area moving perpendicularly to the gallery. The maximum discrepancy in the amplitude is found for the 30% and 80% time steps. The front of the high pressure area is then located in the middle of the slope for the high pressure area moving parallel to the gallery.

While the instrument location is loaded by the perpendicularly to the gallery moving high pressure area dilatation occurs with an amplitude of about 0.6 nstrain for the parallel strain component.

If the slope angle increases the amplitudes can change, but the general features remain ([App. Fig. 1](#), [App. Fig. 2](#), and [App. Fig. 3](#)). The effects in the deformations for successive slope angle changes (between 15° and 90°) are continuous with respect to the deformation processes described for a uniform load. The variations differ for each component. As expected, the effect of the topography increases with an increasing slope angle. An exception is found in the strain component parallel to the gallery. For increasing slope angle in this component the maximum-minimum structure changes. The minimum is completely reduced for a 90° ([Fig. 5.19](#)) slope angle compared to the results for the 30° ([Fig. 5.18](#)) slope model caused by the additional horizontal deformations already mentioned.

The deformation component oriented parallel to the gallery shows amplitudes for the valley model approximately twice as large as found for the uniform barometric pressure load. Therefore, exemplarily the deformations for a 30° valley model type are given in [Fig. 5.20](#) (comp. results for slope model [Fig. 5.18](#)). The deformation components in front of the gallery show symmetrical behavior related to the location of the pressure front for loading and unloading. For the components inside the gallery oriented parallel to the gallery the amplitudes are amplified by a factor 2. For the tilt component oriented parallel to the gallery observed in front of the gallery for the perpendicularly moving high pressure area no signal occurs due to instrument location at the centre of the valley. There the tilt is compensated. The results for a continuous change in the slope angles are summarized in [App. Fig. 4](#), [App. Fig. 5](#), and [App. Fig. 6](#).

In case gallery type B is incorporated, general characteristics of the deformations remain. The deviations in amplitudes related to the gallery type are less than 2%. An exception is found for the strain component perpendicular to the gallery with a deformation amplitude of 0.1 nstrain when the gallery is loaded (Fig. 5.21). For the valley type model an about 2 times bigger signal is found for the strain component parallel to the gallery App. Fig. 7.

Apart from investigations related to changed slope angles the height of the slope is also varied. Exemplarily, the deformations for moving high pressure areas for a 30° slope model type and a slope height of 100 m, 200 m, and 300 m in App. Fig. 8, App. Fig. 9, and App. Fig. 10 are shown. The results for a uniform barometric pressure load are given in Fig. 5.16. As expected, the amplitudes of each component vary, but the general features, as previously described, remain constant. The amplitudes for deformation components oriented parallel to the gallery which are mainly affected by the topography increase with increased slope height. But e.g. the strain component oriented perpendicularly to the gallery found at the end of the gallery is affected through effects caused by the cavity. For increased slope height the amplitudes decrease by about 2% per 100 m, as investigated for the pure cavity effect. The ratio between the amplitudes of the slope heights and the amplitudes related to Fig. 5.16 are similar.

Furthermore the impact of the slope height is investigated for a 90° slope as well as a 90° valley model type. The height varied between 25 m and 300 m. The results for the slope model type are found in App. Fig. 11, App. Fig. 12, and App. Fig. 13, and for the valley model type in App. Fig. 14, App. Fig. 15, and App. Fig. 16. The deformations reflect the results determined for uniform barometric pressure load. The time-dependent amplitude behavior occurs similarly as previously described e.g. for the results of Fig. 5.18.

Calculations for moving high pressure areas are not carried out for each model configuration which is considered for a uniform pressure load. The necessary time to compute one of the six scenarios shown in Fig. 5.18 e.g. is about 16 hours for a workstation with two processors and a tact frequency of 2 MHz and 4 GB RAM. Apart from that fact further investigations would produce no essentially new results.

5 Principle investigations

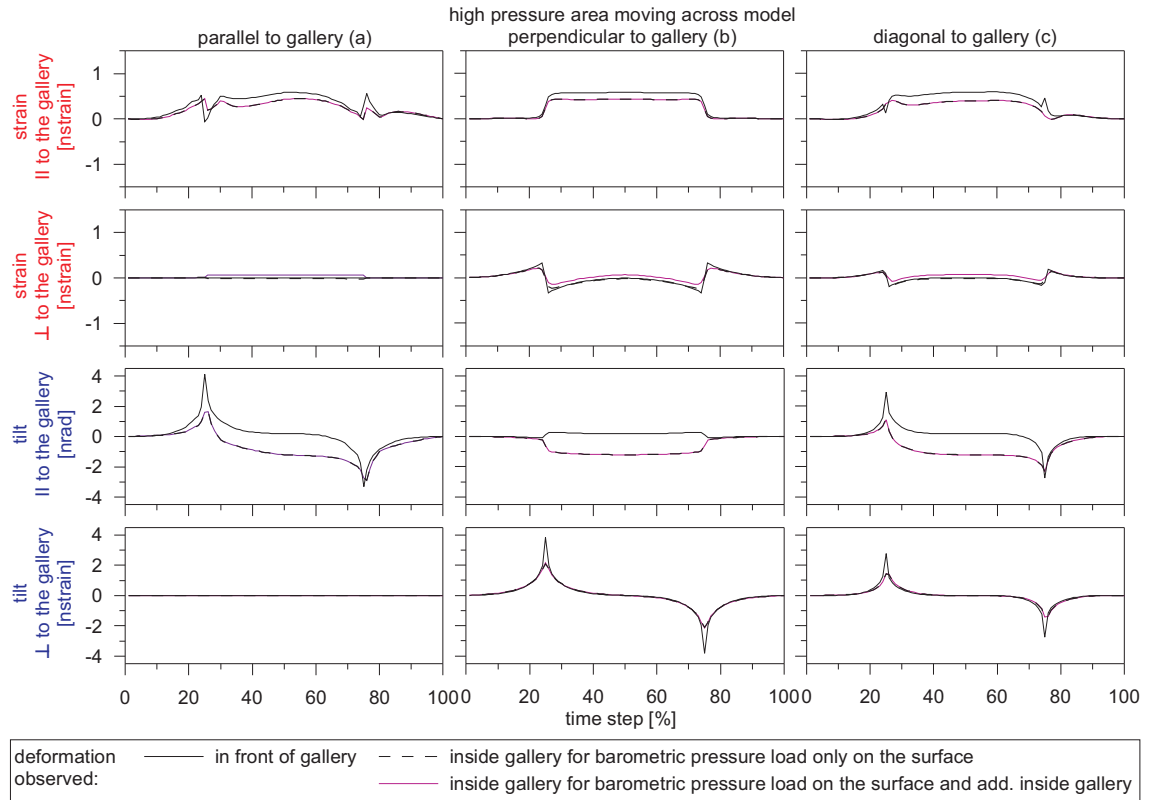


Fig. 5.18: Deformation results for a 30° slope model type and gallery type A (Fig. 5.3a) caused by a moving high pressure area.

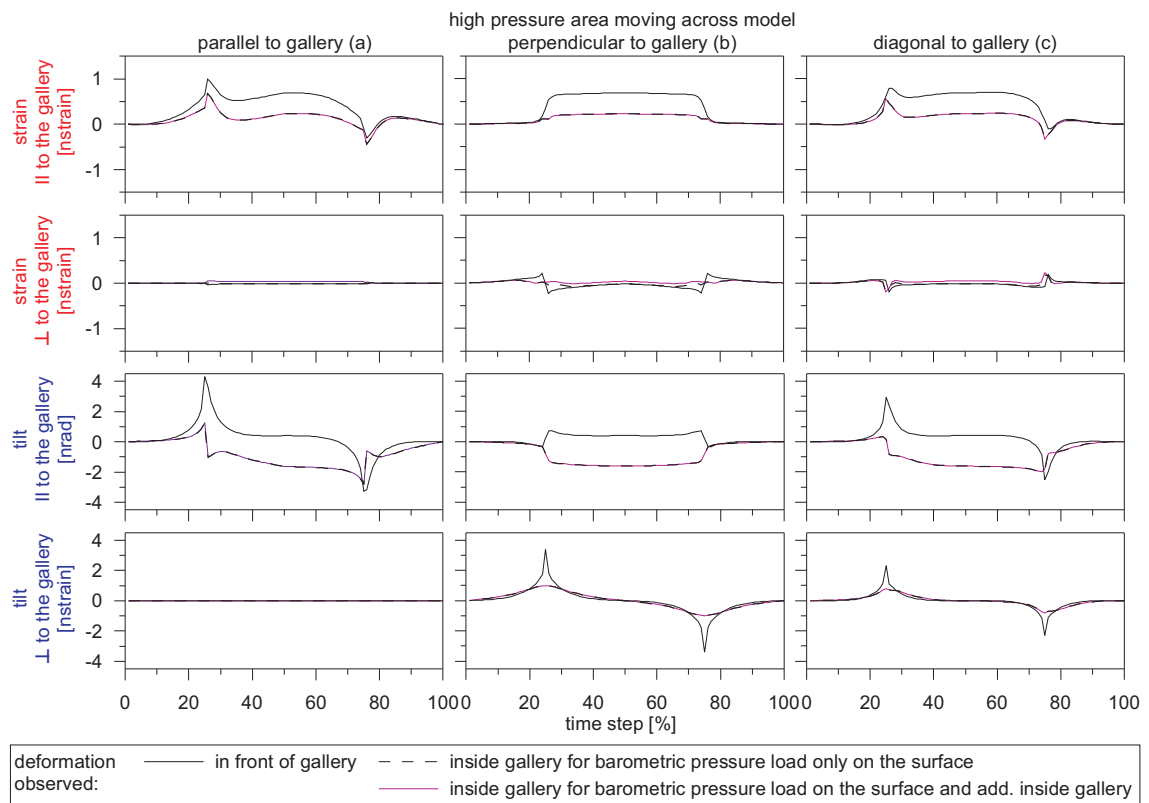


Fig. 5.19: Deformation results for a 90° slope model type and gallery type A (Fig. 5.3a) caused by a moving high pressure area.

5 Principle investigations

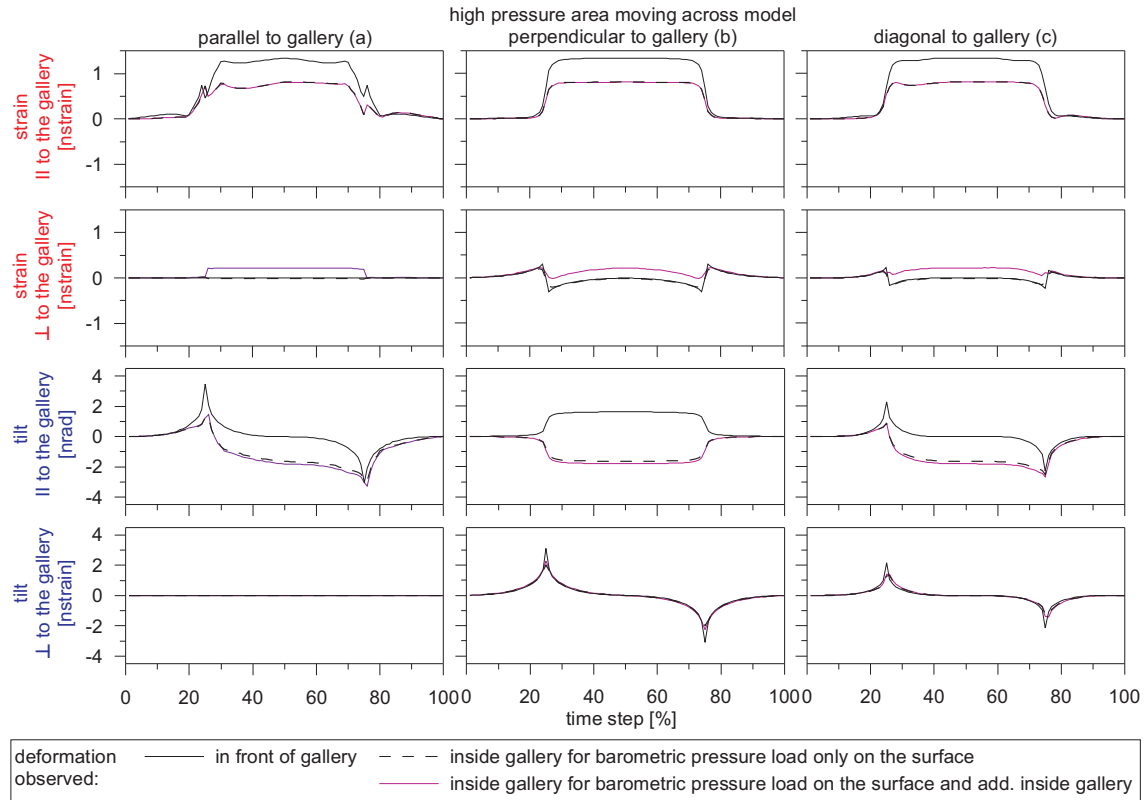


Fig. 5.20: Deformation results for a 30° valley model type and gallery type A (Fig. 5.3a) caused by a moving high pressure area.

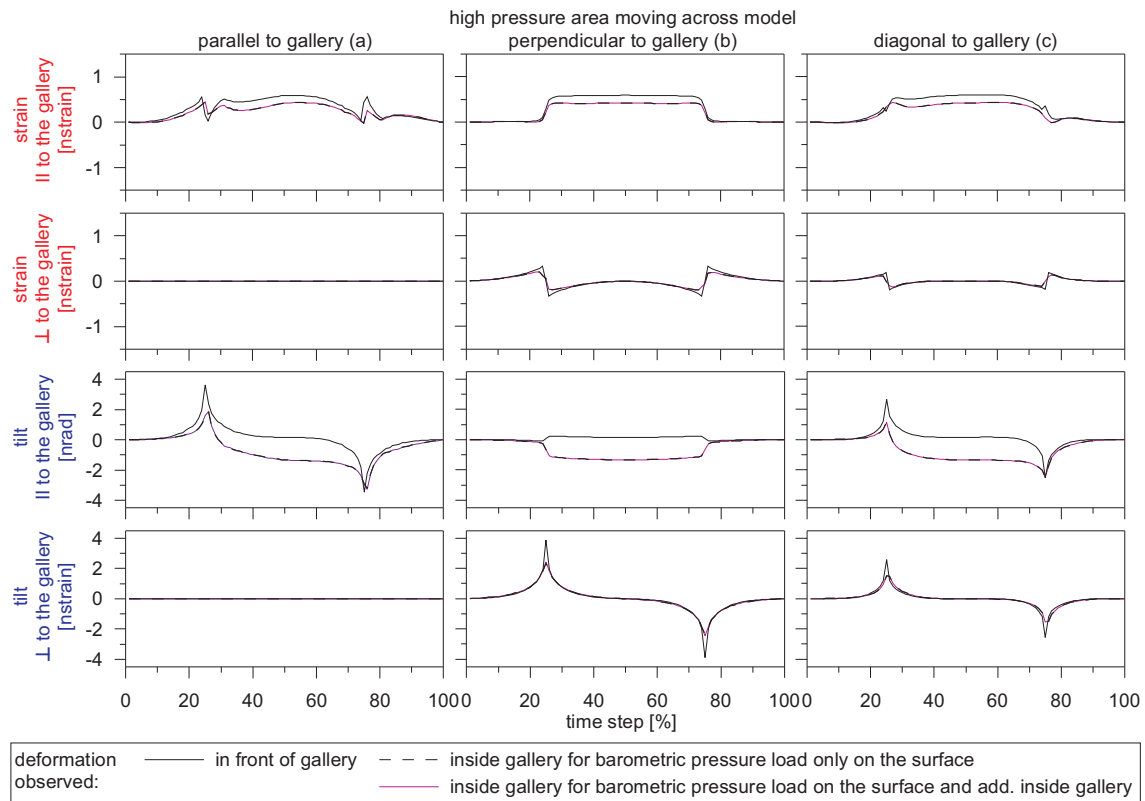


Fig. 5.21: Deformation results for a 30° slope model type and gallery type B (Fig. 5.3a) caused by a moving high pressure area.

5.3.2.2 Effects related to the instrument location

The amplitudes of the strain component perpendicular to the gallery raise the question regarding the effect of the location and the length of the strainmeter. Besides the 2 m base length a 1 m long base is considered. The midpoint of the instruments is located in the middle of the gallery bottom. The results of this investigation are shown exemplarily for the slope models with 30° and 90° slope angles in Fig. 5.22. These two angles are used on the basis of the observatories Moxa (slope angle approx. 20°) and Sopron (slope angle approx. 90°). At the entrance and at the head of the gallery the smallest deformations occur and the amplitudes decrease with increasing distance between the instrument and gallery entrance.

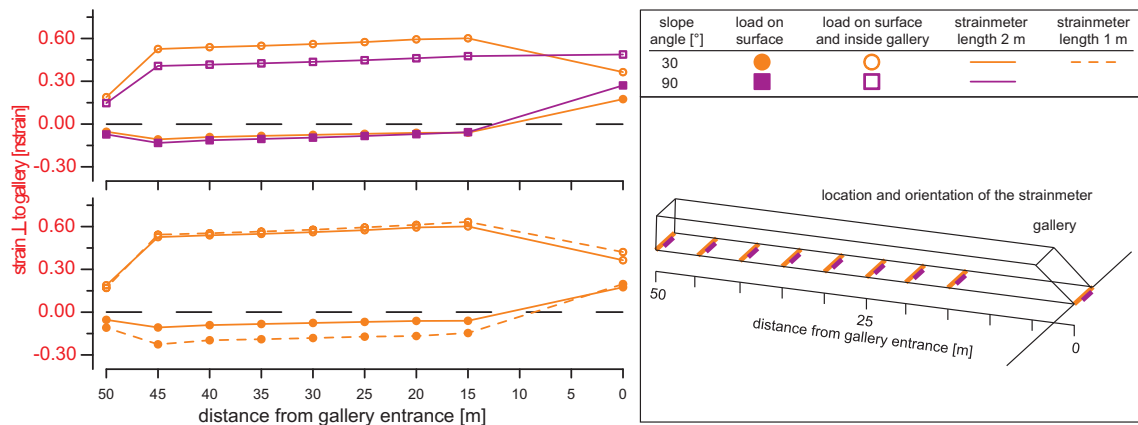


Fig. 5.22: Deformations obtained for the slope and valley models with gallery type A and location of the strainmeter inside the gallery.

Compared to the results of Fig. 5.14 similar deformations are found. The decreased deformations at the entrance and at the end of the gallery are the result of a higher stability against deformations caused by loads at the edges of the cavity. With smaller slope angles, the main acting force due to the load is dominantly vertical. This vertical deformation acts in the gallery for the perpendicular strain component as compression. With larger slope angles the load at the slope acts mostly horizontally, along the gallery extension. This additional force compresses the gallery along its extension and acts against the vertical force. In addition, for the 1 m baseline deformations up to 2 times higher result compared to the 2 m long instrument.

5.3.2.3 Effect of gallery length

Uniform barometric pressure load

Another interesting point is the effect of the gallery length on deformations. Therefore, two models of the slope type with 30° and 90° slope angle are considered with a change in the gallery length between 50 m and 800 m (comp. Fig. 5.3e) considering the gallery type A.

The results (Fig. 5.23) show that generally the effect of the topographic effect decreases with increasing gallery length. For comparison the deformation amplitudes obtained in front of the gallery are also shown.

Strainmeter

The strain component parallel to the gallery has non-linearly decreasing amplitudes for increasing gallery length. For a 50 m long gallery and a 30° slope angle an amplitude of 0.4 nstrain is found and for a 90° slope angle an amplitude of 0.25 nstrain occurs. For both slope angles the amplitudes decreases to -0.19 nstrain with increasing gallery length up to 800 m.

A decrease of the topographic effect is clearly visible in the strain component perpendicular to the gallery. The effect is no longer found for a gallery longer than 350 m for the 30° slope angle. With regard to the 90° slope angle constant deformations emerge for galleries longer than 150 m. The more pronounced decrease for the 90° slope angle can be explained by the larger horizontal contribution due to the barometric pressure load on the slope which compresses the gallery. The constant deformations for long galleries are caused by the cavity effect.

Tiltmeter

The tilt component parallel to the gallery shows, with increasing gallery length, exponentially decreasing amplitudes from -1.36 nrad for 50 m to -0.27 nrad for the 800 m long gallery for the 30° slope angle. Regarding the 90° slope angle, the amplitude for the 50 m long gallery is -1.85 nrad and for the 800 m long gallery -0.22 nrad. For this deformation component the impact of the topography is less for smaller slope angles with shorter galleries. A similar small impact of the topography is obtained in the case of longer galleries with larger slope angles. The deformations are equal e.g. for a model with a 50 m long gallery and a 30° slope angle and for model with an about 100 m long gallery and 90° slope angle.

5 Principle investigations

With a sufficient gallery length (above 800 m), the amplitude will correspond to that of the cavity effect.

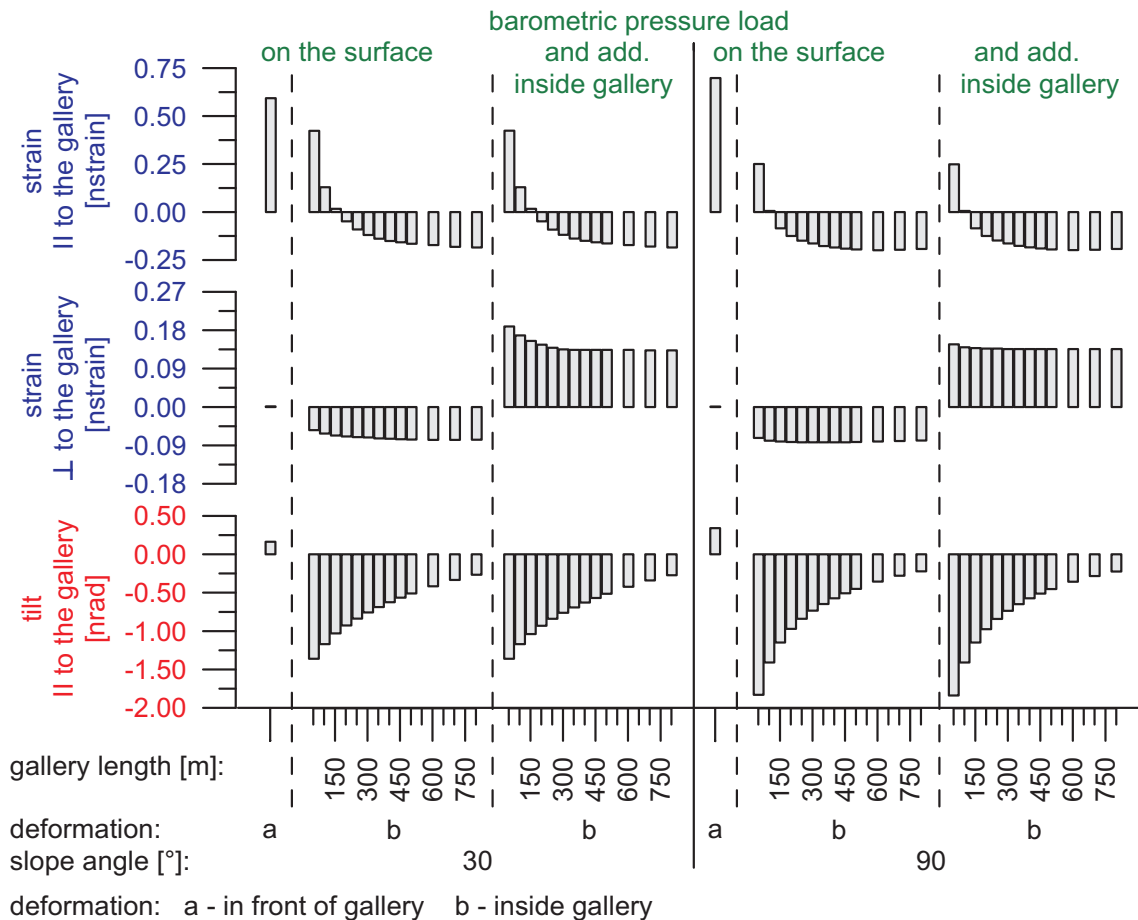


Fig. 5.23: Deformation effects depending on the gallery length (different scaling) for a 30° and 90° slope model (and gallery type A, Fig. 5.3a, e) for a 1 hPa barometric pressure load.

In case of gallery type B the strain component perpendicular to the gallery shows no signal. The strongest disturbing signal occurs in the tilt component parallel to the gallery, which is always detectable when scaled to typical pressure changes. Comparing the results for the valley model (Fig. 5.24) to the slope model type for the deformation components oriented parallel to gallery it follows:

Strainmeter

- the strain component inside the gallery shows a stronger decrease in the amplitudes for increased gallery length (of up to 50% for 800 m length).

Tiltmeter

- the amplitudes for the tilt component inside the gallery decrease less for increased gallery length (for 800 m length the amplitudes are about 15% larger than for the slope model type).

5 Principle investigations

This comparison for the slope and valley model type related to the gallery length also show that the previously strainmeter component is affected by a smaller area in the surroundings of the instrument than the tiltmeter.

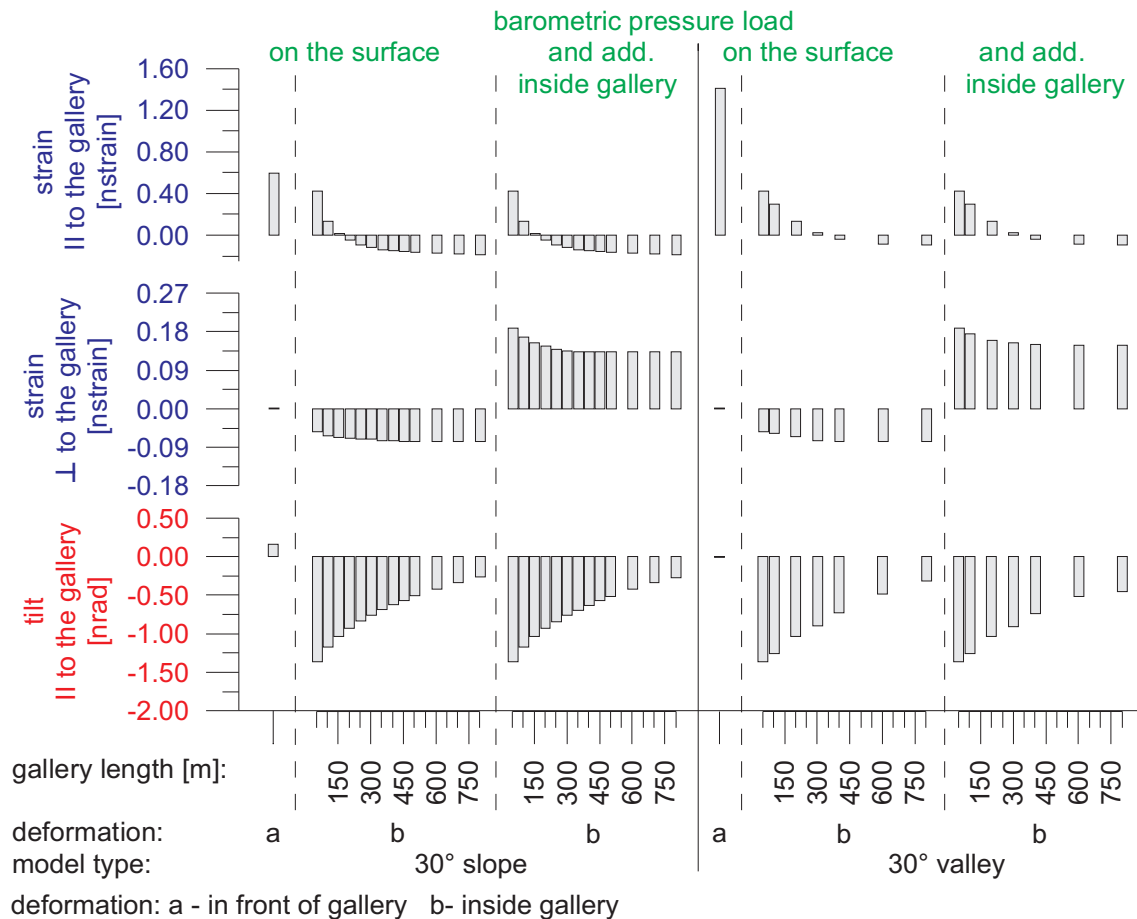


Fig. 5.24: Deformation effects depending on the gallery length (different scaling) for 30° slope and valley model types (and gallery type A, Fig. 5.3a, e) for a 1 hPa barometric pressure load (different scaling, the not shown tilt component perpendicular to the gallery has no signal).

Moving high pressure area

Parallel to the gallery

In the following the results are given for a 30° slope model with gallery type A of a length up to 800 m (Fig. 5.25).

Strainmeter

The characteristics of the deformations for the strain component parallel to the gallery depending on the length remain, but the amplitudes reverse in a similar kind as for the uniform load (Fig. 5.23). As expected, the deformations for the strain components perpendicular to the gallery for the various gallery lengths are in the same order of

magnitude which are below the detection level for a load of 1 hPa. For loads greater than 2 hPa the deformation is detectable.

Tiltmeter

The amplitudes of the tilt component parallel to the gallery are smaller and similar to the results for the uniform load. For a gallery length of 800 m occurs a maximum amplitude of about 0.7 nrad at time step 25% and -1 nrad at 75% for the parallel tilt component inside the gallery. The general deformation characteristics are given for the 50 m long gallery in [Fig. 5.11](#) and [Fig. 5.12](#). Additionally, a local minimum is created with a local amplitude of less than 0.3 nrad, when the front of the high pressure area crosses at the boundary between the slope and the plateau. For the high pressure area moving parallel to the gallery, the perpendicular tilt component has no signal.

Perpendicular to the gallery

Strainmeter

With regard to a perpendicularly moving high pressure area ([App. Fig. 17](#)), the dilatation decreases for the strain component parallel to the gallery up to a gallery length of 150 m and then to practically no signal. For longer galleries compression occurs with -0.2 nstrain at 800 m length for a load of 1 hPa. The study of the pure cavity effect ([Fig. 5.11](#)) shows a change in sign of the maximum-minimum structure for increasing coverage. Here, comparable behavior for increasing gallery length with a maximum deformation of ± 0.2 nstrain is found.

Tiltmeter

As expected, the amplitude of the tilt component parallel to the gallery decreases non-linearly from -1.35 nrad to -0.3 nrad. Here, the amplitude of the tilt component perpendicular to the gallery is also reduced as shown in [Fig. 5.11](#).

The results for the diagonal moving high pressure area given in [App. Fig. 18](#) are composed of signals of the orthogonally moving high pressure areas.

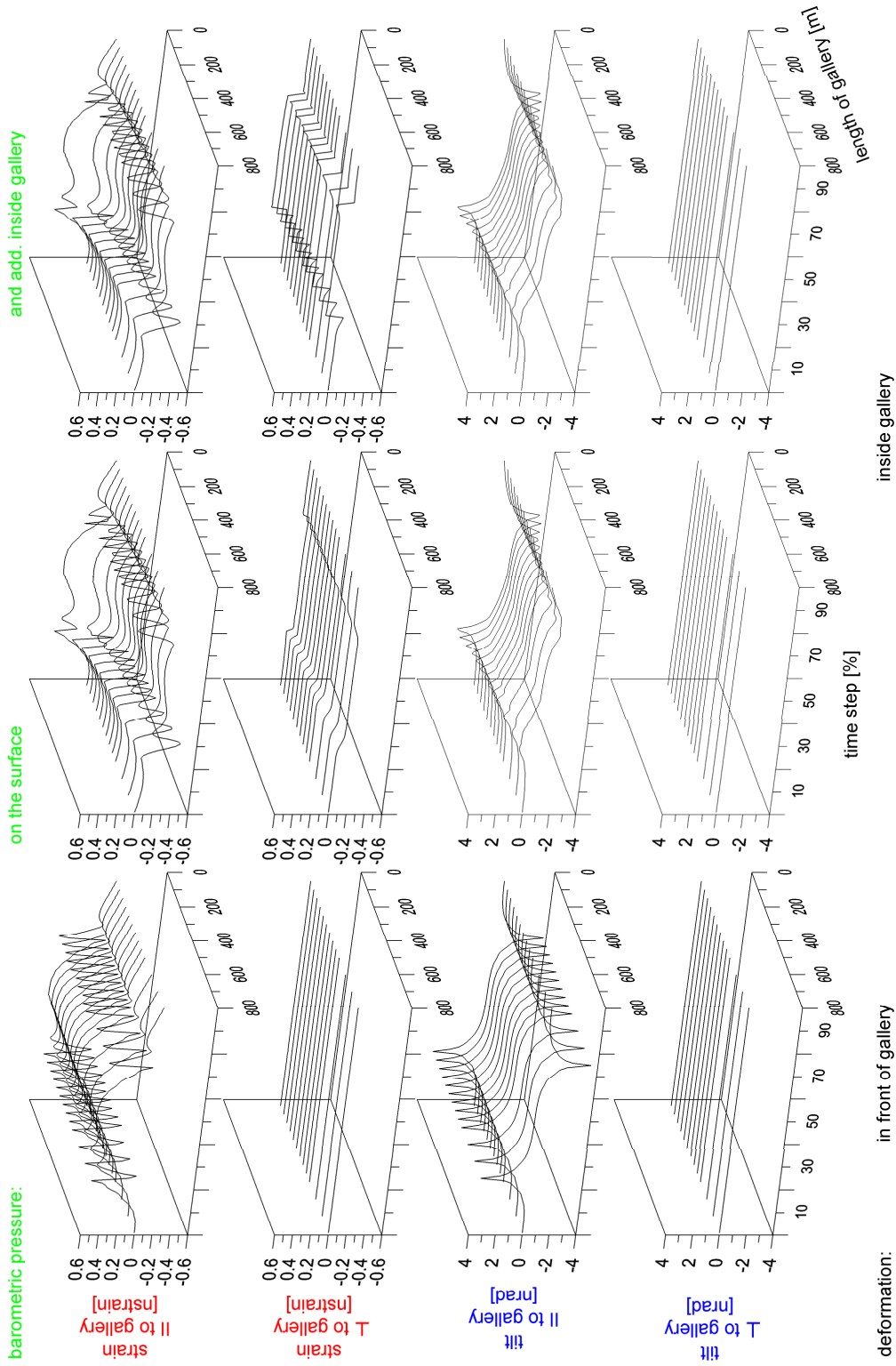


Fig. 5.25: Deformation results for 30° slope model type and gallery of type A with variable lengths (50 m to 800 m) for a parallel to the gallery moving high pressure area.

5.3.2.4 Effect of valley width

One aspect of interest related to valleys is the dependence of deformations on the valley width. The deformation results are found in Fig. 5.26. For this study a valley type model with gallery type A (Fig. 5.3a) and a slope angle of 30° is considered (comp. Fig. 5.3g).

Strainmeter

The deformation amplitudes (Fig. 5.26) decrease non-linearly depending on the valley width. The maximum amplitude of about 1.4 nstrain decreases for a valley width increase from 100 m to 200 m to about 20% for the strain components oriented parallel to the gallery.

The perpendicular strain component in front of the gallery shows no signal. Inside the gallery with barometric pressure load only acting on the surface a slightly increased compression for increased valley width occurs. With the additional load inside the gallery for this component a slight decrease in the deformation is found. For further increasing valley width the amplitudes converge to the results of the slope model type.

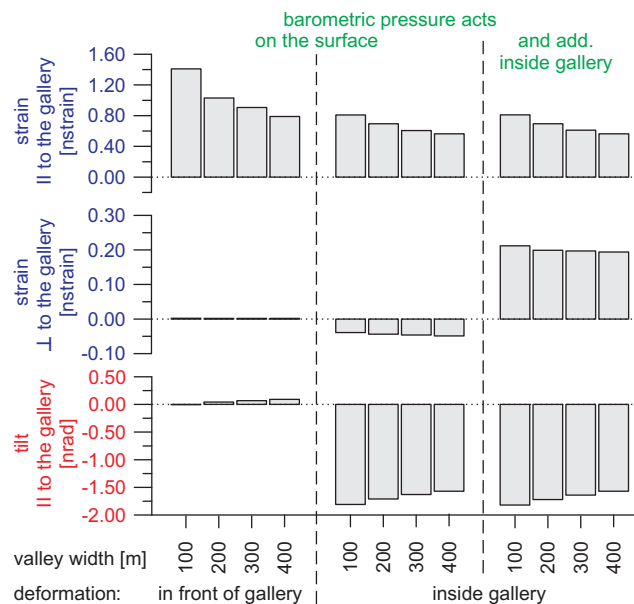


Fig. 5.26: Deformations obtained for the valley type model (slope angle 30°) with gallery type A for variable valley width (different scaling).

Tiltmeter

For the tilt component oriented parallel to the gallery located in front of the gallery (Fig. 5.26) an increasing amplitude emerges of about 0.2 nrad for 400 m valley width caused by the location of the instrument, which is not installed at the valley centre. For

5 Principle investigations

the tiltmeter installed inside the gallery a maximum amplitude of about -1.75 nrad is determined for a valley width of 100 m. For an increased valley width the amplitude decreases. For the tilt component oriented perpendicular to the gallery no signal emerges.

When gallery type B is incorporated (comp. Fig. 5.3b), the strain component perpendicular to the gallery (thus parallel to the slope) is not affected by the changed valley width and thus no additional signal exists. For the tilt component oriented parallel to the gallery amplitudes of less than 10^{-2} nrad occur, which are below the detection level.

Moving high pressure area

The results for a high pressure area moving parallel to the gallery (Fig. 5.27) show similar decreasing amplitudes as for the uniform barometric pressure load. The amplitude characteristics with respect to the location of the high pressure area are outlined in Fig. 5.20. For perpendicularly and diagonally moving high pressure areas deformations occur as shown in App. Fig. 19, and App. Fig. 20. The deformations vary as found in Fig. 5.27. The time-dependent behavior is similar as for the model without fault included.

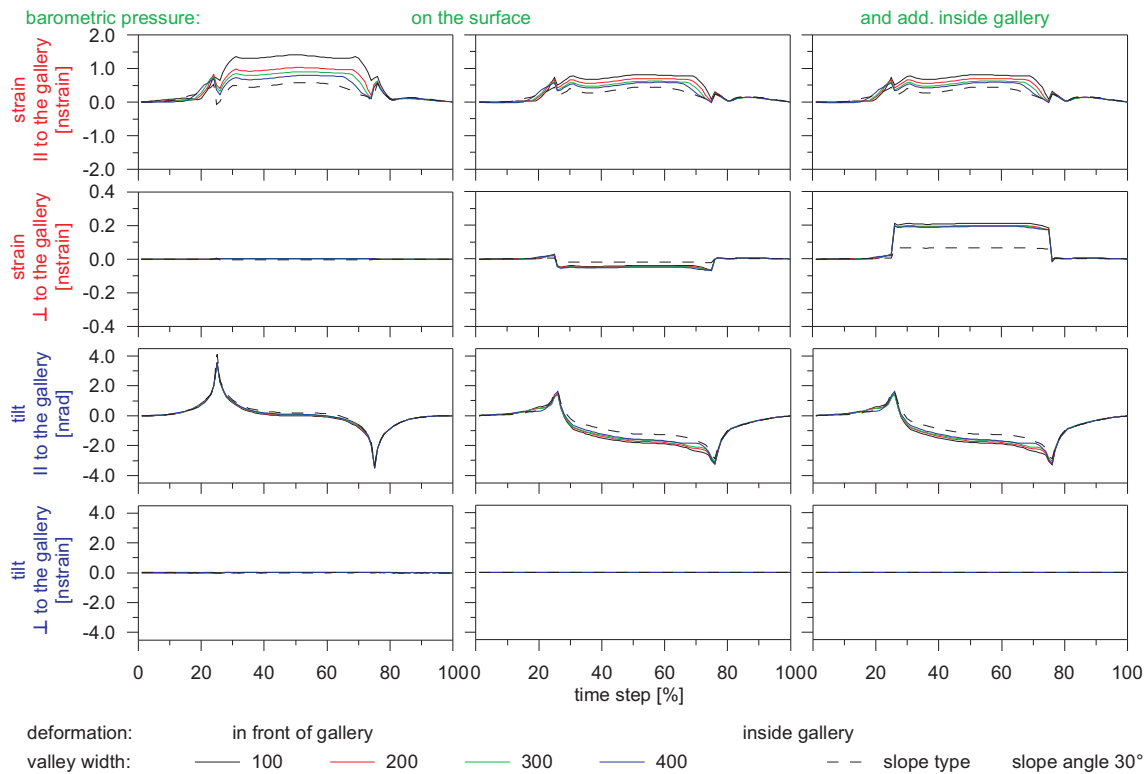


Fig. 5.27: Deformation results for various valley widths and 30° reference slope model and parallel to gallery moving high pressure area (different scaling).

5.3.3 Lithological effects

5.3.3.1 Effect of rock properties for homogeneous parameterized models

Besides the previously discussed impact factors deformations are affected by lithology. In order to estimate the order of magnitude of the lithologic effect, the Young's modulus is changed between 10 GPa and 85 GPa, and the Poisson ratio between 0.2 and 0.4. This range covers typical rocks found in the surroundings of the observation sites of interest (e.g. Lüthke, 1998; Kroner et al., 2005; Steffen 2006; Steffen et al., 2006). For this study four models are used: a slope and a valley type model with slope angles of 30° and each with gallery types A and B included (comp. Fig. 5.3a, b, c, f). The results for the slope model with gallery type A (Fig. 5.28) show a non-linear* relation between the rock parameters and the deformation components. As expected, the biggest effects are found for a low Young's modulus and Poisson ratio with up to several times larger deformations. Especially, this is found in the components parallel to the gallery compared to the topographic effect.

In case of the valley model type (gallery type A included) the strain and tilt components in parallel to the gallery (Fig. 5.29) have larger amplitudes, similar to the amplitudes found in the study of the topographic effect (comp, chapter 5.3.2). In Fig. 5.30 the results for the strain and tilt components perpendicular to the gallery of type B are given. The components not shown are similar compared to the results of the slope model and gallery of type A. Caused by the extension of the gallery type B small amplitudes are obtained, but always below the detection level.

The deformations related to material parameters in the range of those actually occurring at observatory sites (comp. Tab. 6.1) vary less than 5%. The maximum modeled amplitudes are about 7 nstrain for strain and 15 nrad for tilt. Following that induce small-scale material changes in solid rocks (e.g. granite) in vicinity of an instrument site only small signals.

* Although Hooke's law is linear, the non-linear behavior is due to effects of topography, cavity and lithology.

5 Principle investigations

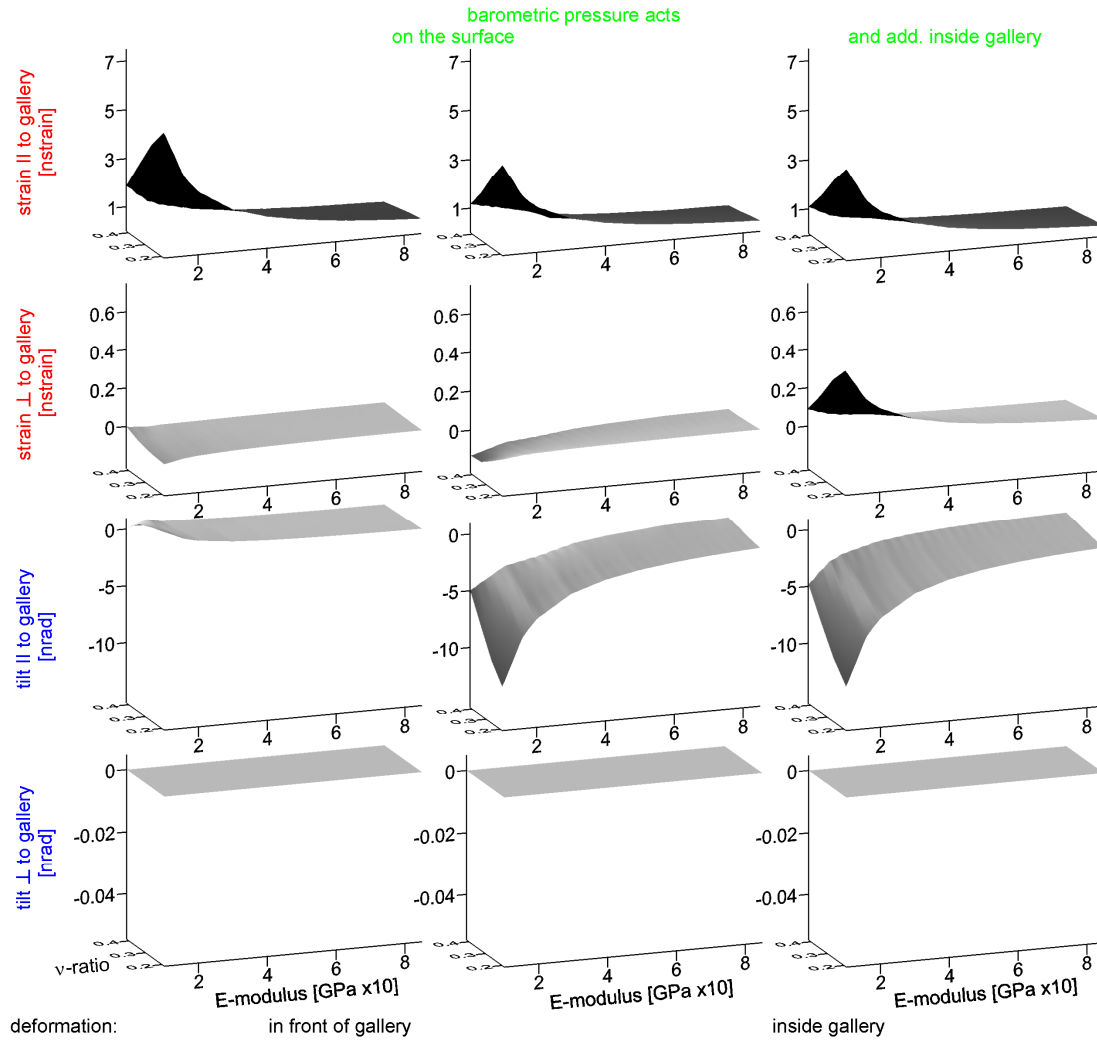


Fig. 5.28: Results for different material parameters for a slope model (slope angle 30°) and gallery type A included (different scaling).

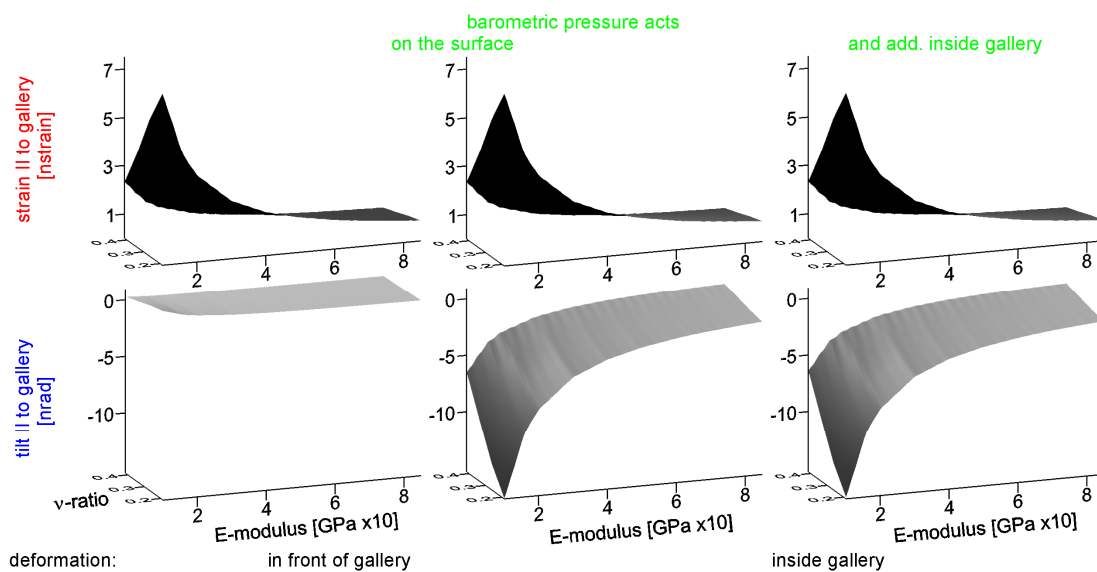


Fig. 5.29: Results for different material parameters for a valley model (slope angle 30°) and gallery type A included.

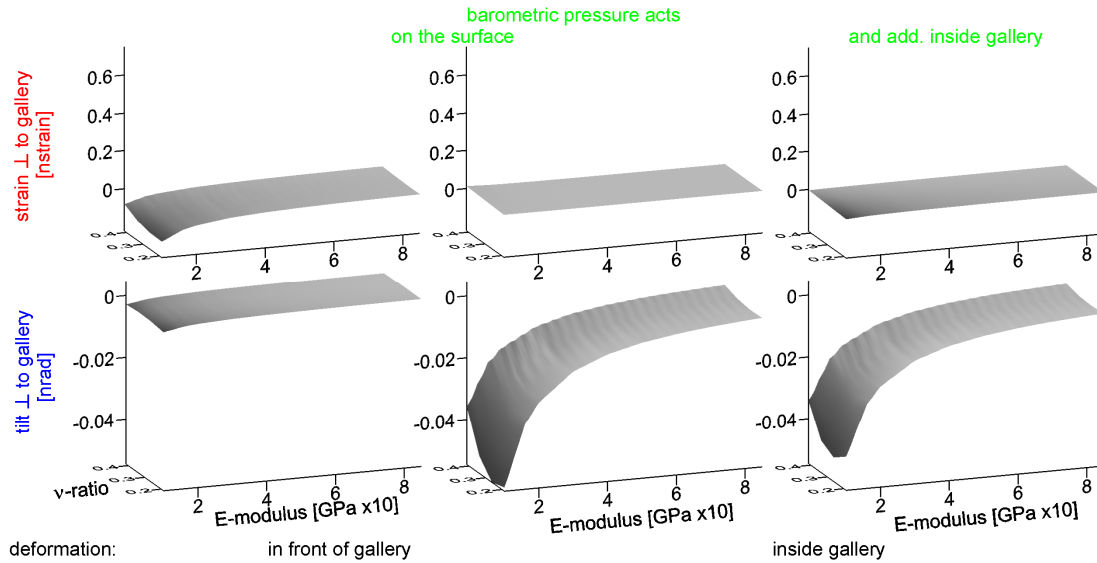


Fig. 5.30: Results for different material parameters for a slope model (slope angle 30°) and gallery type B included.

5.3.3.2 Effect of different lithological units

For studying the effect of lithology units (comp. [Tab. 5.2](#)) adjacent to each other in various distances to the instrument location are considered. The lithological border is moved through the whole plain and 30° slope model types. For maximum distances the models are homogeneously parameterized. Negative distance values for the position of the lithological border denote that the instrument is found in the weaker lithological unit. The assumed instrumentation consists of two orthogonally oriented strainmeters and a tiltmeter (comp. [Fig. 5.3a, b](#) 'deformations in front of gallery'), which are located in the centre of the model. The assumption is that the lithological units are ideally connected, thus no transition zone exists. This case is comparable with a granitic intrusion into weaker sediment, like sandstone. Three different material contrasts are chosen (comp. [Tab. 5.2](#)):

- sandstone – granite (Young's modulus contrast 1:5)
- marlstone – granite (Young's modulus contrast 1:2)
- limestone – granite (Young's modulus contrast 1:1.2)

This selection captures a wide range of existing contrasts. With regard to the previously mentioned conditions maximum deformations can be expected.

Considering the lithological units for the 30° slope model type and gallery type A three model versions are developed ([Fig. 5.31](#)), with the lithological border oriented:

- *version a* - parallel to the gallery ([Fig. 5.31a](#)),

5 Principle investigations

- *version b* - perpendicular to the gallery; The model is firstly parameterized with the properties of the weaker rock. By moving the lithological border the part parameterized with the properties with the more rigid rock is successively increased until the model is homogenously parameterized with properties of the more rigid rock (Fig. 5.31b),
- *version c* - perpendicular to the gallery; The material parameter of the two parts are exchanged with respect to *version b* (Fig. 5.31c).

As loading are considered the static uniform load and the moving high pressure areas are considered (Fig. 5.5, Fig. 5.6).

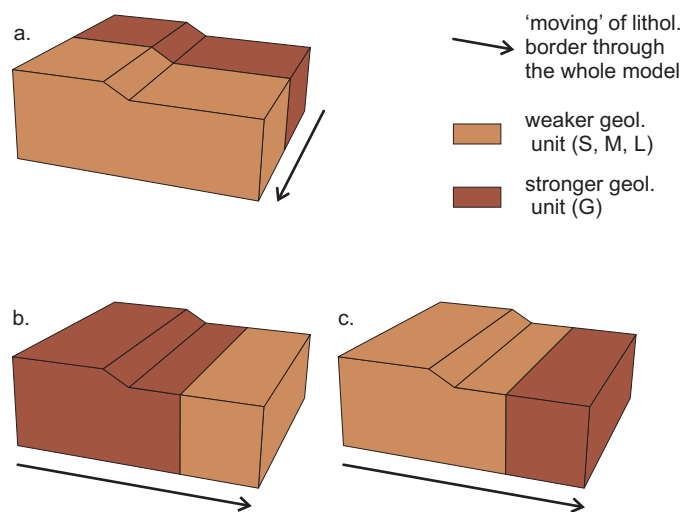


Fig. 5.31: Model conditions for 30° slope model to investigate the effects of lithological units.

Plain model type with uniform barometric pressure load

Deformations are only found for components oriented perpendicularly to the lithological border (Fig. 5.32), thus the components where no signal occurs are not shown. The deformation behavior of the model is sketched in Fig. 5.33 for a uniform barometric pressure load. The weaker unit is more strongly compressed in vertical direction than the more rigid unit, which leads to the following horizontal deformations (largest material contrast considered):

Strainmeter

The maximum amplitude of 3.5 nstrain occur when the instrument is located in the unit with the more rigid material parameter (granite) and a small distance to the lithological border. For increased distance the dilatation decreases to no deformation for a homogeneous granitic material parameter. Compression occurs with a maximum amplitude of about -1 nstrain for distances larger than 60 m between the instrument site

5 Principle investigations

and the lithological border. In this case the instrument is located in the weaker lithological unit. For distances between 0 m and 60 m dilatation is obtained with an amplitude of about 3.3 nstrain. Generally the change in the maximum amplitude corresponds to the variation in the Young's modulus ratio.

Tiltmeter

The bottom of the tiltmeter relative to the top moves always away from the weaker material independent from the location of the lithological border (comp. Fig. 5.33). Depending on the lithological unit where the instrument is located the tilt amplitude decreases for an increasing distance between the lithological border and the instrument site. When the tiltmeter is located in the granitic unit the decrease is more pronounced than for the weaker units.

For the largest material contrast (sandstone-granite) a maximum tilt of 7 nrad is obtained and for the rock combination marlstone-granite a value of about 2.5 nrad. For the model with the smallest contrast (limestone-granite) an amplitude of 0.5 nrad is found. Depending on the material contrast the distance between the lithological border and the instrument location varies, where the impact of the lithological border vanishes. E.g., for the combination limestone-granite the distance is about 50 m and for marlstone-granite about 750 m.

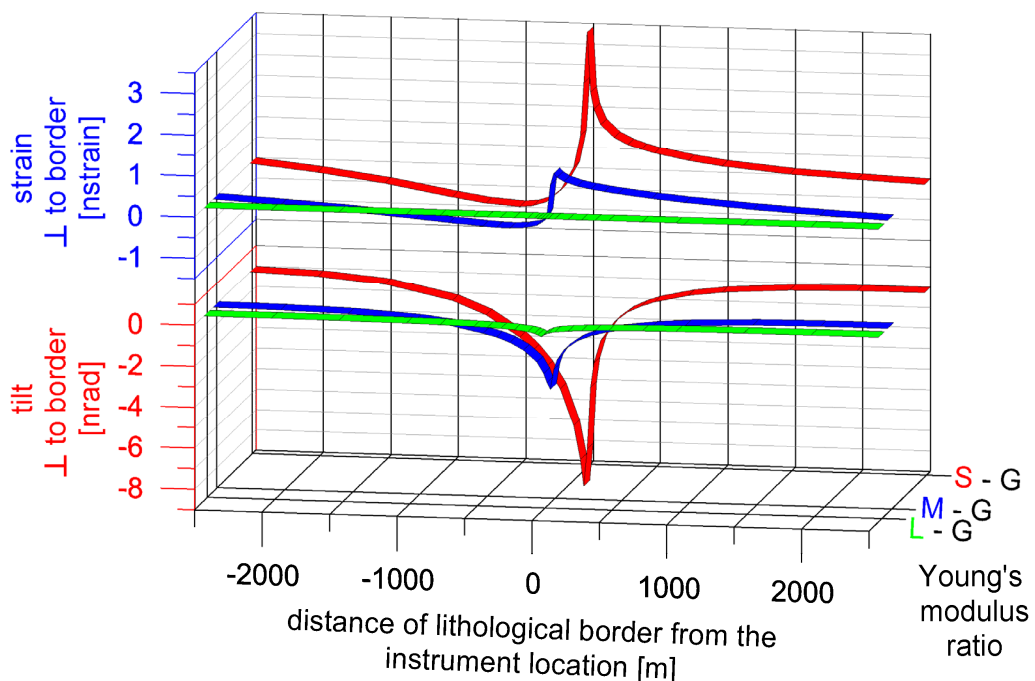


Fig. 5.32: Deformation results for different rock types (G-granite, L-limestone, M-marlstone, S-sandstone) various distances of the lithological border to the instrument location using the plain model type (different scaling).

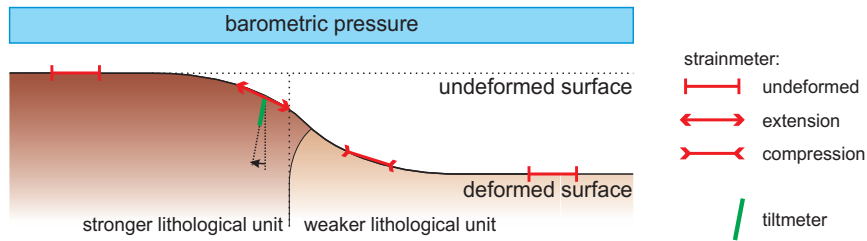


Fig. 5.33: Sketch illustrating deformations related to different adjacent to each other rock types for uniform barometric pressure loading a plain model.

Plain model type loaded by moving high pressure areas

The results for the moving high pressure area (Fig. 5.35) show superimposed signals from the homogenous (comp. Fig. 5.11) models and the impact of the lithological border related to a uniform barometric pressure load (Fig. 5.32). This circumstance is clearly seen for the high pressure area moving parallel to the lithological border (Fig. 5.34). For the perpendicular to the border moving high pressure area only the components oriented perpendicularly to the border show deformations (Fig. 5.35).

For the strain component oriented parallel to the lithological border the time-dependent signals occurs corresponding to the results for the strain component oriented parallel to the gallery for a parallel to the gallery moving high pressure area found in Fig. 5.11. The models with the lithological border in various distances show a continuous change in the amplitudes.

For the strain component oriented perpendicularly to the lithological border the deformation results are caused by superimposed effects of the time-depended barometric pressure load and the lithological border. The deformations caused by the lithological border are in a similar order of magnitude as determined for uniform barometric pressure load (Fig. 5.32). The features in the tilt amplitudes are comparable to the strain components. The diagonally moving high pressure area is composed of, as shown for the other model types, signals of the orthogonally moving high pressure areas.

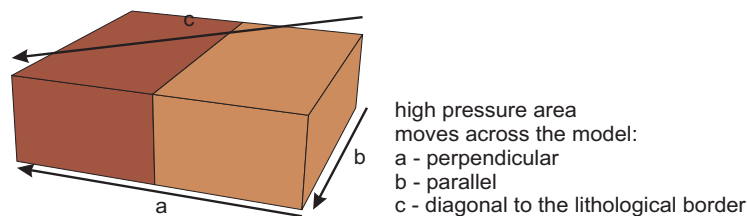


Fig. 5.34: Moving directions of the high pressure area related to the investigation of the impact of two different lithological units on deformations.

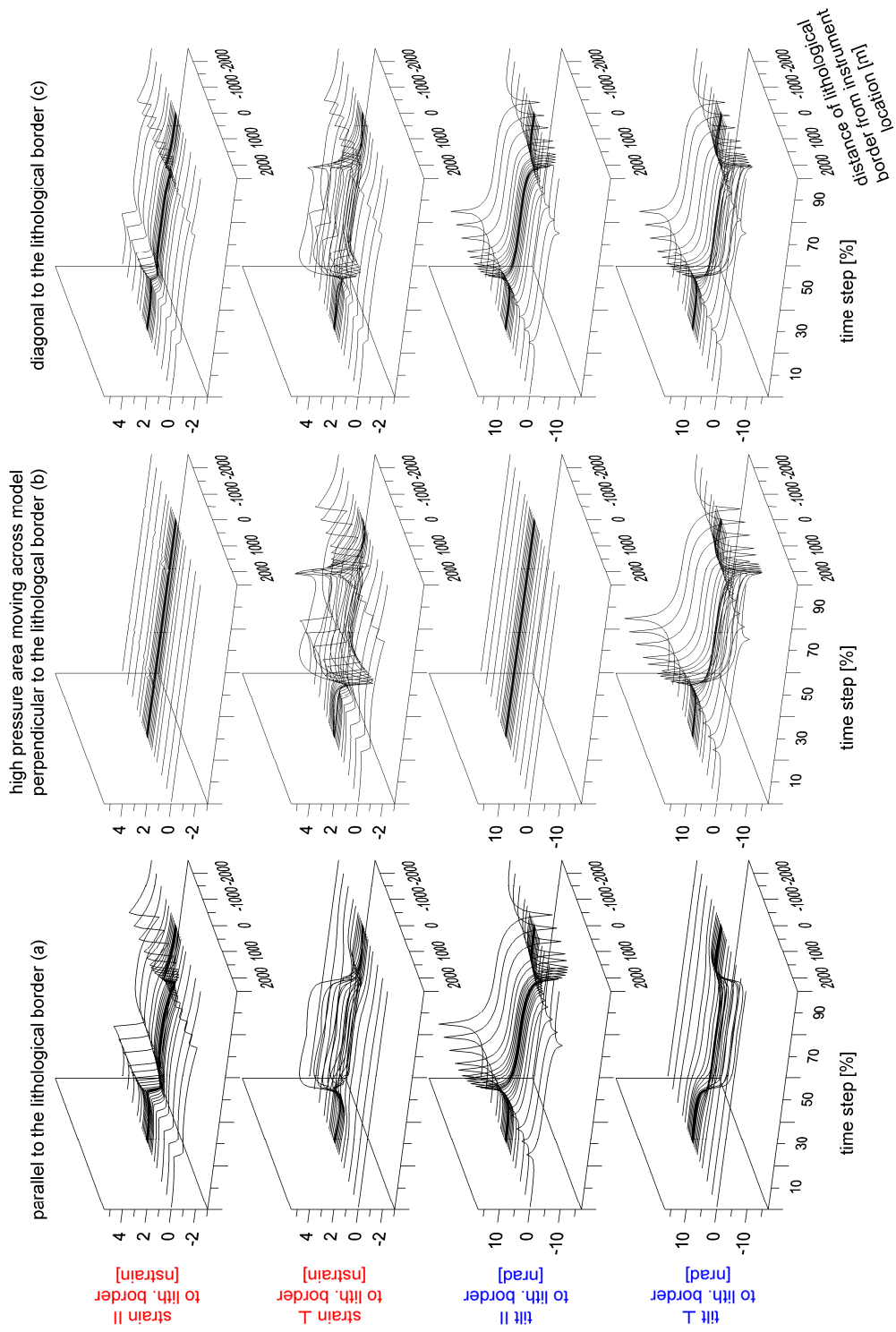


Fig. 5.35: Deformation results for different rock types adjacent to each other (sandstone - granite) in various distances to the instrument location for high pressure areas moving across the plain model type.

Fig. 5.36 shows the amplitudes for the perpendicular strain component in the front of the gallery for a 90° slope model type with a slope height of 300 m if the distance of the lithological border and the instrument location is 0 m and the results. A perpendicular to the lithological border respectively to the topography moving high pressure area is considered. As previously discussed the horizontal deformations are caused by the different amplitudes in the vertical compression of the lithological units. In similar kind due to the different heights of the topography the slope model is compressed, in which additional signals are produced by the scarp (comp. chapter 5.3.2.1, Fig. 5.19).

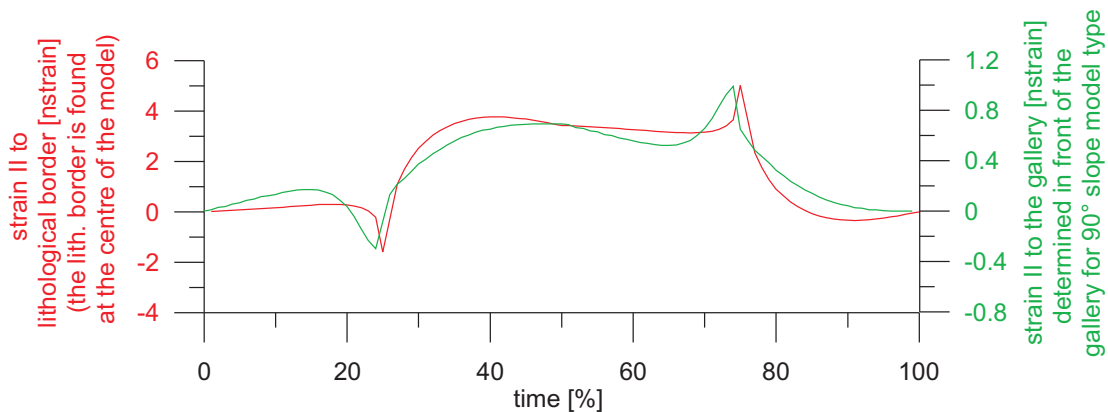


Fig. 5.36: Comparison of strain amplitudes obtained for models containing on the one hand geological and on the other hand topographic features.

30°slope model type and lithological units (version a)

The deformations contain signals which occur from both, topography and lithology (Fig. 5.37). The deformation components oriented parallel to the gallery, thus also parallel to the lithological border are affected by the predominant material present. The deformation components perpendicularly oriented to the gallery show deformation amplitudes which are similar to the results obtained for the plain model type (comp. Fig. 5.32). The amplitudes are in the order of magnitude as obtained for the plain model type, and the effects are due to the lithology.

Related to the previously mentioned models a further investigation is carried out for the moving high pressure area. Fig. 5.28 shows the results for a high pressure area moving parallel to the gallery. The effects superimpose in similar kind as for investigations related to the plain model type (comp. Fig. 5.35). Additionally, effects occur caused by the lithological border and the high pressure area in combination with the topography. For the tilt component oriented parallel to the gallery maximum amplitudes of about 14 nrad are obtained if the model is parameterized homogeneously with sandstone. The effects in this deformation component are only caused by the parameteriza-

5 Principle investigations

tion, the topography and the load, but not by the lithological border. Taking this and the results for the homogeneously parameterized models into account an order of magnitude of the various impact factors can be inferred: lithological units > topography > cavity. The results for a perpendicularly moving high pressure area are found in [App. Fig. 21](#) and for a diagonally moving high pressure area in [App. Fig. 22](#). The deformation component oriented perpendicularly to the lithological border show amplitudes similar to the results obtained by the uniform load.

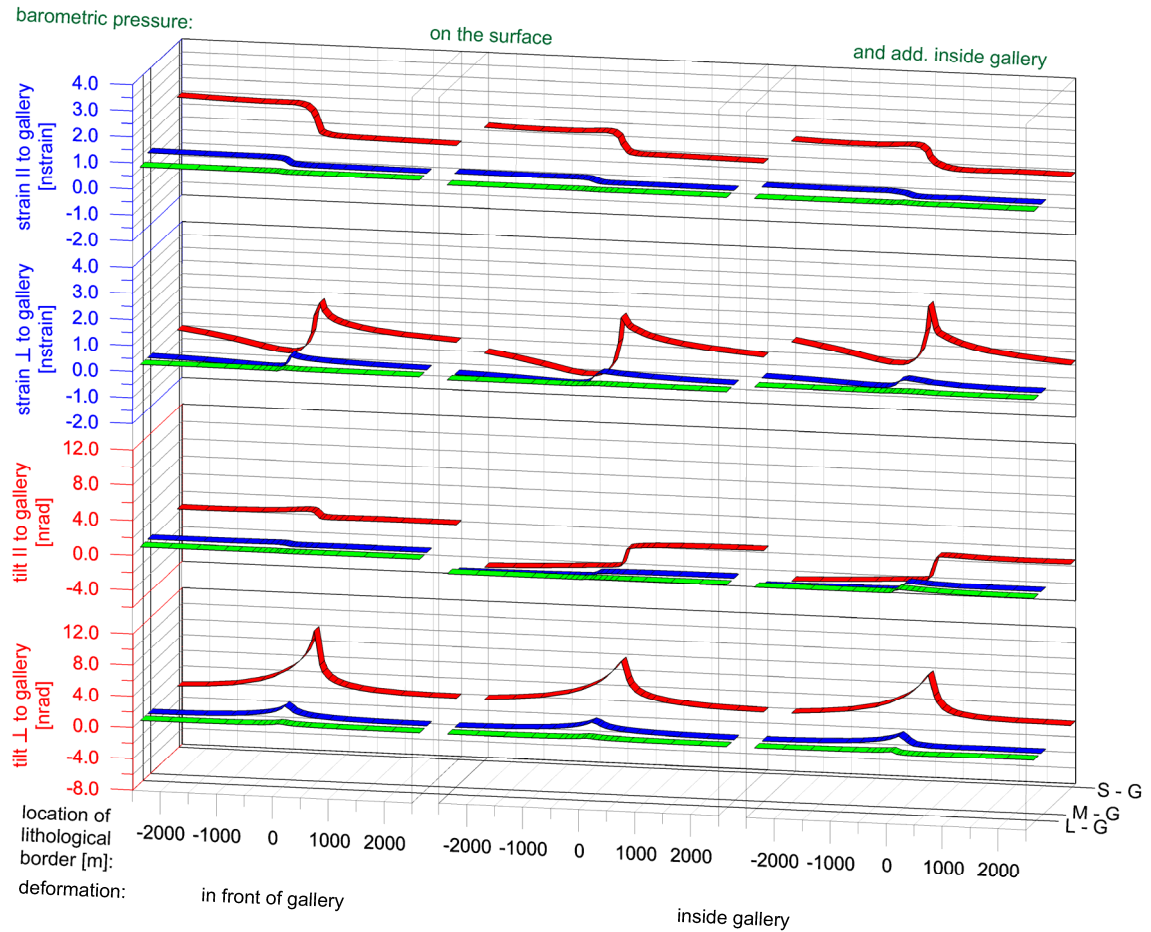


Fig. 5.37: Deformation results for a 30° slope model type and lithological units. The border of the lithological unit is oriented parallel to the gallery (comp. [Fig. 5.31a](#)).

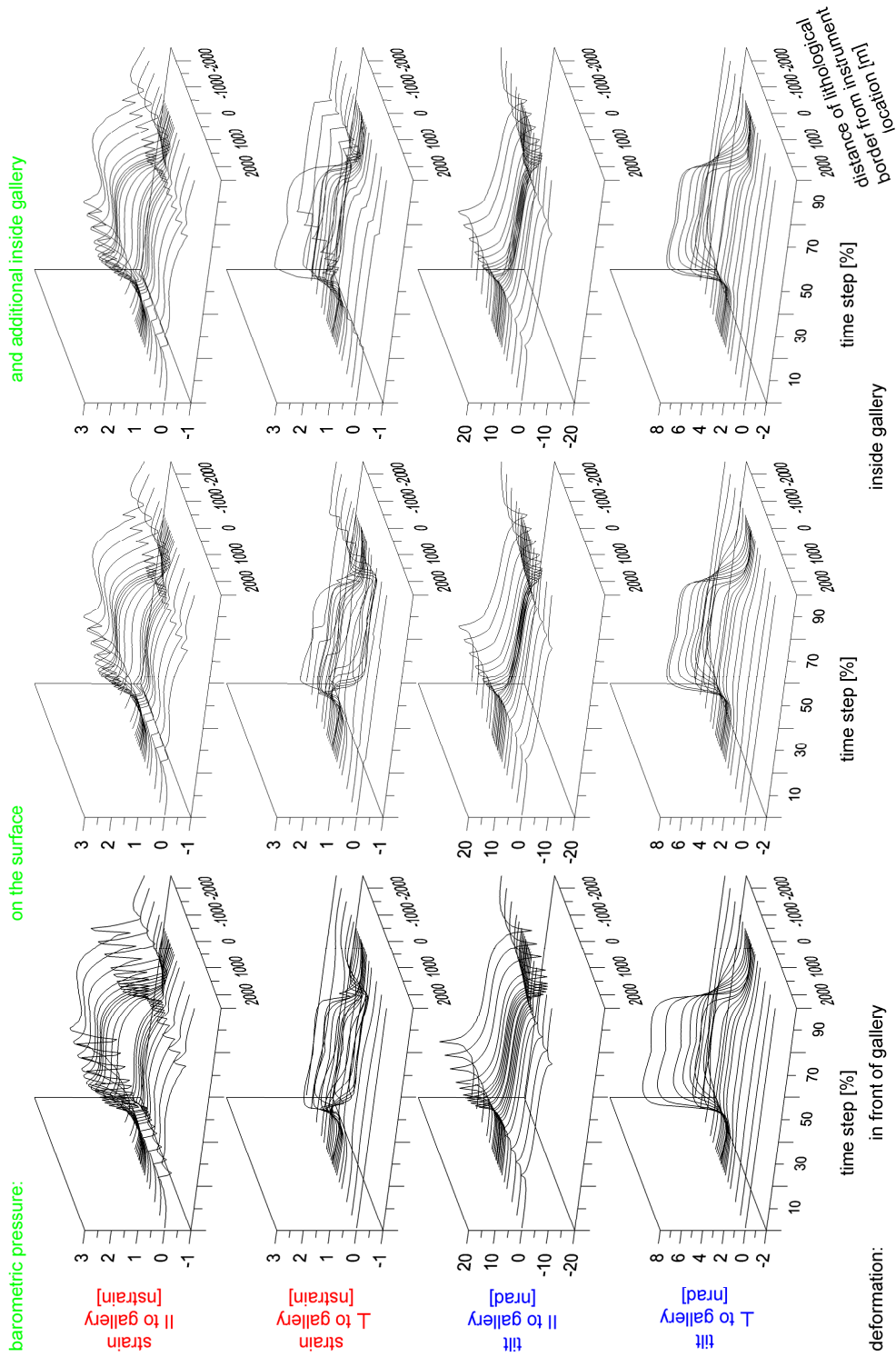


Fig. 5.38: Deformation results for a 30° slope model type with gallery type A included and parallel to the gallery oriented lithological border (comp. Fig. 5.31a) for a parallel to the gallery moving high pressure area (different scaling).

30° slope model type and lithological units (version b, c)

In addition to a lithological border oriented parallel to the gallery a perpendicularly oriented border is investigated. The model, which is used for this study, is sketched in [Fig. 5.31b](#). The resulting deformations are found in [Fig. 5.39](#). Deformations for the components oriented parallel to the gallery show signals which are composed of the effects caused by the topography and lithology. The amplitudes are in the order of magnitude obtained in the previous investigations related to the lithological impacts.

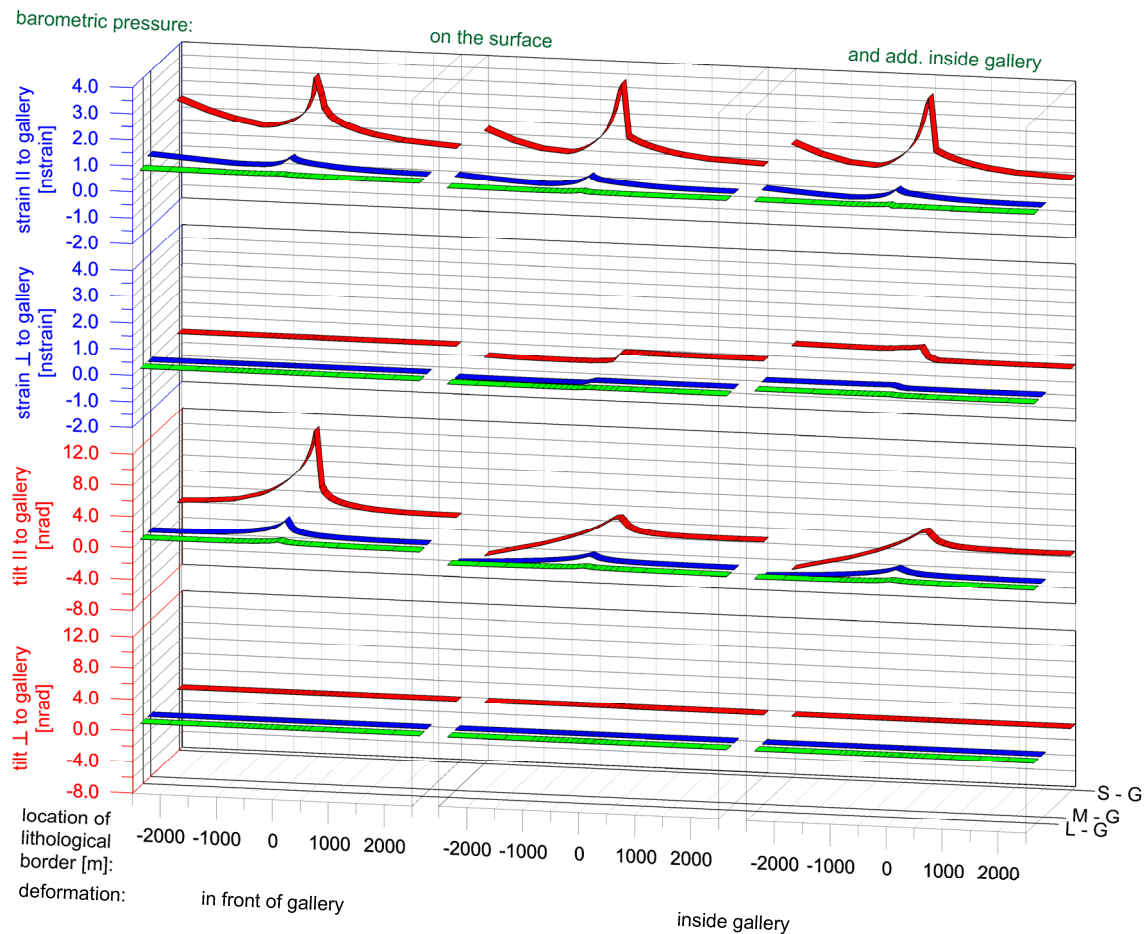


Fig. 5.39: Deformation results for a 30° slope model type and different lithological units. The border of the lithological unit is oriented perpendicularly to the gallery (comp. [Fig. 5.31b](#)).

The results for reversed parameterization of lithological units (comp. [Fig. 5.31c](#)) are found in [Fig. 5.40](#) with amplitudes in the order of magnitude which corresponds to the material contrast sandstone – granite. For the strain component oriented parallel to the gallery located in front of the gallery a reversed behavior depending on the border location occurs. The amplitude of the corresponding tilt component is reversed, thus the dip of the pendulum moves towards the weaker lithological unit, whereas the amplitudes inside the gallery for barometric pressure load on the surface and additionally inside

are about 2.5 times larger than for the results for replaced material parameters (Fig. 5.39). The effects induced by the lithological differences are also up to 4 times bigger than the effects caused by the topography. The results for a high pressure area moving parallel to the gallery are found in App. Fig. 23. The tilt component oriented parallel to the gallery is the strongest affected component with maximum amplitudes of about 17 nrad.

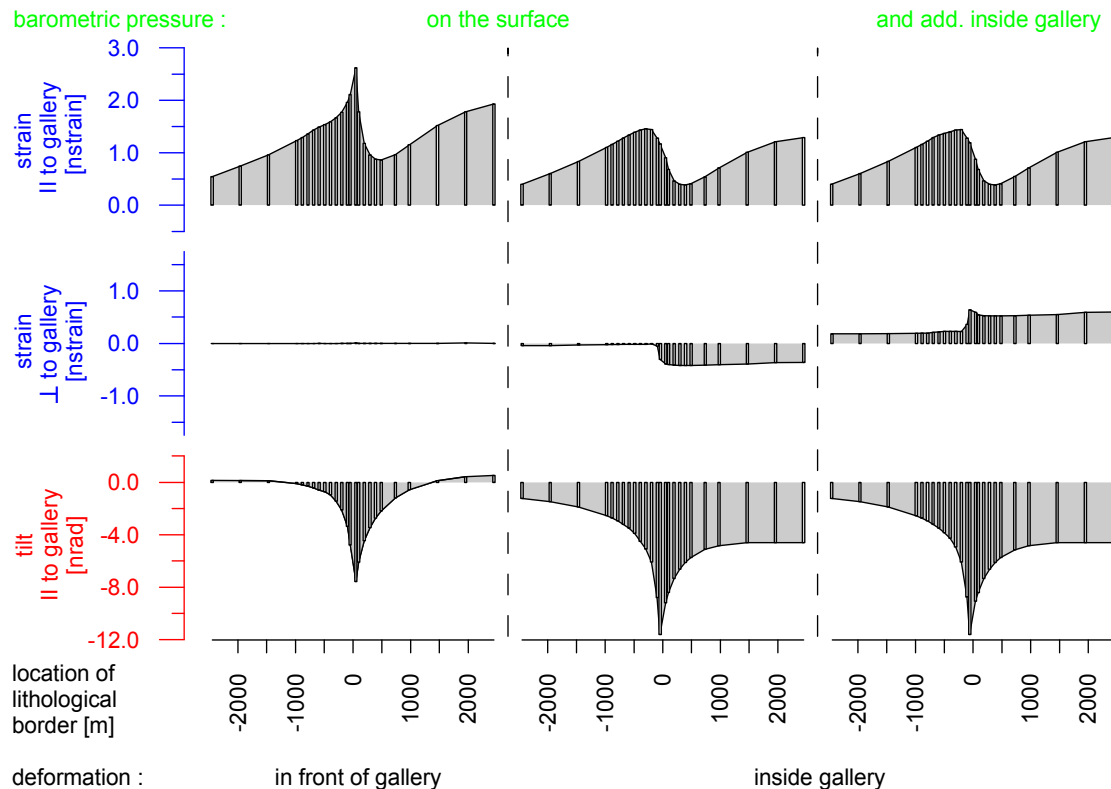


Fig. 5.40: Deformation results for a 30° slope model type and different lithological units (sandstone - granite). The border of the lithological unit is oriented perpendicularly to the gallery (comp. Fig. 5.31c). The tilt component perpendicularly oriented to the gallery is not shown as no signal occurs.

5.3.4 Effects related to faults

5.3.4.1 Effects for the plain model type

Considering additional geological features the impact of a fault in the vicinity of the instrument location is investigated. A plain and a 30° slope model are used (Fig. 5.4).

The results for the plain model type and faults of different sizes are given in Fig. 5.41. As load only moving high pressure areas are considered. Deformations occur by the moving high pressure area across the plain model type similar to the cavity effect (chapter 5.3.1). Based on this, only the differences caused by the fault will be considered in the following.

Strainmeter

For the strainmeter oriented perpendicularly to the pressure front during the passage of the high pressure area increased deformations occur if a fault is present. To explain this Fig. 5.42 is used. The strainmeter is oriented perpendicularly to the fault and a high pressure area moves perpendicularly to the fault across the model. Fig. 5.42a shows the deformations for the plain model and Fig. 5.42b for the model with a fault for a time step less than 25%. Due to the load the fault is opened and thus the strain is increased. For the tilt component a reduced amplitude is found. For later time steps, between 25% and 75%, the fault is closed due to the load above, thus deformations occur as for the plain model.

The dimension of the fault controls the increase and the reduction in the deformation components (Fig. 5.41). The dependency of the amplitude change on the fault dimension is non-linear.

The maximum strain amplitudes for the perpendicularly oriented component occur always before respectively after the pressure front crosses the instrument location. Depending on the fault size the distance varies where the maximum occurs. E.g. for the smallest fault (300 m long, 100 m deep) a distance of about 150 m between the pressure front and the instrument location is determined with an amplitude of 3.42 nstrain.

Related to the parallel to the fault orientated moving high pressure area only for the perpendicular deformation components a difference occurs compared to the results of the plain model type. For time steps less than 25% and larger than 75% (comp. Fig. 5.6) the surface is stretched due to the load in vicinity of the fault. This expands the fault and the deformations discussed are produced. For the strain component perpendicular to the fault, also parallel to the moving direction of the high pressure area, a maximum amplitude of about 0.8 nstrain for the 300 m long fault is determined and about 1.5 nstrain for the 3,000 m long one.

Tiltmeter

The tilt component oriented perpendicularly to the fault only for the high pressure area moving perpendicularly to the fault show significant effects caused by the fault. For the largest fault (3,000 m x 1,000 m) a maximum amplitude occurs 50 m after the pressure front has crossed the instrument location, with an amplitude of 2.3 nrad in the example.

5 Principle investigations

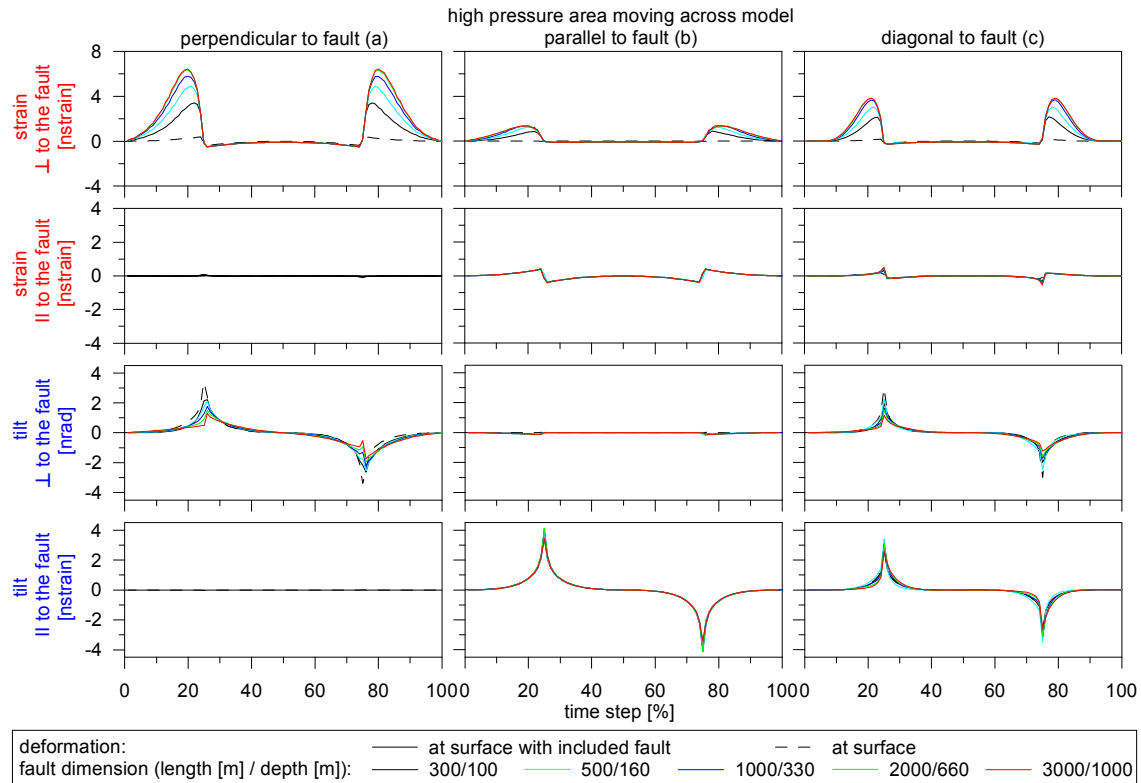


Fig. 5.41: Deformation results for moving high pressure areas for the plain model type and faults.

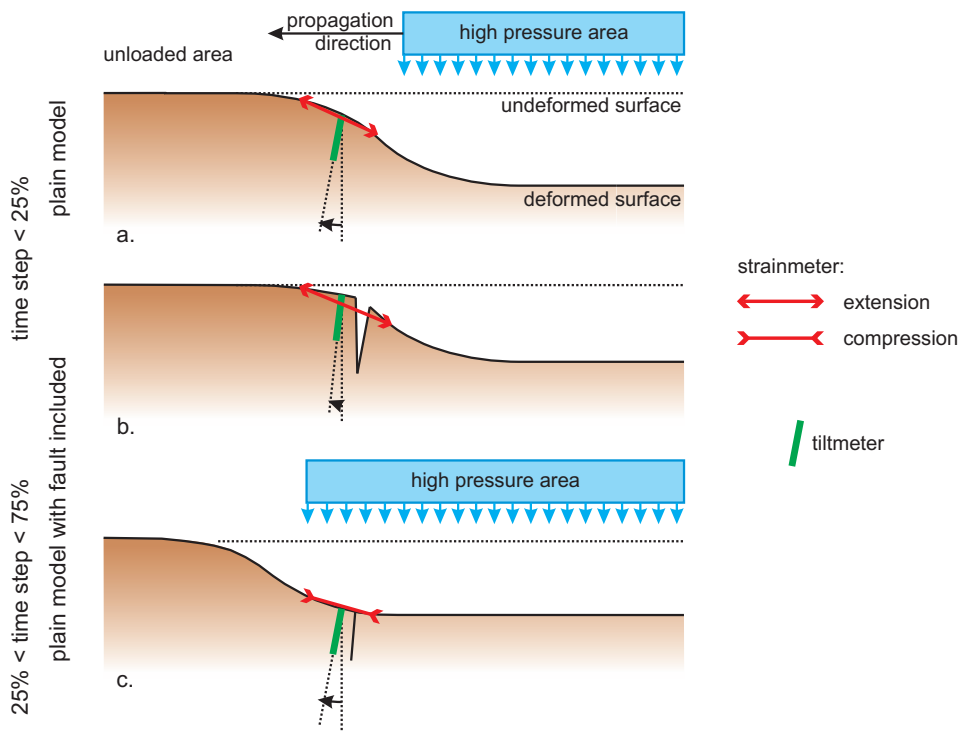


Fig. 5.42: Deformations related to the plain model type and a fault for a moving high pressure area.

5.3.4.2 Effects for the 30° slope model type

For the investigation of the impact of a fault connected to topography and gallery a 30° slope model type with gallery type A (comp. Fig. 5.3a, c) is used. The loads considered are the orthogonally moving high pressure areas. Three cases of fault orientations and positions with a dimension of 300 m x 100 m related to the gallery are investigated:

- oriented parallel with a distance of 50 m to the gallery,
- oriented perpendicularly at the entrance of the gallery,
- oriented perpendicularly 50 m behind the head of the gallery.

The deformations for the first case are given in Fig. 5.43. Compared to the models without faults (comp. Fig. 5.18) differences occur, significant for the strain component oriented perpendicularly to the gallery for the perpendicularly to the gallery moving high pressure area. The missing connection to the surrounding material caused by the fault suppresses the dilatation. The results for the high pressure area moving diagonally to the gallery are found in App. Fig. 24 related to the previously mentioned model.

A similar behavior is found for deformation components oriented perpendicularly to the fault related to the second and third considered model assembly, thus faults oriented perpendicularly to the gallery (Fig. 5.44). In the following some selected results are discussed in detail: If the fault is found at the gallery entrance the strain component oriented parallel to the gallery shows a significant impact (Fig. 5.44). Effects corresponding to the impact of topography do not occur for the parallel to the gallery moving high pressure area. Instead a constant signal is found. For the strain observed in front of the gallery dilatation of about 0.8 nstrain is determined. For to the component located inside the gallery compression of 0.4 nstrain is obtained. The horizontally acting force caused by the load of the hill flank is suppressed. For the strain component practically no signal occurs for the perpendicular to the gallery moving high pressure area. Small, not significant additional effects caused by the fault can be identified for the strain component oriented perpendicularly to the gallery and for the tilt component oriented in parallel. The results for the high pressure area moving diagonally to the gallery are found in App. Fig. 25. The tilt component oriented perpendicularly to the gallery is not affected by the fault.

5 Principle investigations

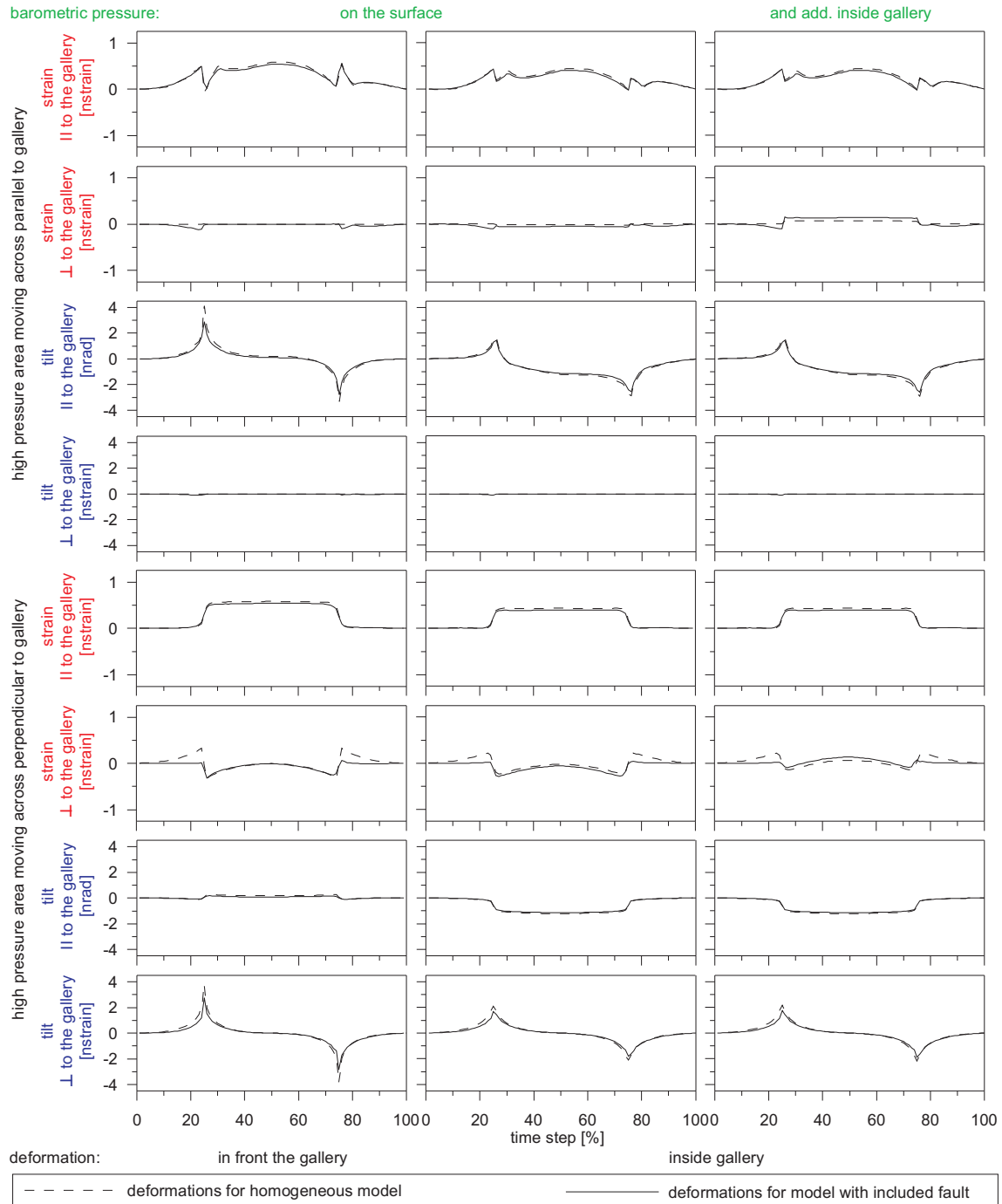


Fig. 5.43: Deformation results for a 30° slope model type and gallery type A. Parallel to the gallery in a distance of 50 m a fault with a length of 300 m and a depth of 100 m is included. For load orthogonally moving high pressure areas are considered.

5 Principle investigations

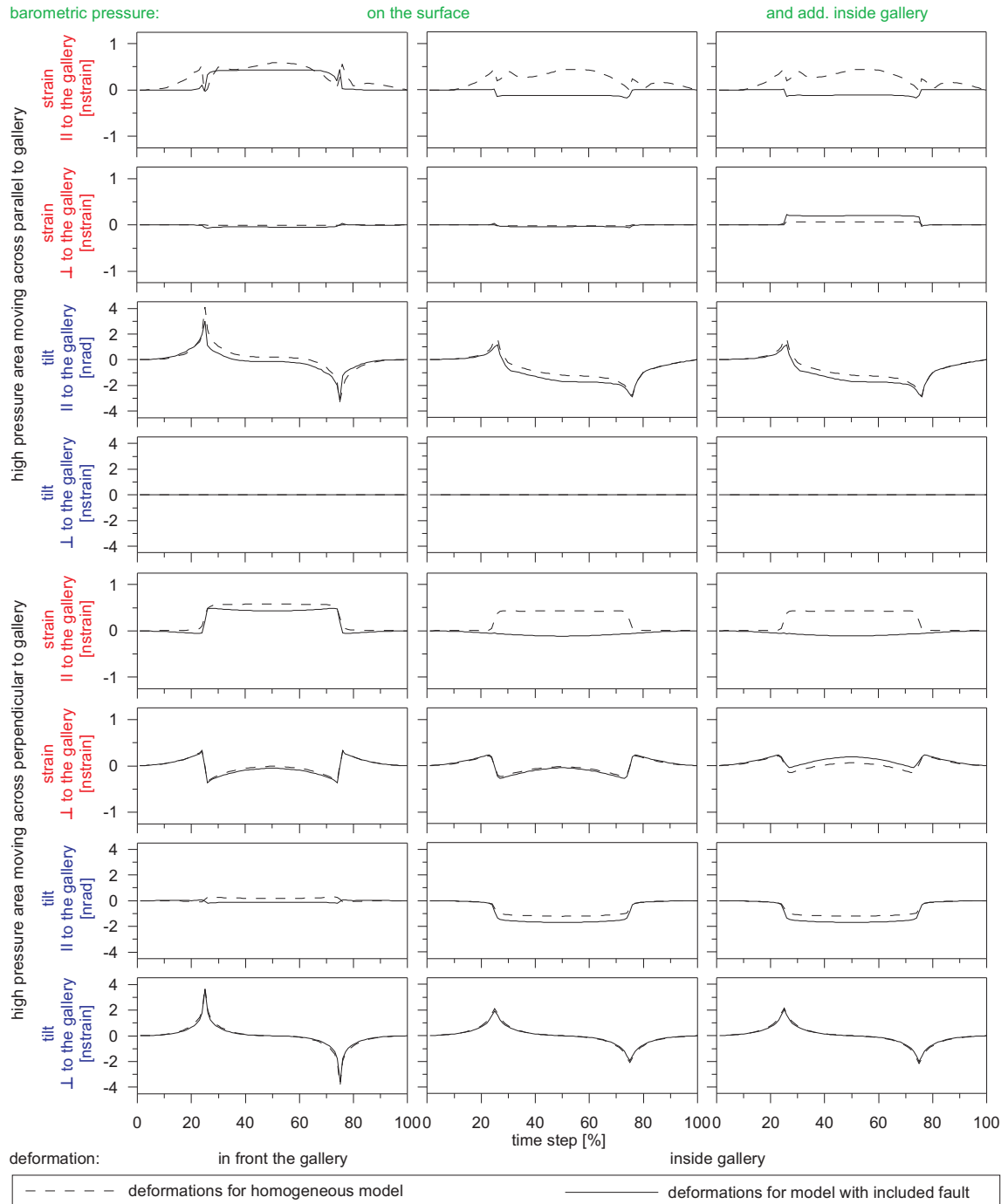


Fig. 5.44: As [Fig. 5.43](#), but the fault is located at the entrance of the gallery and is perpendicularly oriented.

If the fault is located 50 m behind the gallery head the tilt component oriented parallel to the gallery is additionally affected. The results for a high pressure area moving orthogonally to the gallery are shown in [Fig. 5.45](#) and for diagonally moving one in [App. Fig. 26](#). The deformations in front of the gallery are similar to the ones for a plain model type (comp. [Fig. 5.11](#)) for a high pressure area moving parallel to the gallery across the model, the deformations inside the gallery are reduced by about 15%. For

5 Principle investigations

the perpendicular to the gallery moving high pressure area a similar reduction of amplitudes of about 15% is found for the component inside the gallery. Regarding the tilt component in front of the gallery oriented parallel a decrease of about 70% occurs.

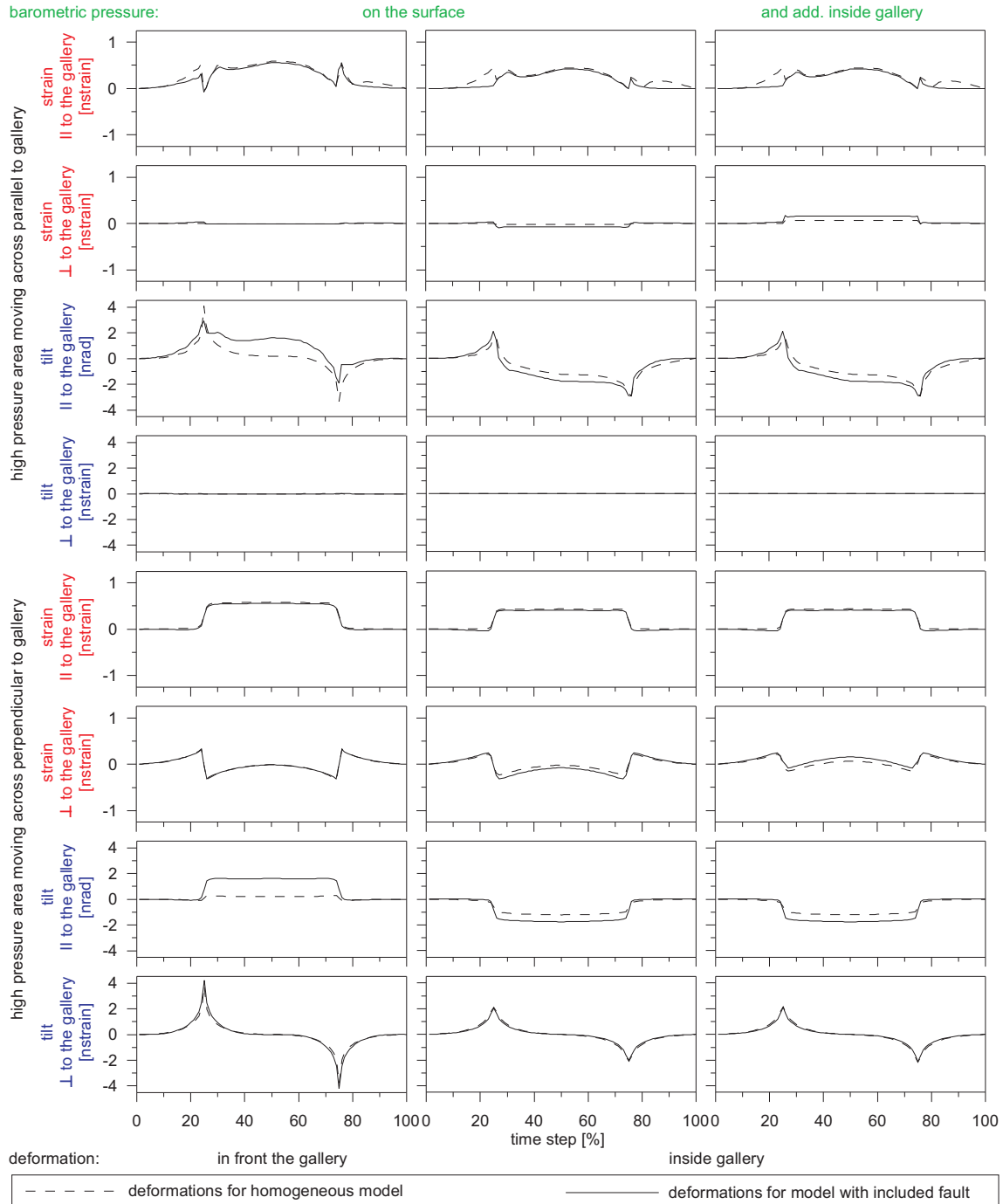


Fig. 5.45: As **Fig. 5.43**, but the fault is located 50 m behind the gallery head and is perpendicularly oriented to the gallery.

5.4 Comparison of modeled and observed deformation amplitudes

For a first comparison of modeled with observed deformations, an example from Moxa Observatory (Jahr et al. 2001) is given. A strong pressure event occurred in November 2004, when only a small amount of rain fell so that the effect on deformations caused by pore pressure changes is small. The observatory is located in a narrow valley with non-equal slope angles. Fig. 5.46a shows the observed, tide and drift reduced values of the EW-strain component and the corresponding barometric pressure. A regression coefficient between the strain amplitude and the barometric pressure is determined with a value of 1.1 nstrain/hPa.

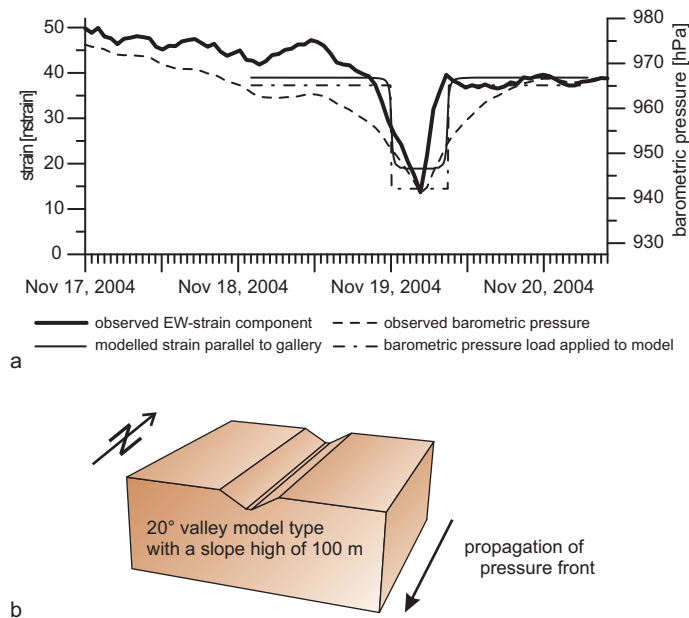


Fig. 5.46: Observed deformations in the EW-strain component and barometric pressure at Moxa observatory compared to modeled deformations (a). The deformation is modeled using a valley model type with a slope angle of 20° and a height of 100 m (b).

The gallery geometry of the observatory is similar to the type B gallery. The observed EW-strain component corresponds to the strain component parallel to the gallery. The topography of the observatory is simplified to a valley model type with a slope angle of 20° and a slope height of 100 m (Fig. 5.46b). This model is selected based on existing models used in this study which reflects as close as possible the observatory condition. The typical moving direction of pressure fronts in Central Europe is west-east oriented, and thus, perpendicular to the topography. A regression coefficient of about 0.8 nstrain/hPa is determined from FE modeling. The difference in the regression coefficients is due to the model parameterization after PREM, which differs in its Young's

modulus from the parameters in the vicinity of the observatory. In addition, the geology is more complex than in the model, consisting of greywacke and schist with faults. Considering this, the two coefficients fit well together. From the investigation by Kroner et al. (2005), similar coefficients resulted. The general deformation processes related to the example can be explained by previously mentioned features and processes (s. chapter 5.3.2.1).

5.5 Discussion

For all considered impact factors (comp. chapter 3.3) significant amplitudes for the assumed instruments (cf. chapter 5.1) are found. The largest effects related to the cavity effect are obtained for the deformation components (strain and tilt) which are oriented perpendicular to the gallery extension (comp. chapter 5.3.1). For the deformations related to topographic effects of the largest amplitudes occur for the components oriented perpendicularly to the topographic features (cf. chapter 5.3.2). Similar results are found for geological features (cf. chapter 5.3.3 and chapter 5.3.4). If a combination of topographic and geologic features is investigated, the amplitudes derived in the separate studies for topographic and geologic effects are amplified by up to a factor of 4. Related to the moving high pressure areas generally a more complex behavior is found for the strain component than for the tilt component.

For the previously mentioned impact factors an estimation of amplitudes for the deformation components is given (Tab. 5.5). In this, realistic conditions are considered. Thus, cases like e.g. instrument sites close to a granitic intrusion (the distance between the border and instrument is smaller than 100 m) are excluded.

In summary, each deformation component is individually affected by the investigated impact factors.

Tab. 5.5: Maximum amplitudes of the different effects calculated in the principle study for 1 hPa barometric pressure load.

effect	strain [nstrain]	tilt [nrad]
cavity	0.5	1
topography	2	2
lithology	3	7
fault	7	2

6 Effects at Central European observatories

Modeling the effects at existing observatories succeeds the investigations discussed in chapter 5. The benefit from case studies is to understand actual occurring disturbances associated with the various impact factors and to separate them.

Comprehensive investigations regarding the effect of barometric pressure variations in observations have been carried out with FE models. Kroner et al. (2005), Steffen (2006), and Steffen et al. (2006) subjected their models with simplified topography of the Black Forest Observatory and the Geodynamic Observatory Moxa to typical barometric pressure events. The resulting displacements could be explained by topographic and cavity effects.

This study returns to an elementary investigation of the physical transfer mechanisms related to barometric pressure changes with FE models. The three topography cases studied in chapter 5 are considered (cf. also Gebauer et al., 2009), but analyze the processes for existing broadband observatories.

6.1 Modeled observatories

Three different topographies, plain, slope, and valley, analyzed in chapter 5 (and also in Gebauer et al., 2009) correspond to the Geodetic Observatory Wettzell (WET), the Sopron Observatory (SOP), and the Geodynamic Observatory Moxa (MOX), respectively. In addition, the Black Forest Observatory (BFO) is chosen to compare the hilly surroundings of the Geodynamic Observatory Moxa valley to the steep hill flanks in the valley of the Black Forest Observatory. All observatories are located in Central Europe (Fig. 6.1). The Geodetic Observatory Wettzell is situated in the centre of the Bavarian Forest. The Sopron Observatory is found east of the Alps. The Geodynamic Observatory Moxa is located in the north of the Thuringian Slate Mountains at the south-eastern margin of the Thuringian Basin, and Black Forest Observatory in the central part of the Black Forest in South-West Germany. The observatories are equipped with similar instrumentation for observations of horizontal deformations such as strain- and tiltmeters.

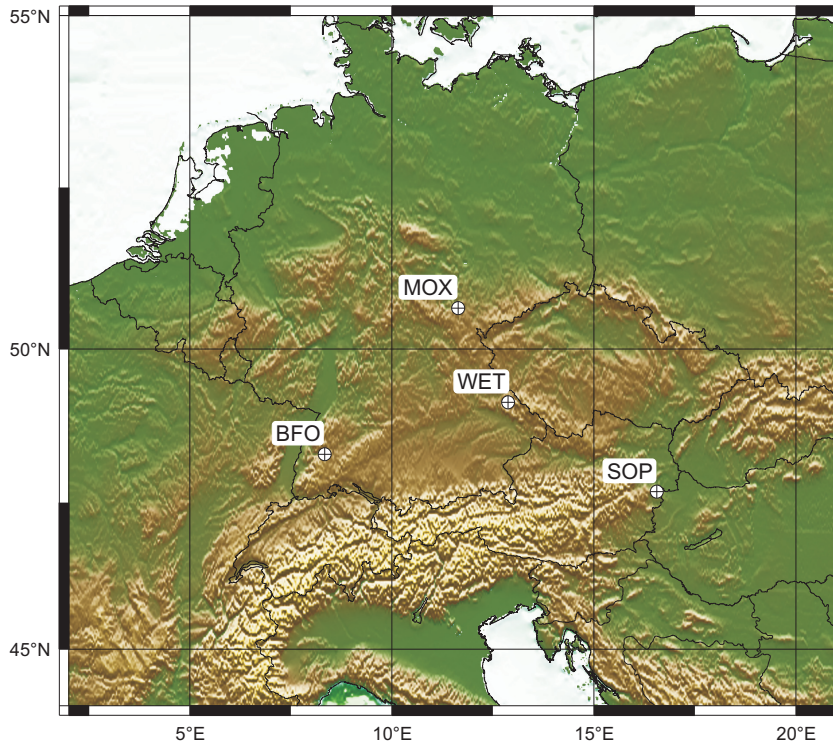


Fig. 6.1: Map of Central Europe and locations of the observatories Moxa (MOX), Wettzell (WET), Black Forest (BFO), and Sopron (SOP).

The models have a dimension of 2,000 m x 2,000 m and at least 500 m of vertical extent. The topography of the observatories is based on digital terrain models with 5 m lateral resolution. In a first step all models except BFO are parameterized after PREM (Dziewonski & Anderson, 1981; Tab. 6.1) in order to compare only the topography and cavity effects at the first three observatories. In a second step station-specific parameters are assigned. The element size of the observatory models varies from some tens of centimeters in the gallery near the location of the instruments to some tens of meters at the model boundaries. The grid size results in occasionally more than 1 million elements.

Tab. 6.1: Material parameters used in the modeling. The rock parameters are taken for Wettzell observatory (WET) from Klügel et al. (2000) and for BFO from Steffen (2006). For Sopron (SOP) the data is supplied by Mentés (pers. comm.) and for Moxa (MOX) by Kroner et al. (2005).

Parameter	PREM	gneiss (WET)	gneiss (SOP)	metapelite (MOX)
density [kg/m ³]	2,600.0	2,714.0	2,700.0	2,710.0
Young's modulus [GPa]	68.8	58.4	45.5	76.5
Poisson ratio [1]	0.28	0.23	0.12	0.25
Parameter	PREM	granite (BFO)	sandstone (BFO)	concrete (BFO)
density [kg/m ³]	2,600.0	2,670.0	2,290.0	2,300.0
Young's modulus [GPa]	68.8	59.7	19.5	33.3
Poisson ratio [1]	0.28	0.27	0.25	0.2

Tests have been carried out to determine the appropriate resolution for each observatory model. Due to the simple topography, the reference models only have some 10,000 elements.

6.1.1 Geodetic Observatory Wettzell

The Geodetic Observatory Wettzell is located in the centre of the model of a wide flat hill (Fig. 6.2). The hill plateau has a height of 630 m above sea level (a.s.l.) with a NS-extent of about 750 m and a west-east extent of about 300 m. The deepest points of the modeled valleys are found in north-east, south-west, and south with about 460 m a.s.l. The considered instrumentation of the observatory includes an ASAKNIA borehole tiltmeter in the west of the observatory and the laser gyroscope about 200 m to the west of the tiltmeter (Schlüter et al., 2007). In the model a tiltmeter length of 10 m is assumed. For determination of the deformation at the location of the laser gyroscope NS and EW strainmeters (base length 20 m) and a tiltmeter (base length 10 m) are considered (Fig. 6.2). All base lengths are selected in order to compare the results of the different observatories and likewise to observations in a further study. The models consist of about 0.25 million tetrahedral elements with an average size at the surface of about 10 m.

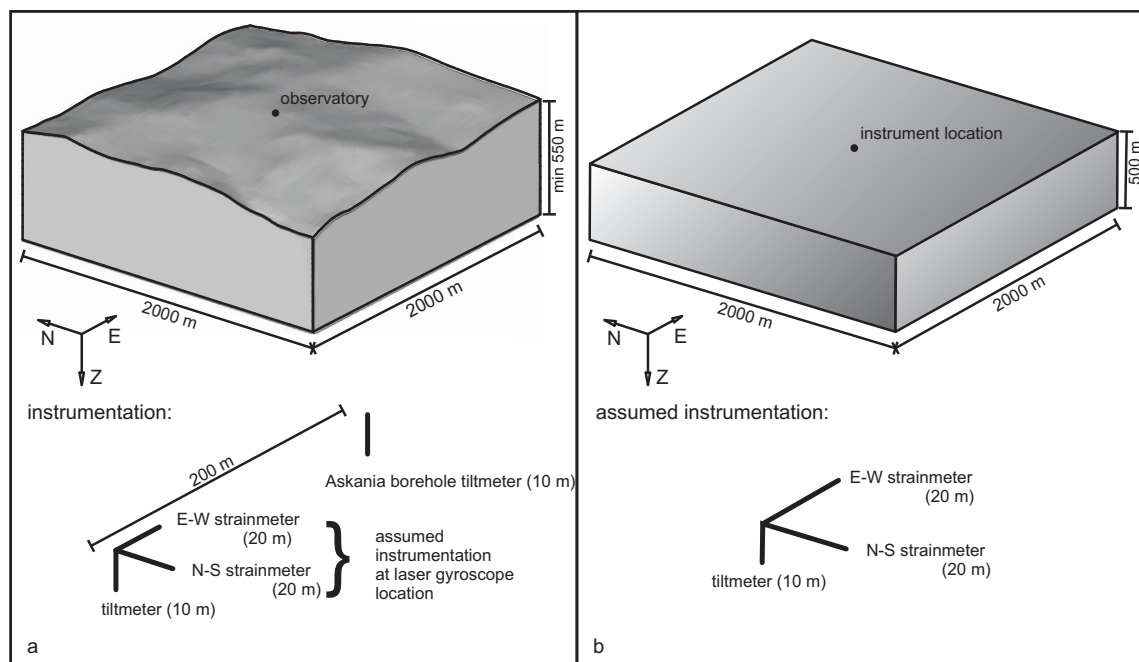


Fig. 6.2: Sketch of the model for the Geodetic Observatory Wettzell (a) and the plain reference model (b) with assumed instrumentation.

6.1.2 Sopron Observatory

The Sopron Observatory is found at the western side of a north-south oriented 500 m long and 300 m wide hill about 270 m a.s.l. (Fig. 6.3; Mentés, 2005; Mentés & Eperné-Pápai, 2006). The top of the hill is 70 m higher than the plain in the north. The western slope has an angle of about 30° , the eastern of about 10° , and the northern of about 15° . In the south, a mountain chain extends from west to east. The observatory is located in an old quarry driven in gneiss (Fig. 6.3). The coverage above the gallery is about 60 m. The gallery is broadened into a seismometer and a pendulum chamber. Deformations are modeled for the 22 m long strainmeter and an assumed borehole tiltmeter (base length 10 m) in the pendulum chamber as well as for the tilt of a seismometer located 1 m in front of the northern wall in the seismometer chamber. The gallery is 47.5 m long and 3 m wide. The angle between the gallery extension and west-east direction is about 26° . The strainmeter is installed in front of the southern wall. The model has about 1.3 million tetrahedral elements with an element size of at least 0.3 m inside the gallery, increasing up to 20 m to the model boundaries.

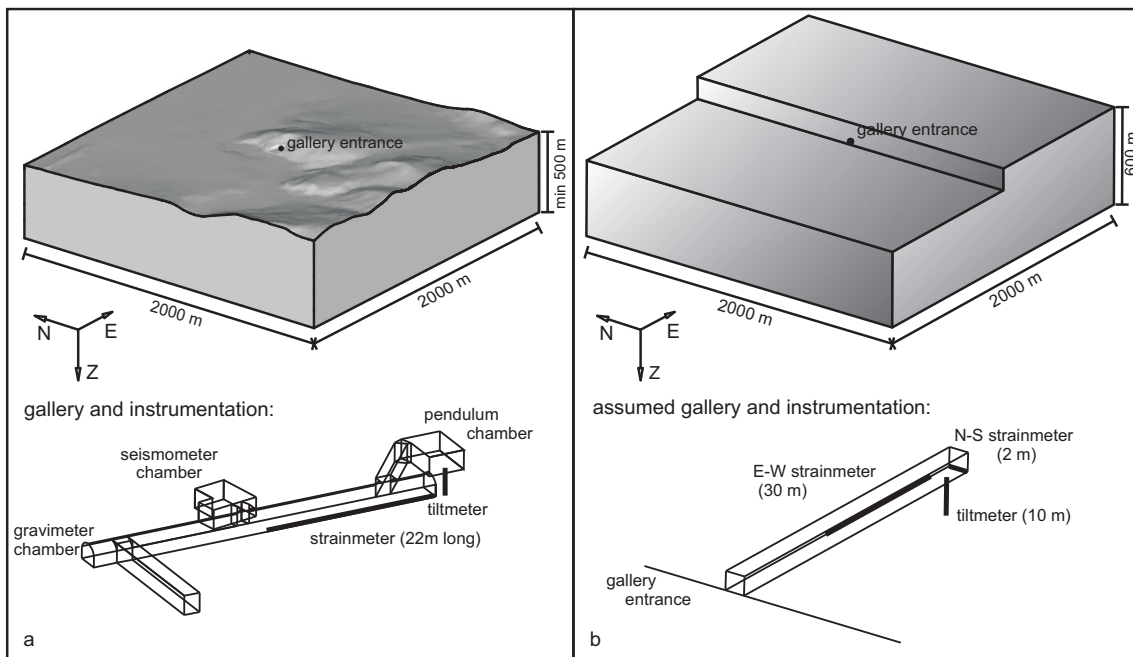


Fig. 6.3: Sketch of the model of Sopron Observatory (a) and the slope type reference model (b) with assumed instrumentation.

6.1.3 Geodynamic Observatory Moxa

The Geodynamic Observatory Moxa is located in a small north-south oriented narrow valley (Jahr et al., 2001). The entrance of the gallery is found at the eastern slope (Fig. 6.4). Two smaller valleys extend nearly orthogonal from the main valley to the west. The plateau in the north and the west of the model has a height of about 500 m a.s.l. The elevation of the observatory is about 50 m lower, and the deepest area in the south-east has a height of 420 m a.s.l. The slope angle for a west-east cross section through the observatory is about 15° for the western flank and about 35° for the eastern flank. The instrumentation for the modeling includes two 26 m long strainmeter in NS and EW direction as well as a seismometer at the southern end of the NS gallery. Deep boreholes of 50 m and 100 m depth exist in front of the observatory about 40 m in the north, where ASKANIA borehole tiltmeters are installed. At the actual depth and additionally at the surface the tilt is determined for instruments with an assumed base length of 10 m. The element size of about 1.3 million tetrahedral elements is at least 0.3 m inside the gallery, increasing up to 20 m at the model boundaries.

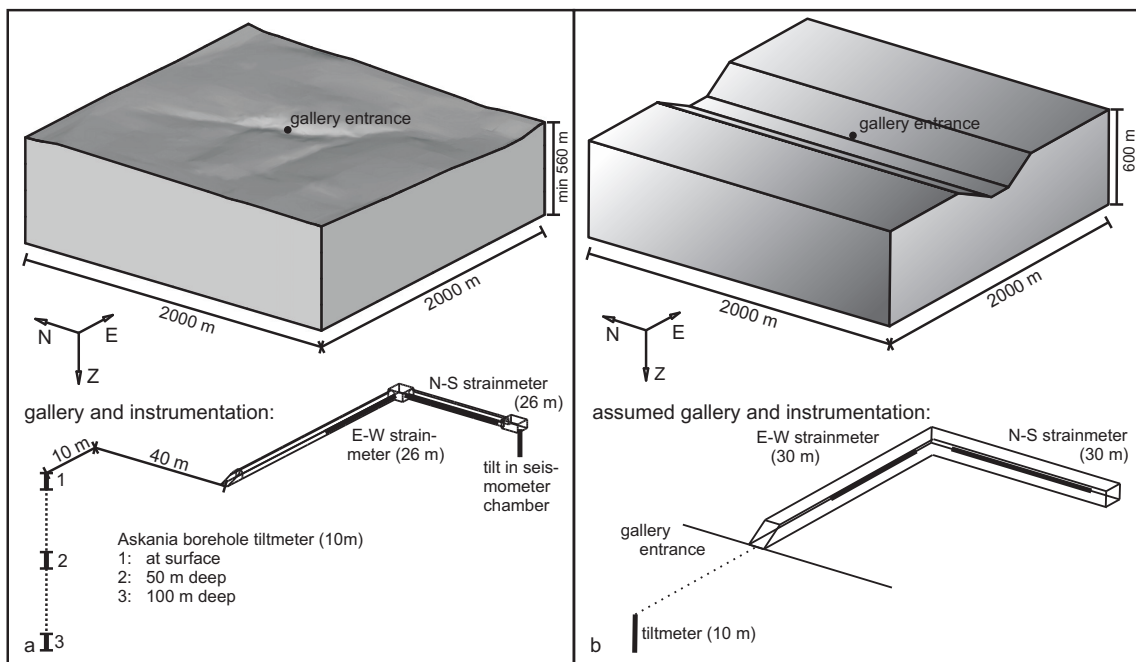


Fig. 6.4: Sketch of the model for Geodynamic Observatory Moxa (a) and the valley type reference model (b) with assumed instrumentation.

6.1.4 Black Forest Observatory

The topography of the Black Forest Observatory has similar characteristics as the Geodynamic Observatory Moxa but with steeper slopes and another slope and valley to the east. The observatory is embedded on the east hill flank of the narrow Heubach valley in a former copper and silver mine. The surrounding rock is granite with a permotriassic sandstone cover of about 120 m on top of the hill. The instruments are installed in a gallery behind an air lock between 530 and 660 m deep in a hill (Fig. 6.5). The rock cover varies between 150 and 176 m. The seismometer components are located in a separate seismometer chamber. Each of the three 10 m long strainmeters is installed in the middle of appropriate 60 m long astral-drifted galleries. The strainmeter in NS direction is parallel to the mountain ridge. A water tube tiltmeter reaches from the north-western to the southern extension. In the former mine two dikes, the 'Anton-Gang' and the 'Heinrich-Gang', were mined and are now left as cavities. Another cavity is the so-called 'Felix Kluff'. At the end of this cavity the pendulum chamber was set up with niches for tilt- and/or seismometers in its western and southern wall. The largest cavity

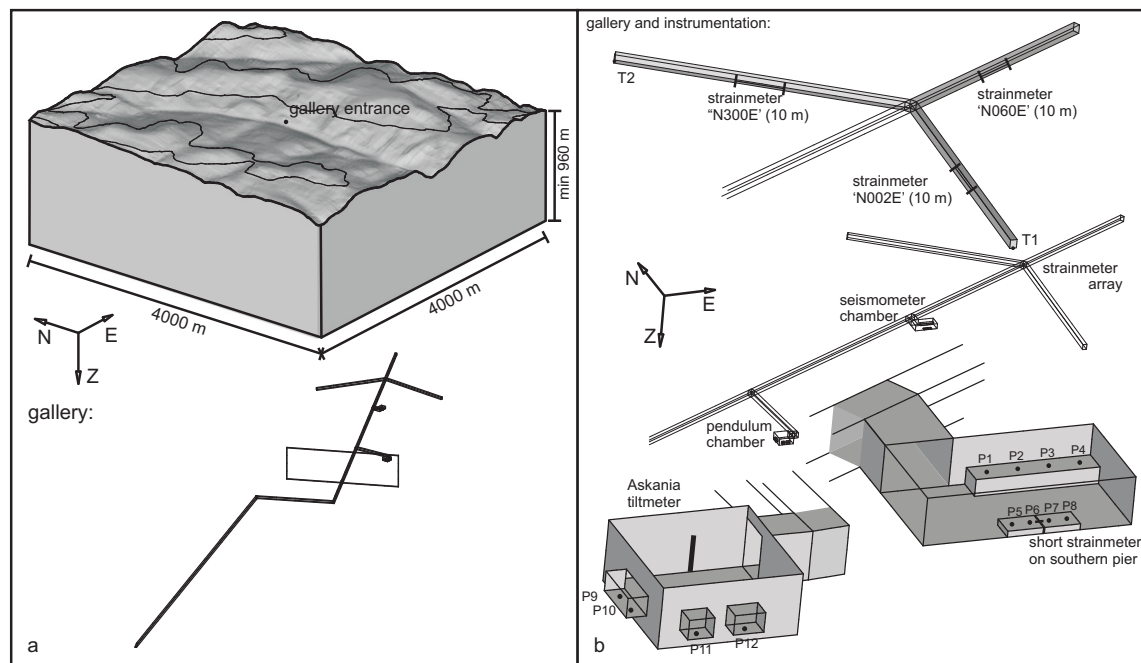


Fig. 6.5: (a) Sketch of the model for the Black Forest Observatory (BFO). The black line marks the boundary between granite (lower part) and sandstone (top). The gallery comprises (from entrance to the end) the Heinrich Gang, the Felix Kluff with the pendulum chamber, the seismometer chamber and the strainmeter array. (b) Instrumentation for the comparison at the BFO: Pendulum chamber: ASKANIA tiltmeter and four points P9 to P12 in niches used in Steffen (2006) for tilt calculations. Seismometer chamber: 8 points at three concrete piers at the northern (P1 to P4) and southern wall (P5 to P8) used in Steffen (2006) for tilt calculations. Strainmeter array: three strainmeter in NW-SE, NE-SW and NS direction as well as a water tube tiltmeter. T1 and T2 denote the two ends of the water tube tiltmeter.

is the Heinrich-Gang with a length of 100 m, a width of 1 m and a height of 30 m. All three cavities are included in the model, which consists of about 1.1 million tetrahedral elements. The size of the elements varies between 10 cm in the gallery and 40 m at the bottom of the model.

6.1.5 Load scenario

The dimension of barometric pressure events varies from a few meters to some 1,000 km. The characteristic velocity of a pressure event is about 10 m/s. The relation between pressure changes and the dimension of pressure cells are approximately proportional (Fortak, 1971). With the chosen model dimension, the effect of barometric pressure changes of smaller dimension can be investigated by moving high pressure areas. Larger dimensions are applied by uniform load to determine the order of magnitude of the deformations.

Identical load scenarios are used for all models. Barometric pressure with a nominal amplitude of 1 hPa is assumed as the source of the loading. It is applied to simulate the passing of a high pressure area, which is taken as typical example for a pressure change. The load acts on the surface and in case of galleries additionally inside, with the exception of the BFO where an air lock is installed. Here, the pressure only affects the gallery up to the air lock. Three directions of moving high pressure areas are considered to determine the deformations (Fig. 6.6a):

- north to south (NS),
- west to east (WE),
- north-east to south-west (NE-SW).

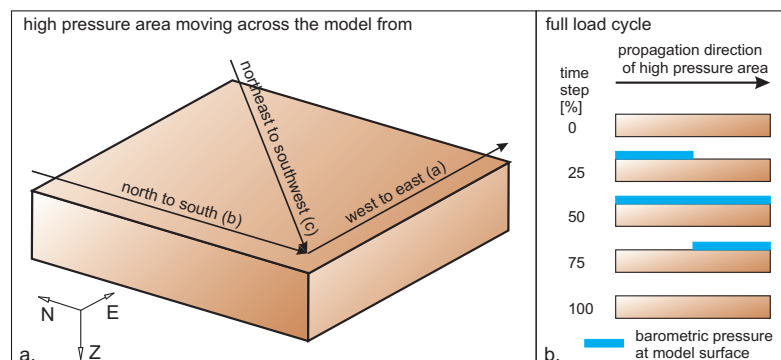


Fig. 6.6: (a) Three different moving directions of a high pressure area over a model. Letters in brackets denote the moving direction of the high pressure area in Fig. 6.7, Fig. 6.9 and Fig. 6.12. (b) Sketch of a full load cycle with the loaded model area at specific time steps.

The time for the passage of the high pressure area is again given in % (Fig. 6.6b) and described in detail in chapter 5.2. Due to the elastic model properties, high pressure areas moving in opposite direction produce the same deformations, but in reverse time order. Thus, it is not necessary to separately investigate them.

6.2 Results

Fig. 5.10 is again used to explain the typical deformation processes for a better understanding of the deformations obtained for the sophisticated models. Here, only the time steps from 0% to 50% will be explained in detail, as similar processes during load and unload occur, which will be shown later. When a high pressure area moves towards an observatory, the partly loaded area in front of the observatory is vertically displaced and therefore horizontal deformations are induced (Fig. 5.10). Three strainmeter positions are exemplarily highlighted in red, which are oriented perpendicularly to the pressure front. The strainmeter on the left with the largest distance to the pressure front will show no or insignificantly small signals. With decreasing distance (strainmeter in centre) dilatation will occur for the strain component oriented perpendicularly to the pressure front, which corresponds to the time steps 0% to 25% in Fig. 6.6. If the high pressure area propagates across the instrument (right strainmeter), the dilatation will change to compression at time step 25%. Thereafter, a decrease in the strain amplitude to a constant level will be observed (time steps 25% to 50%, Fig. 6.6) as long as no further pressure change occurs. As expected for the tilt (green tiltmeter in the centre), the largest amplitudes are found for the highest barometric pressure gradients, when the distance between the tiltmeter and barometric pressure front is the smallest. The lower end of the tiltmeter will move in direction of the unloaded area. In this example, tilt and strain components oriented parallel to the pressure front will show no signal during the passage of pressure fronts. Depending on the topography, the design of the gallery and the location with respect to a pressure front, these components will be differently affected.

The denotations used for the following subsequent discussion are as follows:

- positive strain amplitudes denote dilatation,
- positive amplitude for EW tilt component denotes that the lower end of the tiltmeter moves westwards,
- positive amplitude for NS tilt component denotes that the lower end of the tiltmeter moves northwards.

6.2.1 Geodetic Observatory Wettzell

The deformations for moving high pressure areas at WET are shown in [Fig. 6.7](#) and [Fig. 6.8](#) for a model parameterized after PREM. The considered deformation components are the ASKANIA borehole tiltmeter and the strain and tilt at the laser gyroscope location in EW and NS direction, respectively (see [Fig. 6.2](#) for instrumentation). The deformations for the reference model (plain type) are drawn in green. When comparing the WE and NS moving high pressure area to the NE-SW moving, the combination of the first two explains the general deformation features during the passage of the latter. Thus, also in the case that the high pressure area moves from north-west to south-east, small changes in the deformation process occur, but the main features remain. For the model parameterized with the present gneiss ([Tab. 6.1](#), results not plotted), all deformations are larger by 23% than those for parameterization after PREM.

6.2.1.1 Strain

The strain for WET is at maximum 0.5 nstrain for the referential 1 hPa load ([Fig. 6.7](#)). This value is only reached in the special case when the instrument is located in propagation direction of the high pressure area. The other component then shows smaller amplitudes of about 20%. A NE-SW moving high pressure area produces significant effects in both components ([Fig. 6.7c](#)), which is due to the overlapping of the single processes found for the NS and WE moving high pressure areas ([Fig. 6.7a, b](#)). The value of extension and compression decreases, but both components depict the general deformation process. The response of the strainmeter is according to the discussion of [Fig. 5.10](#) and the beginning of chapter [6.2](#), respectively. It becomes clear that the response of the strainmeter unloading is the opposite movement to loading. If the high pressure area is above the instrument, compression prevails. Extension is only observed when the high pressure area front is approaching or the backside is moving away from the instrument.

For the WE moving high pressure area, detectable deformations of about 0.5 nstrain are found in the EW component ([Fig. 6.7a](#)). The deformation of the reference model is similar to deformations of the observatory model, but shifts in time and amplitude occur, the former due to small differences in the locations of the instruments in both models. The latter originates from topography. The small hill, where the instruments are installed, with its flank offers a larger, uneven area than the reference model to be extended and compressed. As explained, no signal occurs in the NS strain component of

the reference model. In contrast, amplitudes of about 0.05 nstrain emerge for the observatory model, caused by topography.

The NS moving high pressure area shows similar deformations in the NS components when compared to the EW components under load of a WE moving high pressure area. The difference between the reference model and the sophisticated model is nearly negligible. In contrast, a significant difference of about 0.2 nstrain between the models is obtained due to the topography in the EW component.

6.2.1.2 Tilt

In general, the characteristics of the tilt reflect the general processes already discussed. The differences of the observatory model to the reference model are attributed to topography, with larger maximum amplitudes of about 2%. The loaded slopes produce additional horizontal stress, which leads to the amplification. When assuming a WE or NS moving high pressure area the tilt is largest for the component oriented in propagation direction of the high pressure area (Fig. 6.7). The signal of the other component reaches at most 3% of the larger one. For a NE-SW moving high pressure area the signal is smaller than the maximum of the other two cases, but both components are equally affected. For a WE moving high pressure area the obtained EW tilt amplitudes are in the order of about 3 nrad. The time difference in the peaks between the ASKANIA borehole tiltmeter and the laser gyroscope location corresponds to the distance between both instruments and the velocity of the high pressure area. The maximum amplitudes are about 2% larger than those of the reference model and also the point in time of the peaks is shifted (22% vs. 25% and 73% vs. 75%). The latter is due to the fact that the reference tiltmeter is centered in the model, while in the station-specific model the tiltmeters are located west and east of it. The deformations for the NS component are small with amplitudes of at most 0.1 nrad at the location of the ASKANIA borehole tiltmeter. Here, the instrument tilts to south. In contrast, a tilt to north is found at the laser gyroscope location with the first peak indicating the arrival of the pressure front. Another peak slightly to south appears at 73% when the backside of the high pressure area crosses the instrument location. As expected, the reference tiltmeter shows no tilt.

For a NS moving high pressure area the NS component of the tiltmeters demonstrates the general processes. As both instruments are located about the same NS level, the peak times are identical. The EW component tilts in opposite directions for each instrument. At the laser gyroscope location 200 m west of the borehole tiltmeter,

the bottom of the assumed tiltmeter moves eastwards, showing a nearly constant value of 0.1 nrad and for a short period a slight peak when the backside of the high pressure area is at the instruments location. A nearly negligible tilt to west results for the borehole tiltmeter.

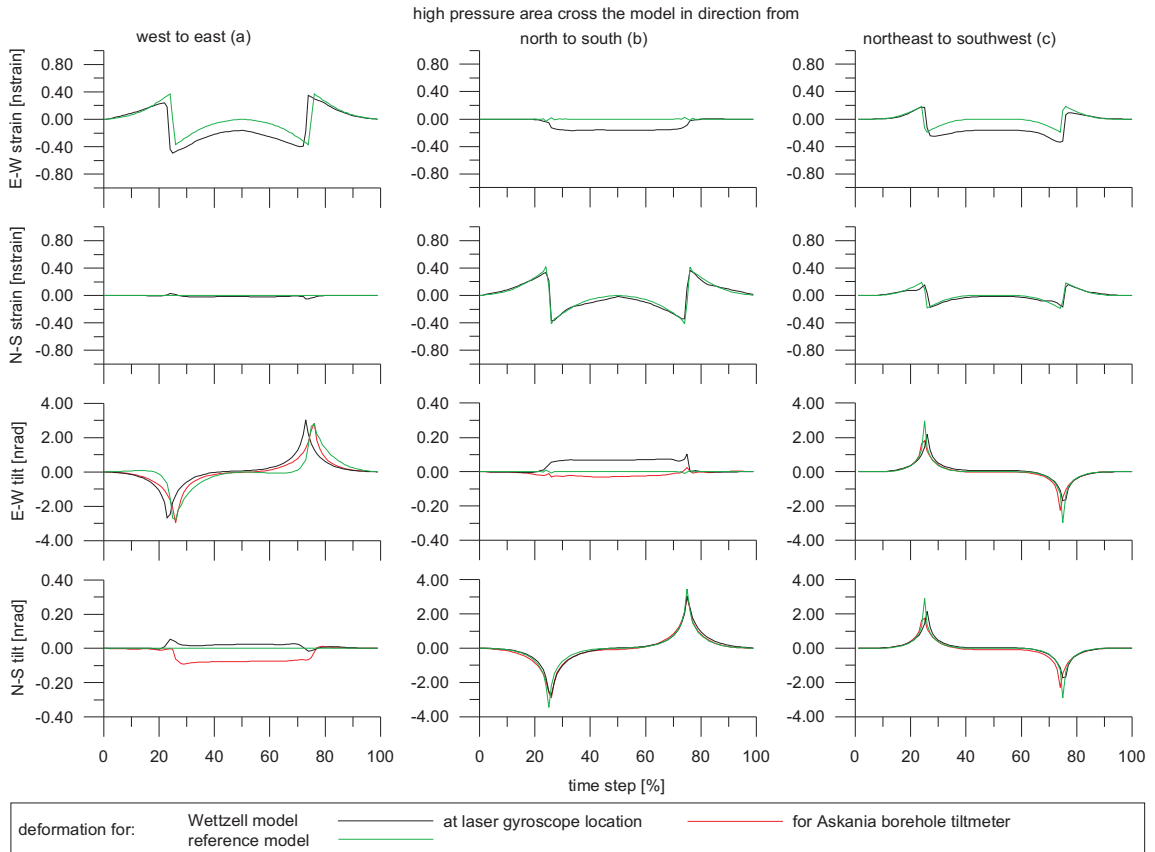


Fig. 6.7: Tilt and strain deformations for instruments at the gyroscope and ASKANIA borehole tiltmeter location at the Geodetic Observatory Wettzell (black and red lines) and the plain reference model (green) for high pressure areas from three different directions; (a) WE moving, (b) NS moving, (c) NE-SW moving high pressure area. Note the different scaling for tilt components. All results refer to 1 hPa of pressure change.

6.2.1.3 Displacements

Fig. 6.8b-d presents the deformation effects at the surface. When the model is completely loaded, the surface is vertically depressed by about 6 to 9 μm (Fig. 6.8b). The largest values are found on top of the hills. The vertical deformation traces well the topography (Fig. 6.8a), and thus a gradient of $-0.2 \mu\text{m}/10 \text{ m}$ can be deduced. The horizontal displacements are also related to topographic features, but are one order of magnitude less than the vertical ones. Here, at most 1 mm is obtained at the largest topographic gradients, which are found in the south-west and north. Fig. 6.8c and d clearly illustrate the horizontal deformations.

6 Effects at Central European observatories

In EW direction displacements of about $1.1 \mu\text{m}$ to east and about $0.6 \mu\text{m}$ to west occur. Displacements to west are found at the western hill flanks (west of the instrument location) and displacements to east at the eastern flanks. A similar behavior exists for the NS displacements with at most $1 \mu\text{m}$ of displacement to north and south, respectively. As the vertical displacement is smallest at lower altitudes, the horizontal displacements seem to have their source in the valleys and disappear at the top of the hills.

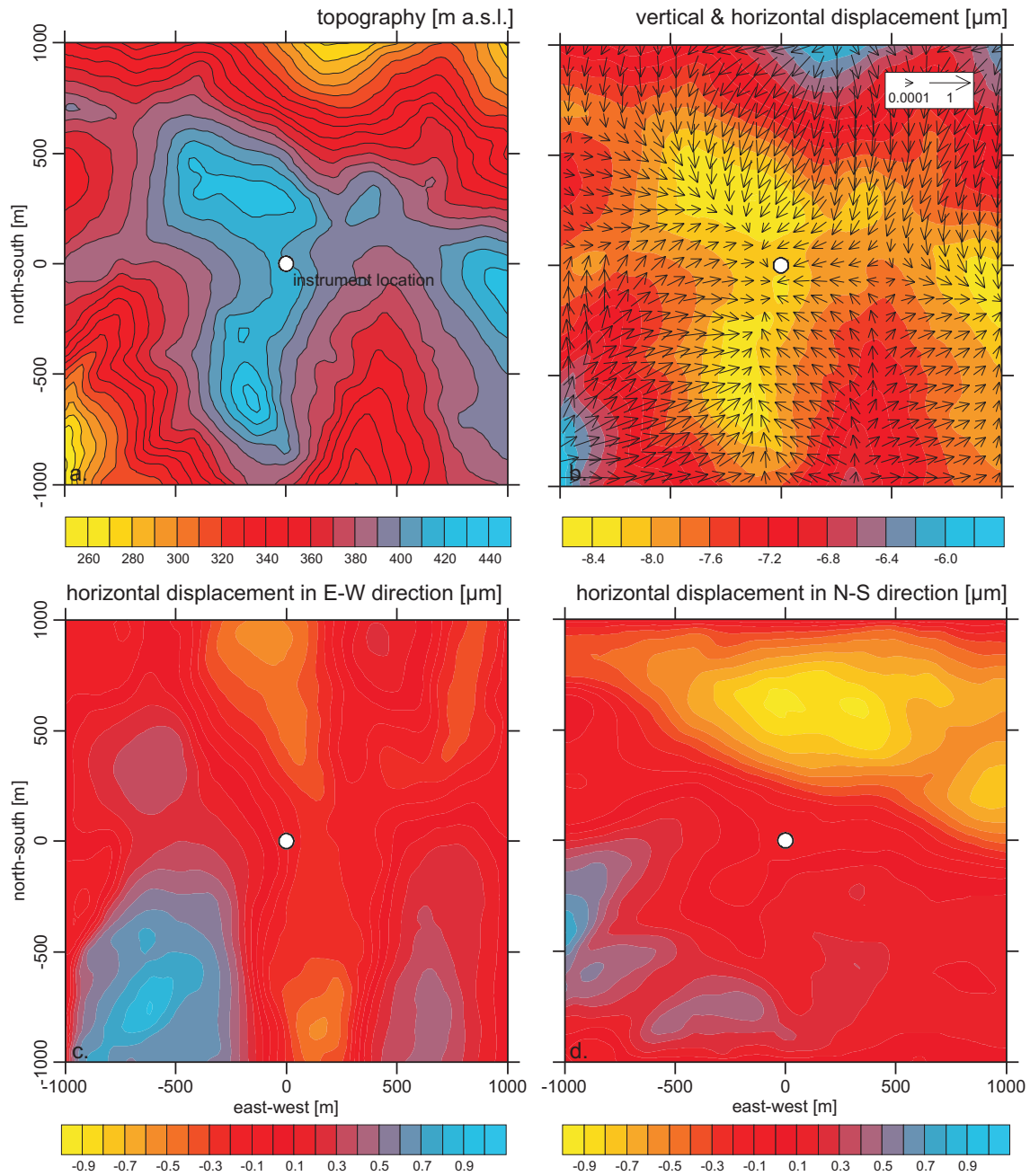


Fig. 6.8: (a) Topography of the model of the Geodetic Observatory Wettzell. (b) horizontal (arrows) and vertical (contour map) displacements for the whole model being loaded by a high pressure area (1 hPa). (c) same as (b), but only for WE displacements. (d) same as (b), but only for NS displacements.

6.2.2 Sopron Observatory

The deformations for SOP and its reference model are shown in Fig. 6.9. The large variety of topographic features of SOP (Fig. 6.3) leads to more variable graphs for the strain components than found for WET. The main characteristics of Sopron's topography are the scarps near the gallery entrance, e.g. the slopes of the northern and the eastern hill. Three features will be important for the discussion of the results: the rotation of the gallery related to EW, the topography in the vicinity of the observatory, and the barometric pressure changes on the hill flanks. The deformations for the reference model are only shown for WE and NS moving high pressure areas, as they explain the general deformation features during a passage of a high pressure area, and as their combination reflects the result for diagonal crossing high pressure areas (see results for WET, chapter 6.2.1). If the present gneiss (Tab. 6.1) is considered, 35% to 50% larger amplitudes are found for the tilt and strain components when compared to those with parameterization after PREM.

6.2.2.1 Strain

The strainmeter at SOP is installed in EW direction. Peaks have maximum amplitudes of about 0.7 nstrain. The strain component shows significant signals even when the pressure front is far away, about 800 m, from the observatory site. The deformation for the WE moving high pressure area in Fig. 6.9 is exemplarily explained with the help of Fig. 6.10. This WE cross section through the observatory shows the undeformed and deformed surface. Arrows next to the gallery denote the acting force induced by the actual load at the strainmeter location. From time step 0% to 20% the strainmeter shows compression (Fig. 6.9a). The distance between the pressure front and the instruments at time step 20% is about 200 m. The compression is caused by vertical displacement of the partly loaded plain west of the observatory (Fig. 6.10a). Horizontal stress acts eastwards and nearly parallel to the strainmeter in EW direction. It is absorbed in the western hill flank of the observatory (Fig. 6.10b). For the next time steps until time step 30%, effects described previously for the plain model type occur (Fig. 6.10c). Until time step 75% increasing compression is observed (Fig. 6.10d), which is due to the increasing load on the eastern hill flank and ongoing unload of the western plain. From time step 75% to 100% the processes are similar to that of time steps 0% - 25%. This loading scenario explains differences to deformations obtained for the reference model, which is discussed in chapter 5 respectively Gebauer et al. (2009).

The strain amplitudes for a NS moving high pressure area show similar features compared to a WE moving high pressure area, but more striking peaks when the pressure front is at the instrument location. The peaks are caused by the extreme topography of the scarp in NS direction. For the NE-SW moving high pressure area the resulting signal is comparable to that of the WE moving high pressure area, but with smaller amplitudes. A small second peak evolves around 35%, which seems to be composed by the humps of the WE and NS moving high pressure area at 65%.

6.2.2.2 Tilt

The maximum tilt amplitude of about 2 nrad for both components is in the expected order of magnitude. The EW tilt component shows already known features (comp. Fig. 6.9 to Fig. 6.7). The differences between the tiltmeter, the seismometer installed inside the gallery, and the tilt of the reference model are less than 0.5 nrad. For the NS component of the reference model no signal is found, which is due to the symmetry of the model parallel to the gallery. The differences of about 0.2 nrad to the tiltmeter and seismometer are mainly caused by the loaded gallery and the resulting cavity effect. The tiltmeter is located 1 m in front of the southern wall of the pendulum chamber (Fig. 6.3). Relative to the lower end of the tiltmeter, the upper end moves northwards caused by the compressed chamber. The seismometer is located 1 m in front of the northern wall of the seismometer chamber, thus southward tilting occurs. The differences of some 0.1 nrad seem to be insignificant, but for pressure changes in the range of e.g. 10 hPa they become relevant.

For the NS moving high pressure area, both instruments show a constant tilt to east of 0.35 nrad when the gallery is loaded. The lower end of the instruments moves westwards, which is caused by the barometric load at the hill flanks. The tilt direction is in agreement with the results of the reference model. The difference in the amplitude is explained by the topography. Due to the larger slope height and the plateau of the reference model, a larger amplitude is found. The NE-SW moving high pressure area leads to general effects with smaller maxima in both components.

6.2.2.3 Displacements

Fig. 6.11 shows the topography and the deformation effects at the surface for a completely loaded model, respectively. At SOP, the surface is vertically depressed by about 4.5 to 6.5 μm (Fig. 6.11b).

6 Effects at Central European observatories

As found for WET, the largest values occur on top of the hills, tracing the topography. The gradient of $-0.14 \mu\text{m}/10 \text{ m}$ is smaller than for WET due to the different material parameters. The largest horizontal displacement of $1 \mu\text{m}$ is related to the largest topographic gradient found at the scarp and thus close to the gallery (Fig. 6.11b, c and d). Both maxima, in EW as well as in NS direction, are found in the centre of the model near the instruments.

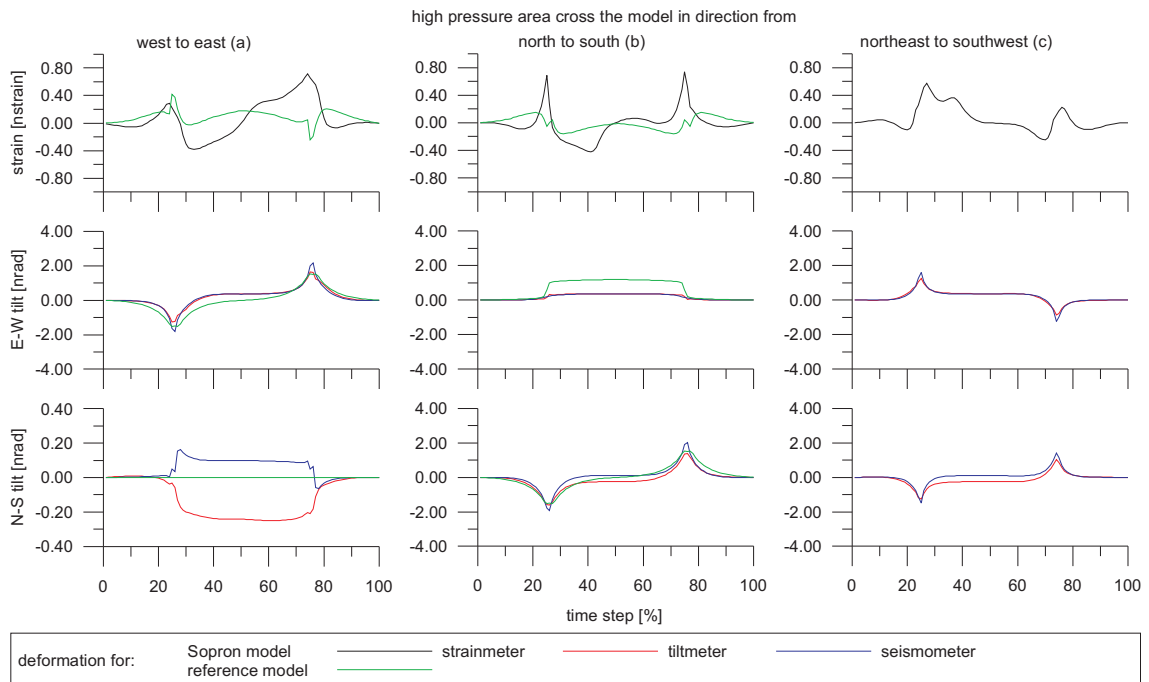


Fig. 6.9: Variations for the (WE) strainmeter (black), the tiltmeter (red) and the seismometer (blue) at Sopron Observatory and the plain reference model (green) for high pressure areas from three different directions; (a) WE moving, (b) NS moving, (c) NE-SW moving high pressure area. Note the different scaling for tilt components. All results are referenced to 1 hPa of pressure change.

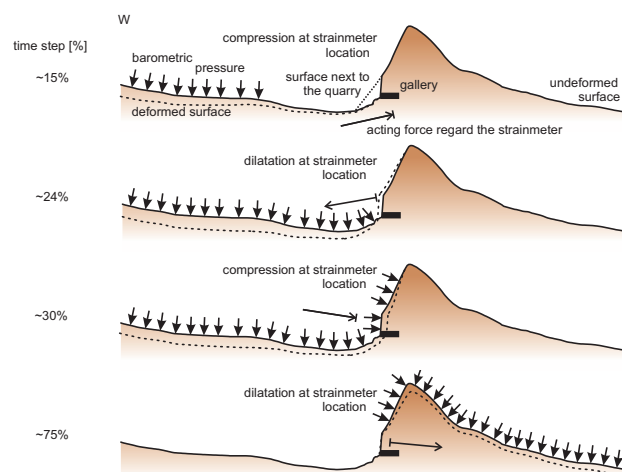


Fig. 6.10: West-east cross section through Sopron Observatory model explaining the deformations for WE moving high pressure area at different time steps. The cross section of the undeformed surface is four times vertically exaggerated. The deformed surface is sketched to illustrate the deformation mechanism. Arrows next to the gallery denote the acting force induced by the actual load at the strainmeter location.

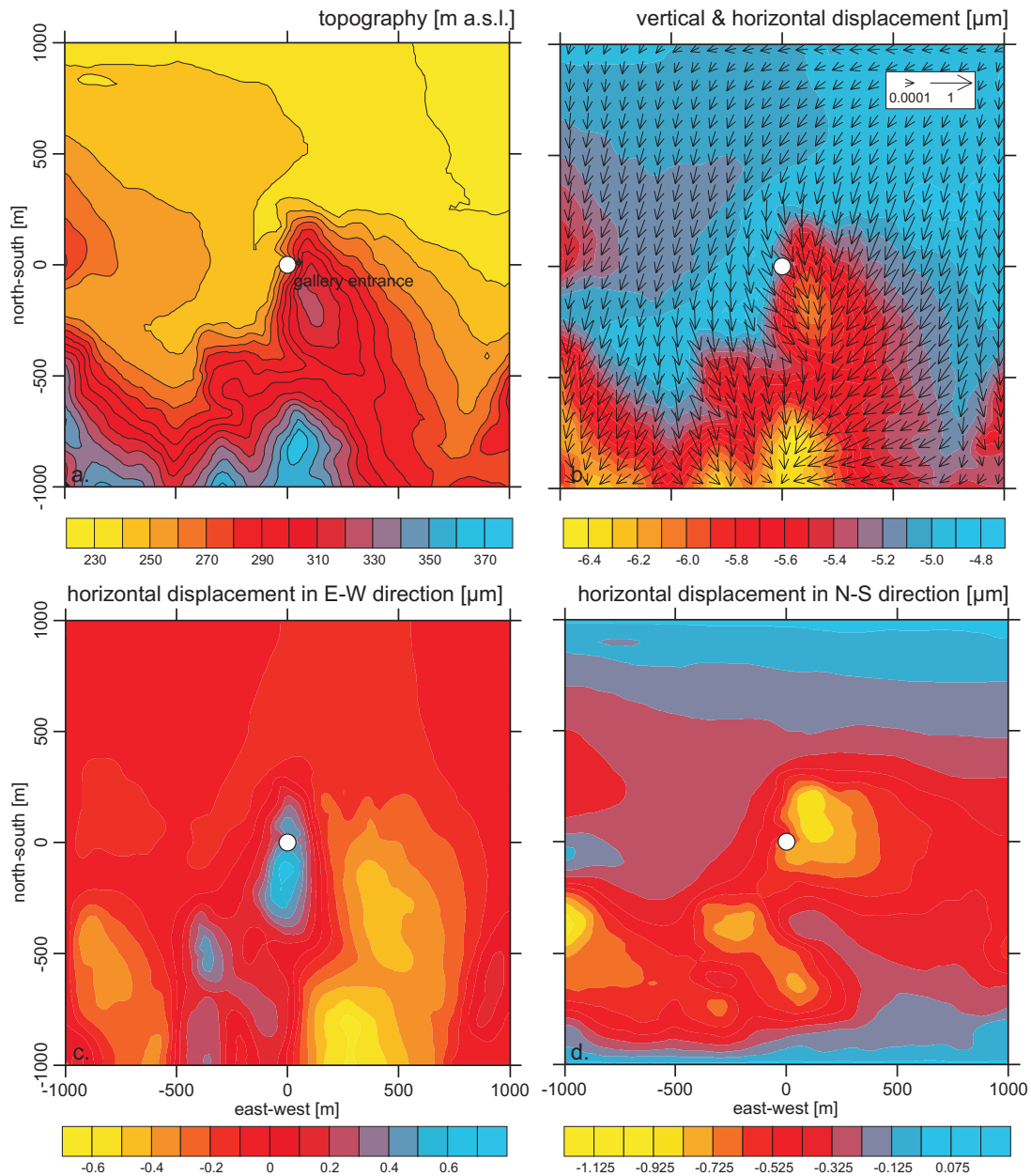


Fig. 6.11: (a) Topography of Sopron Observatory model. (b) horizontal (arrows) and vertical (contour map) displacements when the whole model is loaded by a high pressure area (1 hPa). (c) same as (b), but only for WE displacements. (d) same as (b), but only for NS displacements.

6.2.3 Geodynamic Observatory Moxa

The deformations for MOX and its reference model (Fig. 6.12) are in the range of the previously investigated models. Furthermore, similarities in the deformation process, such as the time step of the peaks and the main tilt directions, are obvious. If the station-specific model is parameterized with the predominant metapelite (Tab. 6.1), the resulting amplitudes are about 5% smaller than with PREM parameterization. Due to

the small differences in the material parameters between the metapelite and PREM, the assignment of the realistic material properties only plays a minor role here.

6.2.3.1 Strain

The EW strain component shows dilatation for a WE moving high pressure area in the first time steps to 25%. If the pressure front reaches the gallery, the maximum amplitude is about 0.25 nstrain, which then decreases to -0.2 nstrain until time step 32%. The associated processes are already described for WET and SOP. For the NS strainmeter a constant compression of 0.11 nstrain is found as long as the instrument area is loaded. Small peaks occur when the front or the backside of the high pressure area crosses the instrument's site. For the NS moving high pressure area a smaller amplitude (about 80%) is obtained for the EW strainmeter and a larger one for the NS-strainmeter. The general deformation process also fits the discussed one for the WE moving high pressure area. The NS strainmeter, which is oriented perpendicularly to the pressure front, shows amplitudes between 0.17 nstrain and -0.28 nstrain. The reference model yields completely different and somewhat large amplitudes for the EW strainmeter. This is again owed to the topography, especially in the case of a WE moving high pressure area. The double peaks around time step 25% and 75% are induced by the two flanks of the hill and its gradient. In the more complex observatory model these flanks are somewhat smoother, especially in the transition from flank to valley bottom. Thus, only one peak is found for this model. Expected signals occur for the NS component in the reference model. For the WE moving high pressure area is obtained no signal. For the NS moving high pressure area are found about the same deformations as for the sophisticated model. The latter results are induced by the main topographic and gallery features of both models in NS direction. The flanks play a minor role for this strain component.

6.2.3.2 Tilt

Four different instrument locations are used for the comparison. In addition to the seismometer at the end of the gallery (Fig. 6.4), three different depths (0 m, 50 m, and 100 m) of a tiltmeter in a borehole are selected. The tilt graphs generally agree with the results for WET and SOP. Expected results also emerge for the reference model. Hence, the results are not discussed in detail, but a relation between depth of an instrument and its maximum tilt is inferred. The induced EW tilt by the WE moving high pressure area shows a maximum amplitude for tiltmeter A1 of 3.05 nrad. Tiltmeter A2 and A3 peak at 1.28 nrad and 0.89 nrad, respectively. For the seismometer 2.17 nrad

6 Effects at Central European observatories

are inferred. In view of the depth of the borehole tiltmeters, the amplitudes decrease logarithmically with increasing installation depth, which can be deduced from the modeling:

$$\text{tilt} = -0.46 \cdot \ln(\text{depth}) + 3.05.$$

The amplitude of the seismometer is affected by the cavity and the topographic effect. No correlation, however, is found for the NS tilt (max. amp. 0.12 nrad). Here, the lower end of the tiltmeter always tilts northwards, which is caused by the valleys NS extent. For the NS moving high pressure area, the nearly symmetrical behavior of amplitudes in view of loading and unloading reflects the valley geometry where MOX is situated. Tiltmeter A3 shows a tilt to west caused by the non-uniform slope angles west and east of the valley bottom. A tilt eastwards is determined for the other three instruments. The amplitudes of the NS components are almost equal to the amplitudes of the EW component affected by the WE moving high pressure area.

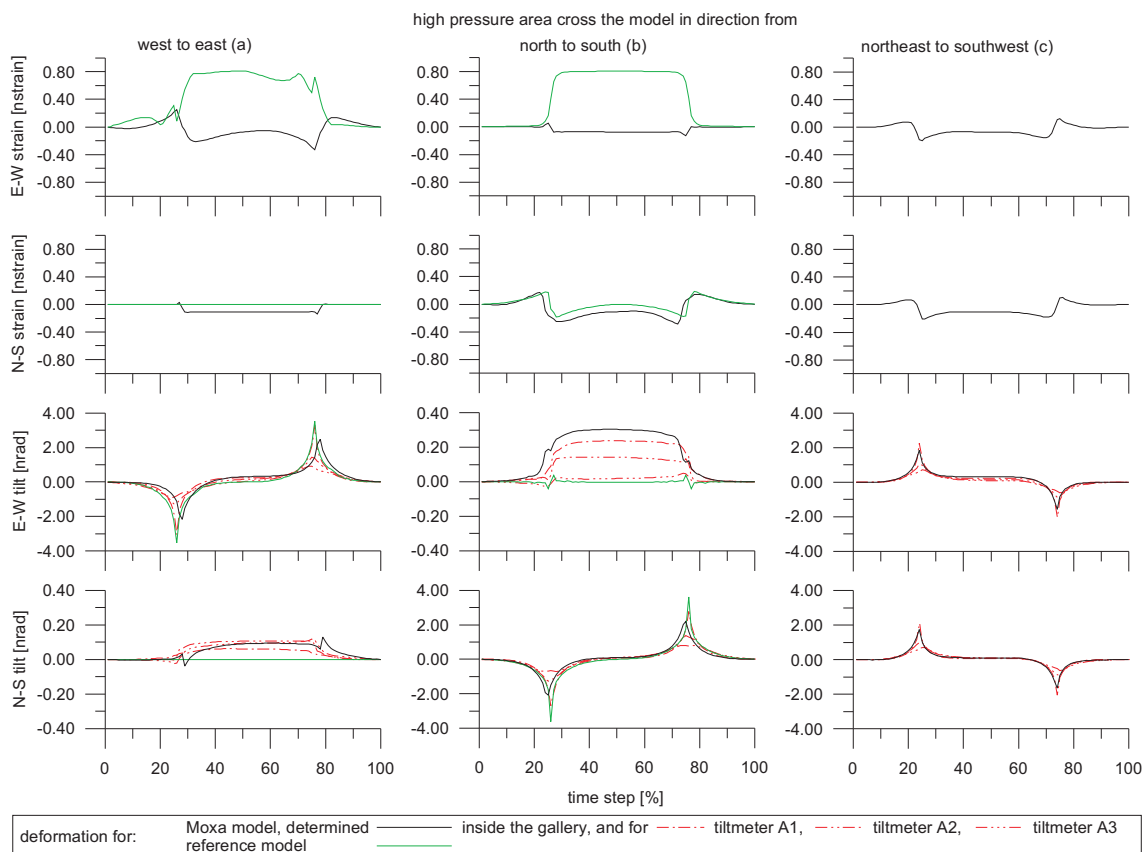


Fig. 6.12: Variations for the strainmeter (black), three tiltmeters at different depth in a borehole (red) and the seismometer (black) at the Geodynamic Observatory Moxa and the plain reference model (green) for high pressure areas from three different directions; (a) WE moving, (b) NS moving, (c) NE-SW moving high pressure area. The strainmeter and seismometer are installed inside the gallery, the tiltmeters in the valley bottom in front of the gallery. Note the different scaling for tilt components. All results are referenced to 1 hPa of pressure change.

6.2.3.3 Displacements

As can be seen from Fig. 6.12, large differences emerge for the EW strainmeter comparing the results for MOX to its reference model. The differences are caused by the topography, which is explained in detail by Fig. 6.13.

At MOX, vertical displacements between 5.6 and 7.2 μm are found when the model is fully loaded (Fig. 6.13b). The isolines of displacement agree, as for WET and SOP,

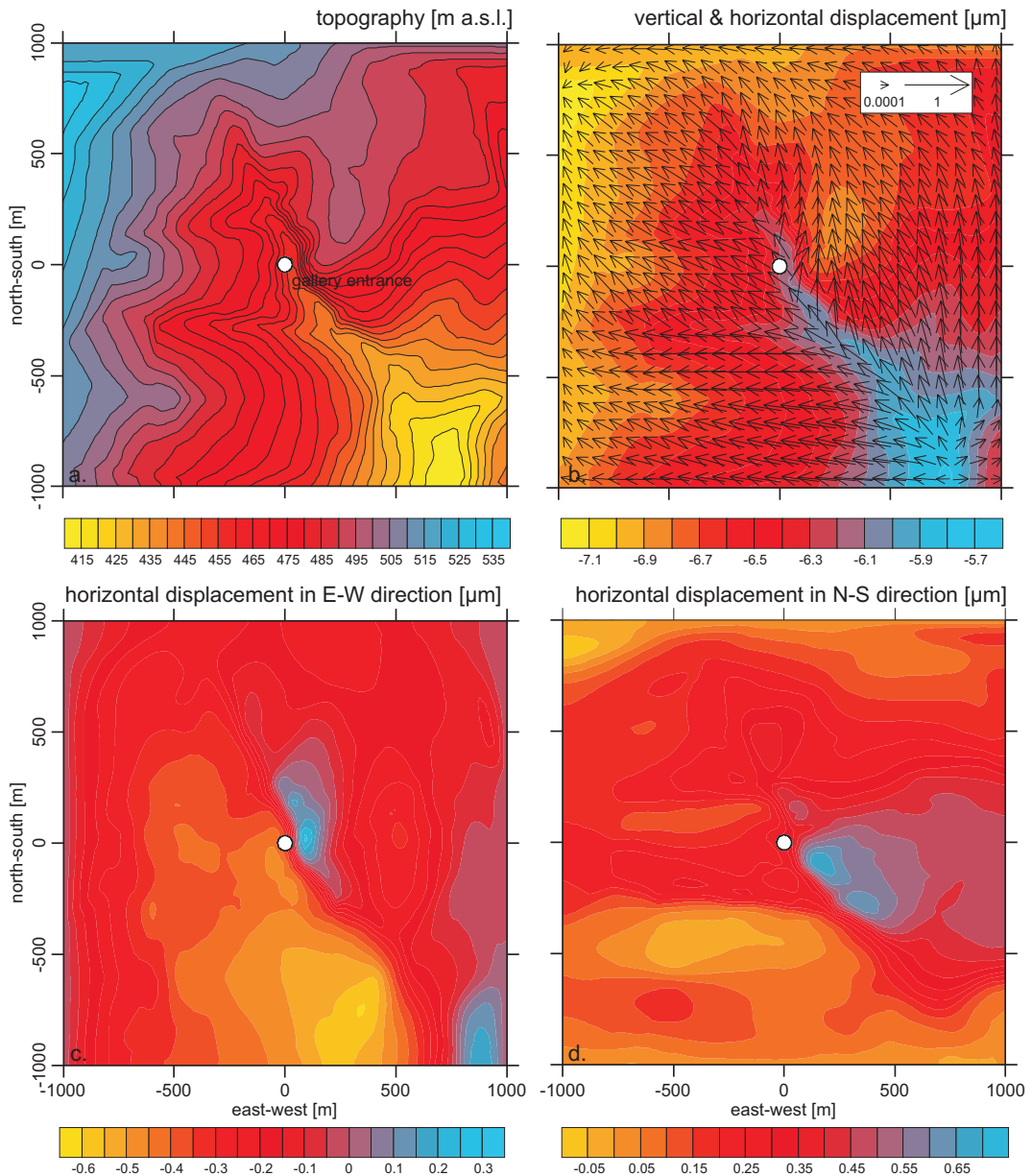


Fig. 6.13: (a) Topography of the model of the Geodynamic Observatory Moxa. (b) horizontal (arrows) and vertical (contour map) displacements when the whole model is loaded by a high pressure area (1 hPa). (c) same as (b), but only for WE displacements. (d) same as (b), but only for NS displacements.

quite well with the topography (Fig. 6.13a), resulting in a displacement-to-height gradient of $-0.13 \mu\text{m}/10 \text{ m}$. The largest horizontal displacements correlate with the largest gradients in topography. These gradients occur south-east of the gallery entrance, which lead to displacements in the gallery area (Fig. 6.13c and d).

In EW direction about $0.3 \mu\text{m}$ are determined, in NS direction up to $0.7 \mu\text{m}$. The area of equal displacement at the location of the EW strainmeter shows large variations in EW direction, but the baseline is only 26 m. Hence, this instrument is insignificantly affected (see Fig. 6.12 at time step 50%). The same applies to the NS strainmeter. Only selected areas of the model show no displacement in one of the directions. This is related to the topography with no pronounced plateaus, mountain ridges or wide valleys. Interestingly, such an area is found close to the gallery for the EW displacements. The topographic features in the gallery area with a slight slope on the western valley side and a steep on the eastern side shift the zone of no displacement from the expected valley bottom into the eastern slope.

6.2.4 Black Forest Observatory

The tilt and strain results for BFO are presented in Fig. 6.14, but only for a WE moving high pressure area as the effects for the other two directions can be deduced from the results for the observatories discussed previously. The deformations are determined from a model having the most realistic rock parameters (see Tab. 6.1). Furthermore, due to the complex surroundings of the observatory no reference model is analyzed.

6.2.4.1 Strain

The three strainmeters are differently affected by a WE moving high pressure area (Fig. 6.14a). Compression occurs for the NE-SW and the NW-SE strainmeter, while for the NS strainmeter quite small extension is determined. Between time step 25% and 35% as well as between time step 75% and 85% two peaks appear. They are closely related to the passage of the front over the gallery and especially at the instrument location. The double peak is caused by the topography around the gallery. Tributary valleys north and south of the gallery enlarge the slope area that transmits the pressure of the high pressure area into the rock. The distance from slope to slope over the gallery is shorter in NE-SW direction than the distance in NW-SE direction, and, thus, the gallery of the NE-SW strainmeter is more shortened than the gallery of the NW-SE strainmeter. This leads to effects of about 0.4 nstrain for the NE-SW strainmeter when com-

pared to about 0.1 nstrain for the NW-SE strainmeter. The NS strainmeter is not strongly affected owing to its location under the NS oriented mountain ridge.

6.2.4.2 Tilt

All components (Fig. 6.14b-e) display the generally expected tilt behavior for a WE moving high pressure area. Two peaks, the first to west and the second to east, are found for the EW component. The time step of their appearance depends on the position of the instrument relative to the pressure front. The NS component shows a tilt either to north or south depending on the installation site of the instrument inside the gallery. The maximum values of the tilt differ strongly. For the water tube tiltmeter a maximum tilt of about 0.2 nrad emerges (Fig. 6.14b). Much larger effects of up to 5 nrad are obtained for the other instrument sites, whereas tilts in the seismometer chamber are larger as the ones in the pendulum chamber.

The NS component of the ASKANIA tiltmeter at the northern wall in the pendulum chamber tilts, due to the cavity effect and its long baseline of 1.8 m, to south at a constant level of about 1 nrad (Fig. 6.14c). In addition to the typical effects found for the EW component and an aligned high pressure area, the EW component shows a tilt in opposite direction after each of the two peaks (time steps 30% and 80%). At first, it seems that the tilt effect rapidly diminishes, but then it is reactivated for a short period. Thereafter, the tilt tends to follow the typical observed effects: constant value in the middle and decreasing to zero at the end of the load process. A possible explanation for this could be on the one hand the large cleft Heinrich-Gang in the west and on the other hand the gallery geometry in form of the access tunnel north-east of the tiltmeter. Either one or probably both interact with the instrument transferring the deformation in form of a cavity effect.

The NS components of the seismometer chamber set an example for the cavity effect (Fig. 6.14d). Points on the pier at the northern wall tilting to north (with 3 – 5 nrad) and points at the southern wall tilting to south (about 4 nrad) agree with general considerations of Harrison (1976a). The same holds, needing more discussion, for the EW component in the seismometer chamber and both components in the pendulum chamber. A tilt to west of about 1 nrad is determined for points P9 and P10, both located in niches in the western wall of the pendulum chamber, under full load (Fig. 6.14e). Points P11 and P12 only perform a small tilt, which results from their location in the middle of the niches in the southern wall. In the NS component only P9 tilts to north, due to its position close to the northern wall. P10 to P12 are close to or within the

6 Effects at Central European observatories

southern wall, thus emerging tilts to south. In the seismometer chamber all locations present a tilt to east with the largest values of about 1.5 nrad at P4, the point closest to the eastern wall (Fig. 6.14d). For the southern piers all points have about the same value of 0.5 nrad, while for the northern pier differences of 1 nrad yield between P1 and P4. In the NS component the difference between P1 and P4 doubles. In contrast, the difference at the southern pier is negligible. Thus, under full load the small height of the southern piers and their position in the middle of the chamber lead to small and similar effects for all points on these two piers. The northern pier, connected to both the

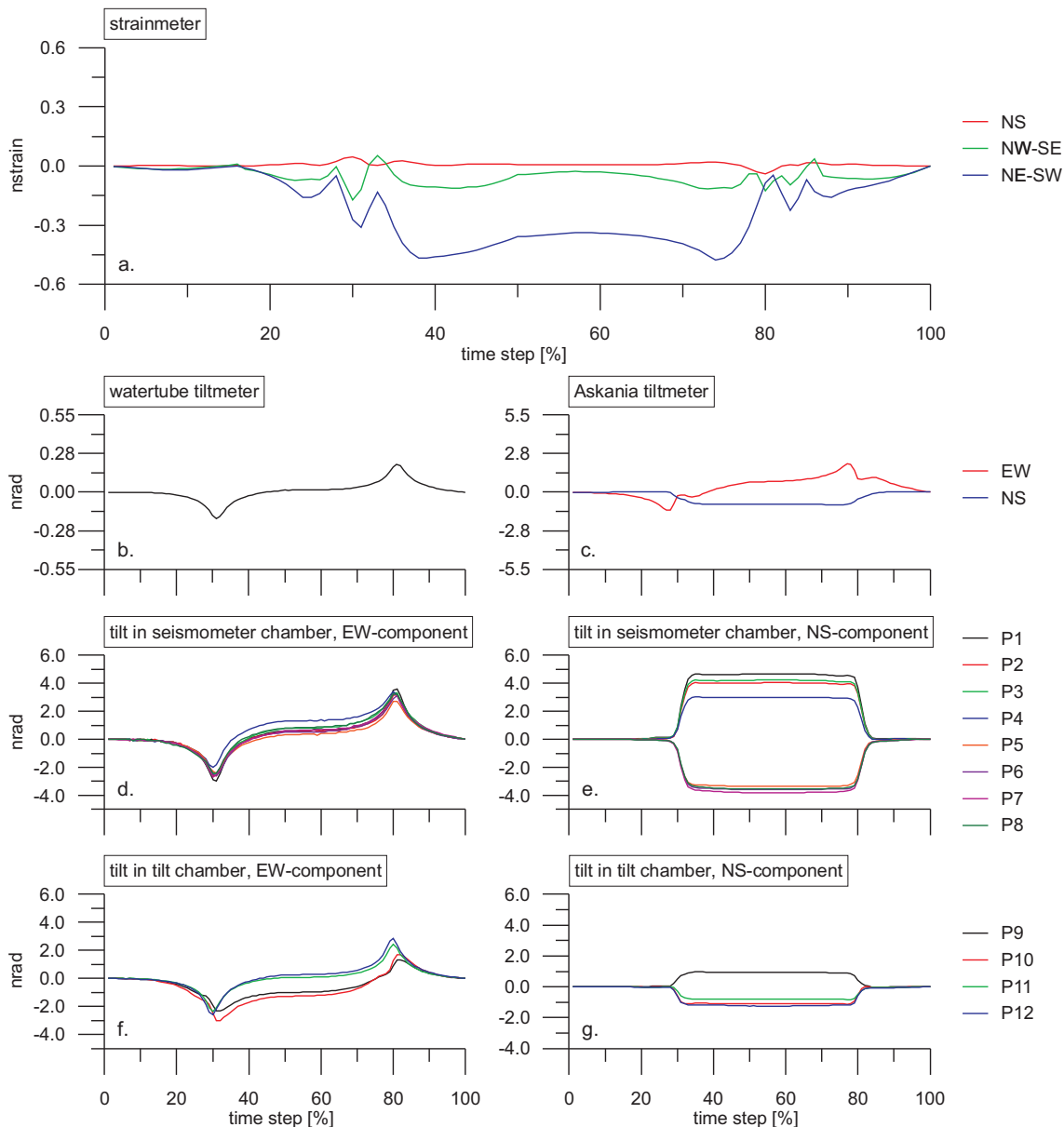


Fig. 6.14: Deformations at the Black Forest Observatory for (a) the three strainmeters in NE-SW (blue), NW-SE (green), and NS direction (red), (b) the water tube tiltmeter, (c) the ASKANIA tiltmeter (d) the seismometer points in the seismometer chamber and (e) the tiltmeters in the niches in the pendulum chamber. Note the different scaling for tilt components. All results are referenced to 1 hPa of pressure change.

northern and eastern walls, generates larger and position-dependent effects to be observed with both components of the instruments. Furthermore, it is noteworthy that the tilt in the NS component under full load is larger than the one of the EW component, indicating a strong contribution from the cavity effect.

6.2.4.3 Displacements

The surface displacements for the BFO are plotted in (Fig. 6.15b-d). As for the other observatories, horizontal and vertical displacements are related to the topographic features (Fig. 6.15a).

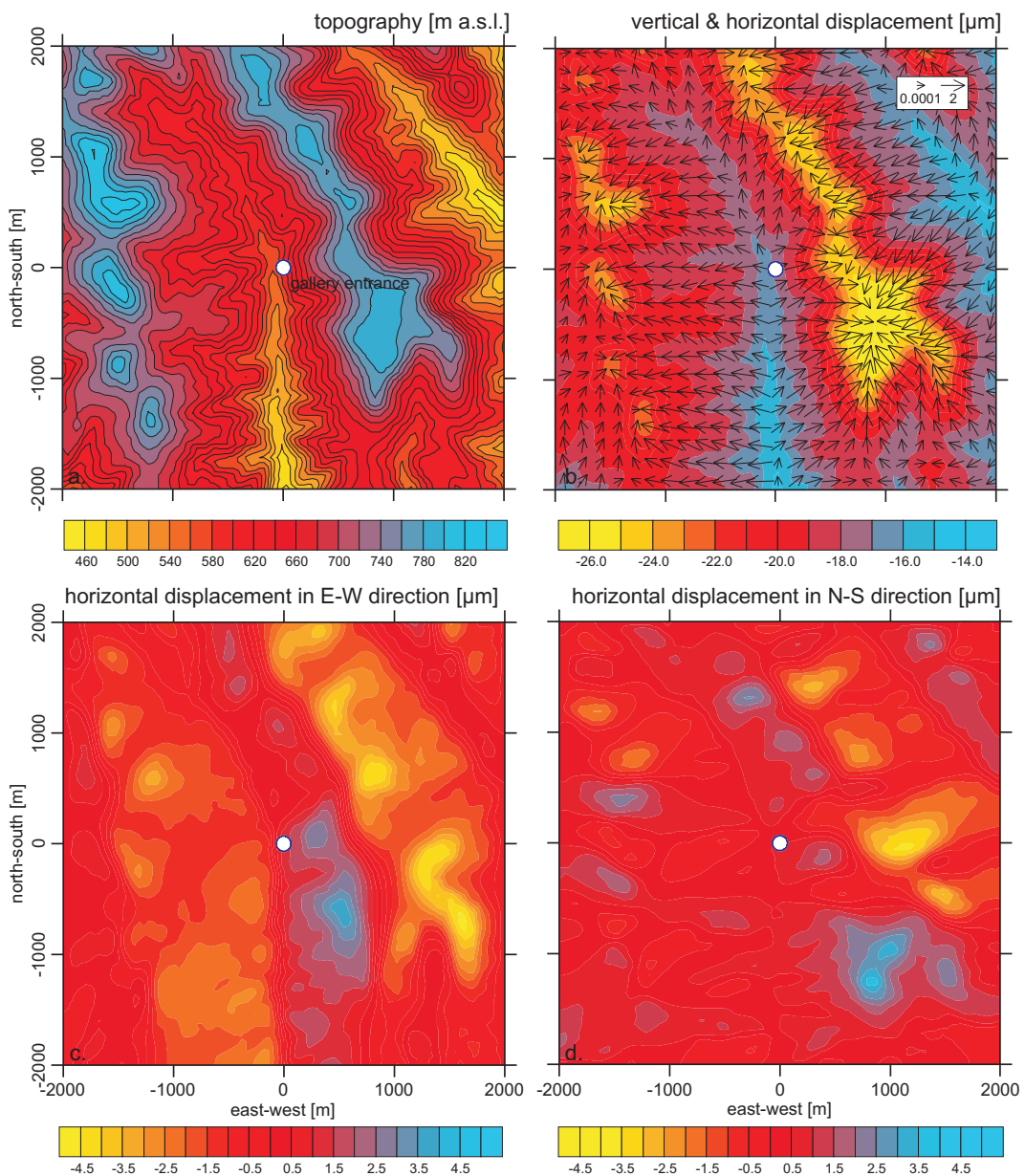


Fig. 6.15: (a) Topography of the Black Forest Observatory model. (b) horizontal (arrows) and vertical (contour map) displacements when the whole model is loaded by a high pressure area (1 hPa). (c) same as (b), but only for WE displacements. (d) same as (b), but only for NS displacements.

The values are much larger with up to 27 μm of vertical displacement. The sandstone on top of the mountains represents a weak material producing larger deformations than a hard rock such as granite. This is supported when comparing the vertical displacement gradient. For sandstone $-0.5 \mu\text{m}/10 \text{ m}$ are determined, while for granite $-0.25 \mu\text{m}/10 \text{ m}$ are obtained. In the gallery area, where the largest topographic gradients are found, the horizontal displacements are largest with about 3 μm (arrows in Fig. 6.15b). Separated into the two components (Fig. 6.15c and d), EW displacements of $\pm 3 \mu\text{m}$ evolve on both hill flanks. For the NS component at least 2 μm result in the northern tributary valley of the Heubach valley, and in the southern part of the valley east of the gallery. These maxima in both directions are transferred into the rock and lead to large compressions in NE-SW direction, which corresponds to the observations with the NE-SW strainmeter at the BFO.

6.3 Discussion

Significant deformations are found for all observatories and especially for the components that are oriented perpendicularly to the pressure front. This confirms results by Kroner et al. (2005), Steffen (2006), Gebauer et al. (2009) and investigations related to chapter 5. All tilt and strain variations illustrate several typical processes that are independent of the chosen observatory and the instrument location. Nevertheless, these processes are altered due to local topography and cavity effects, in which the latter strongly depend on the location of an instrument inside a gallery. Both topography and the cavity effect can be accounted for as source. The comparison to the reference models for WET, SOP and MOX shows that the WET reference model with plain topography can explain the main deformations. For SOP and MOX substantial differences are especially found for the strain components. In contrast, the tilt amplitudes of the observatory and the reference model agree well.

6.3.1 Strain

The characteristics of the strain components can generally be summarized as follows: When the pressure front reaches the location of the instrument extension occurs. Thereafter the sign changes and during a full load compression is observed. When the backside of a high pressure area is approaching, the sign changes again to extension. This process is found for WET, MOX and BFO, for the latter with the exception of the NS strainmeter. This strainmeter mainly shows extension even under full load. Steffen

et al. (2006) trace that back to the large cleft of the Heinrich-Gang. A completely different effect exists for SOP. The interaction of topographic features, mainly the slope at the entrance, and the gallery (cavity) results in effects that are quite difficult to separate.

The order of magnitude is comparable for all observatories. Again the Sopron Observatory differs from the other observatories with the largest values up to 0.7 nstrain. The thickness of the rocks above the galleries does not seem to affect the amplitudes, which may be related to the different rock parameters (Tab. 6.1) as well as gallery length and topography. Strain rates at the Geodetic Observatory Wettzell, where the instruments are located at the surface, at the Geodynamic Observatory Moxa (35 m of rock and gravel cover) and at the Black Forest Observatory (170 m sandstone and granite cover) are comparable with values of about 0.4 nstrain. Gebauer et al. (2009) and chapter 5 show a clear depth and gallery length dependence of the strain signal, but they also determine a non-linear relation between the rock parameters and the strain components with quite large contributions for small Young's moduli such as for the sandstone at Black Forest Observatory. The variations in depth, gallery length, topography, and rock material interact thus lead accidentally similar results in this study.

Former investigations for MOX by Kroner et al. (2005) and Steffen et al. (2006) outline differences in the strain amplitudes, which are caused by the simplified topography used for MOX. Steffen et al. (2006) also investigated the strain at BFO with a simplified FE model. A comparison of the latter work to this study shows no significant differences, which might be related to the distance of these instruments to the surface. The rock cover at BFO is much larger (by a factor of 5) when compared e.g. to MOX.

6.3.2 Tilt

The tilt results of this study are in agreement with the expected process described in Fig. 5.10. For the component aligned in moving direction of the high pressure area the largest effects occur when the pressure front or its backside is found above the instrument. The tilting direction is pointing towards the load. Tilts during the full load are related to topography (e.g. WET) and/or cavity effects (e.g. BFO). For the other component mostly much smaller values are derived. Here, the BFO is an exception. As mentioned before this is due to the cavity effect. The maximum amplitudes are in the order of some nrad for all observatories with the largest values obtained for the BFO.

For monitoring the tilt of the laser gyroscope at WET 6 platform tiltmeters type 'Lippmann' have been installed [Klügel \(2003\)](#). He found a good correlation between tilt and barometric pressure for short pressure events (e.g. passage of thunderstorms). The effect is in the range of -5 nrad/hPa to 11 nrad/hPa for different locations at the laser gyroscope platform. At present this is attributed to instrumental effects. The modeled tilt amplitudes are about 3.4 nrad for parameterization with gneiss. These amplitudes are in the order of the observed magnitude.

[Steffen \(2006\)](#) focused on tilts at BFO induced by a WE moving high pressure area. He modified the FE model created by [Steffen et al. \(2006\)](#) including the pendulum chamber and the concrete piers in the seismometer chamber. In this study the model is used with two upgrades, the topography with higher resolution and the gallery loaded until the air lock. [Steffen \(2006\)](#) did not load the gallery. [Tab. 6.2](#) compares the tilts under full model load at time step 50% of this study and [Steffen \(2006\)](#). In general, the main characteristics during a high pressure area passage agree well between this study ([Fig. 6.14](#)) and [Steffen \(2006\)](#) ([Fig. 5](#)). For points P1 to P4 on the northern pier in the seismometer chamber the increase in tilt amplitudes of the EW component and the decrease tilt amplitude of the NS component remains, but values of this study are up to 100% larger. This seems to be exclusively related to the topography as the gallery geometry was kept. The difference in the NS component is between 0.8 and 1.6 nrad, in the EW component between 0.4 and 1.1 nrad. Thus, effects in the NS component are increased by up to 50%. In the EW component factors of up to 14 are determined, but this has to be put into perspective of the small amplitudes. Interestingly, the sign changes for P1. This may also be related to the small amplitudes in the EW component. Both, this study and the work of [Steffen \(2006\)](#) demonstrate the importance of the local instrument setting. Similar results are found for the southern pier. Here, a difference of about 2 nrad is found for the NS component. The difference in the EW component is, also compared to the northern pier, smaller. The tilts in the pendulum chamber exhibit large differences in the amplitudes and for points in the western wall (P9 and P10) also in the direction. The latter is related to the loaded gallery up to the air lock. This means that also the Heinrich-Gang, a huge cavity, is loaded, which induces additional deformations in the nearby pendulum chamber. The distance is about 50 m. As the seismometer chamber is farther away (about 150 m), the effect there is less. Thus, the changed values in the pendulum chamber compared to the results of [Steffen \(2006\)](#) are mainly produced by cavity effects.

Tab. 6.2: Tilt estimates of the EW and NS components for the 12 points in the seismometer and pendulum chamber at BFO (Fig. 6.5) under full load (time step 50%) from this study and from Steffen (2006). Units in nrad/hPa.

	EW	NS	EW	NS	EW	NS	EW	NS
	P1		P2		P3		P4	
This study	0.61	4.66	0.56	4.03	0.78	4.21	1.31	3.00
Steffen (2006)	-0.53	3.05	0.04	2.71	0.33	2.42	0.67	2.24
	P5		P6		P7		P8	
This study	0.34	-3.36	0.50	-3.59	0.61	-3.80	0.81	-3.55
Steffen (2006)	-0.05	-1.53	0.15	-1.46	0.30	-1.30	0.26	-1.32
	P9		P10		P11		P12	
This study	-1.00	0.93	-1.27	-1.11	0.06	-0.82	0.25	-1.25
Steffen (2006)	-0.19	-0.15	0.19	0.45	0.56	-0.56	0.21	-0.06

6.3.3 Displacements

When the model is completely loaded, the surface is vertically depressed by several millimeters depending on the material parameters of the rock. The largest values for the vertical displacement are generally found on top of the hills, whereas the 27 mm at BFO are the maximum of all observatories. The vertical deformation traces well the topography. The gradients of vertical displacement per height also depend on the material parameters. Between $-0.13 \mu\text{m}/10 \text{ m}$ (SOP) and $-0.5 \mu\text{m}/10 \text{ m}$ (BFO) are inferred. The horizontal displacements are related to topographic features, but an order of magnitude smaller than the vertical ones. At the largest topographic gradients up to $3 \mu\text{m}$ emerge. The horizontal displacements have their source in the valleys and vanish at the top of the hills.

6.4 Brief comparison to observations

In Fig. 6.16, a comparison is exemplarily done for observations with the strainmeter at SOP in January 2007. From January 18th on the winter storm 'Kyrill' moved eastward over Central Europe. Originally a low pressure area, it evolved into an unusually violent European winter storm, forming an extratropical cyclone with hurricane-strength winds. Fig. 6.16a shows the raw data in red. The negative values denote extension. In a relative case, a change to smaller values reflects a compression and to larger values an extension. After reduction of the tidal signal (green), the main features of the raw data remain in the reduced graph (brown).

A comparison to environmental variations such as barometric pressure (Fig. 6.16b) and temperature (Fig. 6.16c) pinpoints a strong correlation to barometric pressure. The red graph in Fig. 6.16b presents a calculated strain signal. The barometric pressure

signal is multiplied with the regression coefficient of 4.88 nstrain/hPa that was determined with the FE model for the observatory under full load. The regression factor determined from data analysis of that time span is 5.51 nstrain/hPa. Both residual time series after pressure reduction are compared in [Fig. 6.16c](#). [Mentes & Eperné-Pápai \(2002\)](#) derived a regression coefficient of 4.4 nstrain/hPa from data analysis. The difference between the data derived coefficients is caused by length of the time series used in the example. Thus, the regression coefficient from the modeling fits quite well to both factors from data analysis. Using the regression factor, the effect of 'Kyrill' is removed from the strainmeter data ([Fig. 6.16c](#)). In [Fig. 6.17](#) for the same time span the reductions with regression coefficients are compared for tilt components at the BFO from the modeling and the data analysis. From the observation data, a clear correlation is found for the barometric pressure and the tilt and drift corrected EW tilt ([Fig. 6.17a](#)). The NS tilt is anti-correlates in selected time increments. For the EW tilt, the coefficient of 0.716 nrad/hPa derived from the modeling only differs by 5% from the one determined from the data (0.683 nrad/hPa). Hence, the reduced EW tilt signals in [Fig. 6.17b](#) agree well. The NS tilt reduction coefficients (modeled and derived from the data) show a larger difference ([Fig. 6.17c](#)) compared to the EW component. The regression coefficient is determined to -0.865 nrad/hPa from the modeling and to -0.579 nrad/hPa from the data. The differences are due to phase shifts between barometric pressure and tilt, and regional contributions induced by pressure sources outside the model area. The air lock at BFO acts as a single-pole low-pass filter [Richter et al. \(1995\)](#) with a cut-off period of 36 h for barometric pressure variations [Zürn et al. \(2007\)](#). Thus, both the pressure inside and outside interacts, which has to be further investigated.

The FE models can be used successfully for the determination of reduction coefficients of high and low pressure areas of larger extent. For the reduction of small-scale events, detailed information on the local pressure field is of importance, which directly follows from the findings of the present study. Therefore the set-up of local barometric pressure arrays is recommended.

6 Effects at Central European observatories

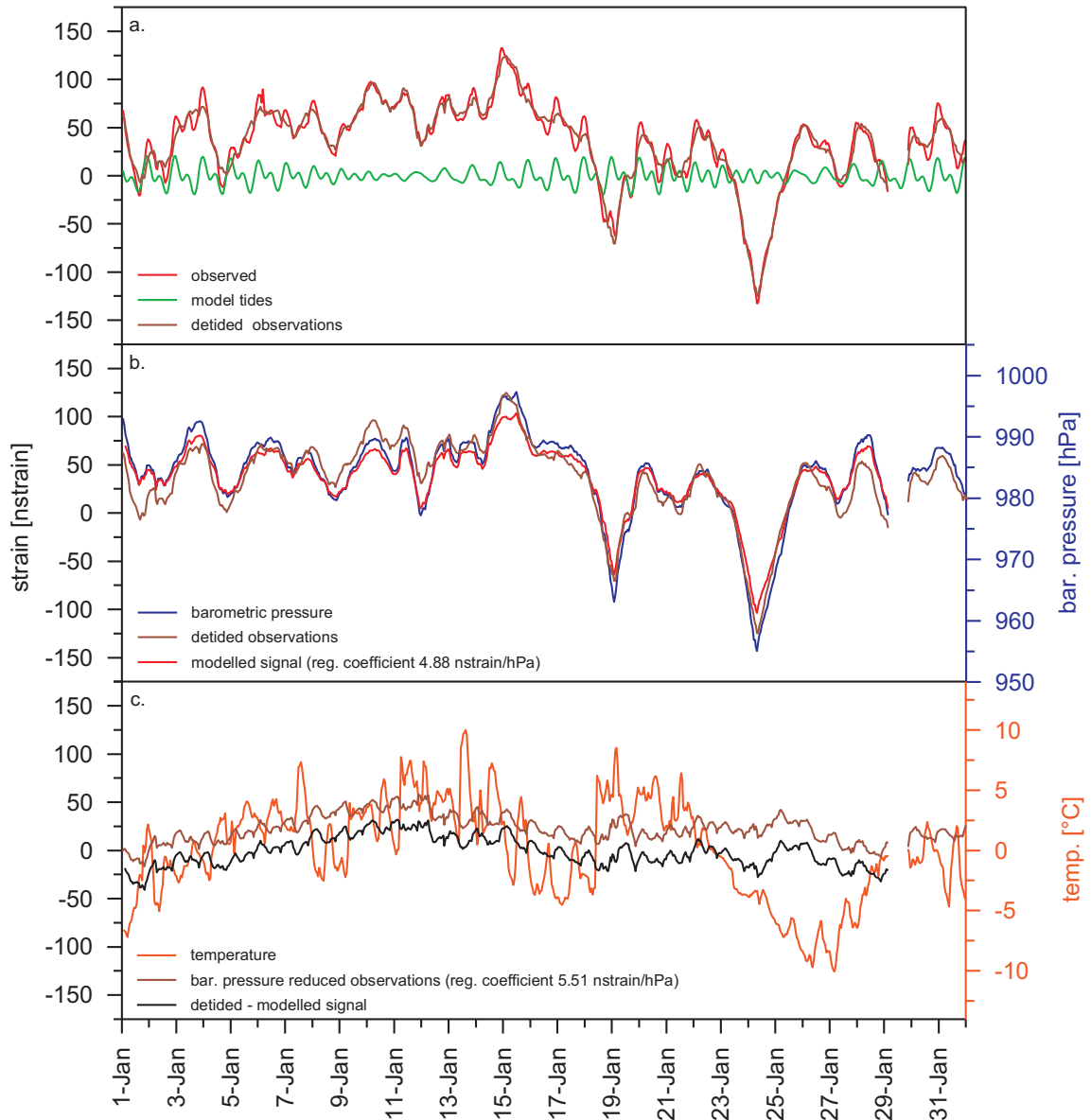


Fig. 6.16: Comparison of observed and calculated signals at Sopron Observatory from January 1st 2007 to February 1st 2007 (31 d). On the afternoon of January 18th the windstorm 'Kyrill' reached the German and Dutch coasts moving eastward over Central Europe. (a) strainmeter observation (red) and reduced signal (brown) for model tides (green); (b) detided strainmeter observation (brown), barometric pressure observation (blue) and strainmeter signal until January 29th calculated from barometric pressure signal with a regression coefficient obtained from modeling results for full load (time step 50%); (c) tide and barometric pressure reduced strainmeter data, from modeling (red), from data analysis (brown), and temperature (orange). Negative values denote extension.

6 Effects at Central European observatories

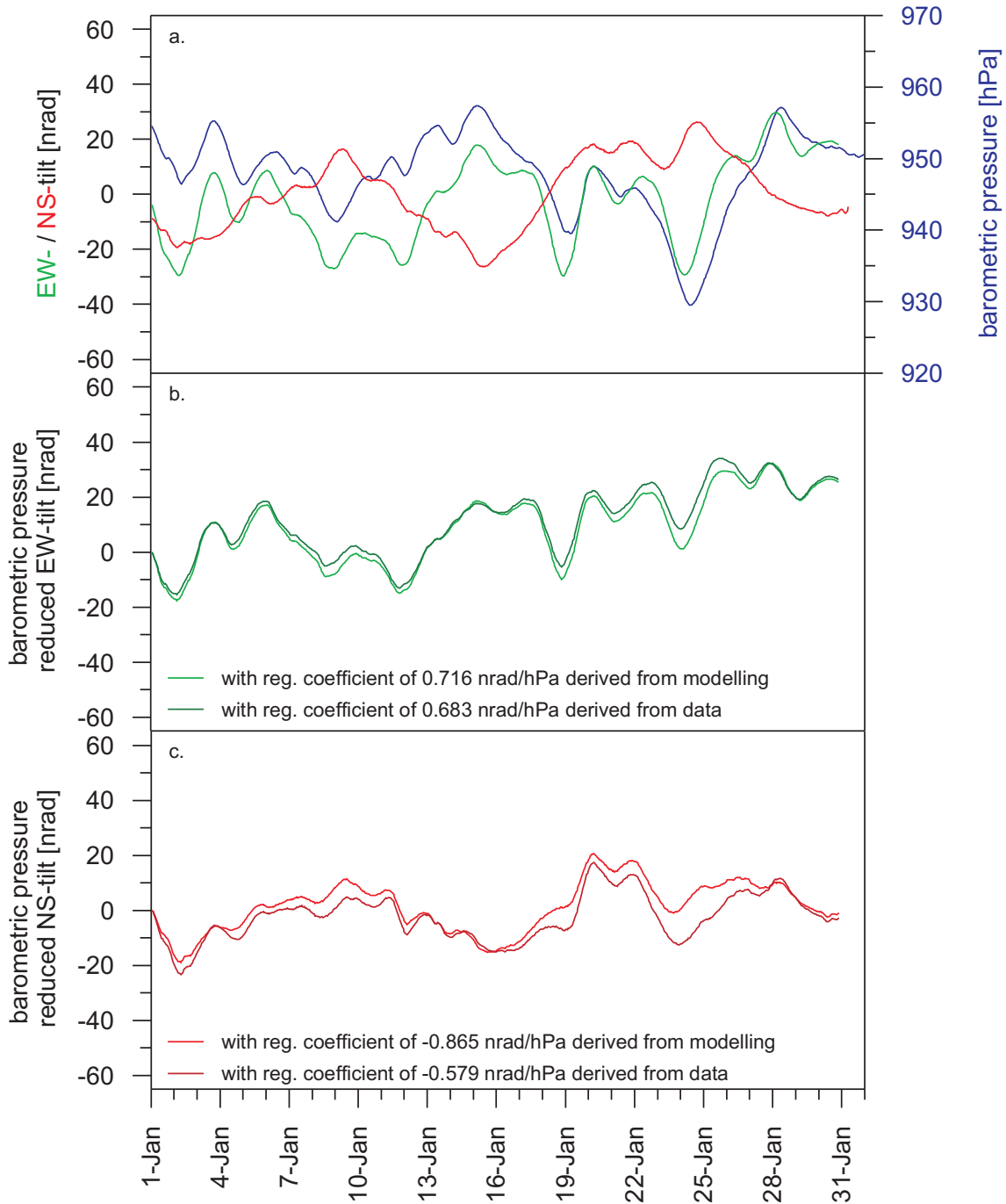


Fig. 6.17: Comparison of observed signals at Black Forest Observatory from January 1st 2007 to February 1st 2007 (31 d). On the afternoon of January 18th the winter storm 'Kyrill' reached the German and Dutch coasts moving eastward over Central Europe. (a) Tilt observations in NS (red) and EW component (green) are tide- and drift-reduced and barometric pressure observation (blue). (b) EW-tilt observations tide, drift, and barometric pressure reduced with regression coefficient derived from modeling (light green) and from data analysis (dark green). (c) NS-tilt observations tide, drift, and barometric pressure reduced with regression coefficient derived from modeling (light red) and from data analysis (dark red).

7 Investigation of deformations related to Central Europe

As mentioned in the introduction, this investigation is carried out with regard to effects caused by topography and crustal heterogeneities on regional scales. The focus is on the locations of observatory sites (BFO, MOX, SOP, WET), which are studied in detail in chapter 6. In addition on the location Trieste (TRS) is considered.

7.1 Model of Central Europe

For the investigation of large-scale deformations a model of Central Europe (Fig. 7.2) is developed taking into account the results of the 'EuCRUST-07' project (Tesauro et al., 2008). The dimensions are 1975 km in east-west, 1759 km in north-south, and 750 km in vertical direction. The Earth's curvature can be neglected as investigations regarding postglacial rebound or subduction zones by Amelung & Wolf, 1994; Fleming et al., 2003; Wolf, 1984; Morra et al., 2006; Wu & Johnston, 1998; Wu et al., 1998 and Wu, 2004 have shown. For the modeling it is important to avoid additional effects by distorted topography or geological units. Thus, the geometry and the coordinate depending load were transformed into a Cartesian coordinate system by azimuthal Lambert projection.

The topography is derived from the digital terrain model (DTM) ETOPO2 (Smith & Sandwell, 1997; Fig. 7.1). The boundaries between the layers: mantle, lower crust, upper crust, and 'sediments' (Fig. 7.2) are taken from the 'EuCRUST-07' model. The term 'sediments' is not geology-related used, but as a region of lower seismic velocities. Additionally, for modeling reasons, only a thickness of 5 km and larger is considered for the sediments. The different rock units are parameterized after averaged values of PREM (Dziewonski & Anderson, 1981) for the various depth levels and additionally the upper crust after simplified geological units using the values of 'EuCRUST-07' model (Tab. 7.2).

The models are developed using *HyperMesh* and *ABAQUS*. Each layer is meshed separately and afterwards combined to the final model using the 'Tie' constrain (Abaqus Inc., 2007). The final models consist of about 2.6 million linear tetrahedral

7 Investigation of deformations related to Central Europe

elements (Abaqus Inc., 2007). The element size of the lower crust, upper crust, and 'sediments' is about 5 km. In the surroundings of the five observatory sites the mesh is subsequently refined to an element size of 10 m, in order to be able to determine displacements at defined nodes.

Five model types are developed (comp. Tab. 7.1, Fig. 7.2):

- model 1: without topography, homogenous parameterization with parameters of the 'sediments',
- model 2: with topography, homogenous parameterization with parameters of the 'sediments',
- model 3: without topography, parameterization after PREM,
- model 4: with topography, parameterization after PREM,
- model 5: with topography, parameterization after PREM and additionally with lateral inhomogeneities.

Furthermore, the material parameters of the upper crust and the mantle based on model 4 are modified, thus four additional models exist.

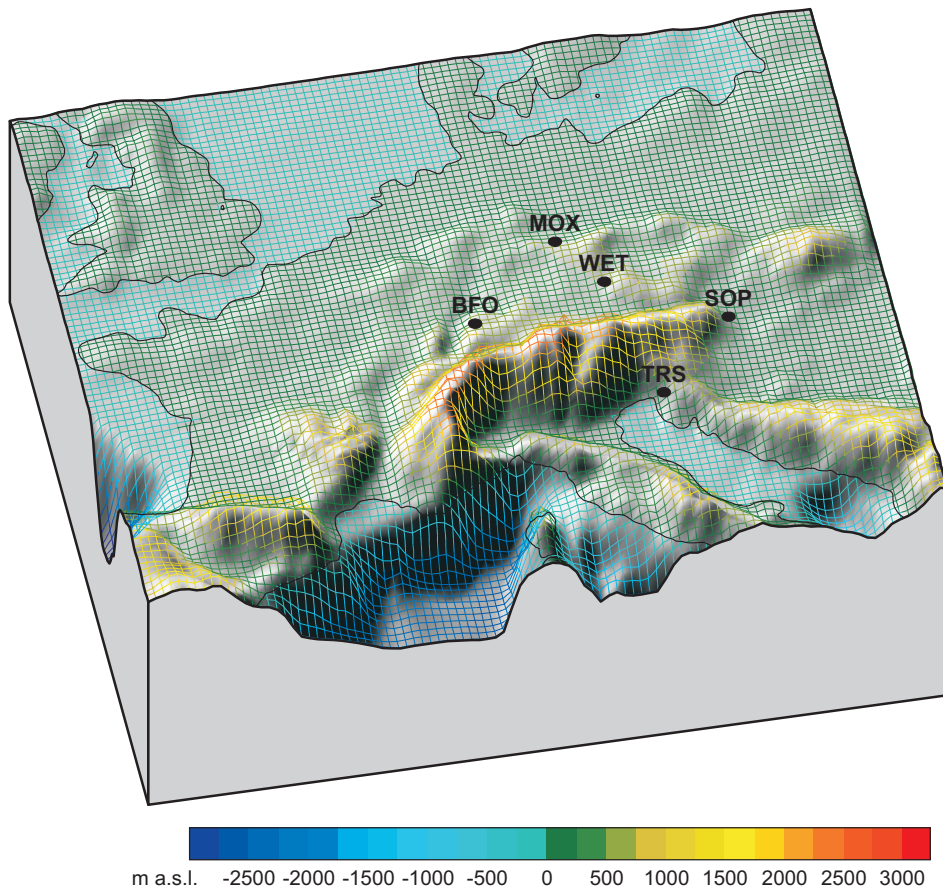


Fig. 7.1: Digital Terrain Model (DTM) used in modeling of Central Europe derived from Etopo2 (80x vertical exaggeration).

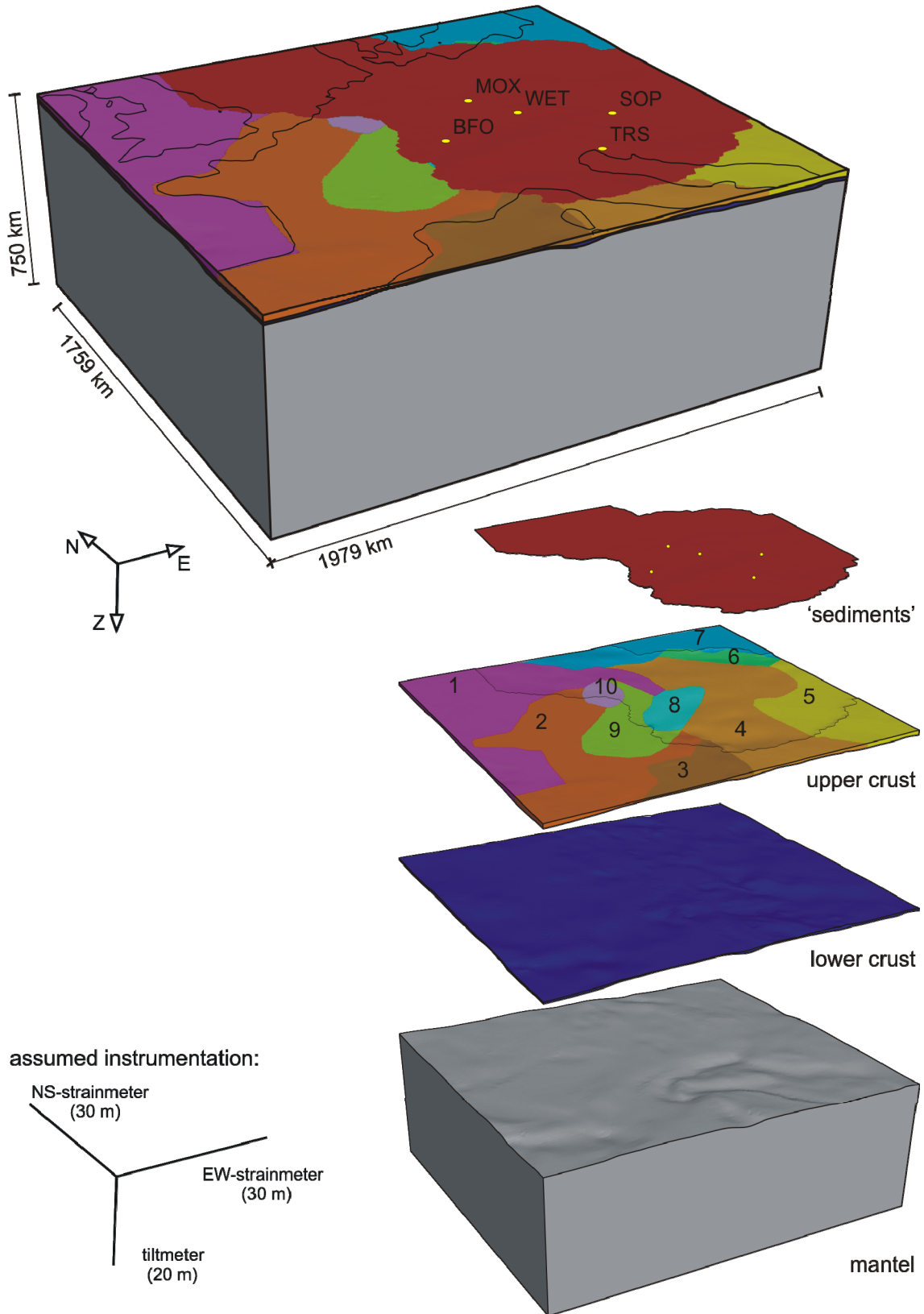


Fig. 7.2: Model set-up for investigations related to Central Europe and assumed instrumentation at observatories considered. The colors mark units with identical the material parameters (comp. Tab. 7.1, Fig. 7.2).

7 Investigation of deformations related to Central Europe

Tab. 7.1: Model types and parameterization for Central Europe.

<i>model</i>	1			2			3		
<i>topography</i>	-			x			-		
	ρ [kg/m ³]	E [GPa]	ν	ρ [kg/m ³]	E [GPa]	ν	ρ [kg/m ³]	E [GPa]	ν
'sediments'	2,700	68.0	0.2812	2,700	68.0	0.2812	2,700	68.0	0.2812
upper crust	2,700	68.0	0.2812	2,700	68.0	0.2812	2,900	111.0	0.2549
lower crust	2,700	68.0	0.2812	2,700	68.0	0.2812	3,377	173.0	0.2791
mantle	2,700	68.0	0.2812	2,700	68.0	0.2812	3,744	263.0	0.2852
<i>model</i>	4			5					
<i>topography</i>	x			x					
	ρ [kg/m ³]	E [GPa]	ν	ρ [kg/m ³]	E [GPa]	ν			
'sediments'	2,700	68.0	0.2812	2,700	68.0	0.2812			
upper crust	2,900	111.0	0.2549	¹	¹	¹			
lower crust	3,377	173.0	0.2791	3,377	173.0	0.2791			
mantle	3,744	263.0	0.2852	3,744	263.0	0.2852			
<i>model</i>	6			7			8		
<i>topography</i>	x			x			x		
	ρ [kg/m ³]	E [GPa]	ν	ρ [kg/m ³]	E [GPa]	ν	ρ [kg/m ³]	E [GPa]	ν
'sediments'	2,700	68.0	0.2812	2,700	68.0	0.2812	2,700	68.0	0.2812
upper crust	2,700	68.0	0.2812	2,700	68.0	0.2812	2,700	68.0	0.2812
lower crust	3,377	173.0	0.2791	3,377	173.0	0.2791	3,377	173.0	0.2791
mantle	3,744	263.0	0.2852	3,670	191.4	0.29	3,670	200.0	0.2900
<i>model</i>	9			10					
<i>topography</i>	x			x					
	ρ [kg/m ³]	E [GPa]	ν	ρ [kg/m ³]	E [GPa]	ν			
'sediments'	2,700	68.0	0.2812	2,700	68.0	0.2812			
upper crust	2,700	68.0	0.2812	2,700	68.0	0.2812			
lower crust	3,377	173.0	0.2791	3,377	173.0	0.2791			
mantle	3,670	210.0	0.2900	3,670	215.0	0.2900			

¹ material parameters after 'EuCrust-07' (comp. [Tab. 7.2](#))

Tab. 7.2: Material parameters of the upper crust derived from 'EuCrust-07' ([Tesauro et al., 2008](#)).

Region		ρ [kg/m ³]	E [GPa]	ν
1	North Sea / Rhine	2,820	84.6	0.2500
2	West	2,800	88.3	0.2500
3	Mediterranean	2,820	86.0	0.2500
4	Middle-East-Europe	2,790	89.4	0.2500
5	East	2,810	84.3	0.2500
6	Tornquist Suture Zone	2,860	85.8	0.2500
7	North	2,830	96.6	0.2500
8	Alps	2,760	82.8	0.2500
9	Burgundy	2,765	84.3	0.2500
10	West-Belgium	2,780	91.9	0.2500

7.2 Barometric pressure load

The different models of Central Europe are loaded with the following load cases:

- uniform barometric pressure load
- barometric pressure cap (Fig. 7.3a):
- centre at Moxa with diameters of 100 km, 200 km, and 300 km
- centre 350 km south of Moxa with diameters of 100 km, 200 km, and 300 km
- storm event 'Kyrill' in January 2007 (Fig. 7.3b)

The uniform pressure load and the barometric pressure cap are used to determine the principle deformation behavior. The results obtained for the pressure field of storm 'Kyrill' are used to compare modeled and observed deformations.

The pressure field associated with 'Kyrill' (Fig. 7.3b) is calculated from data of 42 European locations (comp. App. Fig. 27). The barometric pressure acts at the whole model surface. Due to the inhomogeneous distributed pressure stations the interpolated grid probably reproduces not precisely the real conditions. Coast-specific effects are negligible for all observatories except Trieste (TRS).

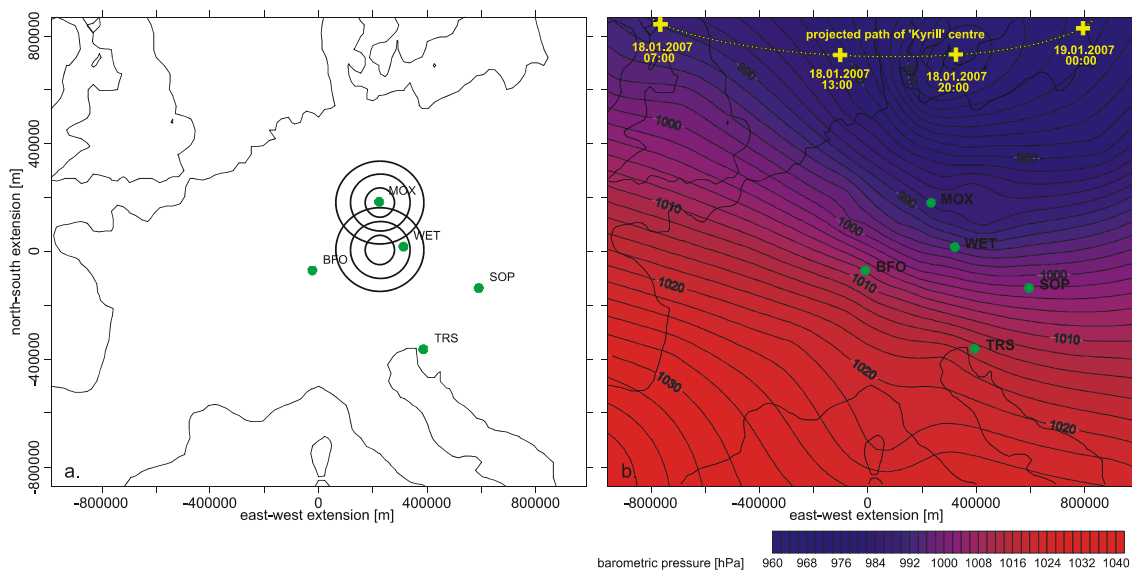


Fig. 7.3: (a.) Barometric pressure cap above the Geodynamic Observatory Moxa and 350 km south of it with diameter of 100 km 200 km and 300 km. (b.) Barometric pressure field for Central Europe on January 1st 2007 at 20:00 MEZ. Additionally shown is the simplified path of the 'Kyrill' centre.

7.3 Results

7.3.1 Uniform barometric pressure load for model 1 – 5

The resulting displacements for model 1 of Central Europe (comp. [Tab. 7.1](#)) are found in [Fig. 7.4](#) which is used for quality estimation and as reference for model 2. The model 1 is homogeneously parameterized after PREM with values of the first few meters of the crust. Therefore, it is to be expected that no significant displacements occur except for uniformly in the vertical direction. The model is vertically compressed by 86.2 mm. The anomalies in the horizontal displacements occur by numerical effects.

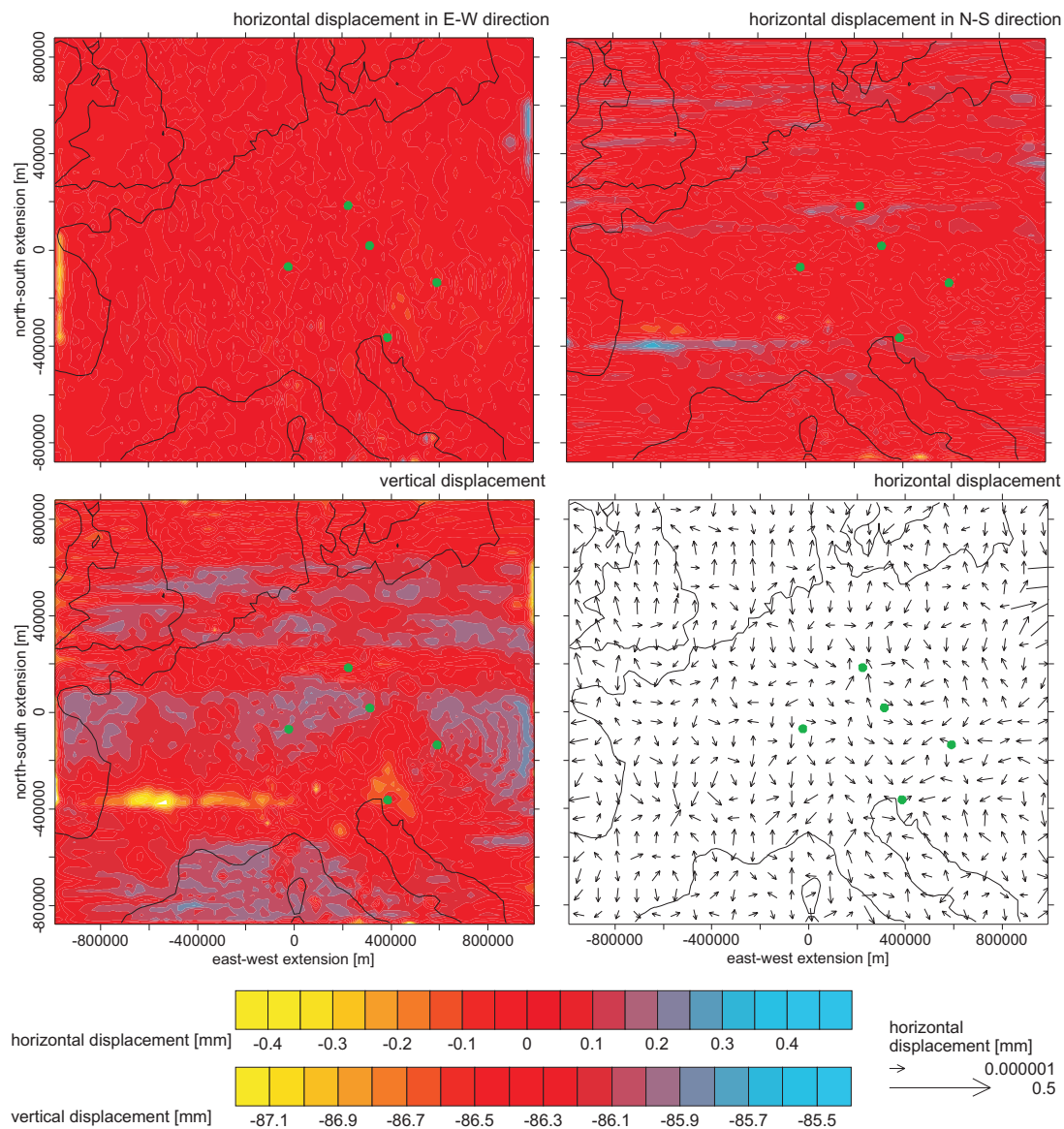


Fig. 7.4: Displacements for model 1 (comp. [Tab. 7.1](#)) and a uniform barometric pressure load of 1 hPa.

7 Investigation of deformations related to Central Europe

In order to determine the effect of the topography the model 2 is used. The results are given in [Fig. 7.5](#). The displacements clearly reflect the impact of the topography. For the vertical displacements an average amplitude at the surface of 86.3 mm is determined with variations between 85.4 mm and 87.2 mm. Regions like the Alps are more vertically displaced than the bottom of the Mediterranean Sea. For the horizontal direction emerges that topographic regions with strong gradients experience displacements with an amplitude of about 0.5 mm in direction towards the higher areas. This behavior is also found in the principle study on local effects and the investigations for the observatories.

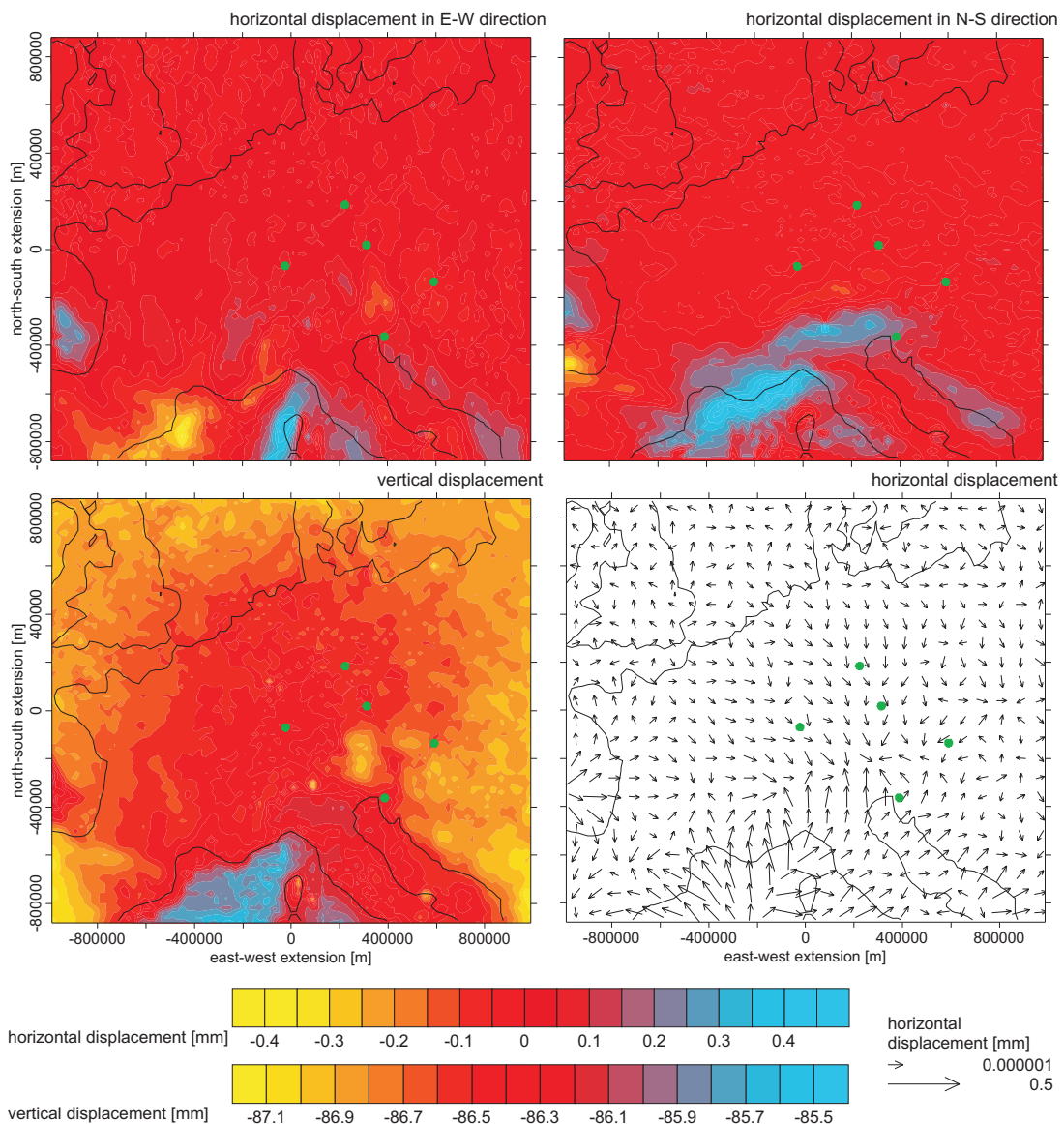


Fig. 7.5: Displacements for model 2 (comp. [Tab. 7.1](#)) and a uniform barometric pressure load of 1 hPa.

7 Investigation of deformations related to Central Europe

In order to determine the effect (Fig. 7.6) of changes in the layer thickness on displacements ('sediments', upper crust, lower crust, and mantle) the model 3 is used. This model has no surface topography and parameterized after PREM. The displacements show amplitudes which correlate with the layer topography (e.g. the Alps and the deep sea area). From this follows a reversed relief that is as a boundary between the crust and the mantle the Mohorovičić discontinuity. Additionally, in the area of the Mediterranean Sea the oceanic crust is thinner than the continental crust. The vertical displacements are in the range of 1.2 mm. Due to the topography of the layers and the barometric pressure load horizontal displacements with maximum amplitudes of about 0.25 mm are generated.

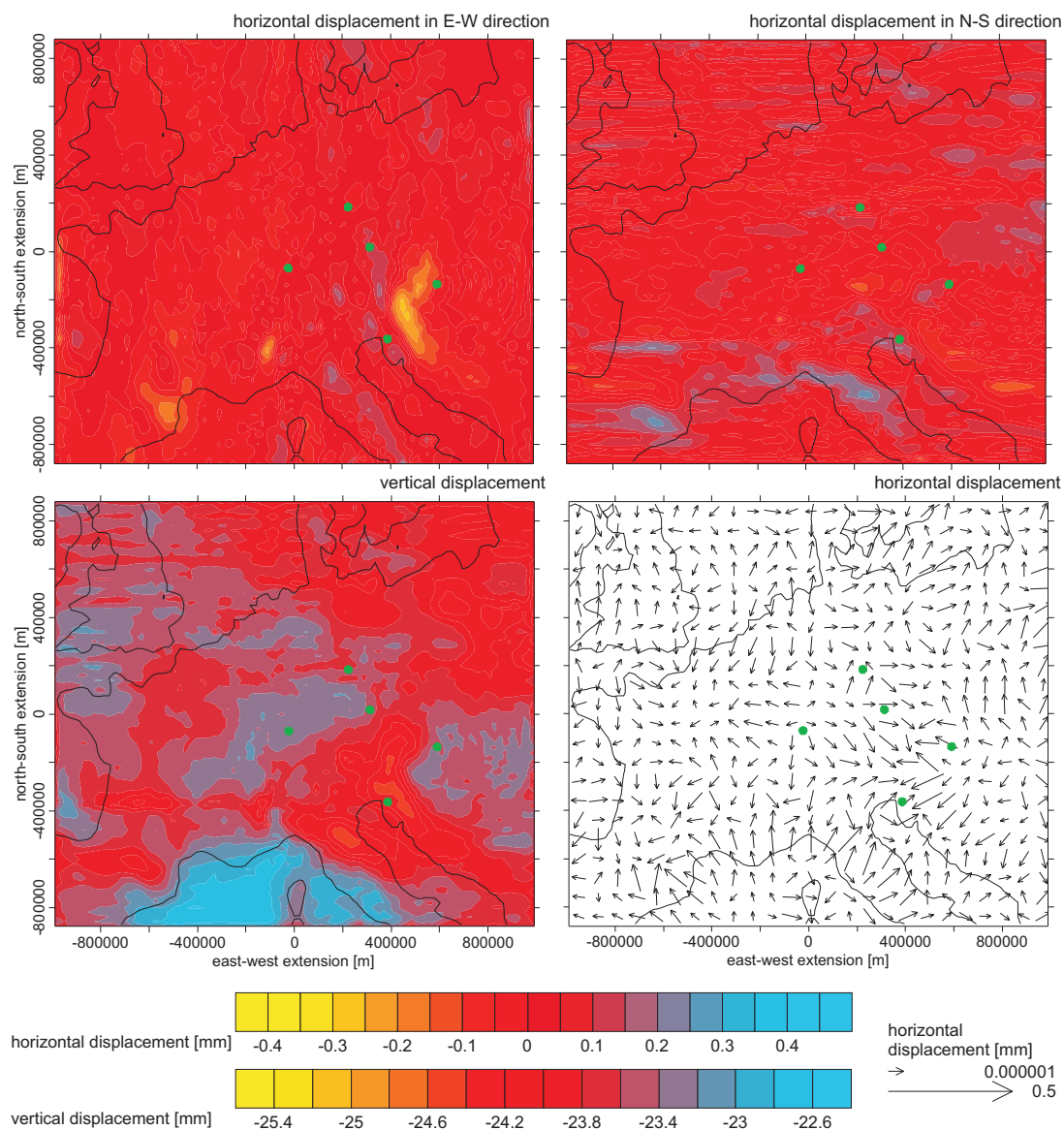


Fig. 7.6: Displacements for model 3 (comp. Tab. 7.1) and a uniform barometric pressure load of 1 hPa.

7 Investigation of deformations related to Central Europe

If the surface topography (ETOPO02) is additionally taken into account (model 4), the displacements reflect more strongly the surface topography than in the case of model 3 (Fig. 7.7), but the main signal is caused by the deeper layers. In the displacements in EW- and NS-direction the Alps and the scarp of Mediterranean Sea are identifiable, and the amplitudes range between -0.35 and 0.35 mm. In vertical direction a weak signal occurs in the area of the Tornquist suture, where the crust is thickened. There, an amplitude of 0.6 mm related to the surroundings occurs for the vertical displacements.

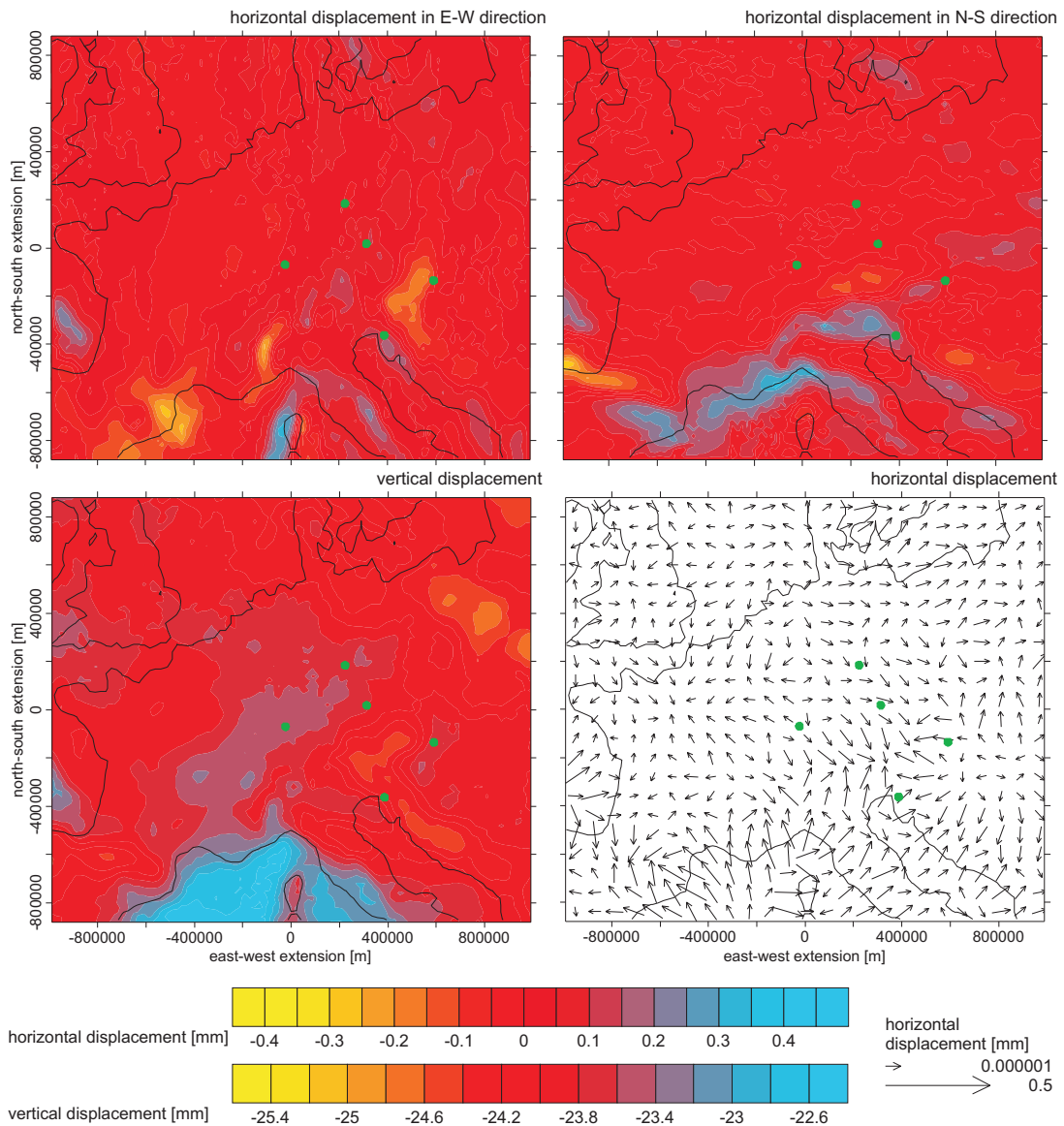


Fig. 7.7: Displacements for model 4 (comp. Tab. 7.1) and a uniform barometric pressure load of 1 hPa.

7 Investigation of deformations related to Central Europe

In model 5 the topography, the different layers parameterized after PREM, and lateral inhomogeneities for the upper crust are considered (comp. Fig. 7.2, Tab. 7.1, and Tab. 7.2). The results for a 1 hPa uniform barometric pressure load are shown in Fig. 7.8. Apart from the results of model 3 and 4 additional signals are found, especially, for vertical displacements of the Tornquist suture, where the material is weaker than in the vicinity. The amplitudes are in the same order of magnitude as for model 3 and 4.

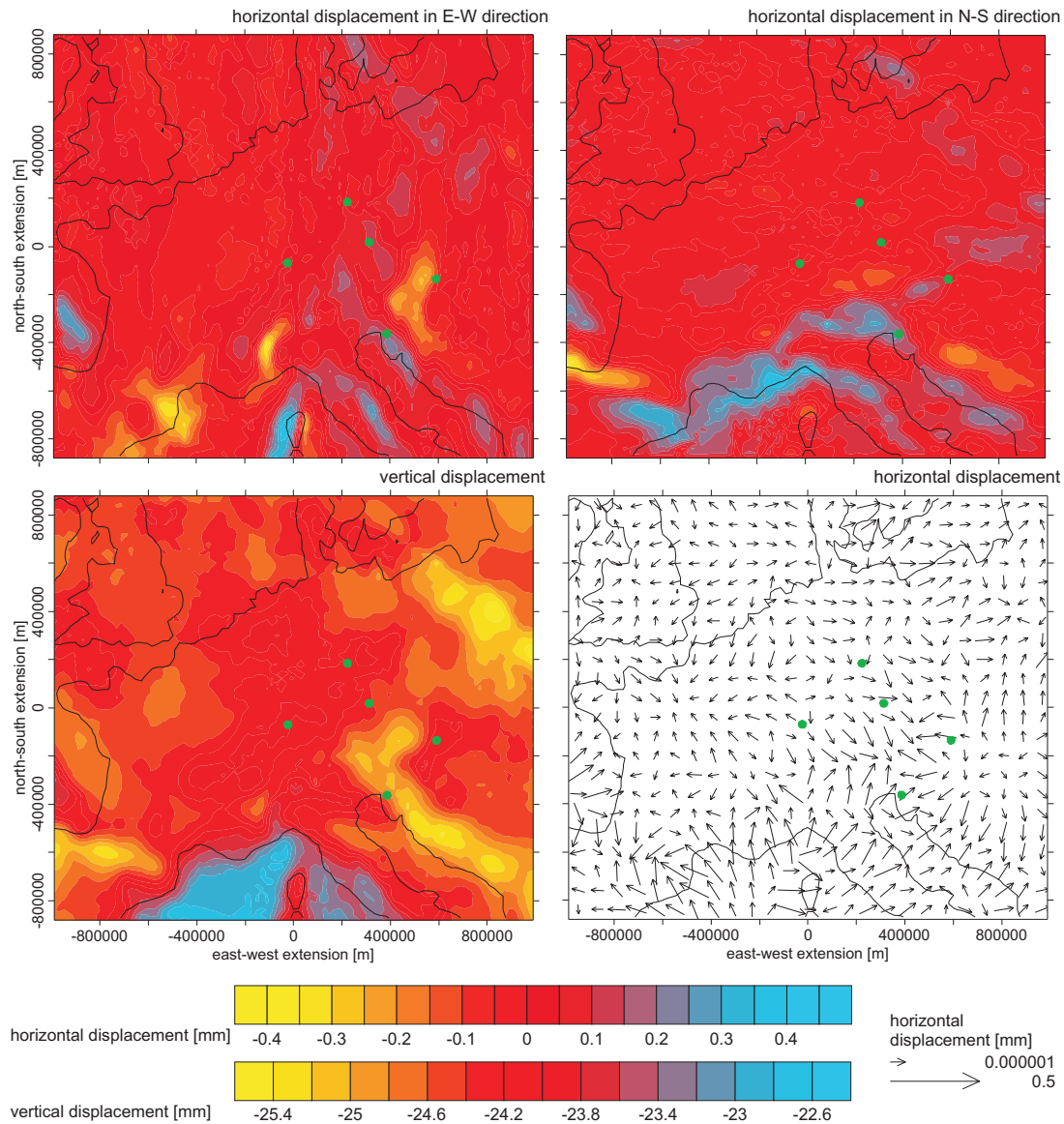


Fig. 7.8: Displacements for model 5 (comp. Tab. 7.1) and a uniform barometric pressure load of 1 hPa.

From these results follows that for uniform barometric pressure load related to displacements as many features as possible (topography, vertical and lateral changing material parameters) have to be considered. Therefore, further investigations are carried out for a barometric pressure cap and real weather scenarios are applied as load to estimate site dependent deformations changes with regard to the topography and lateral inhomogeneities. The main point of interest is the time-dependent relative changes at an observatory site.

7.3.2 Barometric pressure cap

A barometric pressure cap as load source is a simplification for a high pressure area and allows to analyze the deformations (displacement, strain, tilt) and to determine the order of magnitude of corresponding amplitudes. As shown in Fig. 7.3, barometric pressure caps with diameters of 100 km, 200 km, and 300 km are used as load. The diameters are selected according to actual occurring pressure scenarios. For the study, in the first case the centre of the cap is located at the broadband observatory Moxa and in the second case 350 km in the south of it.

For the models 1 to 5 the deformation is calculated. Exemplarily, the results are shown for the model 5 and pressure caps, which are directly located above MOX (Fig. 7.9). For increasing diameter of the cap the amplitude of the vertical displacements becomes larger (Fig. 7.9a, b, c). As expected the direction of horizontal displacements points to the centre of the pressure cap with maximum amplitudes of 0.02 mm at the border of the pressure cap with a diameter of 300 km (Fig. 7.9 e, f). The deformations related to the pressure centre are nearly rotational-symmetric. Effects caused by the topography and geological inhomogeneities are not identifiable. For the pressure caps located 350 km south of MOX similar results are found.

For better comparison east to west running cross sections through MOX are shown for the deformations derived from the different loads and models (Fig. 7.10, Fig. 7.11). The results for the pressure caps of 100 km, 200 km, and 300 km using model 5 are given in Fig. 7.10. In a distance of approximately 750 km from the load centre the vertical deformation is 0 mm, for larger distances an uplift of maximum 0.001 mm occurs for 1 hPa. The maximum amplitudes are -0.0560 mm, -0.0864 mm, and -0.1107 mm at the centre of the loaded area. Several models types of Central Europe are loaded with the 1 hPa pressure cap of 300 km in diameter (Fig. 7.11). The three models 3, 4, and 5 lead to amplitudes differing within 2%. For model 3 (without topography) the surface is

7 Investigation of deformations related to Central Europe

set to sea level height. Thus, the 'sediments' and the upper crust (comp. Fig. 3.1) are thinner than for model 4 and 5, respectively. Based on this, the vertical deformation amplitude is lower for model 3 than for model 4 (Fig. 7.11). For the model 5 larger deformations than for 3 and 4 are found, caused by the in average weaker upper crust (comp. Fig. 7.2, Tab. 7.1, and Tab. 7.2).

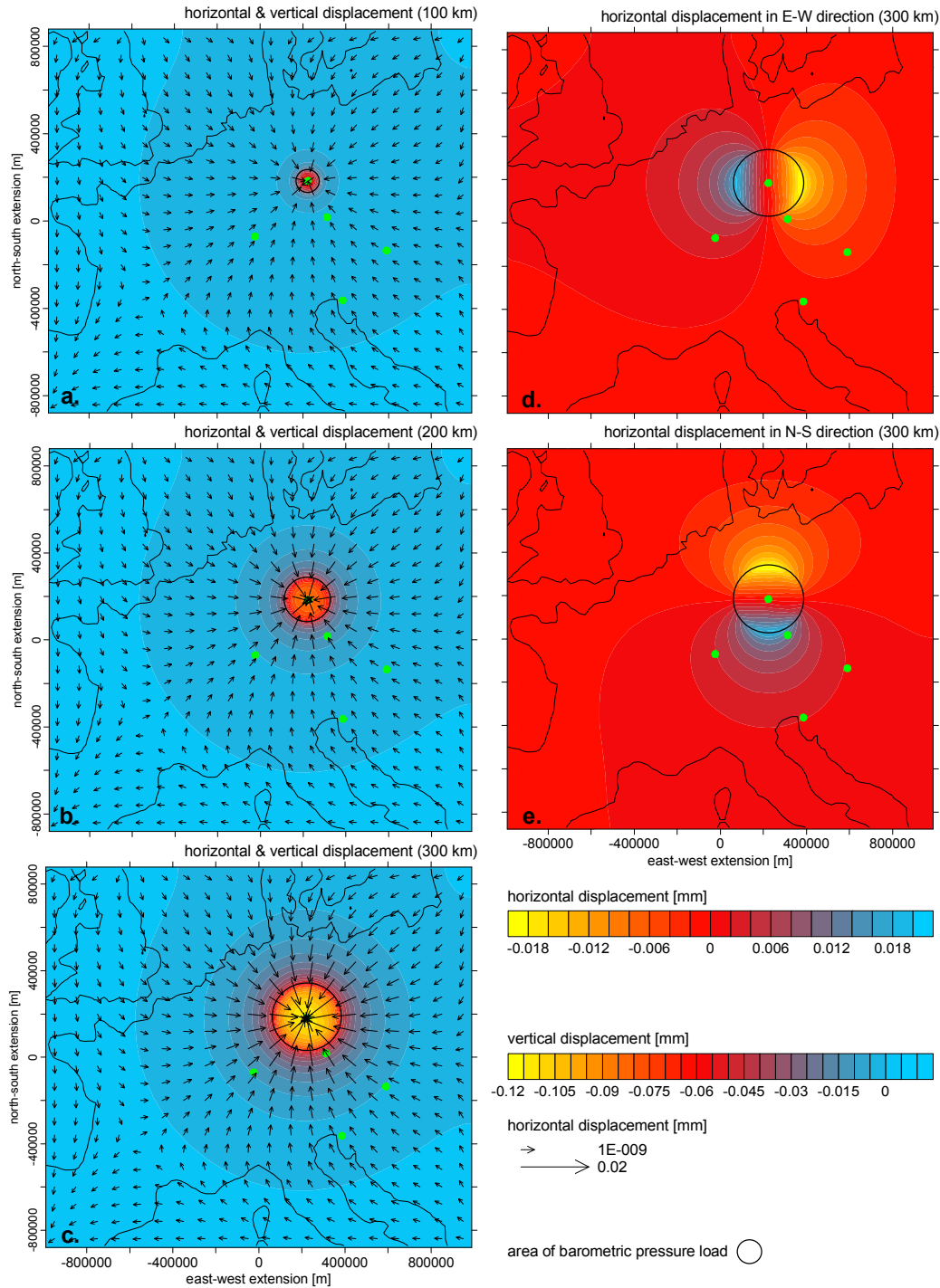


Fig. 7.9: Displacements obtained at the surface for a 1 hPa barometric pressure cap of 100 km, 200 km and 300 km diameter above the geodynamic observatory Moxa using the model 5 (comp. Fig. 7.2, Tab. 7.1, and Tab. 7.2).

7 Investigation of deformations related to Central Europe

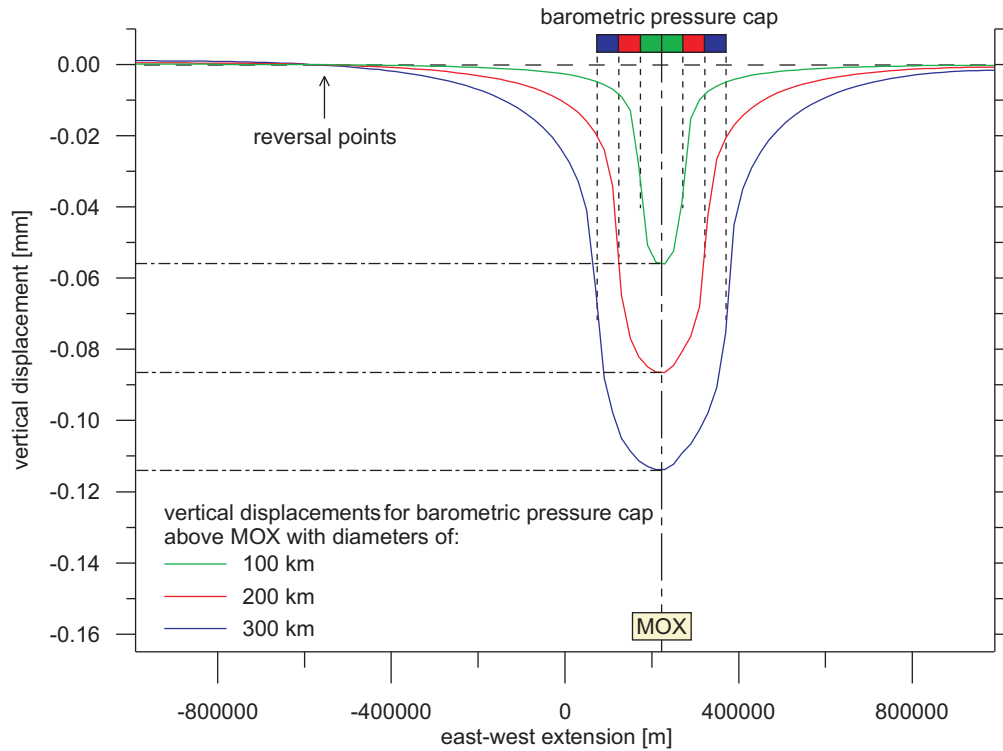


Fig. 7.10: Vertical deformations for an east-west cross section through the Geodynamic Observatory Moxa for a 1 hPa barometric pressure cap with a diameter of 100 km, 200 km and 300 km using the model 5 (comp. Fig. 7.2, Tab. 7.1, and Tab. 7.2).

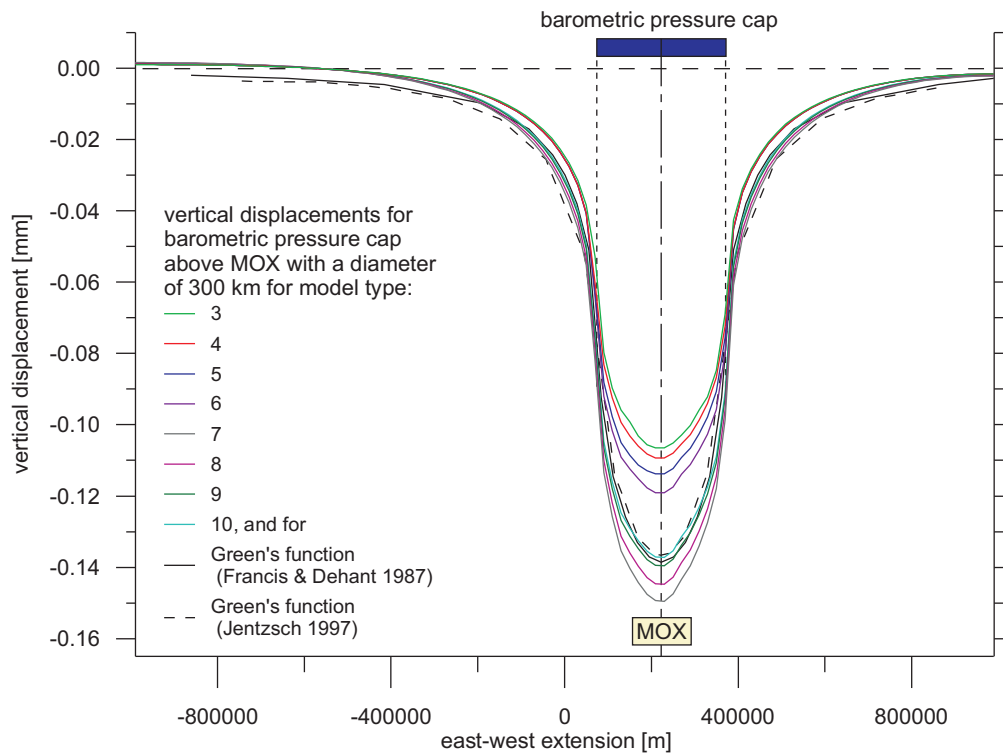


Fig. 7.11: Vertical deformations for an east-west cross section through the Geodynamic Observatory Moxa for a 1 hPa barometric pressure cap with a diameter of 300 km the model 3, 4, 5, 6, 7, 8, 9, 10, and Green's functions (comp. Fig. 7.2, Tab. 7.1, and Tab. 7.2).

A commonly used method to model displacements is based on Green's functions. Displacements based on this approach are calculated for the identical area and barometric pressure load as used for the FE models. Exemplarily, the results obtained from Green's functions published by Francis & Dehant (1987) and Jentzsch (1997) are given for comparison, as all available Green's functions yield similar results. Compared to the results for model 3, 4, and 5 about 20% larger deformations occur using the Green's function approach. The smaller amplitudes of the FE models are caused by the model conditions. The vertical extension (750 km) in contribution with the boundary condition of model bottom, which is not allowed to move in the vertical, controls the order of magnitude of vertical compression for the load.

The Finite-Element method abstracts a mathematical problem. Based on this for each model is taken into account assumptions and simplifications, which reflects as well as possible the problem under investigation. In this case it concerns the parameterization of the mantle. Following that the response of the FE model (3, 4, and 5) is reduced with respect to the modeled vertical displacements of Green's function.

The FE models (3, 4, and 5) show no significant changes in deformations related to effects of topography and lateral inhomogeneities. Model 4 with surface topography was selected for modifications for the material parameters of the different layers.

In a first step the whole upper crust is parameterized with the material properties of the 'sediments' (model 6) to study the effect of the upper crust. The deformation amplitude increases, as expected, by about 8%. Similar results for changed material parameters and layer thicknesses of the upper and lower crust are found by comparing the different existing Green's functions (Farrell, 1972; Francis & Dehant, 1987; Jentzsch, 1997; Pagiatakis, 1990; Merriam, 1992; Guo et al., 2004).

In a second step the material conditions of the mantle are varied, for the previously mentioned reason, to estimate the effect of the mantle. Therefore, the Young's modulus is changed in the range of values of the upper mantle of PREM. The model 10 with a Young's modulus of 215 GPa and a Poisson ratio of 0.29 yields the best results with regard to the comparison to the Green's function.

Apart from the displacements, strain and tilt deformations are investigated for the barometric pressure cap (Fig. 7.12). For this investigation the models 3 and 5 are used. Based on these two models the effects caused by the topography and lateral inhomogeneities can be analyzed.

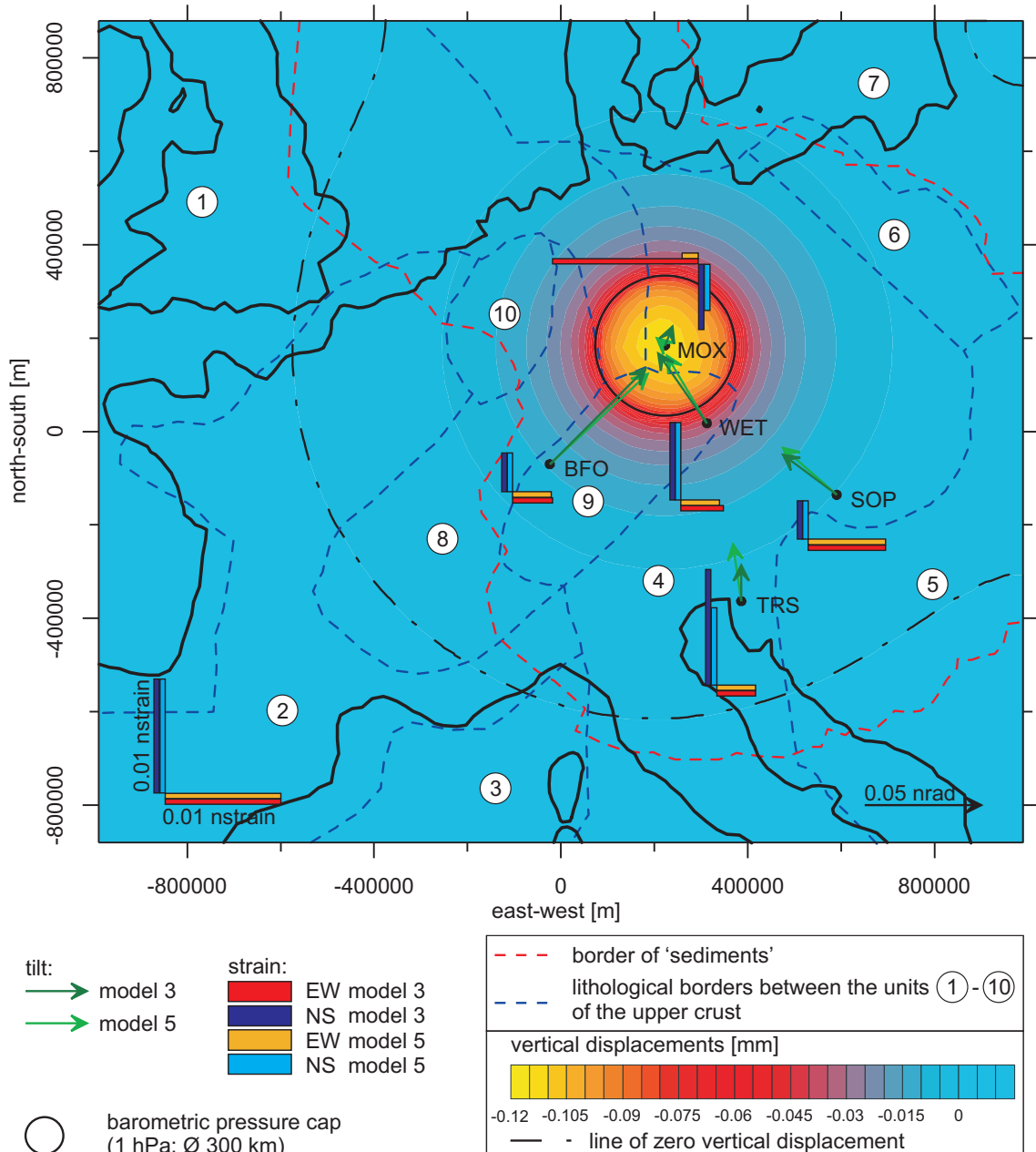


Fig. 7.12: Strain and tilt amplitudes calculated at the five observatory sites for model 3 and 5. As load the 1 hPa barometric pressure cap is considered. Additionally, the borders of the 'sediments' and different rocks of the upper crust (1-10) are shown (comp. Fig. 7.2, Tab. 7.1, and Tab. 7.2). The vertical displacement is obtained from model 5.

The amplitudes obtained for the strainmeters (comp. Fig. 7.2) are always below the detection level (comp. chapter 3.1), but the deformations reflect the expected behavior. For MOX, where the centre of the barometric pressure cap is located, compression is found. For the other considered observatory sites differing dilatations emerge in which for increasing distance the strain amplitudes decrease. The EW- and NS-strain components at the observatories have different amplitudes depending on the position related to the barometric pressure cap. At the observatory site SOP compared to TRS a larger

amplitude for the EW-strainmeter occurs and for the NS-component a smaller one with deformations in order of magnitude below the detection level. Both observatories have a similar distance to MOX. Thus, an assumed strainmeter oriented to the pressure centre monitors similar amplitudes. Furthermore, due to the very small amplitudes numerical effects can not be excluded, which is indicated by the differences of calculated EW- and NS-strain amplitudes of MOX. The tilt amplitudes at the observatory sites show maximum amplitudes in the order of magnitude of about 0.06 nrad for 1 hPa barometric pressure change (Fig. 7.12). The arrows in Fig. 7.12 represent the moving of the pendulum tip in direction of the centre of the barometric pressure cap, and for increasing distance of the observatory sites the amplitudes decrease. At the site MOX no signal is expected, but the calculations show insignificant amplitudes in northern direction. Possibly, this is caused by boundary effects. An indication for this is the line of zero vertical displacement. Based on the theory this isoline should be circular, but is not found to be in the modeling results. The differences for the tilts determined from models 3 and 5 are less than 5% in direction and amplitude. Related to this result the effects caused by topography and geology are negligible.

7.3.3 The 'Kyrill' event

For comparing the modeled with observed deformations an actual weather scenario is studied - the winter storm 'Kyrill' in January 2007. For a time window from January 16th 00:00 CET to January 22nd 00:00 CET, the displacements are determined with the barometric pressure fields available (comp. Fig. 7.3b) using the models 3, 4, and 5 (Fig. 7.13). Comparing the results of the three models only negligible differences for the vertical and horizontal components are found. The comparison of the FE modeled displacements with those calculated using a Green's function (Jentzsch, 1997), shows for the vertical component about 20% larger signals, as found for investigation related to the pressure cap. Apart from that the time-dependent behavior fits well.

The horizontal components are affected by the barometric pressure distribution. The centre of 'Kyrill' moves from west to east across the British Isles, the North Sea, Denmark, and the Baltic Sea (comp. Fig. 7.3b), thus the isobars in the middle and south of the area under investigation are oriented east-west. Considering that, it can be expected that for the EW-component only small signals occur at the observatories (Fig. 7.13). Due to the pressure field the south of the model is more compressed than the north and, thus, for the NS-component an amplitude in southern direction exists.

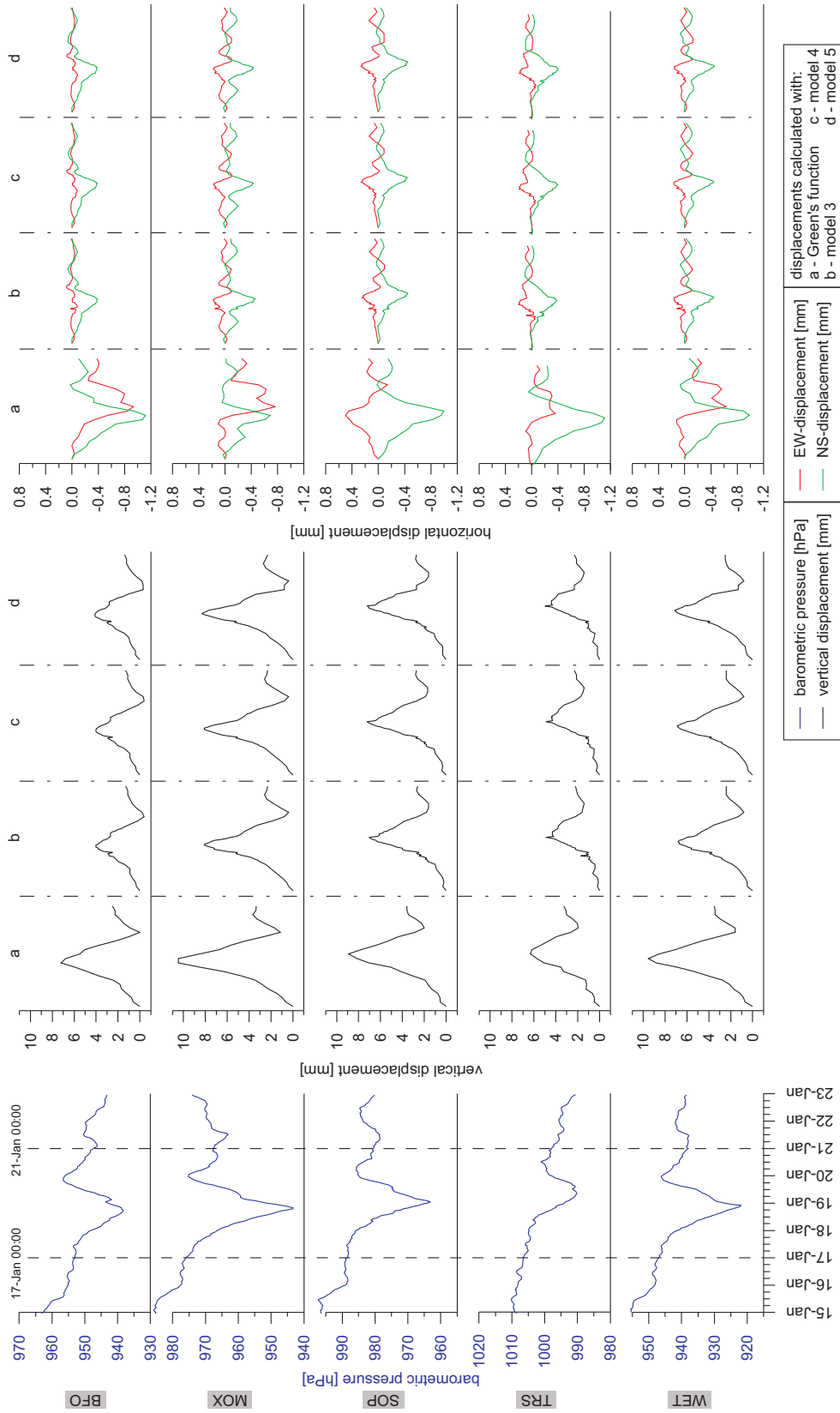


Fig. 7.13: Modeled displacements at the observatories BFO, MOX, SOP, TRS, and WET for the storm 'Kyrill' in January 2007. The results are obtained from Green's functions (pers. comm. Klügel, 2009), and the model types 3, 4, and 5. The first column shows the displacements for Green's function and the observed pressure at each observatory from January 16th 00:00 CET to January 22nd 00:00 CET. The results for FE modeled vertical displacements are given in the second column and horizontal displacements in the third column of the four models for same time window.

7 Investigation of deformations related to Central Europe

Additionally, the displacements are determined for the same barometric pressure scenario and model 10 (Fig. 7.14). Comparing the vertical displacements with the results derived from the Green's function a good correlation is found for the observatory sites SOP and WET, but not as good at the other sites considered. These reflect mainly the effects of the changed layer thickness. For each observatory an individual Green's function should be considered. The thickness of the 'sediments' related to the observatory sites varies in the range of about 5 km, but also important is the crust thickness.

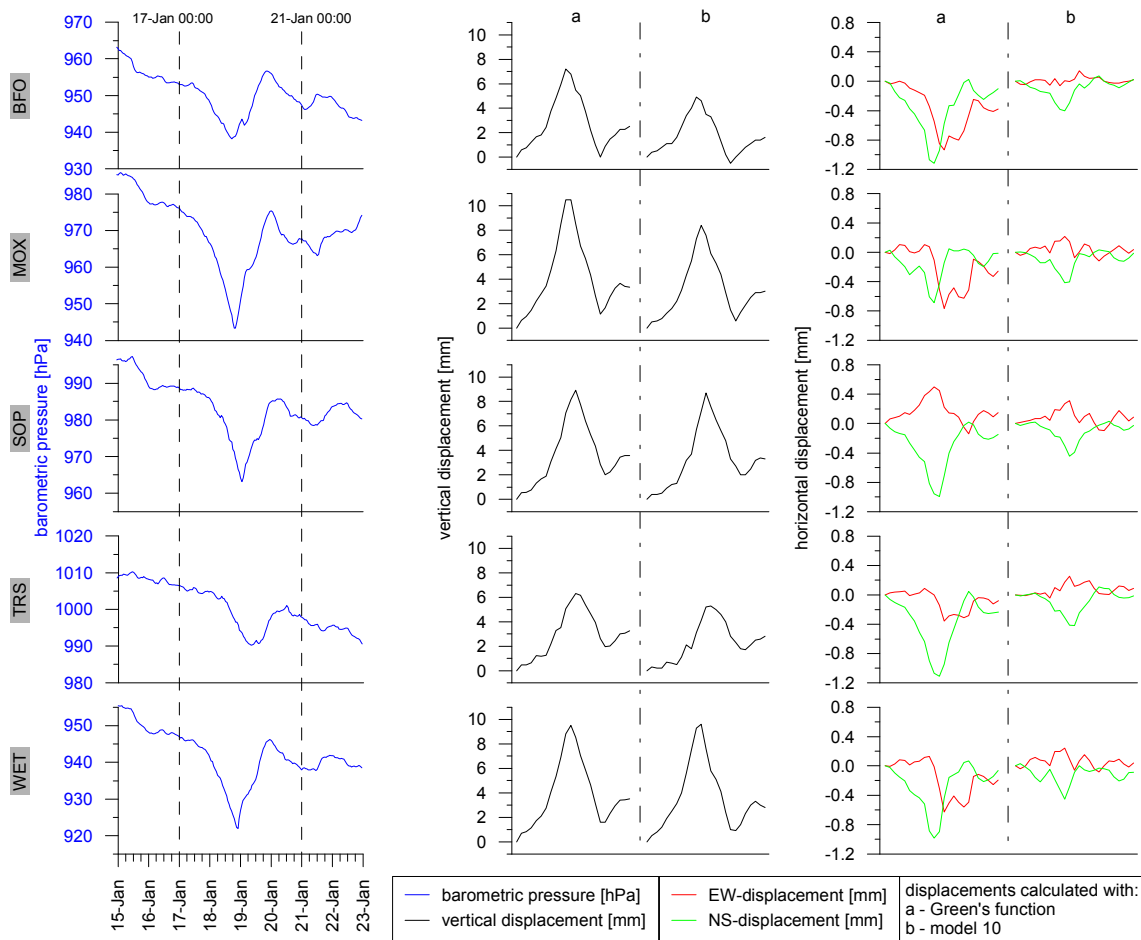


Fig. 7.14: Comparison of the displacements calculated with Green's function and model 10 for the 'Kyrril' event.

The horizontal components calculated with the Green's function lead to larger signals than for the FE models. This is probably caused by the different conditions of the FE models and the Green's functions. For the analytical calculation the whole Earth is considered, but only the area of interest is loaded by barometric pressure. It follows that boundaries, as found in the FE models, are not existent and displacements are not restricted at the border of the area of interest. Based on that, only the time-dependent

7 Investigation of deformations related to Central Europe

behavior for the horizontal displacement from FE modeling and Green's function is comparable.

The displacements for the barometric pressure field of 'Kyrill' at January 16th 20:00 CET (Fig. 7.15d) shows Fig. 7.15a calculated for model 5. On the interest of deformation only the relative changes of an observatory site are important and not the regional distribution, following a constant value can be subtracted. In this case a complete deformation field, this is calculated by the uniform barometric pressure load (Fig. 7.15b). The difference vertical displacements to the barometric pressure load of 'Kyrill' yields a value of 0.998 (Fig. 7.15c) Thus topographic and geologic features do not affect significantly the deformation, which is again confirmed.

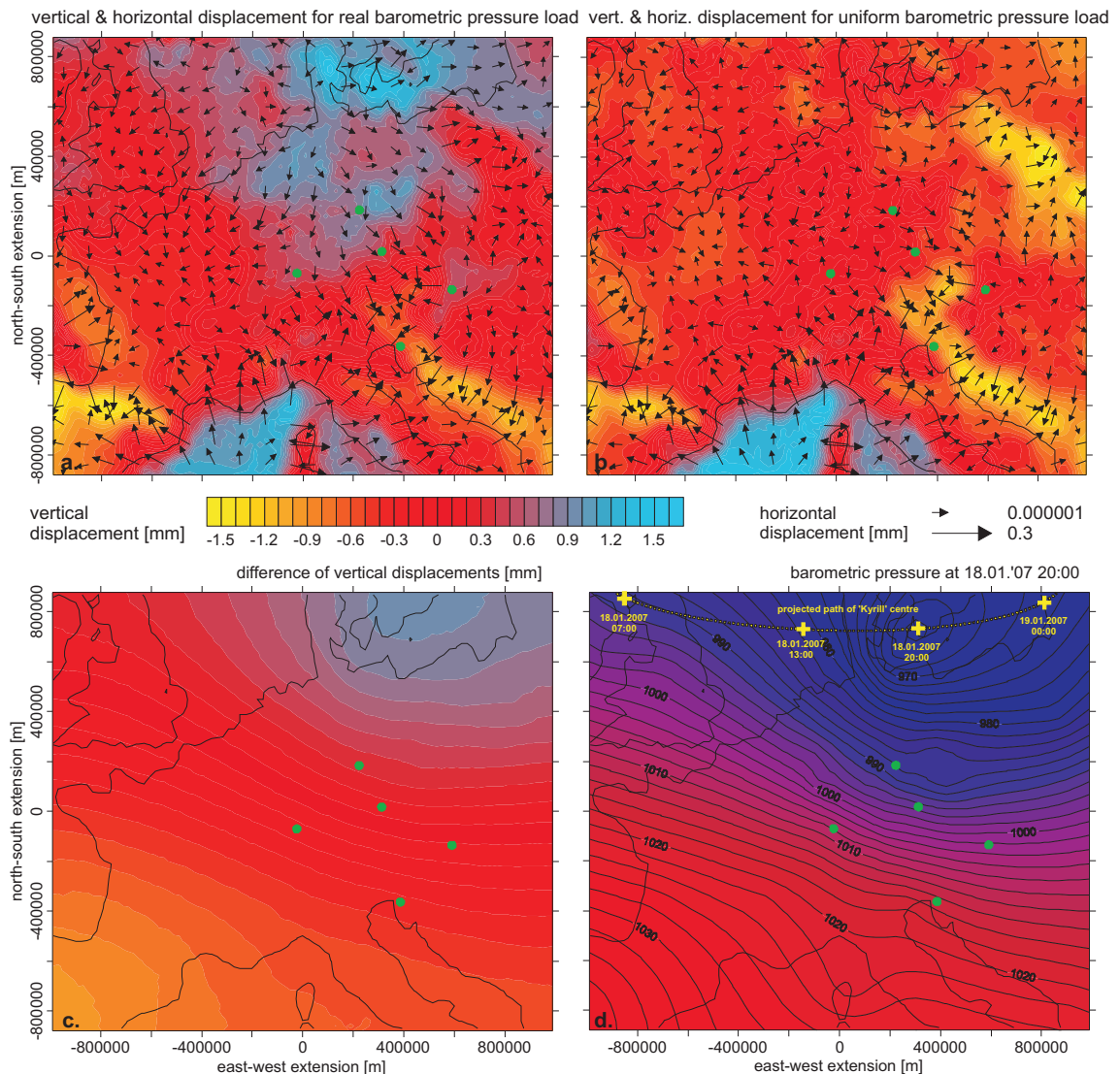


Fig. 7.15: Comparison of the deformations for an actual barometric pressure field (d): 'Kyrill' event at January 16th 20:00 CET (a) and uniform barometric pressure change of 1 hPa (b). (c) the difference of the vertical displacements (a)-(b).

For January 2007 the gravity residuals from the superconducting gravimeter CD 034 (Jahr et al., 2001; Kroner et al., 2004) are used to compare observed and modeled deformations (Fig. 7.16). The time series is cleaned from earthquakes and detided (Fig. 7.16a). For the reduction of the atmospheric attraction a 3d atmospheric reduction with a sample rate of 6 hours is used (pers. comm. Kroner, 2009; also cf. Abe et al. 2009), which is then interpolated to hourly values (Fig. 7.16b). Additionally, the local hydrological effect (Fig. 7.16b) is reduced (Naujoks, 2008). Dividing the resulting gravity variations (Fig. 7.16c) by the free air gradient ($-3086 \text{ nm/s}^2/\text{m}$) results in vertical displacements, which are compared with vertical displacements modeled with Green's functions and with results of the FE models 4 and 10 (Fig. 7.16d, e).

The vertical displacements using the Green's function is calculated for the 6-hourly meteorological data and with the 1 h pressure field samples used in this study (comp. chapter 7.2). The deformations related to the 6 hour data show larger amplitudes than for the 1 h ones. Additionally, the latter mentioned deformations correlate better to the observed vertical displacements. The results of the model 4 are again about 20% lower than for the Green's function, as found for the deformations related to the barometric pressure cap (comp. Fig. 7.10, and Fig. 7.11). The vertical displacements calculated from model 10 (comp. Tab. 7.1) correlate very well to the results of the Green's function, for identical barometric pressure fields.

Finally, the results show once again the importance of a sufficient spatiotemporal resolution of the barometric pressure field.

In addition, the tilt at the Geodetic Observatory Wettzell is studied for the barometric pressure scenario of the storm 'Kyrill'. For this, the detided records of the ASKANIA borehole tiltmeter are used for comparison with modeled tilts of the model 10 and Green's functions (Fig. 7.17). For the comparison only the NS-component is used. The negative sign of the tilt amplitude of the NS-component corresponds to a southward moving tip of the tiltmeter. The EW-component shows no signal for model 10 because of the nearly EW running isobars (comp. Fig. 7.3b) which produce no significant signal for the EW deformation components.

7 Investigation of deformations related to Central Europe

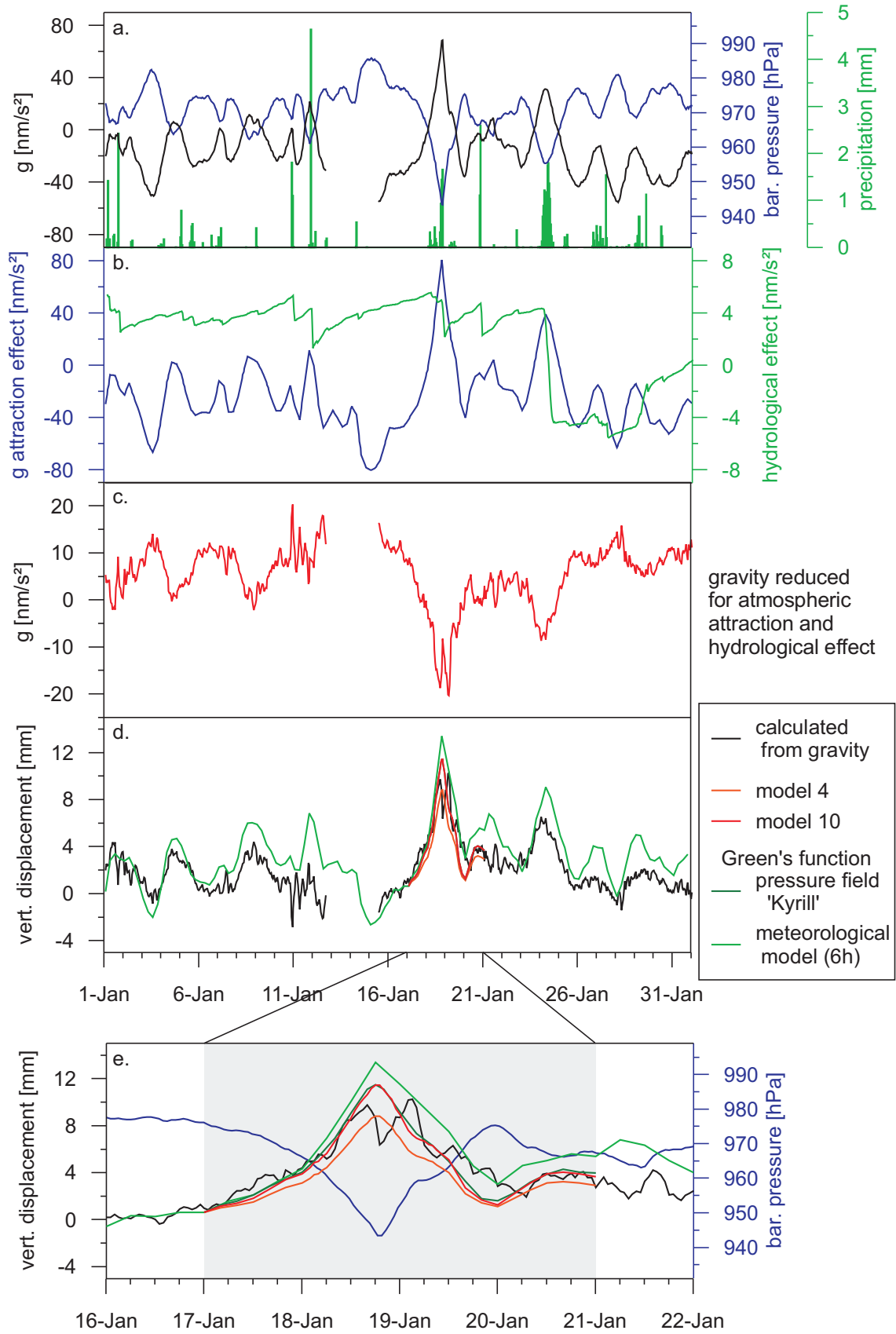


Fig. 7.16: Modeled and observed vertical displacements from the superconducting gravimeter CD034 at MOX.

7 Investigation of deformations related to Central Europe

The amplitudes of the tilts for the models are multiplied by a factor 10 for better comparison. The amplitudes during the investigated time window have maximum values of 0.95 nrad for model 10 and about 1.05 nrad for the Green's function from Jentzsch (1997). This results in a maximum difference between the modeled tilts amplitudes of about 9%. The observed NS-tilt is about 27 times bigger than the modeled are. Regarding this result and the one obtained for the barometric pressure cap (comp. Fig. 7.12) the conclusion is drawn that the tilt and strain amplitudes are mainly caused by the local surroundings (topography, geology), and regional impacts are negligible.

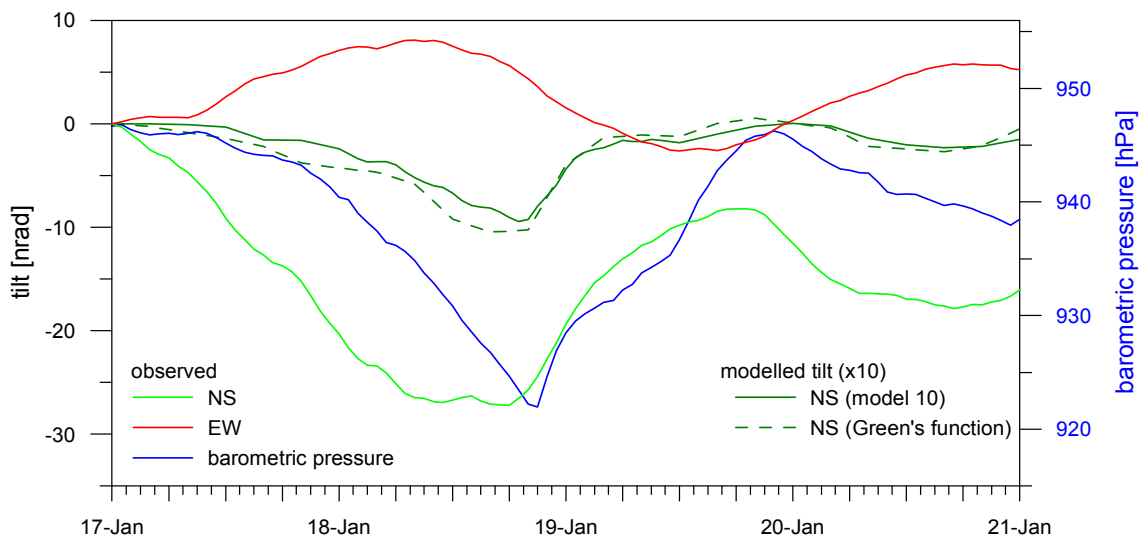


Fig. 7.17: Observed tilt variations at the observatory site WET compared with modeled tilt changes (amplitudes multiplied by factor 10) using the model 10 and Green's function, and barometric pressure in the time window.

7.4 Discussion

The previous FE investigations have shown that significant effects on deformations by the topography and lateral inhomogeneities do not exist on regional scale. The barometric pressure field dominantly controls the deformations with an estimated impact of about 99.8% (comp. Fig. 7.16). It follows that for a general improvement of reductions the spatiotemporal resolution of the loads needs to be enhanced.

8 Discussion, Conclusions and Outlook

For all investigated impact factors the topography, lithology, and fault significant deformations are found. The main results of the principle study and the investigations related to existing observatories can be summarized in the following: Each factor in the vicinity of the observation site has to be considered in the deformation analysis. Furthermore, each deformation component needs to be investigated separately. The dominant effect is found in components oriented perpendicularly to the impact factor.

For the regional deformation investigation no significant effects caused by the topography and geology are found. The amplitudes agree well with observations and modeled deformations based on Green's function.

Box models:

From the study based on the box models follows that the effects are predominantly in an observable order of magnitude. The smallest effects come from the cavity effect, followed by effects of the topography and geological features (lithology, faults). Depending on the parameters, the impact of the lithology can be five times larger than topographic effects, in which the largest deformation occurs for very low Young's modulus and Poisson ratio e.g. for certain types of sandstone (Tab. 5.2). Observatories are mostly located in consolidated bedrock with bigger values for the Young's modulus e.g. observatory Moxa: 76.23 GPa (Kroner et al. 2005), so that this lithologic effect generally plays a minor role compared to the topographic effect.

With regard to the cavity effect, decreasing strain amplitudes are found for increasing coverage, in the order of magnitude of up to 2% per 10 m, assuming a parameterization according to PREM. For the passage of high pressure areas (1 hPa), maximum effects of 0.5 nstrain are obtained for the strain components and about 2.5 nrad for the tilt. Harrison (1976) has already shown that short strainmeters are more strongly affected by the cavity effect than instruments with a longer baseline. The present studies indicate an increase by a factor of up to 100 using a model containing topography. This factor was determined for the 2 m long strainmeter located at the gallery head, compared to the 30 m long strainmeter oriented perpendicularly to the gallery.

From the investigation regarding topographic effects, a clear relation emerges between these effects and the slope angle, as well as the height of the slope. The defor-

mation amplitudes for components parallel to the gallery increase mostly with steepness and height of the slope due to the additional horizontal force caused by the barometric pressure load. The deformations related to the topography are in the order of magnitude of about 2 nstrain for the strainmeter and about 2 nrad for tiltmeters for a 1 hPa uniform barometric pressure load. For an increasing gallery length the amplitudes reduce when the slope angle and height remain fixed.

For geological features such as different adjacent lithological units, or a fault in the vicinity of an instrument site, it can be summarized: Deformation components oriented perpendicularly to the geological features show enhanced or reduced amplitudes depending on the barometric pressure distribution. The maximum deformation amplitudes are of about 7 nstrain for the strainmeter and of about 2 nrad for the tiltmeter for uniform barometric pressure change of 1 hPa.

Related to moving high pressure areas increased deformations especially at the location of the largest pressure gradients often occur for all investigated effects.

Summarizing the main results:

- effects related to topography are approximately one order of magnitude bigger than the pure cavity effect,
- the largest deformation amplitudes are always found for the components oriented perpendicularly to the topography; the difference in the effects is about one order of magnitude,
- compared to a slope situation, a valley can amplify these amplitudes by a factor of two, and
- the main part of the disturbances related to the observatory environments have their origin in the near vicinity, less than 100 m from an observation site.

Observatory sites:

Changes in the barometric pressure load due to the passing high or low pressure areas induce significant effects in observations of different instruments installed at observatories. These effects are clearly modified by the nearby topography and the cavity effect. The surrounding rock affects the results due to its material parameters. Differences are mainly related to the Young's modulus [Kroner et al. \(2005\)](#).

It turns out, that tributary valleys such as in the surroundings of the BFO can increase or decrease the signal depending on the moving direction of high pressure areas, the slope angle of the valley and also the distance of the instrument to the surface and to the mountain ridge. The contribution of the cavity effect in the observations de-

depends on the location of the instrument in a gallery or a chamber, e.g. the distance to a wall or the placement on a pier. The value is controlled by the shape and geometry of the gallery and/or the pier. Separating the cavity effect from the topographic effect is difficult as both commonly interact in a complex manner. Nevertheless, from the present study follows that if the deformation component is oriented perpendicularly to the barometric pressure front, the topographic effect clearly dominates. For aligned components both effects are comparable.

Since the work of [Harrison \(1976\)](#) it is known that the cavity effect acts mainly near-by the walls of the instrument chamber and is minimized at the centre of the chamber. [Steffen \(2006\)](#) has investigated this effect for the BFO. This study confirms his results and also demonstrates the importance of its understanding for other observatories.

The moving direction of a high pressure area is important whether the instruments component is aligned to it, especially in the case of small topographic changes and cavity effects. Deformations due to a NE-SW moving high pressure area, and likewise other directions, can be explained by combining the main effects of the EW and NS moving high pressure area, as above mentioned.

It is also clearly demonstrated that prominent peaks occur in each component at each observatory when the front of a pressure area crosses the instrument site. Here, the gradient of the high or low pressure area and the pressure distribution in near distance are the main sources of the peaks. At least 2 nrad/hPa and 0.2 nstrain/hPa can be deduced from the FE analysis in the case of such an event.

In general, the transfer mechanisms found explain the observations at each observatory of this study. The first comparison to the strainmeter in SOP is already promising to retrieve an adequate reduction algorithm for each observatory. For other multi-sensor observatories the findings can be used to explain and likewise predict deformations. Complex features in topography, gallery, and geological features respectively, have to be investigated separately. Nevertheless, general recommendations for reductions of barometric pressure induced changes in observations that have been drawn by [Kroner et al. \(2005\)](#), [Steffen \(2006\)](#) and [Steffen et al. \(2006\)](#) are supported by the findings of this study. Most important, each deformation component at each observations site requires its individual reduction. For a really effective reduction detailed spatial resolutions of the loads are necessary.

The suggestions given by [Kroner et al. \(2005\)](#), [Steffen \(2006\)](#), [Steffen et al. \(2006\)](#) to reduce a priori disturbing effects in data of horizontal strain-, tilt-, and seismometer

components are confirmed as extended in the present investigations (chapter 5) and Gebauer et al. (2009) for future observation sites, with the essential aspects:

- a simple topography should be preferred,
- a large coverage, at minimum approximately 150 m, should exist above the gallery,
- a simple straight geometry of the gallery should be considered,
- the gallery should be long (about 150 m) with instrumentation sites as far away as possible from topographic changes,
- as already known from Harrison (1976), the instruments should be installed symmetrically and as far away as possible from the gallery walls.

Central Europe:

The general aim of this special study was to investigate the effects of topographic and geologic features on deformations on regional scales. For this different models were developed (chapter 7.1) and loaded by various barometric pressure scenarios (chapter 7.2). Significant differences in the deformation components due to topography and lateral inhomogeneities are not found. The present results show that 99.8% of the observed large-scale deformations stem from the barometric pressure field (Fig. 7.15). This leads to the conclusion that for effective reductions the spatial and temporal resolution of the barometric pressure field and any other loads respectively needs to be substantially increased.

From a comparison between displacements calculated from FE models (model 10) and Green's function good agreements are found for the vertical displacements at the observatories. A further comparison between FE modeled (model 10), Green's function and observed vertical displacements for the case example of MOX a very good correlation emerged (Fig. 7.16). For the regional horizontal deformations, especially for strain and tilt, show a good agreement between the FE model and Green's function (Fig. 7.17). The order of magnitude is presently below the detection level and can be neglected as disturbing signal.

References

- Abaqus Inc. (2007): ABAQUS Documentation, Version 6.7.
- Abe, M., Kroner, C., Neumeyer, J., Chen, X. D. (2009): Assessment of atmospheric reductions for terrestrial gravity observations. *Geophys. J. Int.*, submitted.
- Agnew, D. C. (1986): Strainmeters and tiltmeters, *Rev. Geophys.*, 24/3, 579-624.
- Agnew, D. C. (1987): The continuous measurement of crustal deformation, *Methods in Experimental Physics*, 24B.
- Altair Engineering, Inc. (2008): www.altair.com.
- Amelung, F. & Wolf, D. (1994): Viscoelastic perturbations of the earth: significance of the incremental gravitational force in models of glacial isostasy, *Geophys. J. Int.*, 117, 864-879
- Angenheister, G. (1982): *Physical Properties of Rock: Subvolume A.- Landold-Börnstein Group V Geophysics*, Springer Verlag Berlin Heidelberg, 371 p.
- Asch, G., Jahr, T., Jentzsch, G., Kiviniemi, A., Kääriäinen, J. (1987): Measurement of gravity tides along the 'Blue Road Geotraverse' in Fennoscandia, *Publ. Finnish Geodetic Inst.*, 107, 57 p.
- Askania (1968): Bohrloch-Gezeitenpendel Gbp1 – Betriebsanleitung, Askania-Werke, Berlin (unpublished).
- Barbour, A., Agnew, D. C. (2008): Characterizing noise levels on the PBO borehole seismometers and strainmeters. American Geophysical Union, Fall Meeting 2008, abstract #G21B-0695.
- Beauduin, R., Lognonné, P., Montagner, J. P., Cacho, S., Karczewski, J. F., Morand, M. (1996): The effects of the atmospheric pressure changes on seismic signals or how to improve the quality of a station, *Bull. Seism. Soc. Am.* 86 (6), 1760-1769.
- Beavan, J. & Bilham, R. (1977): Thermally induced errors in fluid tube tiltmeters, *J. Geophys. Res.*, 82, 5699–5704.
- Berckhemer H., J. Zschau, O. Ergünay (1991): The Turkish-German project for earthquake prediction research in NW-Anatolia, a multidisciplinary approach to study the stress field, *Scientific-Technical Contributions to the International Conference on Earthquake Prediction: State-of-the-Art*, Strasbourg, 15-18, 459-476.
- Berckhemer, H. (1991): *Grundlagen der Geophysik*, Wissenschaftliche Buchgesellschaft, Darmstadt, 201 p.
- Berger, J., & Lovberg, R. H. (1969): A laser earth strain meter, *Rev. Sci. Instr.*, 40, 1569-1575.
- Berger, J. & Lovberg, R. H. (1970): Earth strain measurements with a laser interferometer, *Science*, 170, 296–303.
- Bird, P. & Kong, X. (1994): Computer simulations of California tectonics confirm very low strength of major faults. *GSA*, 106(2), 159-174. doi: 10.1130/0016-7606(1994)106<0159:CSOCTC>2.3.CO;2.
- Bonatz, M., Bonn, C., Gerstenecker, C., Kistermann, R., Zschau J. (1983): Tilt measurements across a deep fault zone, *Proc. 9th Int. Symp. Earth Tides*, New York, 695-702.
- Borsa, A. A., Meertens, C., Jackson, M. (2008): Noise characteristics of short drilled and deep drilled braced monuments in the PBO continuous GPS network. American Geophysical Union, Fall Meeting 2008, abstract #G41B-0626.
- Bormann, P. (2002): *New manual of seismological observatory practice (NMSOP) / Volume 1&2*. GeoForschungsZentrum Potsdam, ISBN 3-9808780-0-7.
- Boudin, F., Bernard, P., Longuevergne, L., Florsch, N., Larmat, C., Courteille, C., Blum, P.-A., Vincent, T., and Kammentaler, M. (2008): A silica long base tiltmeter with high stability and resolution: *Rev. Sci. Instrum.*, 79, 034502.
- Braitenberg, C., Romeo, G., Tacceti, Q., Nagy, I. (2006): The very-broad-band long-base tiltmeters of Grotta Gigante (Trieste, Italy): Secular term tilting and the great Sumatra-Andaman islands earthquake of December 26, *J. Geodyn.*, 41, 164-174.

References

- Bodenseewerk Geosystem, Borehole tiltmeter Gpb 10, Tech. Bull. 19, Überlingen, Federal Republic of Germany, 1978.
- Brimich, L., Kohút, I., Kostecký, P. (1998): Influence of the cavity effect on tidal measurements, Proc. 13th Int. Symp. on Earth Tides, Brussels. ed. by B. Ducarme, P. Pâquet, 397-412.
- Byerlee, J. D. (1978) Friction of rocks. *Pageoph*, 116, Birkhauser Verlag.
- Chéry, J., Zoback, M. D., Hassani, R. (2001): An integrated mechanical model of the San Andreas fault in central and northern California, *J. Geophys. Res.*, 106(B10), 22051–22066.
- Chéry, J., Zoback, M. D., Hickman, S. (2004): A mechanical model of the San Andreas fault and SAFOD Pilot Hole stress measurements, *Geophys. Res. Lett.*, 31, L15S13, doi:10.1029/2004GL019521.
- Crossley, D., Hinderer, J., Casula, G., Francis, O., Hsu, H. T., Imanishi, Y., Jentzsch, G., Kääriäinen, J., Merriam, J., Meurers, B., Neumeyer, J., Richter, B., Shibuya, K., Sato, T., Van Dam, T. (1999). Network of superconducting gravimeters benefits a number of disciplines, *EOS*, 80, 11, 121, 125-126.
- d'Oreye, N. F. & Zürn, W. (2005): Very high resolution long-baseline water-tube tiltmeter to record small signals from Earth free oscillations up to secular tilts. *Rev. Sci. Instrum.* 76, 024501, p. 12, doi:10.1063/1.1844451.
- Dal Moro G. & Zadro, M. (1998): Subsurface deformations induced by rainfall and atmospheric pressure: tilt/strain measurements in the NE-Italy seismic area, *Earth and Planetary Science Letters*, 164, 193-203.
- Dziewonski, A. M. & Anderson, D. L. (1981): Preliminary reference Earth model, *Phys. Earth Planet. Inter.*, 25, 297-356.
- Emter, D. & Zürn, W., (1985): Observations of local elastic effects on earth tide tilts and strains, *Earth Tides*, ed. by J.C. Harrison, Van Nostrans-Reinhold, New York, 309-327.
- Emter, D., Wenzel, H.-G., Zürn, W. (1999): Das Observatorium Schiltach, *DGG-Mitteilungen*, 3/1999, 2-15.
- Exß, J. & Zürn, W. (2002): Reduction of noise in horizontal long period seismograms using local atmospheric pressure, *Bull. d'Inf. Marées Terr.*, 137, 10887-10892.
- Fabian, M. (2004): Near surface tilt und pore pressure changes induced by pumping in multi-layered poroelastic half-spaces. PhD-thesis, department geosciences, Friedrichs-Wilhelm-Universität Bonn, No. 229, 121 p.
- Farrell, W.E. (1972): Deformation of the earth by surface loads, *Rev. Geophys. Space Phys.*, 10, 761-797.
- Fischer, K. (2002): Sources and transfer mechanism of seismic noise: Finite-element modeling, *Bull. d'Inf. Marées Terr.*, 137, 10881-10886.
- Fleming, K., Martinec, Z., Wolf, D. (2003): A reinterpretation of the Fennoscandian relaxation-time spectrum for a viscoelastic lithosphere. In: I. N. E. Tziavos, editor, *Gravity and Geoid 2002*, 3rd Meeting of the International Gravity and Geoid Commission, 432-438, Ziti Pub., Thessaloniki.
- Fortak, H. (1971): *Meteorologie*. Berlin und Darmstadt: Carl Habel Verlagsbuchhandlung, p.288.
- Francis O. & Dehant V. (1987): Recomputation of the Green functions for tidal loading estimation. *Bull. d'Inf. Marées Terr.*, 100, 6962-6986.
- Gebauer, A. (2006): Ein Neigungsmesser-Array an der KTB, diploma thesis, Friedrich-Schiller-University Jena, 183 p. (unpublished).
- Gebauer, A., Jahr, Th., Jentzsch, G. (2007): Recording and interpretation/analyses of tilt signals with five ASKANIA borehole tiltmeters at the KTB, *Rev. Sci. Instrum.* 78, 054501, 6p. doi:10.1063/1.2736506.
- Gebauer, A., Kroner, C., Jahr, T. (2009): The influence of topographic and lithologic features on horizontal deformations, *Geophys. J. Int.*, in press, doi:10.1111/j.1365-246X.2009.04072.x.
- Gladwin, M. T. (1984): High precision multi-component borehole deformation monitoring *Rev. Sci. Instrum.*, 55, 2011–2016.
- Gladwin, M. T. & Hart, R. (1985): Design parameters for borehole strain instrumentation, *Pure Appl. Geophys.*, 123, 59-80.

References

- Guo, J. Y., Li, Y. B., Huang, Y., Deng, H. T., Xu, S. Q. & Ning, J. S. (2004): Green's function of the deformation of the Earth as a result of atmospheric loading. *Geophys. J. Int.* 159 (1), 53-68. doi: 10.1111/j.1365-246X.2004.02410.x.
- Gomez, M., Jentzsch, G., Ramatschi, M. and D. Flach (1995): ASKANIA-borehole-tiltmeters: Test of nine different instruments regarding the orthogonality of both channels, *Bull. d'Inf. Marées Terr.*, 121, 9076-9082.
- Graf, A. (1964): Erste Neigungsmessungen mit dem Vertikalpendel in einem 30 m Bohrloch. *Comm. Obs. Roy. Bel.*, 236, Ser. Geophys. Nr. 69, 5ieme Symp. Int. sur la marées terrestres, Brüssel, 249-254.
- Große-Brauckmann, W. and O. Rosenbach (1979): Resolution and stability of borehole tiltmeters. In: A. Vogel (Ed.): *Terrestrial and space techniques in earthquake prediction research*. Vieweg & Sohn, Braunschweig, 712 p.
- Große-Brauckmann, W. (1979): *Untersuchungen der Bodenunruhe im Periodenbereich von 2 min - 1 h mit dem Askania-Bohrlochneigungsmesser*. PhD-thesis, Techn. Univ. Clausthal, 130 p.
- Harrison, J.C. (1976). Cavity and topographic effects in tilt and strain measurements, *J. Geophys. Res.*, 81, 319-328.
- Harrison, J.C., Herbst, K. (1977): Thermoelastic strains and tilt revisited, *Geophys. Res. Lett.*, 4 (11), 535-537.
- Hart, R. H. G., Gladwin, M. T., Gwyther, R. L., Agnew, D. C., Wyatt, F. K. (1996): Tidal calibration of borehole strainmeters: removing the effects of local inhomogeneity, *J. Geophys. Res.*, 101, 25553-25571.
- Hefty, J., & Husar, L (2003): *Satellite Geodesy, Global Positioning System*. Bratislava, STU, 188 p.
- Heidbach, O. and Drewes, H. (2003): 3-D Finite Element model of major tectonic processes in the Eastern Mediterranean. *Geological Society, Special Publication Series*, 212, 261 – 274, doi: 10.1144/GSL.SP.2003.212.01.17.
- Hodgkinson, K., Borsa, A., Dittmann, T., Gallaher, W., Gottlieb, M., Henderson, B., Jackson, M., Johnson, W., Mencin, D., Smith, J. (2008): Completion of the PBO borehole strainmeter network: Network results and review of processing techniques. American Geophysical Union, Fall Meeting 2008, abstract #G21B-0688.
- Holton, J. R. (2004): *An Introduction to dynamic meteorology*, 4th Ed., 88, (International Geophysics) Elsevier Academic Press, 535 p.
- Jacoby H.D. (1966): Das neue Borhloch-Gezeitenpendel nach Graf. *Askania Warte*, 67, 12-17.
- Jahr, T., Jentzsch, G., Andersen, N., Remmer, O. (1991): Ocean tidal loading on the shelf areas around Denmark, *Proc. 11th Int. Symp. Earth Tides*, Helsinki, 1989, Schweitzerbart, Stuttgart, 309-319.
- Jahr, T., Jentzsch, G., Kroner, C. (2001): The Geodynamic Observatory Moxa/ Germany: instrumentation and purposes, *J. Geod. Soc. Japan*, 47 (1), 34-39.
- Jahr, T., Jentzsch, G., Letz, H., Sauter, M. (2005): Fluid injection and surface deformation at the KTB location: modeling of expected tilt effects, *Geofluids*, 5 (1), 20-27.
- Jahr, T., Letz, H., Jentzsch, G. (2006a): Monitoring fluid induced deformation of the earth's crust: A large scale experiment at the KTB location/Germany, *J. Geodyn.*, 41 (1-3), 190-197.
- Jahr, T., Letz, H., Jentzsch, G. (2006b): The ASKANIA borehole tiltmeter array at the KTB location / Germany. – *J. Geodyn.*, 41, 190-197.
- Jahr, T., Jentzsch, G., Gebauer, A. (2006c): Observations of fluid induced deformation of the upper crust of the Earth: investigations about the large scale injection experiment at KTB site, Germany, *Bull. d'Inf. Marées Terr.*, 141, 11271-11276.
- Jahr, T., G. Jentzsch, A. Gebauer, and T. Lau (2008): Deformation, seismicity, and fluids: Results of the 2004/2005 water injection experiment at the KTB/Germany, *J. Geophys. Res.*, 113, B11410, doi:10.1029/2008JB005610.
- Jentzsch, G. (1997): Earth tides and ocean tidal loading. in Wilhelm, H., Zürn, W., Wenzel, H.-G. (Eds.). *Lecture Notes in Earth Science: Tidal Phenomena*. Springer Verlag, 145-167.
- Jentzsch, G. & Koß, S. (1997): Interpretation of long-period tilt records at Blå Sjø, Southern Norway, with respect to the variations in the lake level, *Phys. Chem. Earth*, 22 (1), 25-31.

References

- Jentzsch, G., Knudsen, P., Ramatschi, M. (2000): Ocean tidal loading affecting precise geodetic observations on Greenland: Error account of surface deformations by tidal gravity measurements, *Phys. Chem. Earth (A)*, 25(4), 401-407.
- Jentzsch G., Jahr T., Ishii, H. (2006): News from the Geodynamic Observatory Moxa: the 4-component borehole strainmeter, *Bull. d'Inf. Marées Terr.*, 141, 11245-11252.
- Kaplan, E., Hegarty, C. (2005): *Understanding GPS: Principles and applications*, 2nd edition, ARTECH HOUSE INC, 726 p.
- Klügel, T. (2003): Lokale Einflüsse auf inertielle Erdrotationssensoren, Schlussbericht zum DFG-Forschungsprojekt LOK-ROT. Internal report.
- Kroner, C. & Jentzsch, G. (1999): Comparison of different barometric pressure reductions for gravity data and resulting consequences. *Phys. Earth Planet. Int.*, 115, 205-208.
- Kroner, C. (2001): Hydrological effects on gravity data of the Geodynamic Observatory Moxa. *J. Geod. Soc. Japan*, 47 (1), 353-358.
- Kroner, C., Jahr, T., Jentzsch, G. (2004): Results of 44 months of observations with a superconducting gravimeter at Moxa/Germany, *J. Geodyn.*, 38 (3-5), 263-280, doi:10.1016/j.jog.2004.07.012.
- Kroner, C., Jahr, Th., Kuhlmann, S., Fischer, K. D. (2005): Pressure-induced noise on horizontal seismometer and strainmeter records evaluated by finite element modeling, *Geophys. J. Int.*, 161, 167-178.
- Kümpel, H.-J. (1982): Tilt measurements. What do they tell us? *Terra cognita*, 2, 391-399.
- Kümpel, H.-J. (1988): Gesteinsverformungen durch Porendruckgefälle: Neigungsmessungen in der Umgebung von Brunnen und Interpretation für homogene, poröse, elastische Medien, *Kurzber. aus d. Bauforschung, Ber. Nr. 39*, 145-146.
- Kümpel, H.-J. (1989): Verformungen in der Umgebung von Brunnen. Habilitation thesis. Christian-Albrechts-University Kiel, 198 p.
- Kümpel, H.-J., Varga, P., Lehmann, K., Mentés, G. (1996): Ground tilt induced by pumping – preliminary results from the Nagycenk test site Hungary. *Acta Geod. Geophys Hung.*, 31, (1-2), 67 - 78.
- Lehmann, K. (2001): Porendruckinduzierte Neigungssignale in geringen Tiefen und ihre Modellierung im homogenen Halbraum, PhD-thesis, Friedrichs-Wilhelm-Universität Bonn, Shaker Verlag, 161 p.
- Longuevergne, L., N. Florsch, Elsass, P. (2007): Extracting coherent regional information from local measurements with Karhunen-Loève transform: Case study of an alluvial aquifer (Rhine valley, France and Germany), *Water Resources Research*, 43, W04430.
- Longuevergne, L. (2008): Contribution to hydrogeodesy, PhD-thesis, University Pierre et Marie Curie, Paris, France, 232 p.
- Longuevergne, L., Florsch, N., Boudin, F., Oudin, L., Camerlynck, C. (2008): Coupled mechanical and hydrological modeling of the deformation associated with fractures, *Geophys. J. Int.*, accepted.
- Lüthke, J. (1998): Geologisch-Geotechnischer Bericht zu den Ergebnissen der Erkundung des Untergrundes am Standort des geplanten Ringlasers auf dem Gelände der Fundamentstation Wetzell, Krs. CHAM., unpublished report.
- Melchior, P. (1983): *The tides of the planet earth*, 2nd Edition, Pergamon Press, Oxford, 641 p.
- Mentes, G., Eperné-Pápai, I. (2002): The effect of atmospheric pressure on strain measurement at the Sopron Observatory, Hungary, *Bull. d'Inf. Marées Terr.*, 137, 10901-10906.
- Mentes, G. (2005): Results of tidal research. *Acta Geod. Geoph. Hung.*, 40 (3-4), 293-305.
- Mentes, G. & Eperné-Pápai, I. (2006): Investigation of meteorological effects on strain measurements at two stations in Hungary. *J. Geodyn.*, 41 (1-3), 259-267.
- Merriam, J.B. (1992): Atmospheric pressure and gravity. *Geophys. J. Int.*, 109, 488-500.
- Métivier, L., Greff-Lefftz, M., Diament, M. (2005): A new approach to computing accurate gravity time variations for a realistic earth model with lateral heterogeneities. *Geophys. J. Int.*, 162, 570–574, doi: 10.1111/j.1365-246X.2005.02692.x.
- Morra, G., Regenauer-Lieb, K., Giardini, D. (2006): Curvature of oceanic arcs. *Geology*, 34 (10), 877-880; doi: 10.1130/G22462.1.

References

- Moore, D. E., Lockner, D. A., Summers, R., Shengli, Ma, Byerlee, J. D. (1996): Strength of chrysotile-serpentine gouge under hydrothermal conditions: Can it explain a weak San Andreas fault?, *Geology*, 24 (11), 1041-1044, doi: 10.1130/0091-7613 (1996)024<1041:SOCSGU>2.3.CO;2.
- Naujoks, M. (2008): Hydrological information in gravity: observation and modelling, PhD thesis, Institute of Geosciences, Friedrich-Schiller-University Jena, available online: <http://www.dbthueringen.de/servlets/DerivateServlet/Derivate-16661/Naujoks/Dissertation.pdf>.
- Pagiatakis, S. D (1990): The response of a realistic Earth to ocean tide loading, *Geophys. J. Int.*, 103, 541-560.
- Peters, J. (1978): Tidal measurements using a new long baseline tiltmeter, Institute of Oceanographic Sciences, Birkenhead, Merseyside, England, PhD-thesis, 130 p.
- Rabbell, W. & Zschau, J. (1985): Static deformations and gravity changes at the earth's surface due to atmospheric loading. *J. Geophys.*, 56, 81-99.
- Richter, B., Wenzel, H.G., Zürn, W., Klopping, F. (1995): From Chandler wobble to free oscillations: comparison of cryogenic and other instruments in a wide period range, *Phys. Earth Planet. Inter.*, 91, 131-148.
- Sacks, I. S., Suyehiro, S., Evertson, D. W., Yamagishi, Y. (1971): Sacks-Evertson strainmeter, its installation in Japan and some preliminary results concerning strain steps, *Pap. Meteor. Geophys.*, 22, 195-207.
- SAFOD (2009): http://earthquake.usgs.gov/research/parkfield/safod_pbo.php.
- Sato, T., Harrison, J. C. (1990): Local effects on tidal strain measurements at Esashi, Japan, *Geophys. J. Int.*, 102, 513-526.
- Schlüter, W., Brandl, N., Dassing, R., Hase, H., Klügel, T., Kilger, R., Lauber, P., Neidhardt, A., Plötz, C., Riepl, S. & Schreiber, U. (2007): Fundamentalstation Wettzell – ein geodätisches Observatorium, *Zeitschrift für Vermessungswesen*, 132 (3). 158-167.
- Smith, W. H. F., & Sandwell, D. T. (1997): Global seafloor topography from satellite altimetry and ship depth soundings, *Science*, 277, 1957-1962.
- Schwarz, H. R. (1991): *Methode der finiten Elemente*, B. G. Teubner, Stuttgart, 224 p.
- Scholz, C H. (2000): Evidence for a strong San Andreas fault. *Geology*, 28 (2), 163-166, doi: 10.1130/0091-7613(2000)28<163:EFASSA>2.0.CO;2.
- Seeber, G. (2003): *Satellite Geodesy*, 2nd completely revised and extended edition, Walter de Gruyter Berlin New York, 589 p.
- Silver, P. G., Bock, Y., Agnew, D. C., Henyey, T., Linde, A. T., McEvelly, T. V., Minster, J.-B., Romanowicz, B. A., Sacks, I. S., Smith, R. B., Solomon, S. C., Stein, S. A. (1998): A Plate Boundary Observatory, *IRIS Newsletter*, XVII (2).
- Sorrells, G., G. (1971): A preliminary investigation into the relationship between long-period seismic noise and local fluctuations in the atmospheric pressure field, *Geophys. J. R. astr. Soc.*, 26, 83-98.
- Sorrells, G. G., McDonald, J. A., Der, Z. A., Herrin, E (1971): Earth motion caused by local atmospheric pressure changes, *Geophys. J. R. Astr. Soc.*, 26, 83-98.
- Steffen, H. (2006): The importance of instrument location on barometric pressure induced noise, *Bull. d'Inf. Marées Terr.*, 141, 11293-11302.
- Steffen, H., Kuhlmann, S., Jahr, T., Kroner, C. (2006): Numerical modeling of the barometric pressure-induced noise in horizontal components for the Observatories Moxa and Schiltach, *J. Geodyn.*, 41 (1-3), 242-252.
- Strang, G., Borre, K. (1997): *Linear Algebra, Geodesy, and GPS*, Wellesley-Cambridge Press, 624 p.
- Takahashi, F., Kondo, T., Takahashi, Y. Koyama, Y. (2000): *Very Long Baseline Interferometer*, Ohmsha Ltd., 256 p., ISBN 4-274-9378-8.
- Tesauro, M., Kaban, M. K., Cloetingh, S. A. P. L. (2008): EuCRUST-07: A new reference model for the European crust, *Geophys. Res. Lett.*, 35, L05313, doi:10.1029/2007GL032244.
- Wang, R. (1997): Tidal response of the solid Earth, in Wilhelm, H., Zürn, W., Wenzel, H.-G. (Eds.). *Lecture Notes in Earth Science: Tidal Phenomena*. Springer Verlag, 27-57.

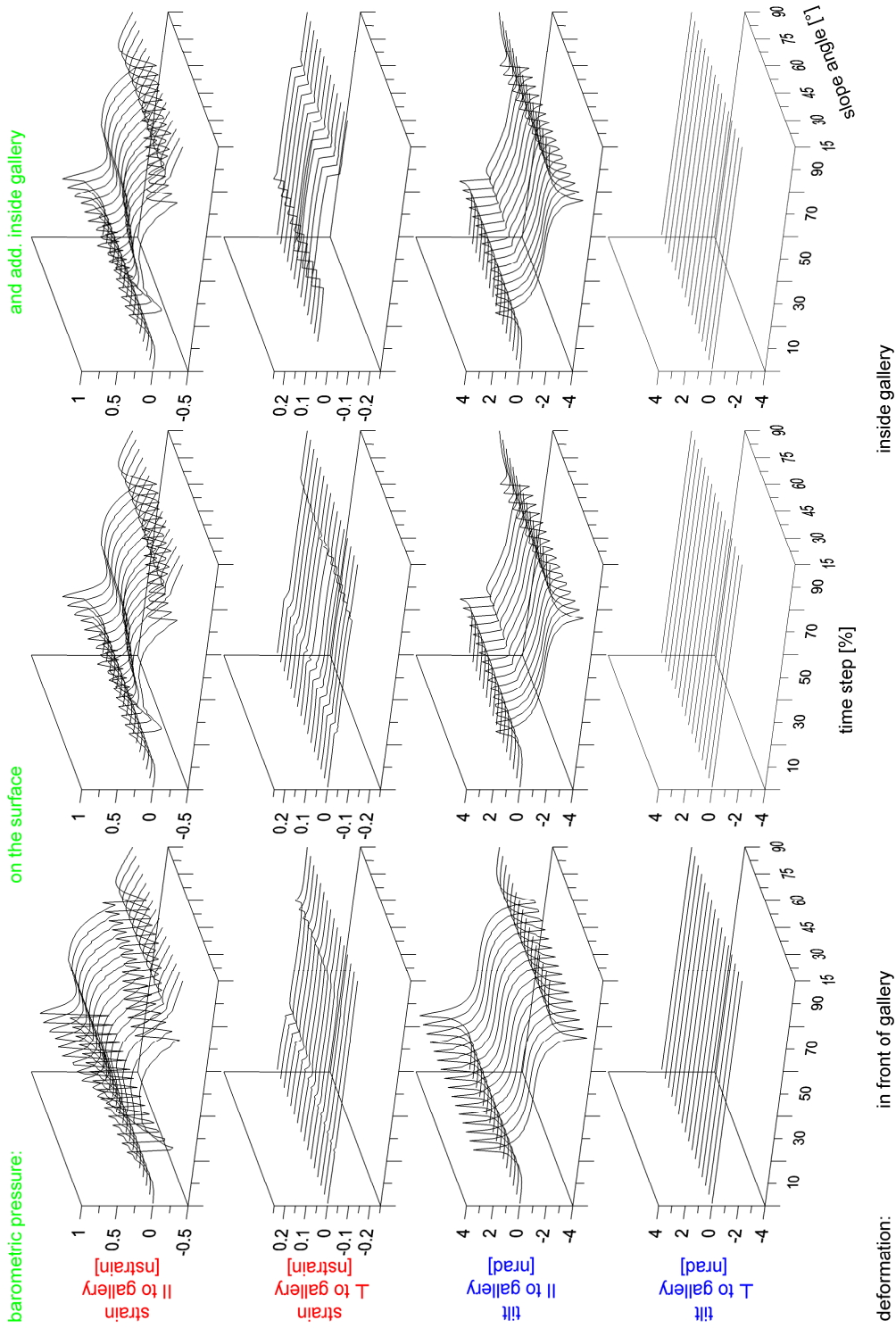
References

- Weise, A. (1991): Groundwater effects on borehole tilt measurements, *Bull. d'Inf. Marées Terr.*, 111, 8073-8085.
- Weise, A. (1992): Neigungsmessungen in der Geodynamik - Ergebnisse von der 3-Komponentenstation Metsähovi. PhD-thesis, Techn. Univ. Clausthal, 180 p.
- Weise, A., G. Jentzsch, A. Kiviniemi and J. Kääriäinen, (1999): Comparison of long-period tilt measurements: results from the two clinometric stations Metsähovi and Lohja, Finland, *J. Geodyn.*, 27, 237-257.
- Westerhaus, M. (1997): Tidal tilt notification along a active fault, *Tidal Phenomena, Lecture Notes in Earth Sciences*, ed. Wilhelm, H., Zürn, W., Wenzel, H.-G., 66, 331-339.
- Wilhelm, H., Zürn, W., Wenzel, H.-G. (1997): *Tidal Phenomena, Lecture notes in Earth sciences*, 66, Springer, 398 p.
- Wolf, D. (1984): The relaxation of spherical and at Maxwell Earth models and effects due to the presence of the lithosphere, *J. Geophys.*, 56, 24-33.
- Wolfe, J. E., Berg, E., Sutton, G. H. (1981): The change in strain comes mainly from the rain. Kipapa, Oahu, *Bull. Seism. Soc. Am.*, 71 (5), 1615-1635.
- Wu, P. & Johnston, P. (1998): Validity of using flat-Earth finite element models in the study of postglacial rebound, in *Dynamics of the Ice Age Earth: A Modern Perspective*, ed. by P. Wu, Trans Tech Publ., Switzerland, 191-202.
- Wu, P., Ni, Z., Kaufmann, G. (1998): Postglacial rebound with lateral heterogeneities: from 2D to 3D modeling. in *Dynamics of the Ice Age Earth: A Modern Perspective*, ed. by P. Wu, Trans Tech Publ., Switzerland, 557-582.
- Wu, P. (2004): Using commercial finite element packages for the study of earth deformations, sea levels and the state of stress, *Geophys. J. Int.*, 158, 401-408.
- Wyatt, F., Beckstrom, K., Berger, J. (1982): The optical anchor - a geophysical strainmeter, *Bull. Seismol. Soc. Am.*, 72, 1707-1715
- Zadro, M., & Breitenberg, C. (1999): Measurements and interpretations of tilt-strain gauges in seismically active areas. *Earth Sci. Rev.*, 47, 151-187.
- Zeumann, S., Weise, A., Jahr, T. (2009): Tidal and non-tidal signals in groundwater boreholes in the KTB area, Germany. in press.
- Zienkiewicz, O. C. (1971): *Methode der finiten Elemente*, VEB Fachbuchverlag Leipzig, 1. Aufl.
- Zienkiewicz, O. C., Taylor, R. L., Zhu, J. Z., Nithiarasu, P. (2005): *The finite element method*, published by Butterworth-Heinemann, ISBN 0750663200, 9780750663205.
- Zoback, M.D. & Healy, J.H. (1984): Friction, faulting, and in situ stress. *Annales Geophysicae*, 2 (6), 689-698. Paris, France: European Geophysical Society, Gauthier-Villars. TIC 234995.
- Zumberge, M. A. & Wyatt, F. K. (1998): Optical fiber interferometers for referencing surface benchmarks to depth, *Pure Appl. Geophys.*, 152, 221-246.
- Zürn, W. & Widmer, R. (1995): On noise reduction in vertical seismic records below 2 mHz using local barometric pressure, *Geophys. Res. Lett.* 22 (24): 3537- 3540.
- Zürn, W. & Neumann, U. (2002): Simplistic models and atmospheric signals in horizontal seismograms, *Bull. d'Inf. Marées Terr.*, 137, 10875-10880.
- Zürn, W., Exß, J., Steffen, H., Kroner, C., Jahr, T., Westerhaus, M. (2007): On reduction of long-period horizontal seismic noise using local barometric pressure, *Geophys. J. Int.*, 171 (2), 780-796.

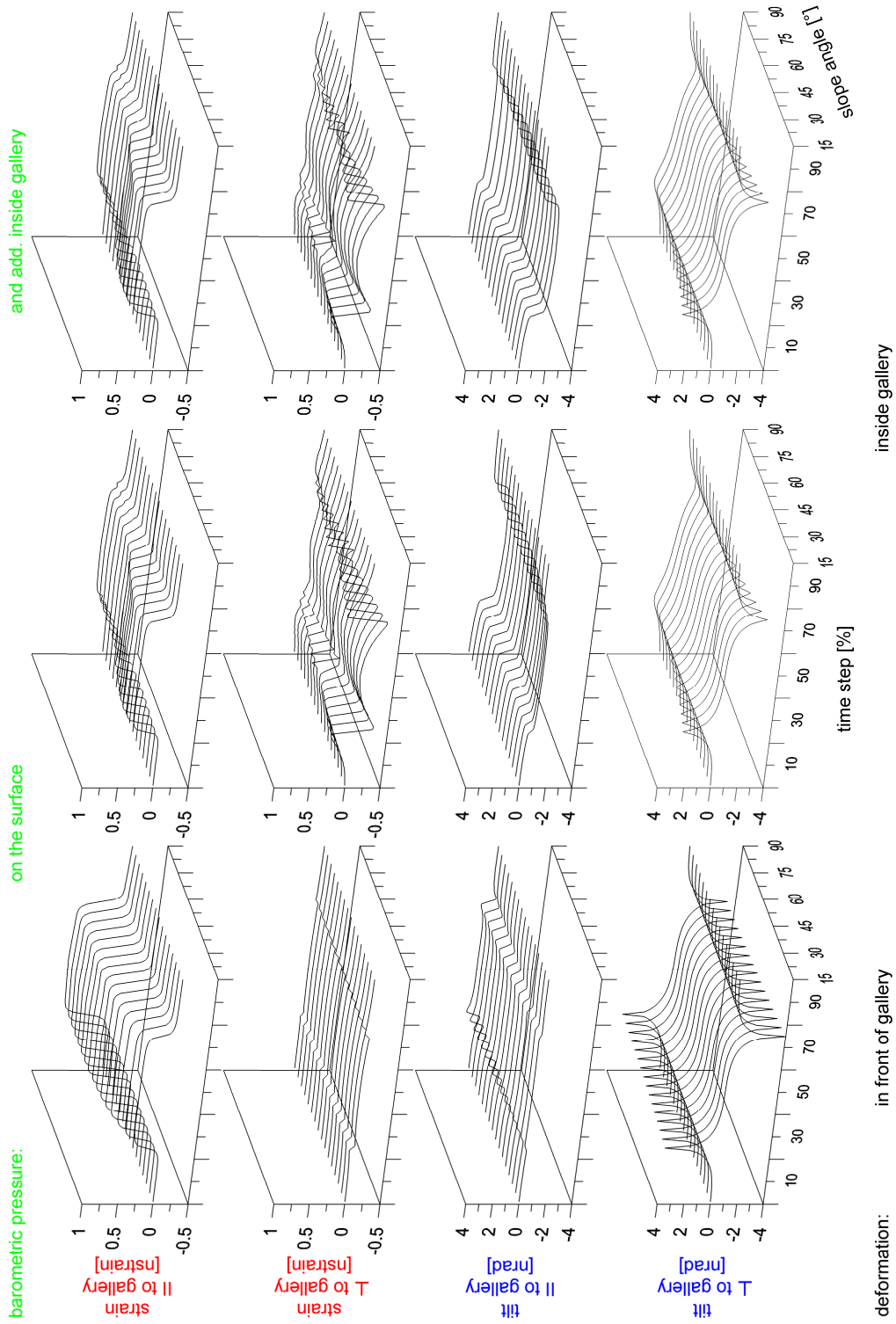
Appendix

Appendix A: Results related to investigations of principle study	136
Appendix B: Barometric pressure grid used in modeling for Central Europe	158

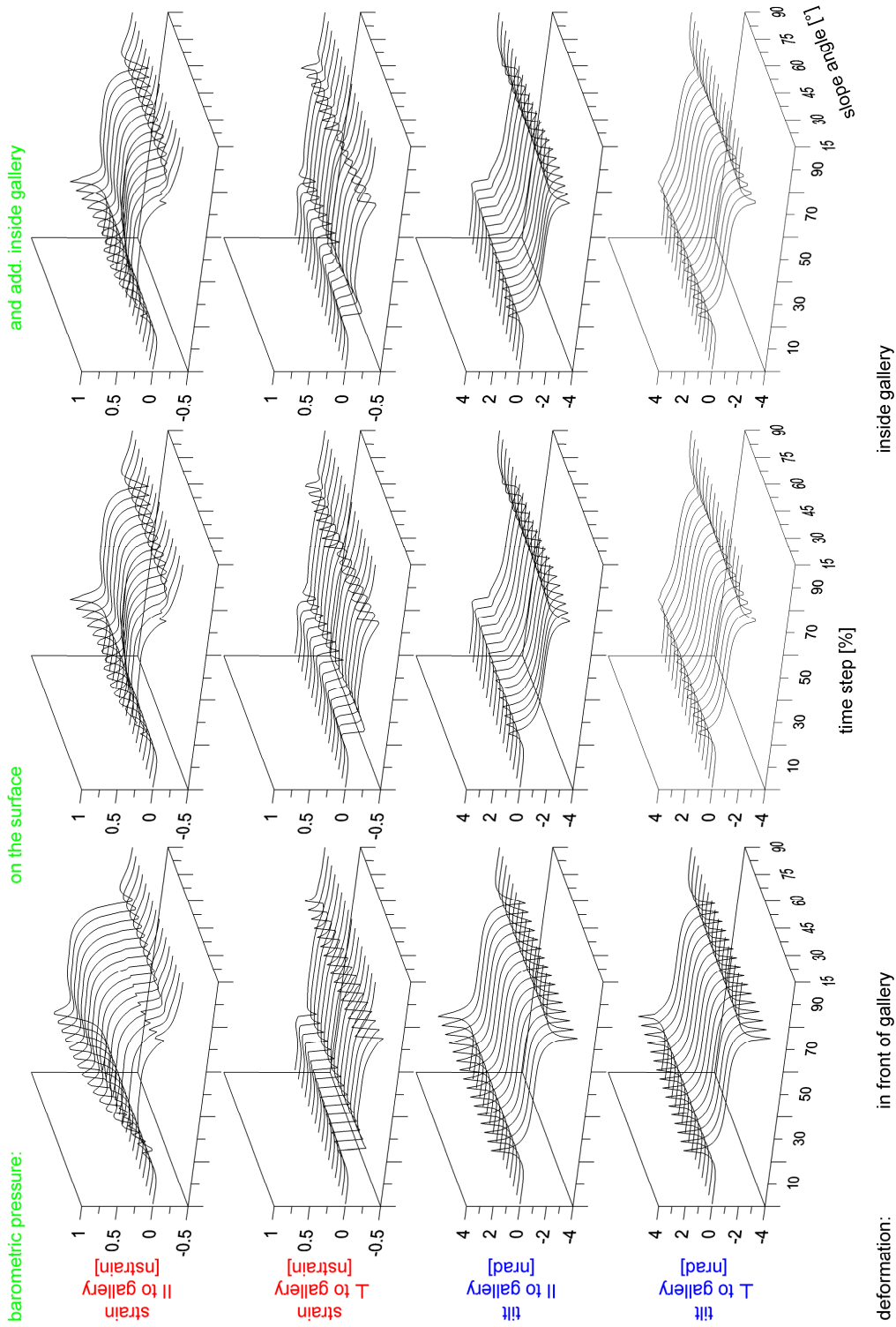
Appendix A: Results related to investigations of principle study



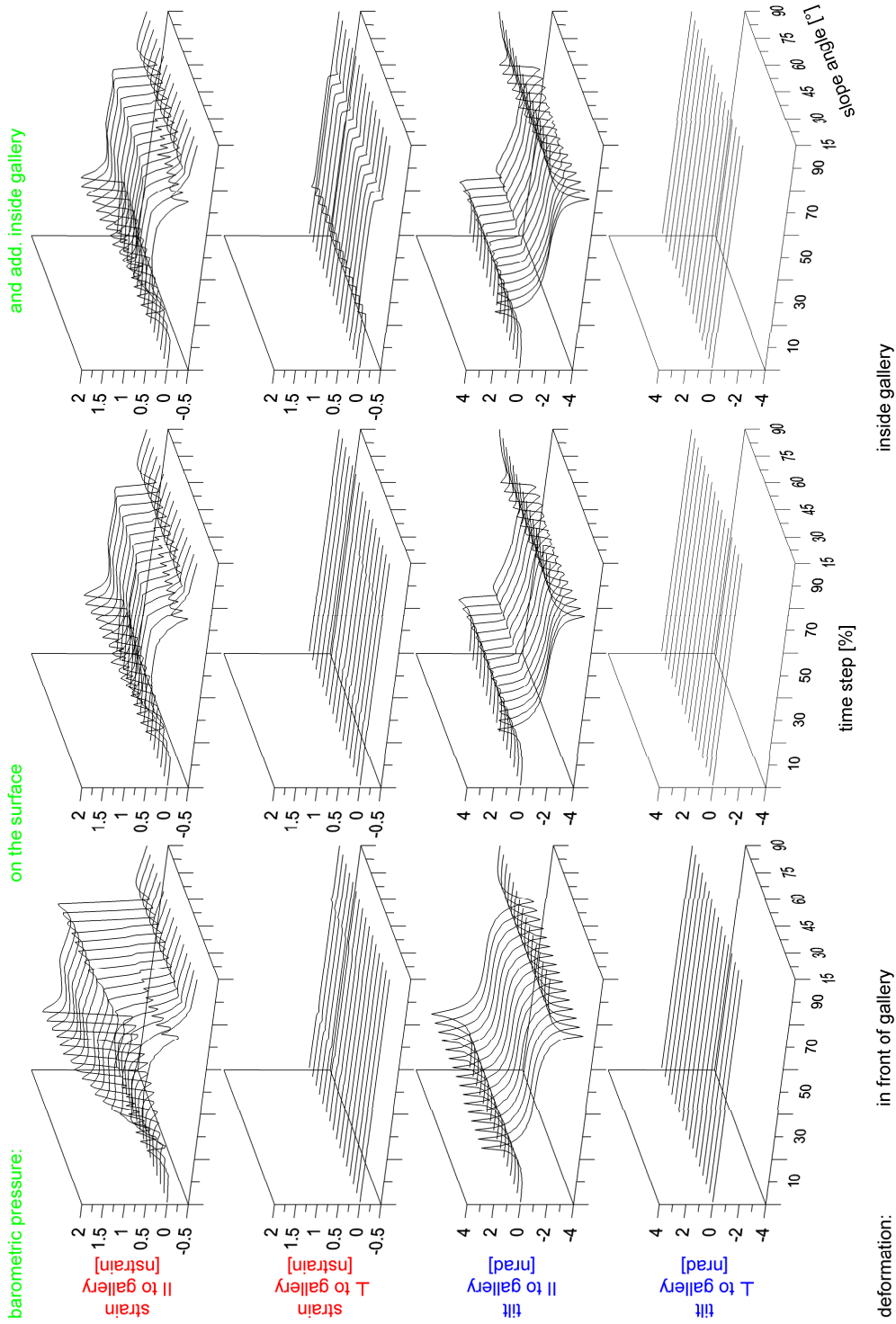
App. Fig. 1: Deformation results for slope model types (slope angle varied between 15° and 90° in 5° step, and 300 m slope height) and gallery type A for the parallel to the gallery moving high pressure area (different scaling).



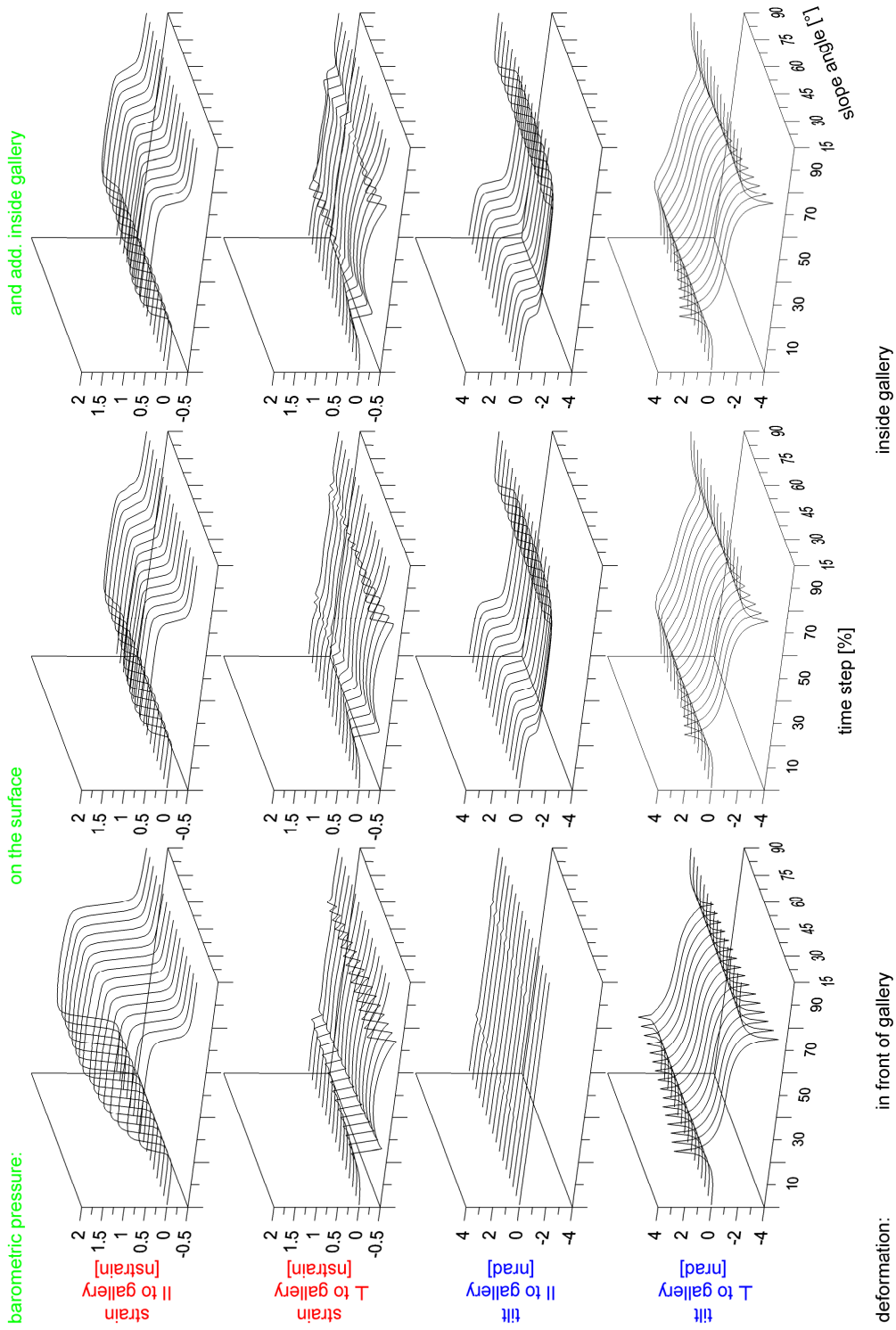
App. Fig. 2: As [App. Fig. 1](#) but for high pressure area moving perpendicularly to gallery.



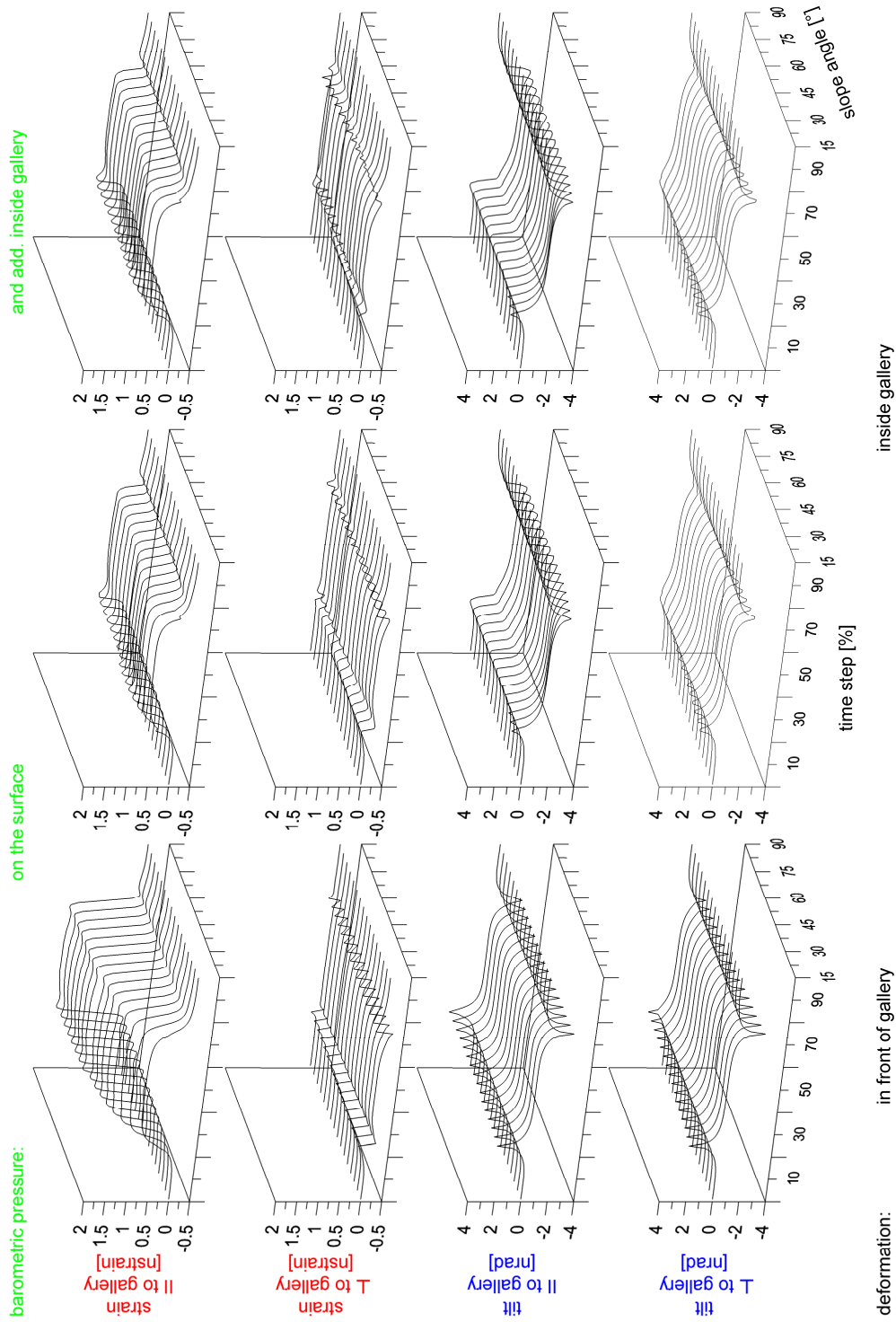
App. Fig. 3 : As [App. Fig. 1](#) but for high pressure area moving diagonally to gallery



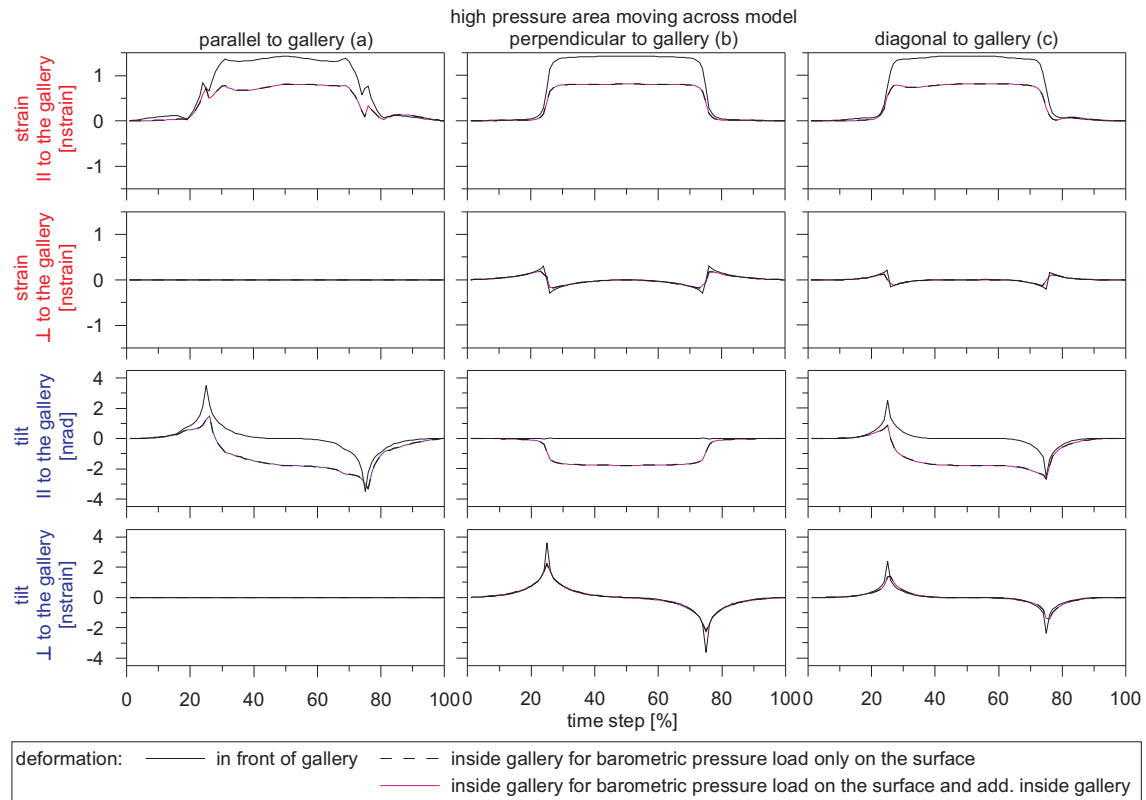
App. Fig. 4: Deformation results for valley model types (slope angle varied between 15° and 90° in 5° step, and 300 m slope height) and gallery type A included for the gallery to the gallery moving high pressure area (different scaling).



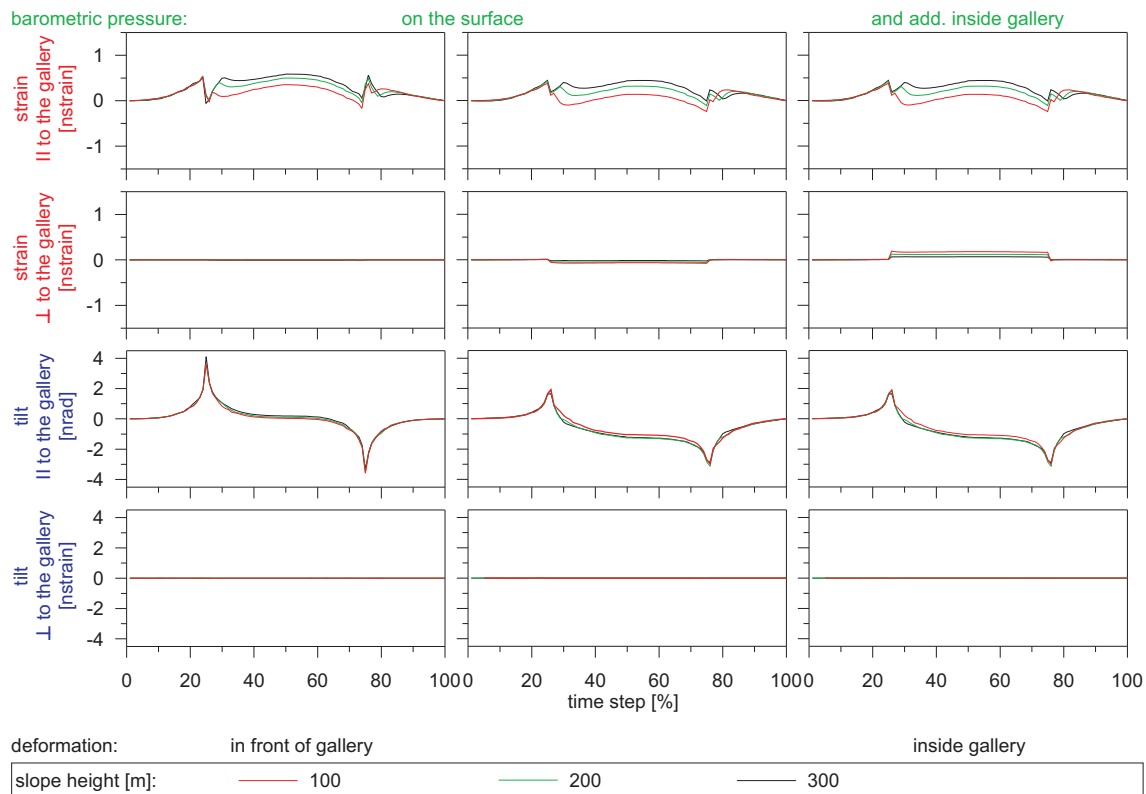
App. Fig. 5: As App. Fig. 4 but for high pressure area moving perpendicularly to gallery.



App. Fig. 6: As App. Fig. 4 but for high pressure area moving diagonally to gallery.

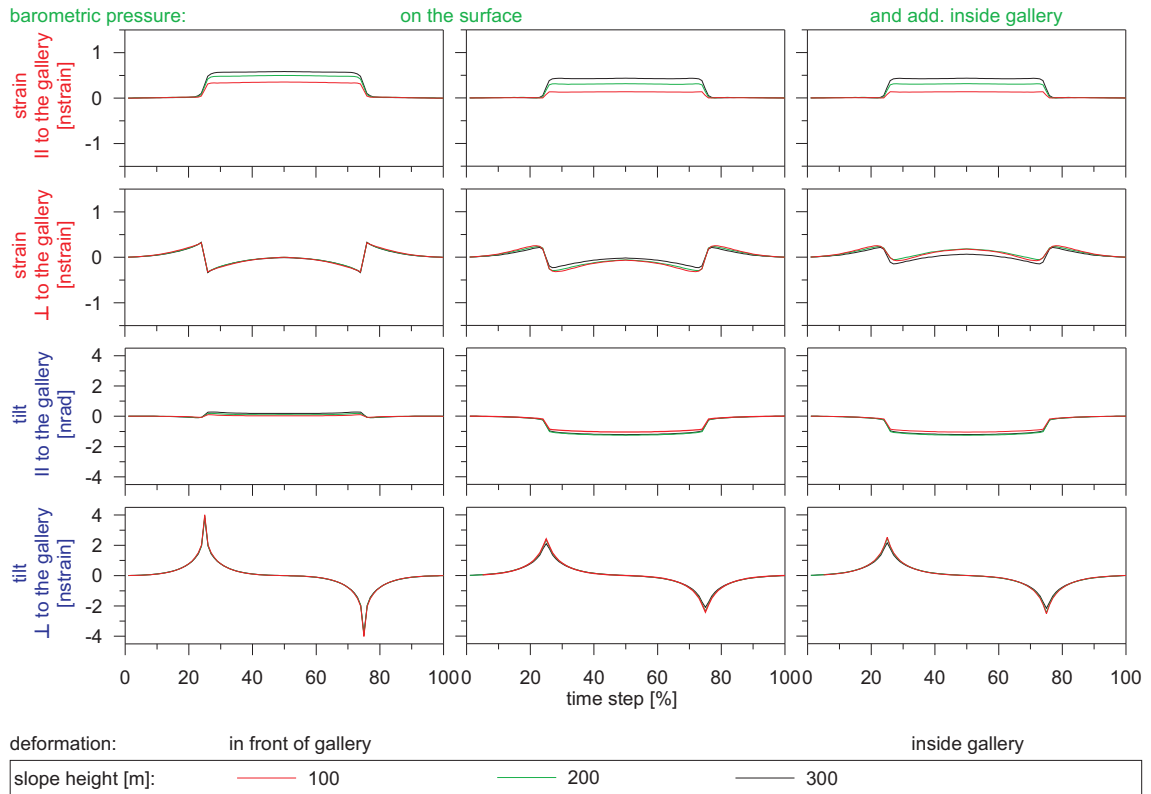


App. Fig. 7: Deformation results for a 30° slope model type of a slope height of 300 m and gallery type B included related to the moving height pressure areas.

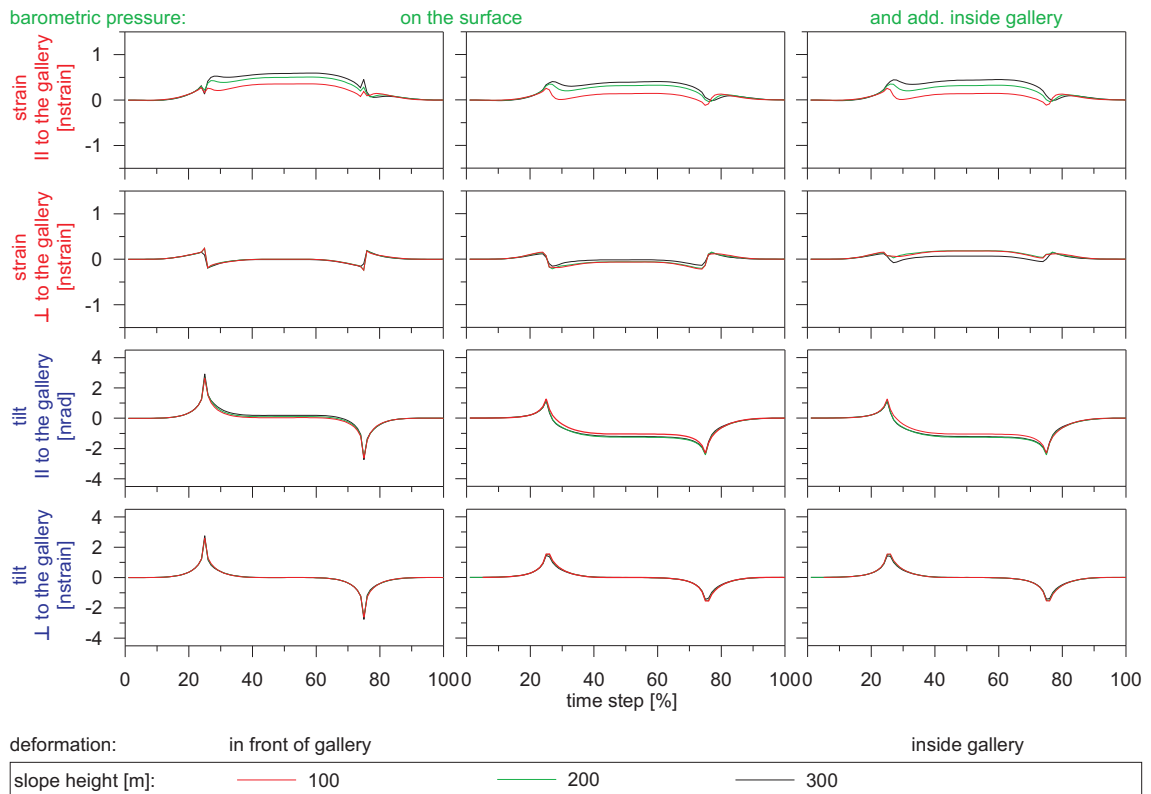


App. Fig. 8: Deformations obtained for the 30° slope model type and gallery type A and high pressure area moving parallel to the gallery.

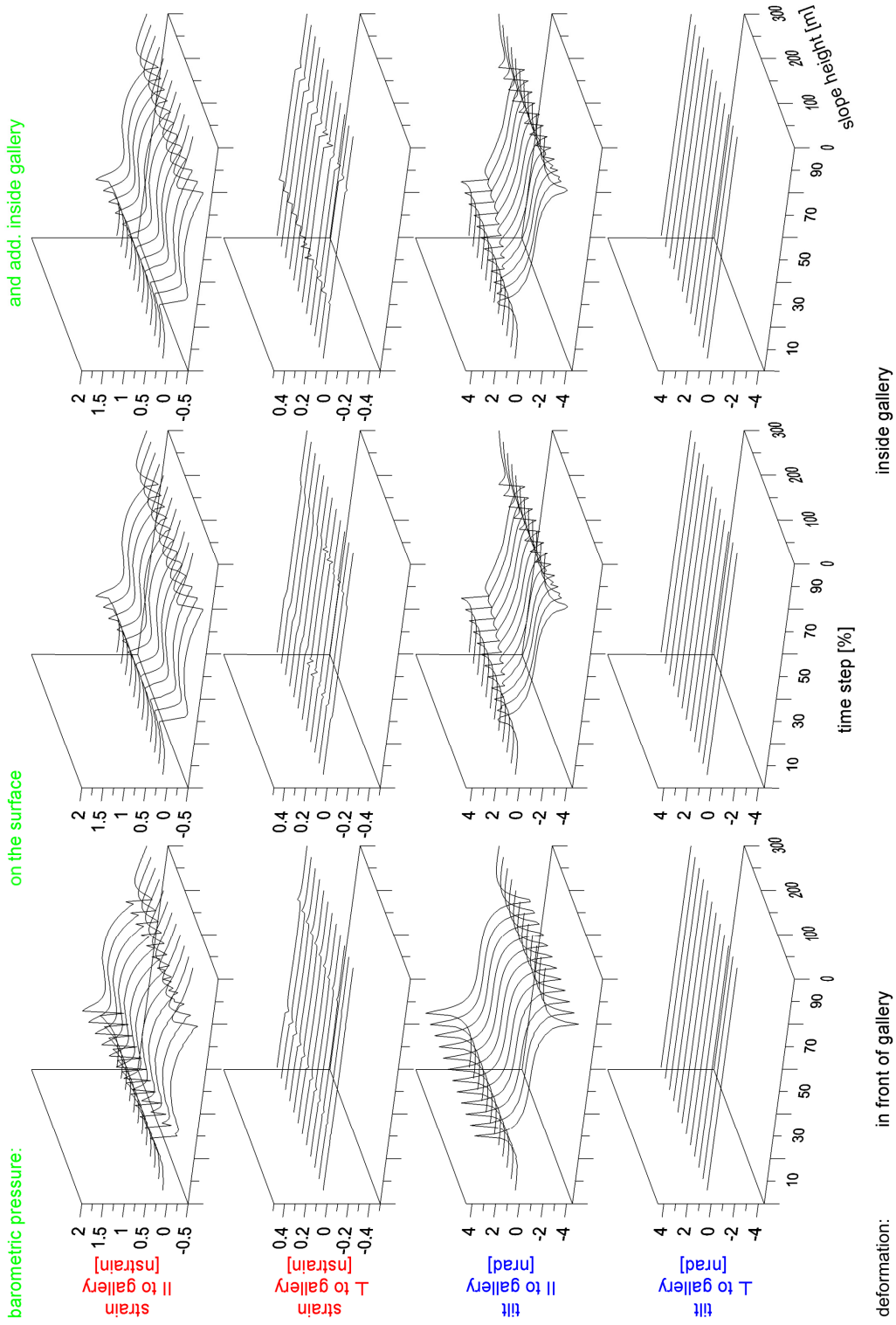
Appendix



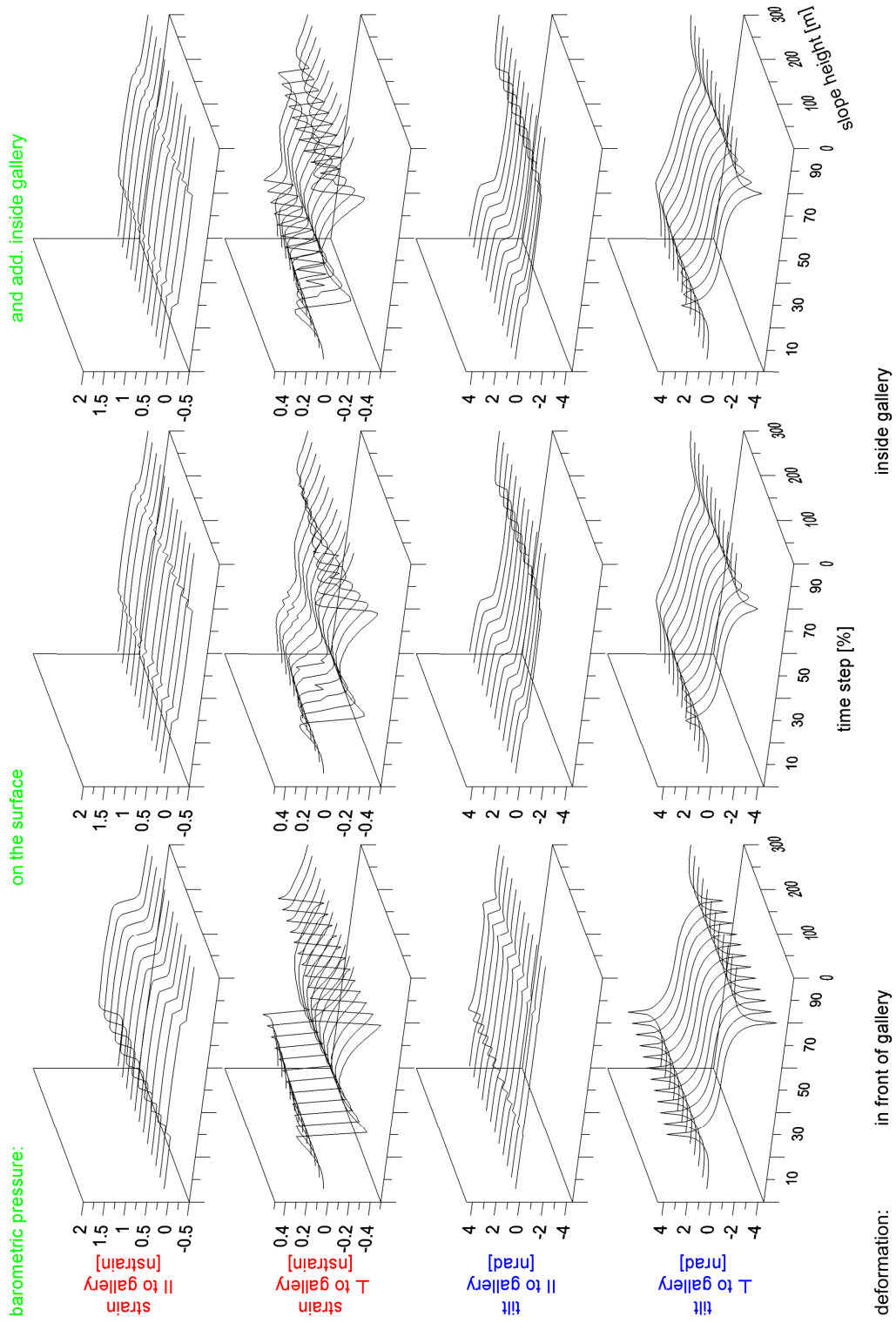
App. Fig. 9: As [App. Fig. 8](#) but for high pressure area moving perpendicularly to gallery.



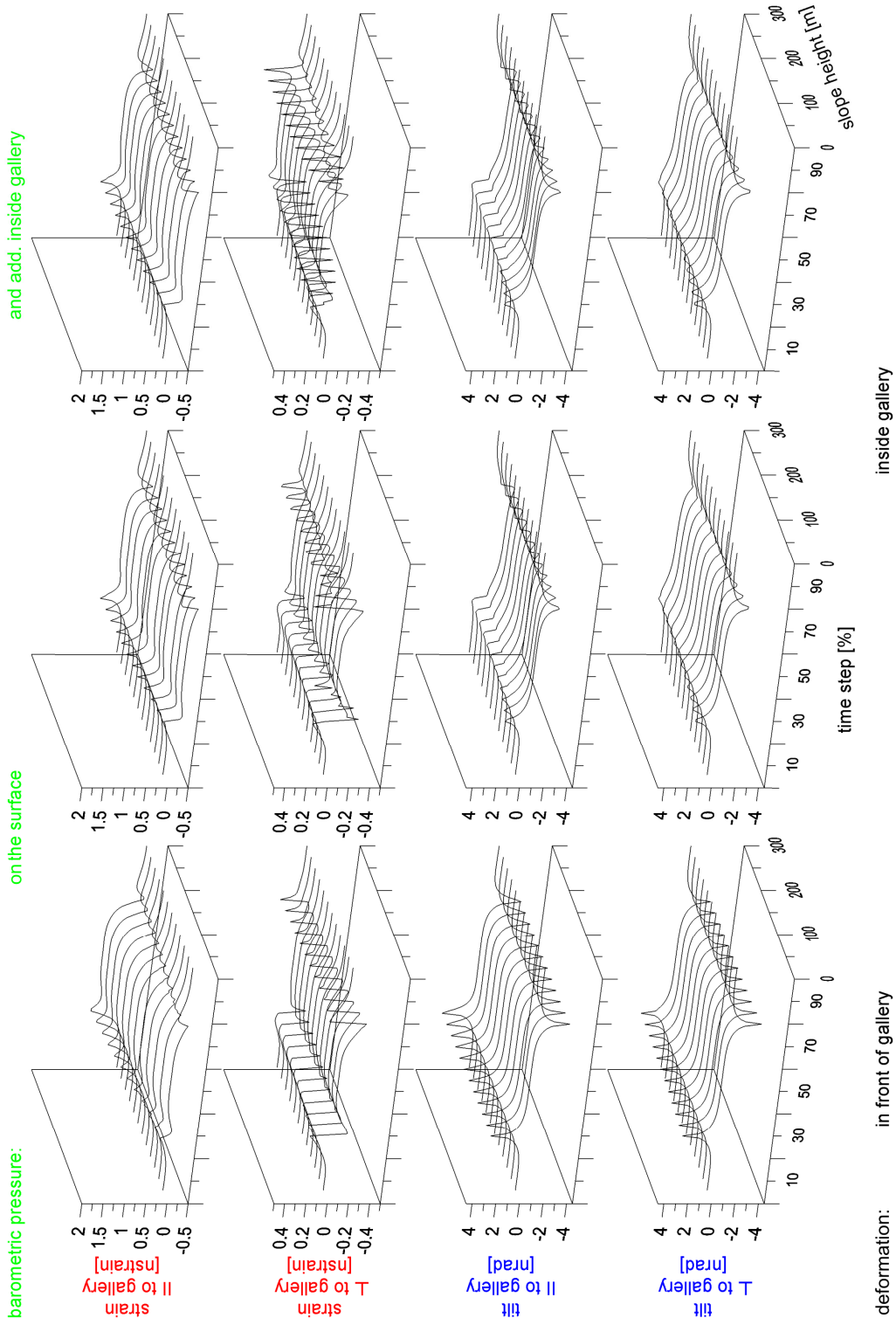
App. Fig. 10: As [App. Fig. 8](#) but for high pressure area moving diagonally to gallery.



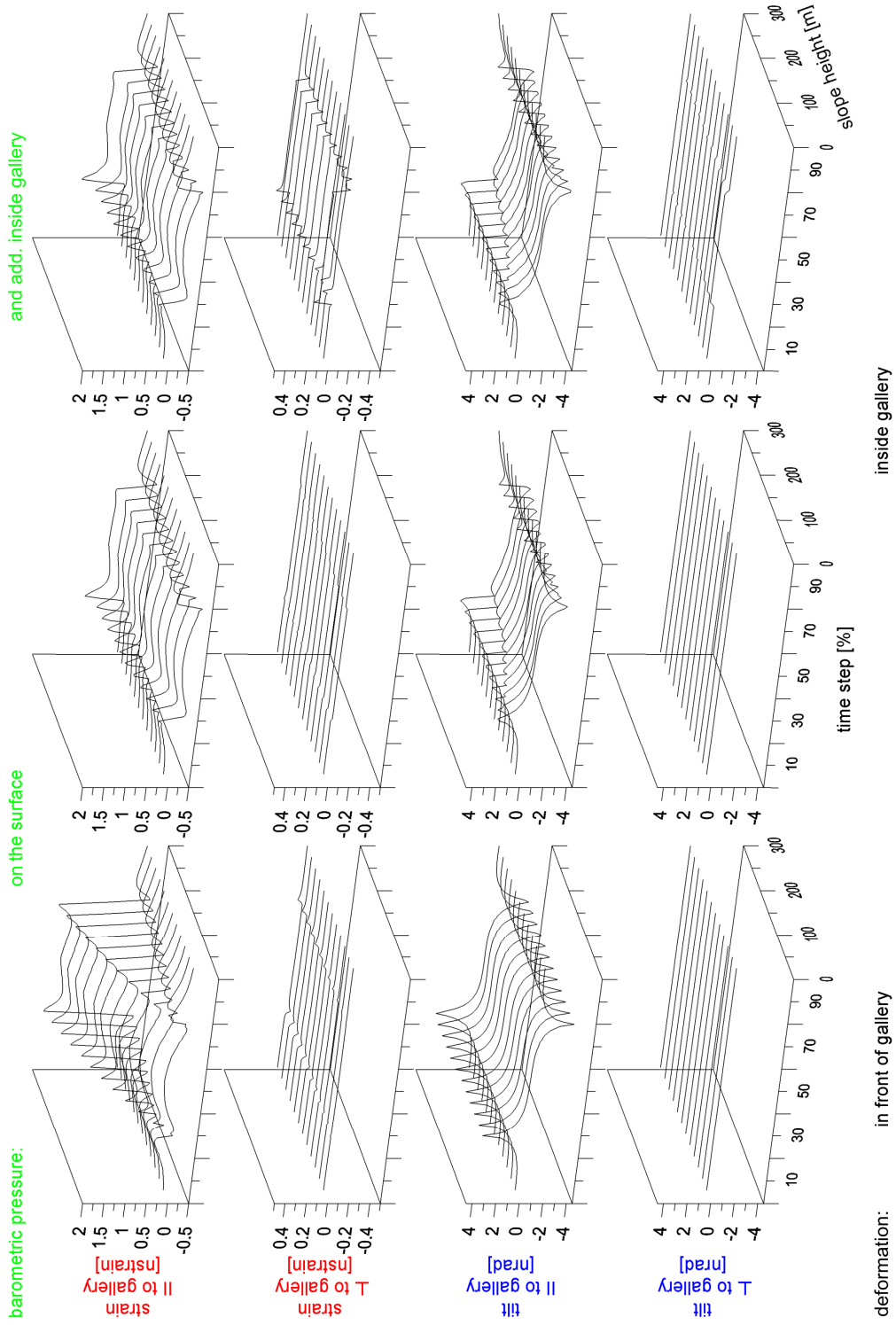
App. Fig. 11: Deformation results for a 90° slope model type (slope height varied between 25 m and 300 m) and gallery type A for the parallel to the gallery moving high pressure area (different scaling).



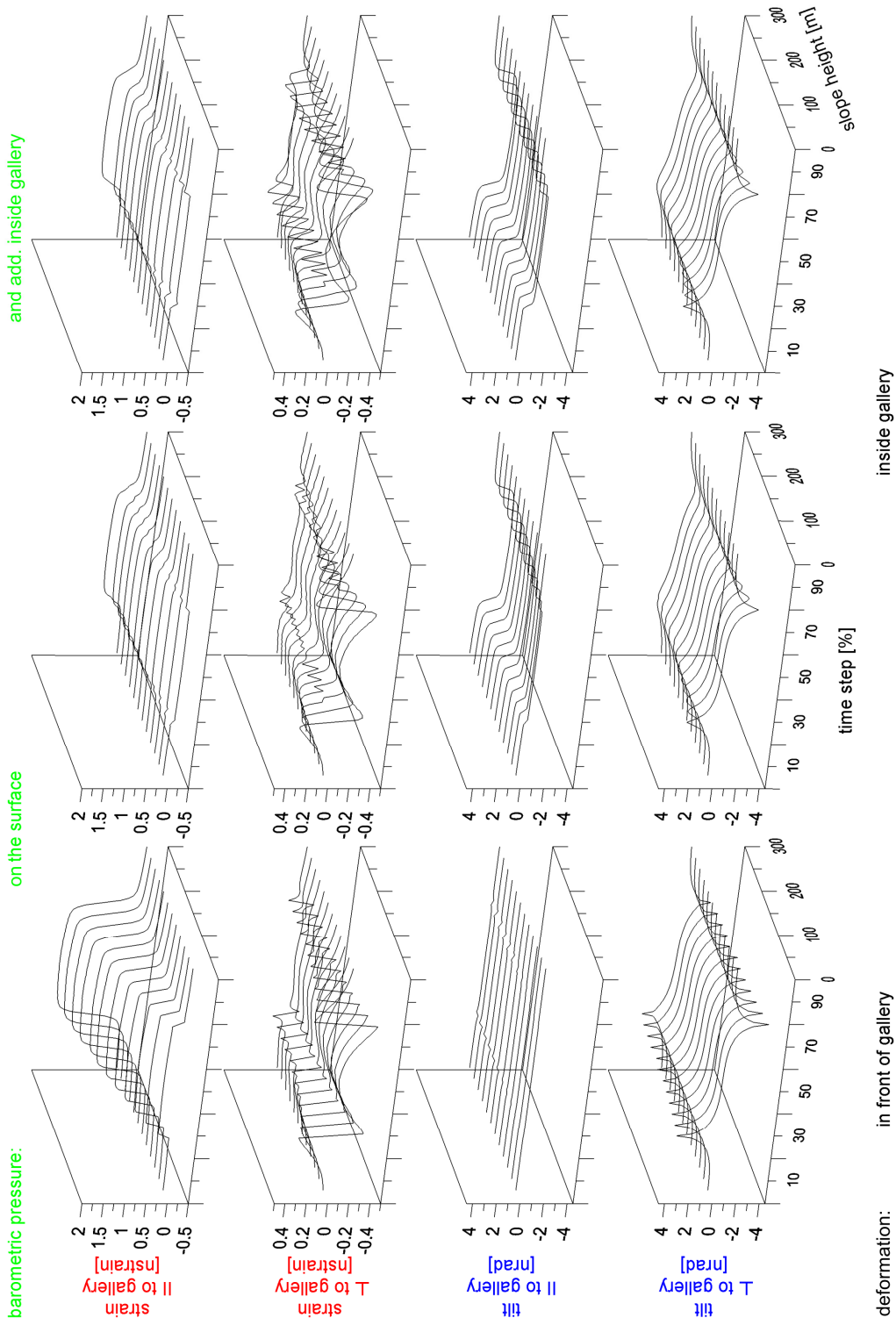
App. Fig. 12: As [App. Fig. 11](#) but for high pressure area moving perpendicularly to gallery.



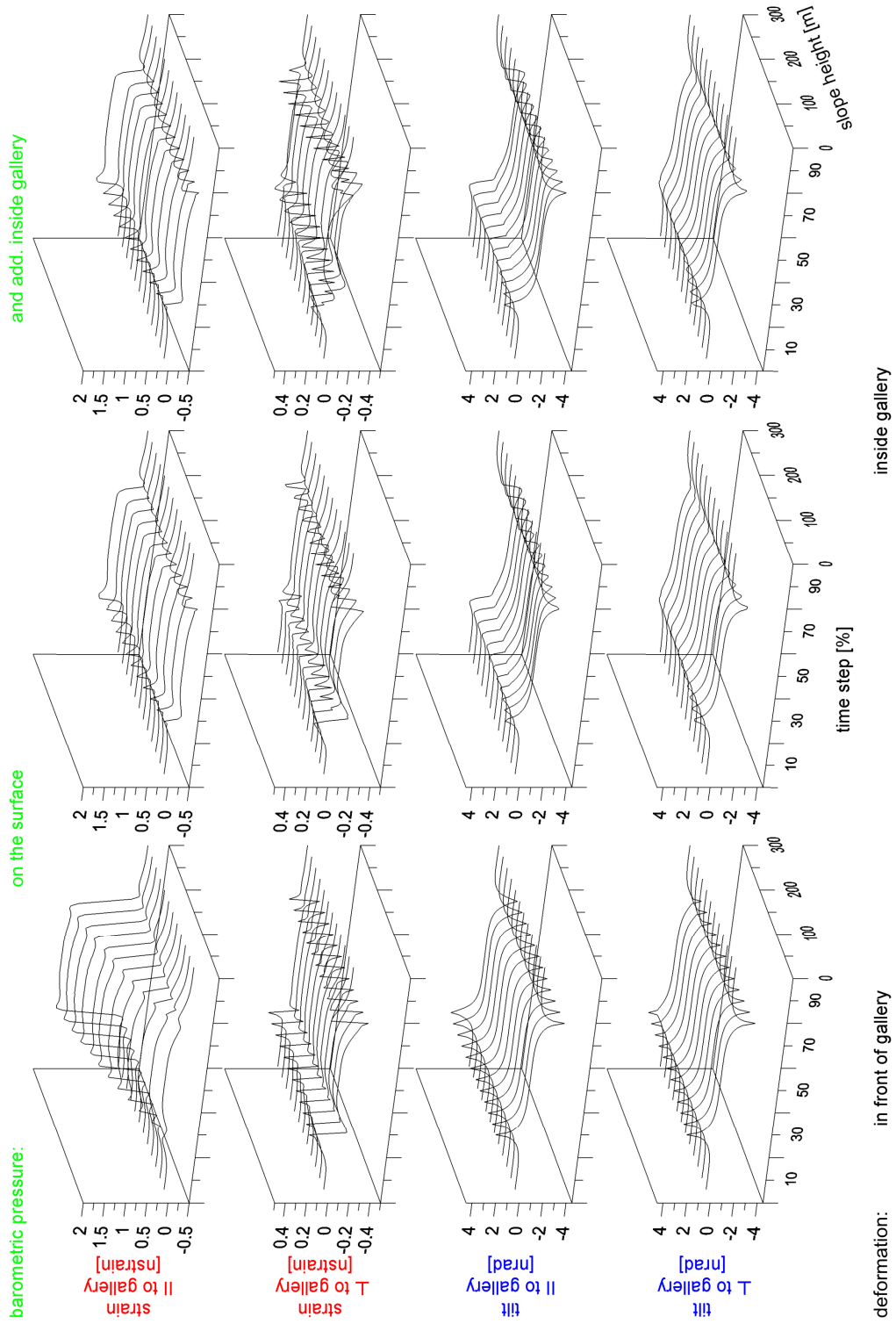
App. Fig. 13: As [App. Fig. 11](#) but for high pressure area moving diagonally to gallery.



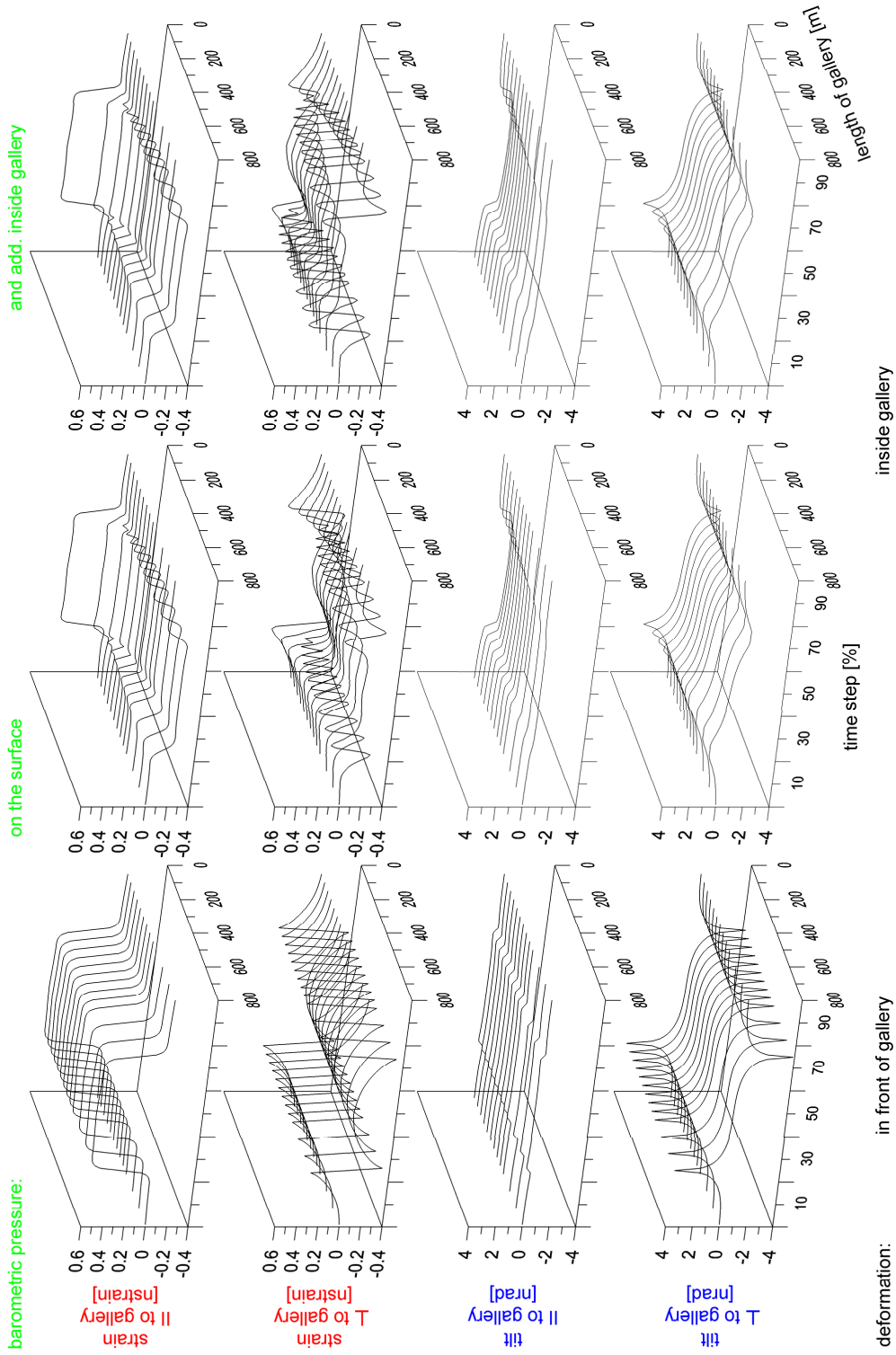
App. Fig. 14: Deformation results for a 90° valley model type (slope height varies between 25 m and 300 m) and gallery type A for the parallel to the gallery moving high pressure area (different scaling).



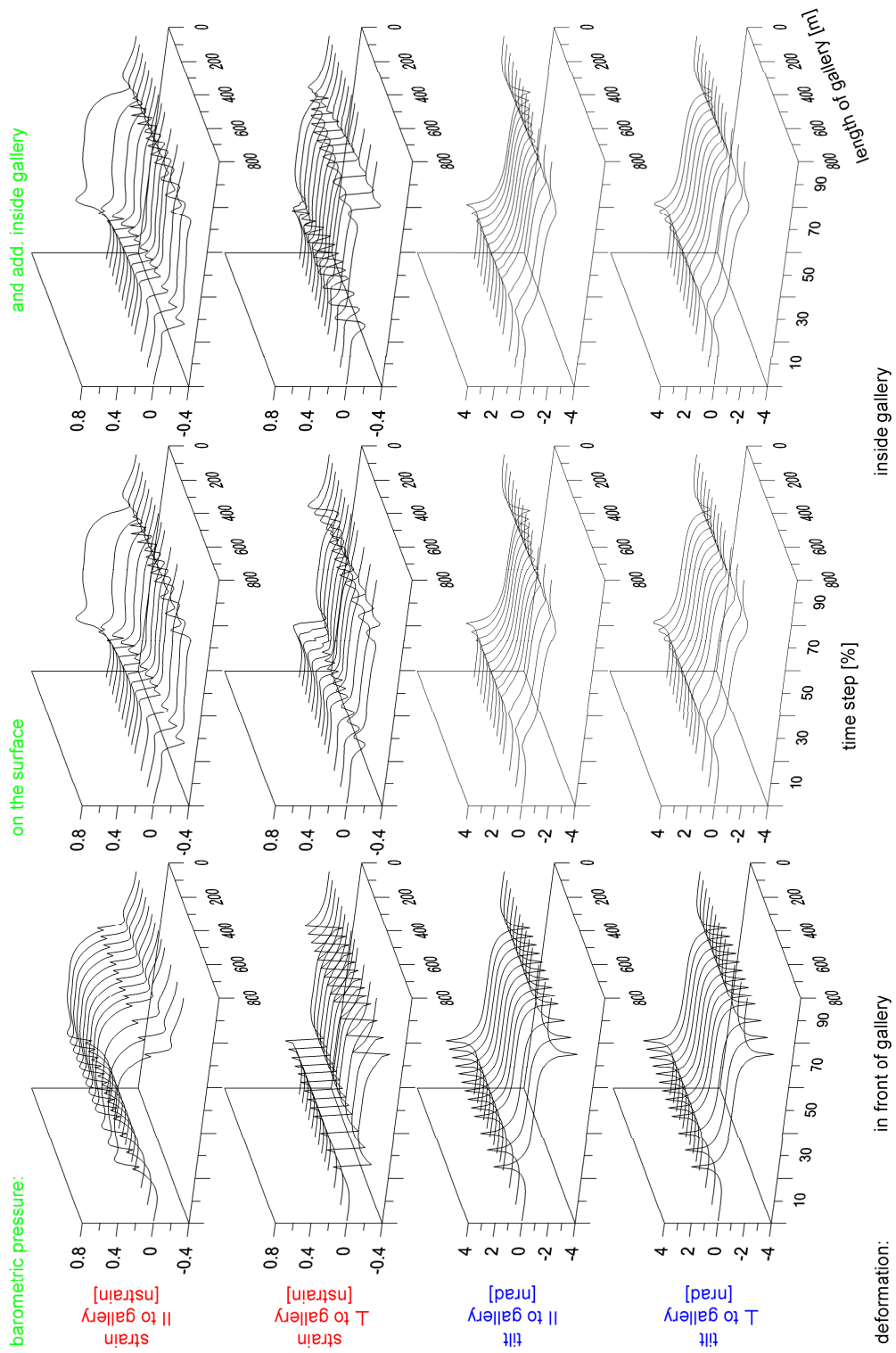
App. Fig. 15: As [App. Fig. 14](#) but for high pressure area moving perpendicularly to gallery.



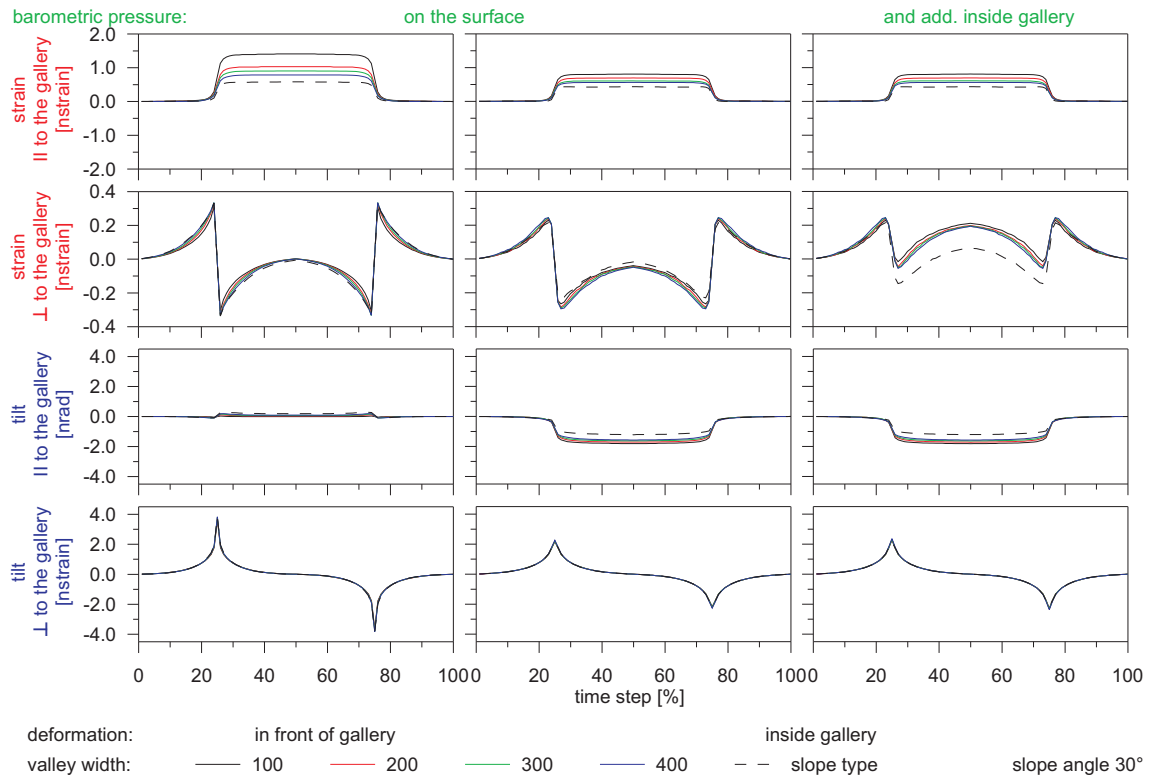
App. Fig. 16: As App. Fig. 14 but for high pressure area moving diagonally to gallery (different scaling).



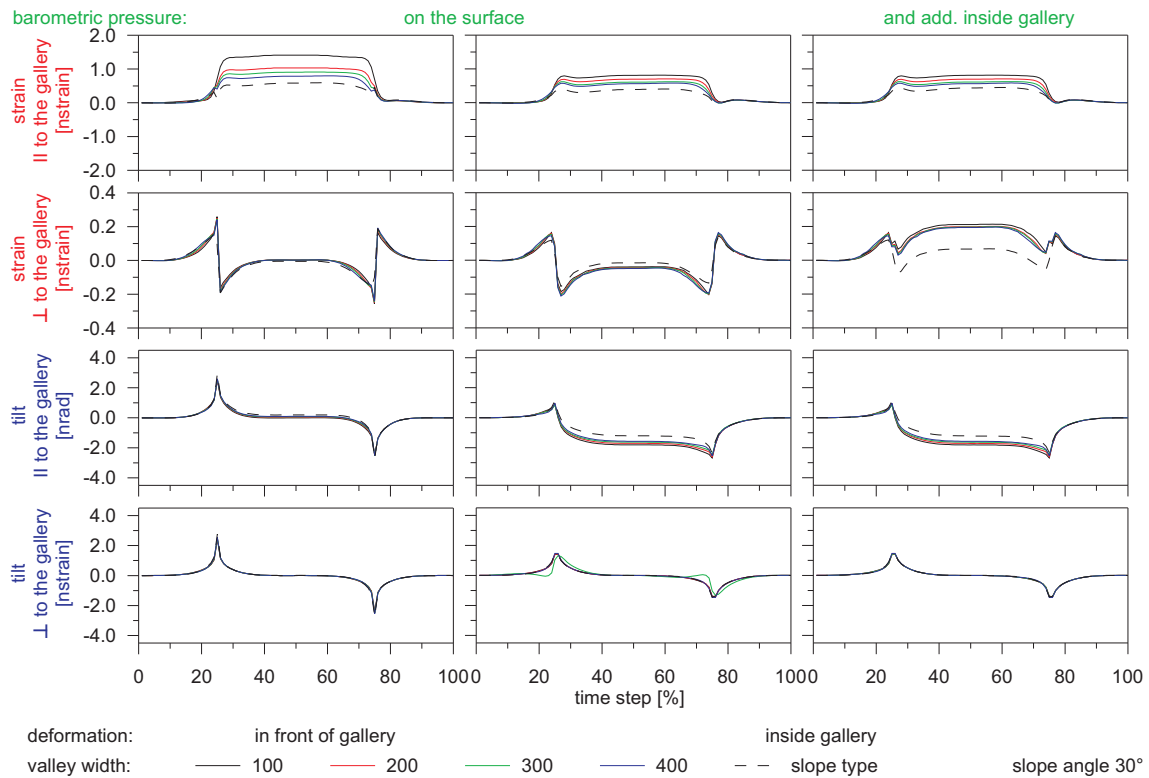
App. Fig. 17: Deformation results for 30° slope model type and variable gallery lengths of type A (50 m to 800 m) for a perpendicular to the gallery moving high pressure area.



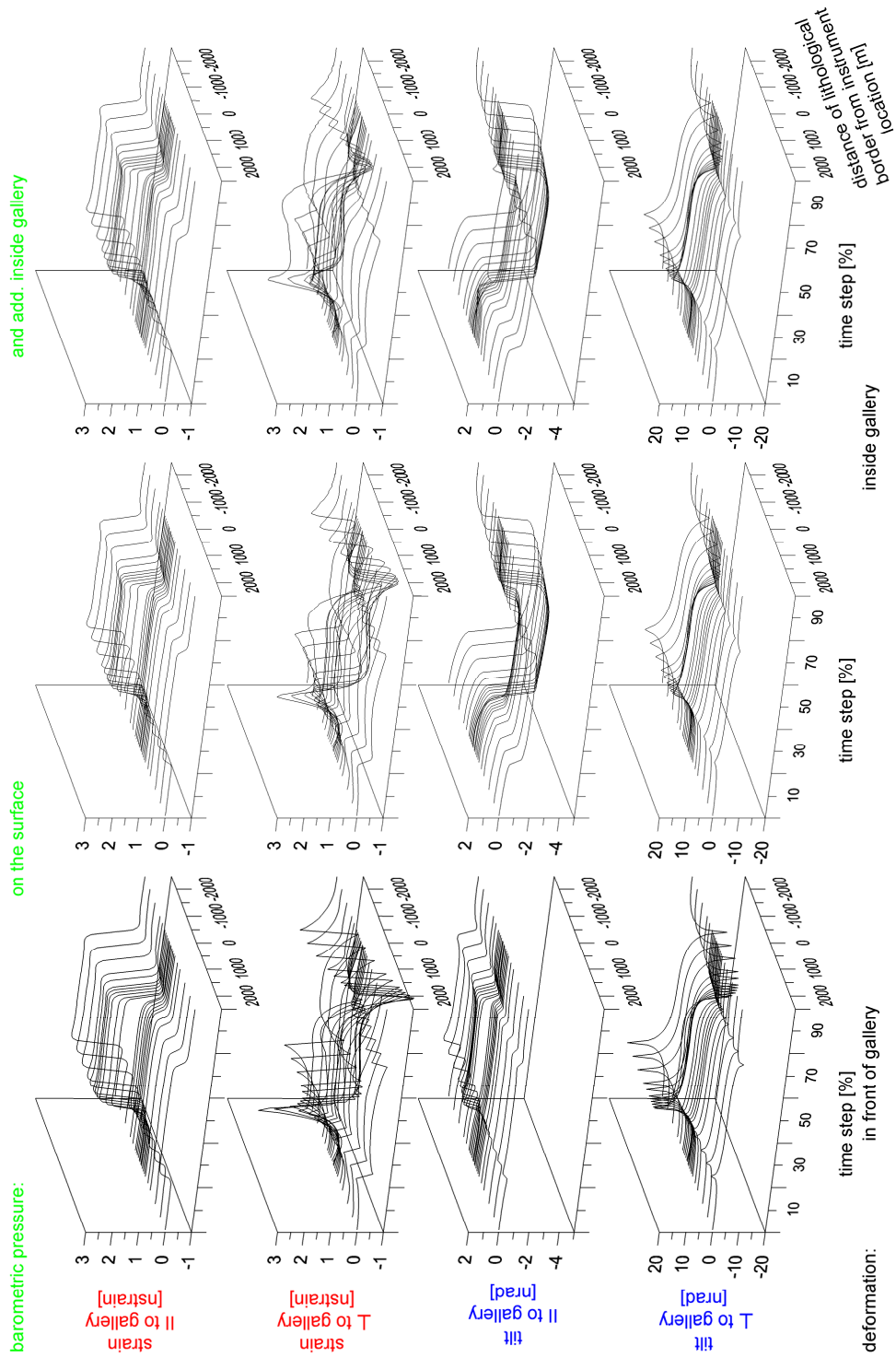
App. Fig. 18: As [App. Fig. 17](#) but for high pressure area moving diagonally to gallery.



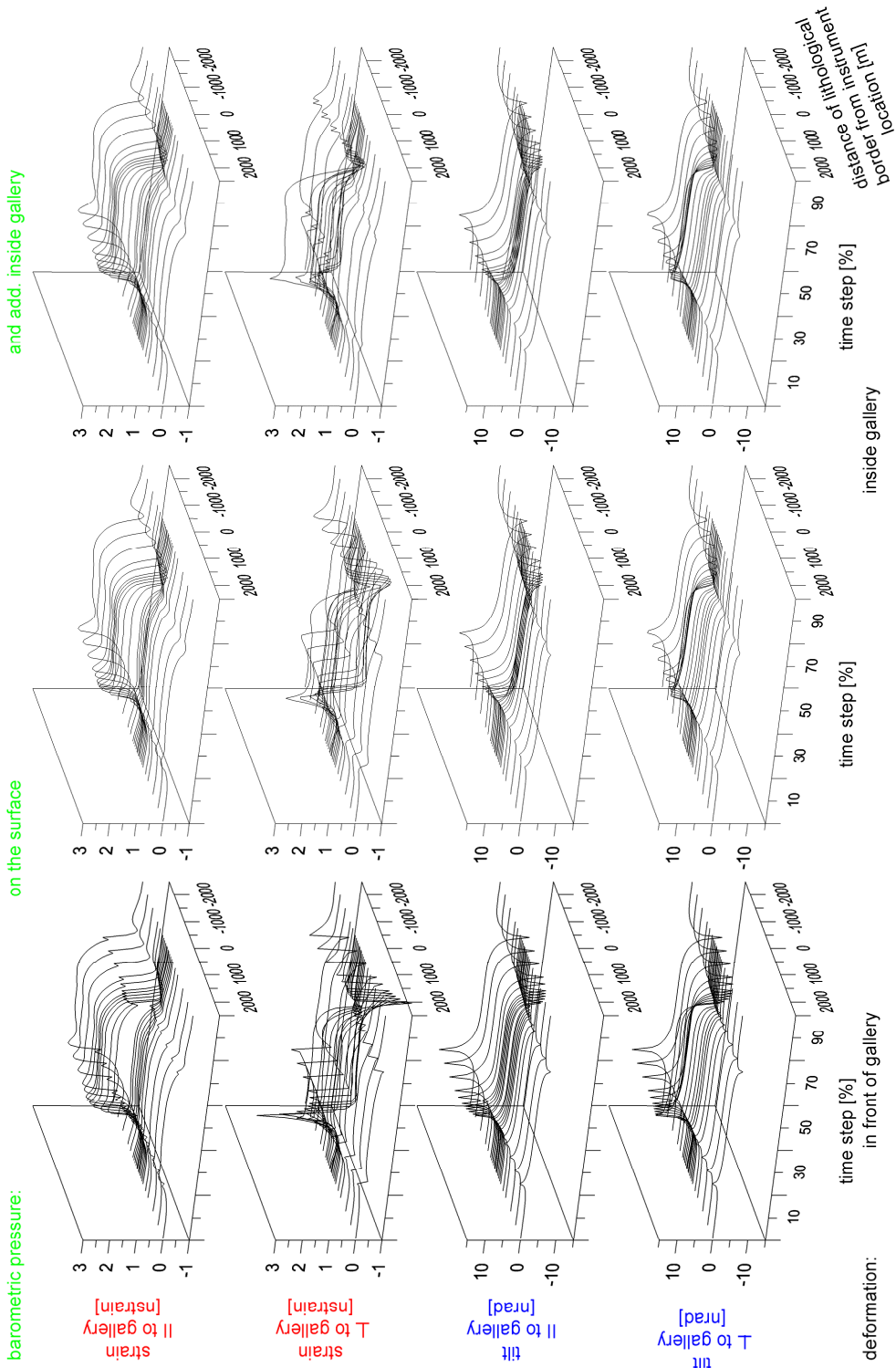
App. Fig. 19: Deformation results for perpendicular to gallery moving high pressure area related to the effect of the valley width and reference slope model for a slope angle of 30° (different scaling).



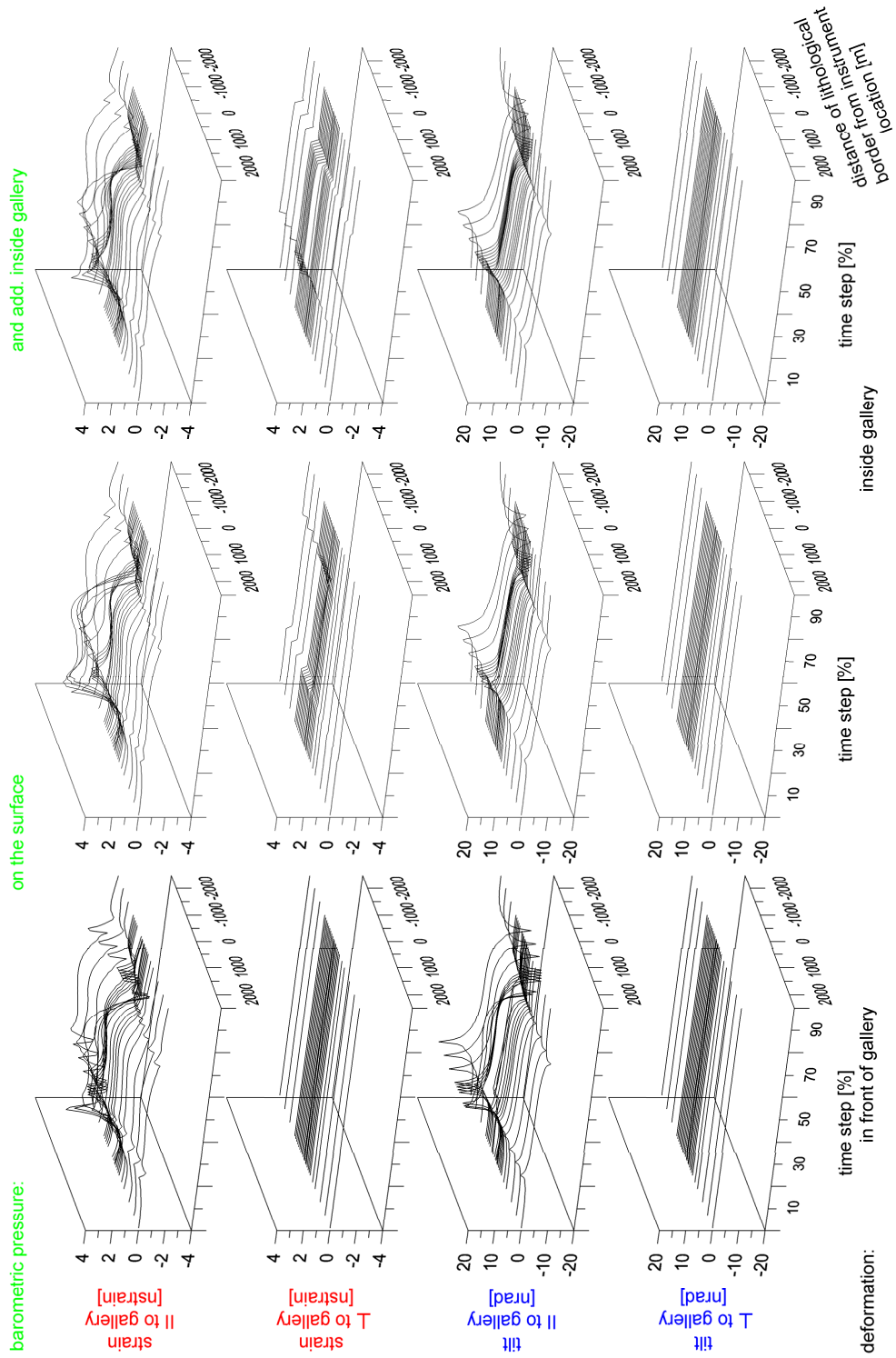
App. Fig. 20: Deformation results for diagonal to gallery moving high pressure area related to the effect of the valley width and reference slope model for a slope angle of 30° (different scaling).



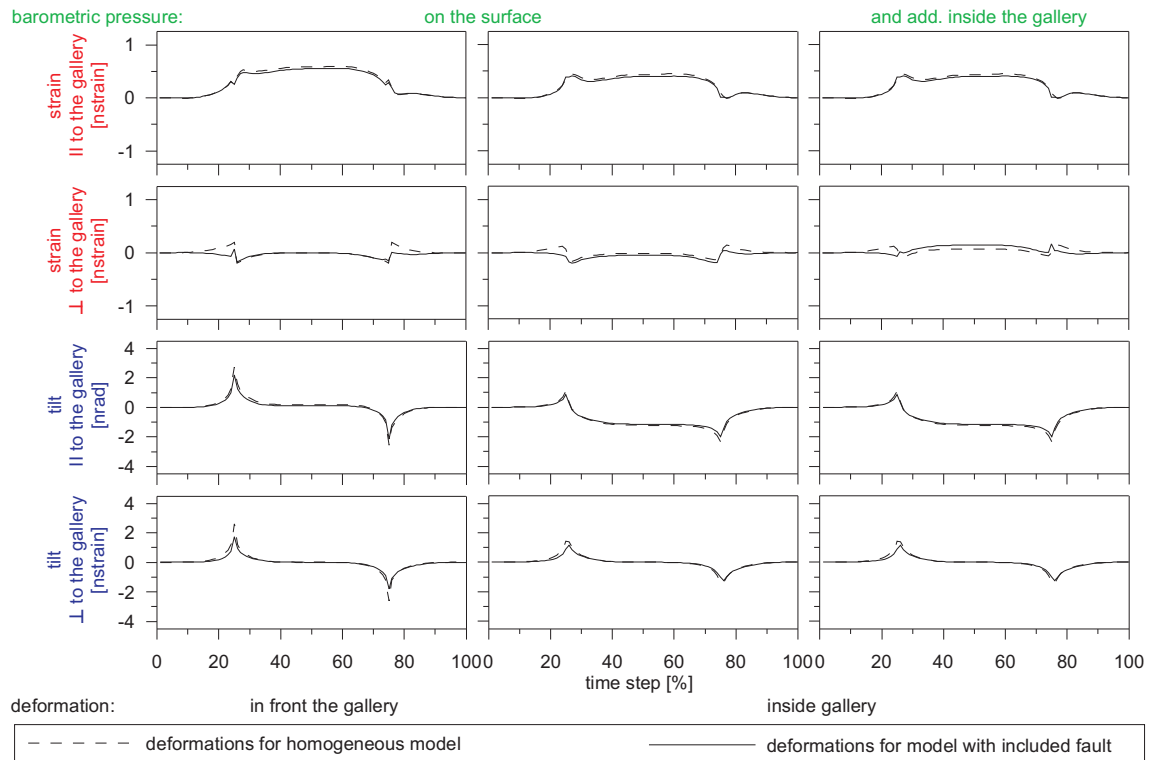
App. Fig. 21: Deformation results for a 30° slope model type and gallery type A and parallel to the gallery oriented lithological border (comp. Fig. 5.31a) for a perpendicular to the gallery moving high pressure area (different scaling).



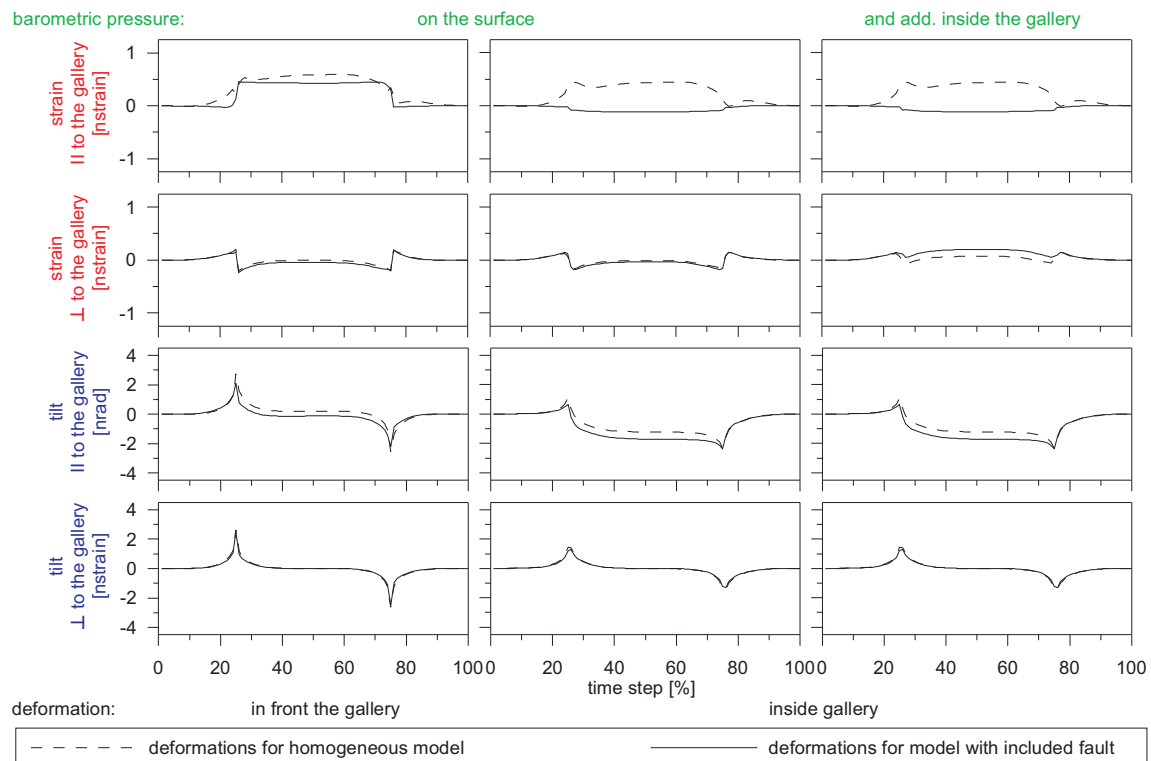
App. Fig. 22: Deformation results for a 30° slope model type and gallery type A and parallel to the gallery oriented lithological border (comp. Fig. 5.31a) for a diagonal to the gallery moving high pressure area (different scaling).



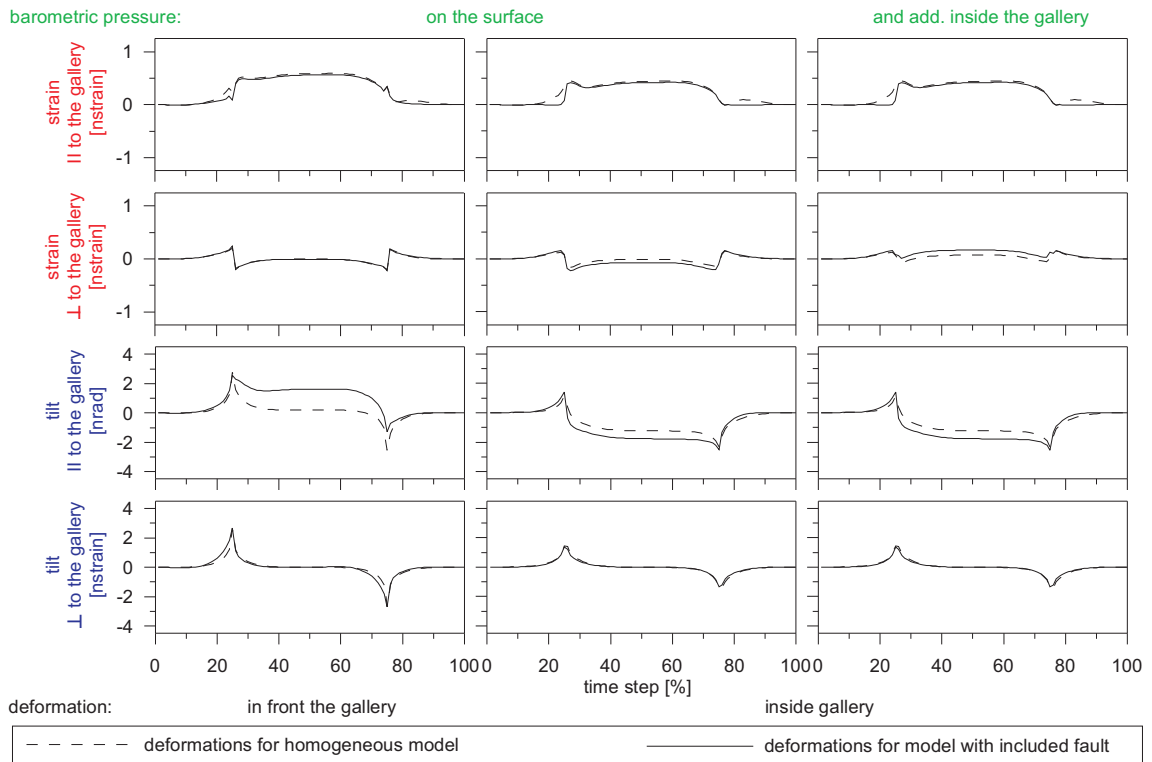
App. Fig. 23: Deformation results for a 30° slope model type and gallery type A and perpendicular to the gallery oriented lithological border (comp. for a parallel to the gallery moving high pressure area). **Fig. 5.31b**



App. Fig. 24: Deformation results for a 30° slope model type and gallery type A. Parallel to the gallery in a distance of 50 m a fault with a length of 300 m and a depth of 100 m is included. For load the diagonally moving high pressure areas are considered.

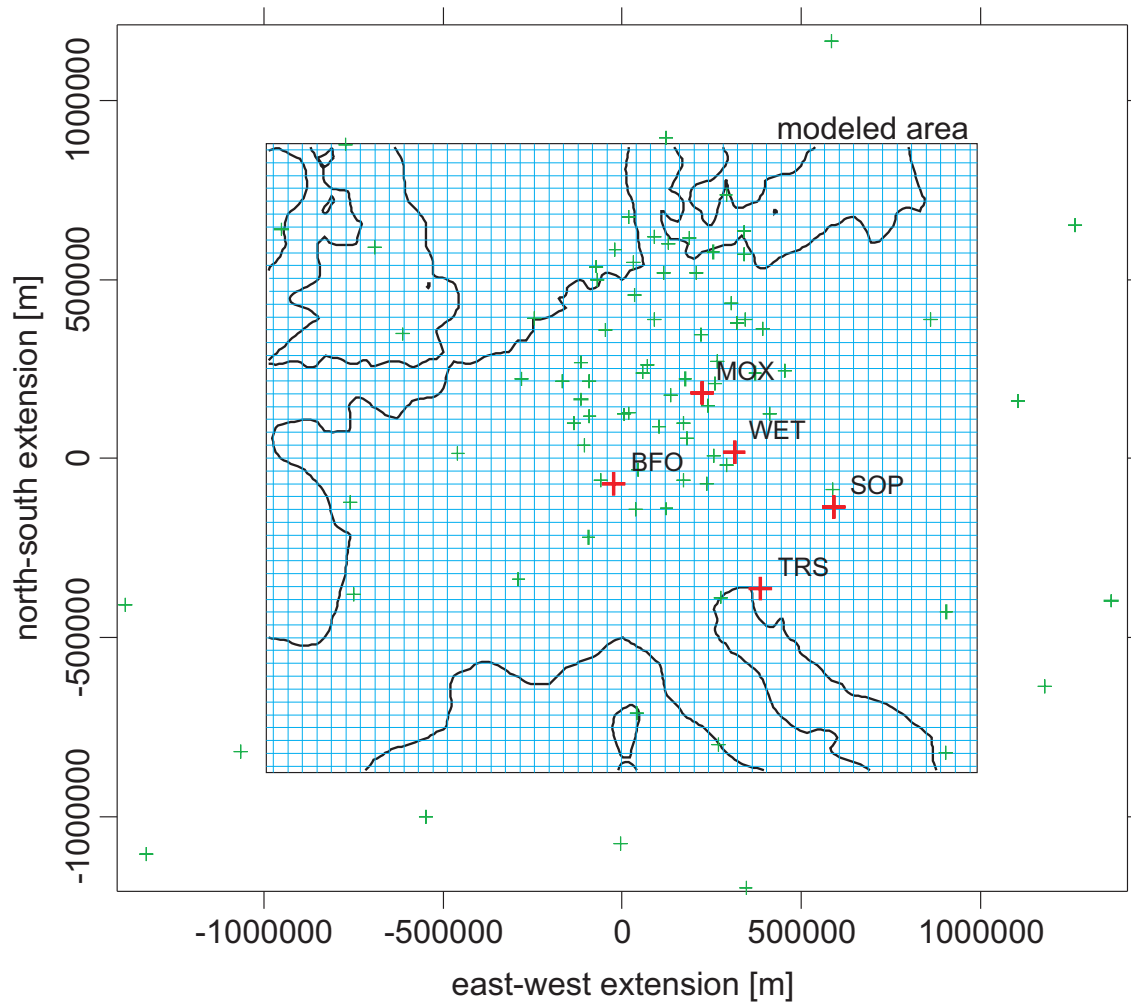


App. Fig. 25: Deformation results for a 30° slope model type and gallery type A and fault located at the gallery entrance, perpendicularly oriented. For load diagonally moving high pressure areas are considered.



App. Fig. 26: Deformation results for a 30° slope model type and gallery type A included and fault located 50 m behind the gallery head perpendicular oriented. For load diagonally moving high pressure areas are considered.

Appendix B: Barometric pressure grid used in modeling for Central Europe



App. Fig. 27: Locations of barometric pressure observations used for calculation of the pressure field and defined rectangular cells loading the model and locations of observatories of interest.

Acknowledgements

First I would like to sincerely thank PD Dr. Corinna Kroner, my supervisor, for providing me this interesting work. Her generous supervision made me feel comfortable in pursuing the subject, and during my work, she had always time for discussion and gave helpful suggestions. Besides her, I am especially indebted to PD Dr. Thomas Jahr. He always listened to my countless questions and had time for very special scientific and sometimes also nonscientific discussions. The financial support from the German Research Foundation is also gratefully acknowledged.

Prof. Dr. Gerhard Jentzsch I want to thank for the possibility to work on my thesis in his working group 'Applied Geophysics' and his role as adviser. Besides them, I would like to thank the other colleagues from the working group and from the Institute of Geosciences of the Friedrich-Schiller-University Jena for the joyful time. Especially, Prof. Dr. Jonas Kley and Jewgenij Torizin are thanked for their help in geological questions.

Prof. Dr. Georg Kaufmann is thanked to examine the present work.

I gratefully acknowledge Dr. Kaspar Fischer and Dr. Holger Steffen, as the Geoqus User Group for helpful encouragement and discussions while working with ABAQUS. For the possibility of calculation the FE models we thank the Department of Geophysics at the Institute of Geology, Mineralogy and Geophysics in Bochum and the Department of Geophysics at Freie Universität Berlin.

I thank Dr. Walter Zürn, Dr. Malte Westerhaus, Dr. Gyula Mentés, Dr. Thomas Klügel, and Dr. Carla Braitenberg for providing detailed data of their observatories, observed time series and valuable discussions.

My thanks go to Andreas Hoffmann for many valuable hints in the Linux and Windows world and the help in speed of light with the one or other evil computer problem.

Selbständigkeitserklärung

Ich erkläre, dass ich die vorliegende Arbeit selbständig und unter Verwendung der angegebenen Hilfsmittel, persönlichen Mitteilungen und Quellen angefertigt habe.

Jena, 10.08.2009

André Gebauer

Curriculum Vitae

Personal details

Name: André Gebauer
Date of Birth: 09 November 1978
Place of Birth: Sömmerda
Nationality: German
Marital status: Unmarried

Education

08/85 to 07/91 Polytechnische Oberschule „Karl-Liebknecht“ Bad Kösen –
Primary and Secondary School
08/91 to 07/93 Domgymnasium – Grammar School in Naumburg
08/93 to 07/97 Landesschule Pforta – Residential School in Schulpforte
07/97 Abitur (A-levels)
10/99 to 07/06 Study of Geosciences at Friedrich-Schiller-University Jena
09/01 Intermediate examination
07/06 Diploma (MSc) in Geophysics
Majors: Geophysics, Physics, Applied Geology, Astrophysics
Thesis: Ein Neigungsmesser-Array an der KTB
since 07/06 PhD student at Friedrich-Schiller-University Jena

Contracts

11/97 to 02/99 Military service at Panzeraufklärungskompanie 140 in Sontra
(07/98 to 11/98 foreign assignment in Bosnia-Herzegovina)
08/97 to 10/97 unskilled worker in construction company
03/04 Leibniz Institute for Applied Geophysics, geophysical land measuring
09/04 to 10/04 Alfred Wegener Institute for Polar and Marine Research in Bremer-
haven, geophysical cruise on the research vessel FS Polarstern
Tasks: refraction seismic and wide angle reflection seismic
04/05 to 05/05 Alfred Wegener Institute for Polar and Marine Research in Bremer-
haven, geophysical cruise on the research vessel FS Sonne
Tasks: refraction seismic and wide angle reflection seismic
07/06 to 07/08 Doctoral student in the working group “Applied Geophysics” at the In-
stitute of Geosciences of the Friedrich-Schiller-University Jena
Scientific Tasks: modeling of structural and geological effects on
deformations of the upper crust
since 07/08 Doctoral student at the Helmholtz Centre Potsdam (Sect. 1.3)
Scientific Tasks: modeling of structural and geological effects on
deformations of the upper crust

Jena, Monday, August 10, 2009

André Gebauer

